THE UNIVERSITY OF CHICAGO

EXPLORATION OF HIGHLY-CORRELATED SYSTEMS ON CLASSICAL AND QUANTUM DEVICES

A DISSERTATION SUBMITTED TO
THE FACULTY OF THE DIVISION OF THE PHYSICAL SCIENCES
IN CANDIDACY FOR THE DEGREE OF
DOCTOR OF PHILOSOPHY

DEPARTMENT OF CHEMISTRY

BY
LEEANN MARIE SAGER-SMITH

CHICAGO, ILLINOIS
AUGUST 2023

To my loving and supportive family

TABLE OF CONTENTS

LIST OF FIGURES

LIST OF TABLES

ACKNOWLEDGMENTS

Many thanks and much admiration goes to David Mazziotti, my Ph.D. advisor, who started me on the path to realizing this research and supported me along the journey. Additional thanks to the members of the Mazziotti Research Group—past and present—who have mentored me throughout my time at the University of Chicago, collaborated on research, and/or supplied moral support: Shiva Safaei, Anthony Schlimgen, Kade Head-Marsden, Ali Raeber, Scott Smart, Jan-Niklas Boyn, Simon Ewing, Daniel Gibney, Anna Schouten, Samuel Warren, Irma Avdic, Lily Payne, Luis Delgado Granados, and Jordan Klevens. Further gratitude to the other members of my committee—Dr. Sarah King, and Dr. Suri Vaikuntanathan—for reading this document critically and evaluating my thesis defense. Moreover, I'd like to acknowledge the Eckhardt Fellowship and the NSF Graduate Research Fellowship for providing financial support throughout my graduate career as well as IBM's Quantum Experience and Amazon Braket for supplying reliable access to quantum computers during the course of my research. Additional thanks to the quantum computing and machine learning communities at large—especially those who answered my questions on Slack and Stack Exchange.

Further, the encouragement that my loved ones have supplied throughout my graduate career should not be overlooked. Thank you so much to my husband—Jordan Smith—for holding my hand through the stressful times that come with big life changes. Thank you to my parents—Kent and Michelle Sager—for always providing the reassurance and love I needed to follow my dreams. Thanks to my extended support system—including my brother, Daniel Sager; the Archambaults, Emily, Jacob, and Matthew; my good friends, Alyssa Osborn, Natasha Chemey, and Anna Fox; my grandparents, both the Sager and Turner variety; my in-laws, the Smith/Arehart/Zwingelberg crew as well as Amanda Sager; and my aunts, uncles, and cousins that are framily as well as family. I am very lucky to have so many people who love me, and I feel very fortunate for needing to make such a lengthy acknowledgement.

ABSTRACT

Elucidation of many chemical behaviors and properties depends on our ability to model the physics of electron-electron interactions at reasonable computational expense with correlation phenomena often being integral to predicting behaviors and properties of molecules and materials of contemporary interest. A particularly sought-after consequence of a type of correlation is superconductivity, which traditionally results from the Bose-Einstein-like condensation of Cooper (electron-electron) pairs. However, all currently-known superconductors condense at either too-low of temperatures or too-high of pressures to be commercially-viable. A possible solution to this limitation is the utilization of excitonic superfluidity arising from the condensation of particle-hole pairs (excitons) which are expected to condense at higher temperatures due to their decreased mass and which can result in the frictionless flow of excitation energy and—in bilayer systems—counterflow superconductivity. The first chapters of this text focus on the identification of the beginnings of exciton condensation in molecular-scale analogues of extended systems in an effort to contribute to rational design of molecularly-scaled exciton condensates. Then, the simulation of both Cooper pair and exciton condensates on quantum devices is described, which establishes a new avenue for the creation and characterization of condensation phenomena and is an important step toward more complex modeling of phenomena with significant quantum long-range order on quantum computers. The following chapters introduce fermion-exciton condensates (FECs)—novel quantum states that simultaneously exhibit the character of superconducting states and exciton condensates and may demonstrate hybrid properties of both. In this thesis, these FECs are computationally and theoretically predicted, described with a model Hamiltonian, and experimentally prepared on a quantum device. Finally, machine learning is used to reduce the many-electron problem to an effective two-electron problem, decreasing effective computational scaling with system size.

PREFACE

> In science one tries to tell people, in such a way as to be understood by everyone, something that no one ever knew before.
>
> —Paul Dirac

Before you lies the culmination of the last five years of my professional life. I began the work that led up to this document in July 2018 during my summer rotation in the Mazziotti group when we asked the deceptively-simple question: "Is it possible to have a system that demonstrates both superconductivity and exciton condensation?" Many months—and much back-and-forth with David (my advisor), Shiva (a post-doc that mentored me), and several reviewers—later, we had our answer: "Yes." Rather than satisfying my curiosity, this answer—as all good answers do—led to more questions. Now that we knew that this so-called fermion exciton condensate (FEC) was possible, we asked "What sorts of systems will demonstrate an FEC? What sorts of properties will those systems have? Can FECs be realized experimentally?" These questions have motivated much of my work over the past five years and led to additional insights along the way.

First, although molecular systems that demonstrate superconductivity are well-studied, we needed to elucidate the types of systems that may demonstrate exciton condensation in their ground state, which led to works on exciton condensation in molecular systems presented in Part II. Further, quantum devices provide one of the few avenues for the experimental preparation of quantum systems directly available to us theorists. With a goal of directly preparing a FEC on a quantum device, I first gained insight by preparing exciton condensates and condensates of Cooper pairs on quantum systems as presented in Part III. Then, in Part IV, I introduce FECs with my first paper in the Mazziotti group and go on to answer a few of the above questions by leveraging the information gained from studying exciton and Cooper pair condensation to introduce a model Hamiltonian that describes FECs and prepare a FEC on a quantum device. I predict that my future work at Saint Mary's

College—where I'm to start as the new Assistant Professor of Physical Chemistry in Fall Semester 2023—will likely continue to focus on exploring fermion-exciton condensates.

The only section of this document that does not fit this narrative is my recent interest in Machine Learning approaches for quantum chemistry, which is presented in Part V. This study is alternatively motivated by a desire to decrease the expense of quantum chemical computations, which scales prohibitively with system size—a distinct but worthy goal.

In this thesis, I try to follow the edict of Dirac and make my work as understandable as possible to a general chemistry audience who may not be familiar with electronic structure theory, reduced density matrix approaches, condensation phenomena, quantum computation, and machine learning. As such, I provide chapters preliminarily introducing these topics. Unless previously familiar, I suggest that readers engage with Chapters 1 and 2 as a primer before approaching the rest of this document. Further, while Part V can be understood without Chapter 3, it is a good resource to review before reading the rest of this document. Introductions to both quantum chemistry and machine learning are given in Chapters 6 and 13, respectively, immediately preceding the chapters for which they are relevant.

While this thesis only contains a selection of my work on which I was the primary author, all of the works to which I have contributed are given by Refs. [4, 5, 11–25]. Chapter 4 is additionally included in this document as a previous version of Ref. [24] where I focus on Bechgaard-like TTF van der Waal heterostructures before Anna reworked the project into its current, much-improved, published form which instead focuses on a nickel TTF polymer similar to those studied by John Anderson's group.

I want to thank you, the reader, for taking the time to peruse this document. I hope that it helps you in your own research or in your understanding of my work.

LeeAnn M. Sager-Smith

Chicago, IL
May 2023

Part I

The Preliminaries

CHAPTER 1

INTRODUCTION TO QUANTUM CHEMISTRY

Quantum chemistry involves describing chemical energies, properties, behaviors, and processes using theoretical tools based on the tenants of quantum mechanics in an attempt to discover, understand, and/or predict some chemical phenomenon. As the Schrödinger equation defines the state of a quantum system, determining the behavior of an atom or molecule can be accomplished by exactly solving the Schrödinger equation. However, the Schrödinger equation can only be exactly solved for one-electron atoms or molecules. The problem of quantum mechanics was perhaps best summarized by P. A. M. Dirac—a pioneer of early quantum mechanics—in 1929:

> The underlying physical laws necessary for the mathematical theory of a large part of physics and the whole of chemistry are thus completely known, and the difficulty is only that the exact application of these laws leads to equations much too complicated to be solvable.

Realization of a practical quantum mechanical theory, then, requires approximate methods for the calculation of wave functions and prediction of observables including energy, equilibrium geometries, etc. The development and implementation of such methodologies have been at the heart of quantum chemistry over the past century, and all implementations of quantum mechanical principles in this dissertation are accomplished via such approximate methodologies.

1.1 The Electronic Hamiltonian

The state of a quantum system can be found via the time-independent, non-relativistic Schrödinger equation given by [9, 26–31]

$$\hat{H}|\Psi\rangle = E|\Psi\rangle \tag{1.1}$$

with the molecular system being specified according to a wave function ($|\Psi\rangle$) and a Hamiltonian ($\hat{H}$). Equation (1.1) is an eigenvalue equation which yields a set of eigenstates $\{|\psi_k\rangle\}$ that are stationary states of the Hamiltonian and a related set of eigenvalues $\{E_k\}$ that correspond to the energies of those states. Determining an adequate set of solutions ($\{|\psi_k\rangle\}$) allows for the predictions of molecular properties of interest.

As the total energy for an atom or molecule is determined by kinetic energy as well as the Coulombic interactions between nuclei and electrons, the Hamiltonian for a molecular system (in atomic units) is given by [9, 27–31]

$$\hat{H} = -\sum_I \frac{1}{2M_I}\nabla_I^2 + \sum_{I<J} \frac{Z_I Z_J}{r_{IJ}} - \sum_i \frac{1}{2}\nabla_i^2 - \sum_{I,i} \frac{Z_I}{r_{Ii}} + \sum_{i<j} \frac{1}{r_{ij}} \tag{1.2}$$

where nuclei are indexed by I, electrons are indexed by i, Z_I is the charge of a given nucleus, M_I describes the mass of a nucleus, r_{ab} describes the distance between two particles, and ∇^2 is the Laplacian

$$\nabla^2 = \frac{d^2}{dx^2} + \frac{d^2}{dy^2} + \frac{d^2}{dz^2}. \tag{1.3}$$

A common simplification that is often applied to Eq. (1.2) is the Born-Oppenheimer (BO) approximation [30, 32]. In the BO approximation, the nuclei are assumed to be stationary with respect to the electrons. This leads to zero nuclear kinetic energy and constant nuclear-

nuclear Coulombic energy and yields the electronic Hamiltonian

$$\hat{H}_e(\vec{R}) = -\sum_i \frac{1}{2}\nabla_i^2 - \sum_{I,i} \frac{Z_I}{r_{Ii}} + \sum_{i<j} \frac{1}{r_{ij}} \tag{1.4}$$

which is parameterized by a given, fixed configuration of nuclear positions $\vec{R}$. The electronic Schrödinger equation is hence

$$\hat{H}_e(\vec{R})|\Phi\rangle = E_e(\vec{R})|\Phi\rangle \tag{1.5}$$

which will have electronic eigenstates given by $|\phi_k\rangle$. Once the electronic Schrödinger equation has been solved, one can write a related effective nuclear Hamiltonian

$$\hat{H}_N = -\sum_I \frac{1}{2M_I}\nabla_I^2 + E_e(\vec{R}) \tag{1.6}$$

where $E_e(\vec{R})$ are the eigenvalues of the electronic Schrödinger equation—implying that the nuclei move on an effective potential surface determined by the electronic energy. The eigenstates of the nuclear Schrödinger equation

$$\hat{H}_N|\chi\rangle = E_N|\chi\rangle \tag{1.7}$$

—denoted as $|\chi_k\rangle$—correspond to the nuclear wavefunctions.

Given a solution to the nuclear Schrödinger equation ($|\chi_k\rangle$) and a given set of solutions to the electronic Schrödinger equation ($\{|\phi_k\rangle\}$), the total system wave function is then given according to

$$|\Psi\rangle = |\Phi(\vec{R};\vec{r})\rangle|\chi(\vec{R})\rangle \tag{1.8}$$

which indicates that the nuclear and electronic degrees of freedom are decoupled. However, this overall wave function is not a solution to the overall molecular Schrödinger equation as

can be seen from the decoupling term:

$$(\hat{H} - E)|\Psi\rangle = -\sum_I \frac{1}{2M_I}\left(|\chi_k\rangle\nabla_I^2|\phi_k\rangle + 2\nabla_I|\chi_k\rangle\nabla_I|\phi_k\rangle\right). \tag{1.9}$$

While this decoupling term needs to be considered under certain conditions—such as systems in fields with strongly fluctuating nuclear degrees of freedom—, it can often be ignored due to the large nuclear mass (M_I) in the denominator. As such, the Born-Oppenheimer approximation will be invoked throughout this thesis, and only electronic chemistry—electronic Hamiltonians and electronic wave functions—will be considered for molecular systems.

1.2 Hartree Fock Theory and Second Quantization

1.2.1 Introduction of the Hartree Fock Method

The simplest approximation for the solution of the electronic Schrödinger equation is the Hartree Fock method [30, 33–35], which employs a mean field approximation. In this approximate methodology, we consider a system of non-interacting electrons having a Hamiltonian of the form

$$\hat{H} = \sum_i h(i) \tag{1.10}$$

where $h(i)$ encompasses both kinetic energy and potential energy of the i^{th} electron with the electron-electron potential experienced for that single electron being the average potential arising from the presence of the other electrons, yielding an effective one-electron Hamiltonian [30]. The one-electron Hamiltonian $h(i)$ has a corresponding eigenvalue equation given by

$$h(i)|\gamma_J(\vec{x}_i)\rangle = \epsilon_J|\gamma_J(\vec{x}_i)\rangle \tag{1.11}$$

where $\vec{x}_i$ represents both the spatial and spin coordinates for electron i, where $\{\gamma_J\}$ is the set of eigenfunctions of $h(i)$ which can be taken to be a set of spin orbitals, and where the corresponding eigenvalue (ϵ_J) is thus the orbital energy of the J^{th} spin orbital.

Because the N-electron Hamiltonian given in Eq. (1.10) is a sum of one-electron Hamiltonians, the eigenfunctions for the overall Hamiltonian are given by a simple product of the spin orbital wave functions (i.e., Hartree product) or

$$|\Psi_H(\vec{x}_1, \vec{x}_2, \ldots \vec{x}_N)\rangle = |\gamma_I(\vec{x}_1)\rangle|\gamma_J(\vec{x}_2)\rangle \cdots |\gamma_K(\vec{x}_N)\rangle. \tag{1.12}$$

The related eigenvalues (E) are therefore a sum of the spin orbital energies of each spin orbital contributing to $|\Psi_H\rangle$ or

$$E = \epsilon_I + \epsilon_J + \cdots + \epsilon_K. \tag{1.13}$$

This Hartree product, however, doesn't account for the antisymmetry of fermionic particles, which necessitates that a many-electron wave function obey

$$|\Psi(\vec{x}_1, \ldots, \vec{x}_i, \ldots, \vec{x}_j, \ldots, \vec{x}_N)\rangle = -|\Psi(\vec{x}_1, \ldots, \vec{x}_j, \ldots, \vec{x}_i, \ldots, \vec{x}_N)\rangle \tag{1.14}$$

upon interchanging the coordinates of any two electrons i and j. However, we can obtain appropriately antisymmetrized wave functions through defining the Hartree Fock wave function as a Slater determinant given by

$$|\Psi_{HF}\rangle = \frac{1}{\sqrt{N!}} \begin{vmatrix} \gamma_1(1) & \gamma_2(1) & \cdots & \gamma_N(1) \\ \gamma_1(2) & \gamma_2(2) & \cdots & \gamma_N(2) \\ \vdots & \vdots & \ddots & \vdots \\ \gamma_1(N) & \gamma_2(N) & \cdots & \gamma_N(N) \end{vmatrix} \tag{1.15}$$

where we have simplified the representation for the spatial and spin coordinates for electron i from $\vec{x}_i$ to simply i. This Slater determinant can be conveniently represented using the wedge product of Grassmann algebra [36, 37] according to

$$|\Psi_{HF}\rangle = |\gamma_1(1) \wedge \gamma_2(2) \wedge \cdots \wedge \gamma_N(N)\rangle \tag{1.16}$$

with the normalization constant assumed. As required by antisymmetry, Eq. (1.16) does indeed satisfy

$$|\gamma_1(1)\wedge\cdots\wedge\gamma_i(2)\wedge\cdots\wedge\gamma_j(3)\wedge\cdots\wedge\gamma_N(N)\rangle = -|\gamma_1(1)\wedge\cdots\wedge\gamma_j(2)\wedge\cdots\wedge\gamma_i(3)\wedge\cdots\wedge\gamma_N(N)\rangle. \tag{1.17}$$

A single wedge product of orbitals—such as that shown in Eq. 1.16—is the simplest antisymmetric wave function capable of representing the ground state of an N-electron system. In quantum mechanics, the variational principle [9, 27–31] states that the expectation value of the Hamiltonian for any trial wave function $|\Psi_{tr}\rangle$—i.e., the energy of the trial wave function E_{tr}—will always follow

$$E_{tr} = \frac{\langle\Psi_{tr}|\hat{H}|\Psi_{tr}\rangle}{\langle\Psi_{tr}|\Psi_{tr}\rangle} \geq \langle\Psi_{gs}|\hat{H}|\Psi_{gs}\rangle = E_{gs} \tag{1.18}$$

where $|\Psi_{gs}\rangle$ and E_{gs} are the true ground state electronic wave function and electronic energy, respectively. From this variational principle, then, the best single orbital wedge product wave function ($|\Psi_o\rangle$)—i.e., the best Hartree Fock wave function—is the one that yields the minimum expectation value for the full electronic Hamiltonian

$$E_o = \langle\Psi_o|\hat{H}|\Psi_o\rangle \tag{1.19}$$

and hence yields the minimum electronic energy (E_o) for a wave function of this functional form. By minimizing electronic energy with respect to the choice of spin orbitals, the Hartree

Fock equation can be derived, and the Hartree Fock ground state can be identified. This process will be further outlined in Sec. 1.2.3.

1.2.2 The Notation of Second Quantization

Up until this juncture, we have utilized first quantization [30, 38–40]—the original notation of quantum mechanics with which the reader may have greater familiarity. However, another notation—called second quantization—is utilized throughout this dissertation. While second quantization introduces no new physics, it is often a convenient representation for treating many-electron systems. To construct the formalism of second quantization, we first need to define operators which change the number of particles within a system. A creation operator $\hat{a}_i^\dagger$ acts on an arbitrary N-electron wave function to produce a $(N+1)$-electron wave function by creating an electron in the spin orbital γ_i. This is formally defined according to

$$\hat{a}_i^\dagger|\Psi_N\rangle = |\Psi_{N+1}\rangle = |\gamma_i(N+1) \wedge \Psi_N\rangle \tag{1.20}$$

where—by convention—electrons are numbered from right to left. Similarly, an annihilation operator $\hat{a}_i$—which is the adjoint of the creation operator $\hat{a}_i^\dagger$—acts on an arbitrary N-electron wave function to produce a $(N-1)$-electron wave function by annihilating an electron in the spin orbital γ_i according to

$$\hat{a}_i|\Psi_N\rangle = |\Psi_{N-1}\rangle = \int \gamma_i^*(N)|\Psi_N\rangle dN. \tag{1.21}$$

Note that—as is required by antisymmetry—the order that the creation and annihilation operators are applied is important as

$$\hat{a}_i^\dagger \hat{a}_j^\dagger|\emptyset\rangle = |\gamma_i(2) \wedge \gamma_j(1)\rangle \tag{1.22}$$

is distinct from

$$\hat{a}_j^\dagger \hat{a}_i^\dagger |\emptyset\rangle = |\gamma_j(2) \wedge \gamma_i(1)\rangle = -|\gamma_i(2) \wedge \gamma_j(1)\rangle \tag{1.23}$$

where $|\emptyset\rangle$ is the null vector consisting of no electrons in no spin orbitals. This leads to the following anticommutation relationship:

$$\{\hat{a}_i^\dagger, \hat{a}_j^\dagger\} = 0 = \hat{a}_i^\dagger \hat{a}_j^\dagger + \hat{a}_j^\dagger \hat{a}_i^\dagger. \tag{1.24}$$

Similarly, it can be shown that the anticommutation relationship for annihilators is given by:

$$\{\hat{a}_i, \hat{a}_j\} = 0 = \hat{a}_i \hat{a}_j + \hat{a}_j \hat{a}_i. \tag{1.25}$$

Furthermore, an anticommutation operator for the interchange of a creation and an annihilation can be shown to be

$$\{\hat{a}_i, \hat{a}_j^\dagger\} = \delta_j^i = \hat{a}_i \hat{a}_j^\dagger + \hat{a}_j^\dagger \hat{a}_i \tag{1.26}$$

where δ_j^i is the Dirac delta function such that $\delta_j^i = 1$ if $i = j$ and $\delta_j^i = 0$ if $i \neq j$.

Note that these anticommutation relationships are consistent with the Pauli exclusion principle as for $i = j$, $\hat{a}_i^\dagger \hat{a}_i^\dagger = -\hat{a}_i^\dagger \hat{a}_i^\dagger = 0$, which implies that two electrons can not be created in the same spin orbital γ_i or

$$\hat{a}_i^\dagger |\gamma_k \wedge \cdots \wedge \gamma_l\rangle = 0, \quad \text{if } i \in \{k, \ldots, l\}. \tag{1.27}$$

Additionally, as $\hat{a}_i \hat{a}_i = -\hat{a}_i \hat{a}_i = 0$ for $i = j$, an electron in a given spin orbital can not be destroyed twice or

$$\hat{a}_i |\gamma_k \wedge \cdots \wedge \gamma_l\rangle = 0, \quad \text{if } i \notin \{k, \ldots, l\}. \tag{1.28}$$

Using the definitions from above, the molecular electronic Hamiltonian first introduced

in Eq. (1.4) can thus be represented as

$$\hat{H} = \sum_{i,j} {}^1H^i_j \hat{a}^\dagger_i \hat{a}_j + \sum_{i,j,k,l} {}^2V^{i,j}_{k,l} \hat{a}^\dagger_i \hat{a}^\dagger_j \hat{a}_l \hat{a}_k \tag{1.29}$$

in second quantization where the one-electron term is given by

$${}^1H^i_j = \int \gamma^*_i(1) \left[-\frac{\nabla^2_1}{2} - \sum_k \frac{Z_k}{r_{1k}} \right] d1 \tag{1.30}$$

and the two-electron term is given by

$${}^2V^{i,j}_{k,l} = \int\int \gamma^*_i(1)\gamma^*_j(2) \left(\frac{1}{r_{12}}\right) \gamma_k(1)\gamma_l(2) d1 d2. \tag{1.31}$$

The energy in second quantization is hence

$$E = \langle \Psi | \hat{H} | \Psi \rangle \tag{1.32}$$

$$= \sum_{i,j} {}^1H^i_j \langle \Psi | \hat{a}^\dagger_i \hat{a}_j | \Psi \rangle + \sum_{i,j,k,l} {}^2V^{i,j}_{k,l} \langle \Psi | \hat{a}^\dagger_i \hat{a}^\dagger_j \hat{a}_l \hat{a}_k | \Psi \rangle \tag{1.33}$$

$$= \sum_{i,j} {}^1H^i_j {}^1D^i_j + \sum_{i,j,k,l} {}^2V^{i,j}_{k,l} {}^2D^{i,j}_{k,l} \tag{1.34}$$

where ${}^1D^i_j = \langle \Psi | \hat{a}^\dagger_i \hat{a}_j | \Psi \rangle$ and ${}^2D^{i,j}_{k,l} = \langle \Psi | \hat{a}^\dagger_i \hat{a}^\dagger_j \hat{a}_l \hat{a}_k | \Psi \rangle$ are elements of the one-fermion and two-electron reduced density matrices, respectively, which will be introduced in Chapter 2.

1.2.3 Hartree Fock Theory in Second Quantization

To derive the Hartree Fock equation—following the approach taken in Prof. Mazziotti's Advanced Quantum Chemistry Course (CHEM-362) [41]—, the N-electron Schrödinger equa-

tion can be contracted onto the space of single electrons as follows:

$$\langle\Psi|\hat{a}_p^\dagger\hat{a}_q\hat{H}|\Psi\rangle = E\langle\Psi|\hat{a}_p^\dagger\hat{a}_q|\Psi\rangle. \tag{1.35}$$

By inserting Eq. (1.34) and introducing a three-particle reduced density matrix

$${}^3D_{l,m,n}^{i,j,k} = \langle\Psi|\hat{a}_i^\dagger\hat{a}_j^\dagger\hat{a}_l^\dagger\hat{a}_n\hat{a}_m\hat{a}_l|\Psi\rangle, \tag{1.36}$$

Eq. (1.35) can be transformed into

$$\sum_{i,k}{}^1H_k^i\left[{}^2D_{q,k}^{p,i} + \delta_q^{i\,1}D_q^p\right] + \sum_{i,j,k,l}{}^2V_{k,l}^{i,j}\left[{}^3D_{q,k,l}^{p,i,j} + \delta_q^{i\,2}D_{k,l}^{p,j} - \delta_q^{i\,2}D_{k,l}^{p,i}\right] = E^1D_q^p. \tag{1.37}$$

This one-particle contracted Schrödinger equation is exact; however there are insufficient equations to uniquely solve for the equation's variables.

If we apply the Hartree Fock assumption—i.e., assume that the particles are statistically independent—, then we can assemble the higher reduced density matrices via Grassman wedge products of the one-fermion reduced density matrix according to

$$\frac{1}{2!}{}^2D_{k,l}^{i,j} = {}^1D_k^i \wedge {}^1D_k^j l = {}^1D_k^{i\,1}D_l^j - {}^1D_l^{i\,1}D_k^j \tag{1.38}$$

and

$$\frac{1}{3!}{}^3D_{p,q,r}^{i,j,k} = {}^1D_p^i \wedge {}^1D_q^j \wedge {}^1D_r^k. \tag{1.39}$$

Substituting Eqs. (1.38) and (1.39) into our contracted Schrödinger equation yields

$$\sum_{i,k}({}^1I - {}^1D)_i^{q\,1}H_k^{i\,1}D_p^k + 2\sum_{i,j,k,l}({}^1I - {}^1D)_i^{q\,1}D_l^{j\,2}V_{k,l}^{i,j\,1}D_p^k - 2\sum_{i,j,k,l}({}^1I - {}^1D)_i^{q\,1}D_k^{j\,2}V_{k,l}^{i,j\,1}D_p^l = 0 \tag{1.40}$$

where I is the identity matrix. Defining the Coulomb and Exchange matrices to be

$$ {}^1J_k^i = \sum_{j,l} {}^1D_l^{j\,2}V_{k,l}^{i,j} \tag{1.41} $$

and

$$ {}^1K_l^i = \sum_{j,k} {}^1D_k^{j\,2}V_{k,l}^{i,j} \tag{1.42} $$

respectively, Eq. (1.40) can be further simplified to

$$ \sum_{i,k} ({}^1I - {}^1D)_i^q \left[{}^1H + 2{}^1J - 2{}^1K \right]_k^i {}^1D_p^k = 0. \tag{1.43} $$

If we define the Fock matrix to be

$$ {}^1F = {}^1H + 2{}^1J - 2{}^1K \tag{1.44} $$

and recognize the definition of matrix multiplication from Eq. (1.43), then the final form of the Hartree Fock equation is

$$ ({}^1I - {}^1D){}^1F{}^1D = 0. \tag{1.45} $$

The solutions are the eigenvectors of the Fock matrix according to the following eigenvalue equation

$$ {}^1F\,\vec{c}_i = \epsilon_i\,\vec{c}_i \tag{1.46} $$

where $\vec{c}_i$ is the vector of expansion coefficients for the basis set of atomic orbitals with the resultant linear combinations forming the Hartree Fock spin orbitals. As the Fock operator depends on its eigenfunctions, the Hartree Fock equation isn't linear and needs to be solved iteratively until self-consistency is reached.

The solution to the Hartree Fock equations yields an orthonormal set of Hartree Fock spin orbitals and their associated orbital energies. For an N-electron system, the orbital

wedge product of the N spin orbitals with the lowest energies corresponds to the Hartree Fock ground state $|\Psi_o\rangle$. This Hartree Fock ground state—while not the true ground state due to the assumption of statistically-independent electrons—does recover approximately 99% of the absolute energy for a wide array of atoms and molecules while having only $O(r^4)$ scaling, where r is the size of the basis set (i.e., the number of atomic orbitals in your orbital basis set). Note that as the size of the basis set for a given Hartree Fock calculation is increased, the computational expense increases and the Hartree Fock ground state energy decreases—becoming closer to the absolute ground state energy E_{gr}.

1.3 Post-Hartree Fock Theory and Electron Correlation

As Hartree Fock theory treats electrons as independent of each other with electron-electron interactions treated in an averaged manner, Hartree Fock is incapable of capturing electron correlation and hence fails to reach the absolute ground state energy, even in the infinite basis set limit. This correlation energy, while often only around one percent of the total absolute electronic energy, is still quite large when considering chemical reactions and physical processes. However, the Hartree Fock ground state ($|\Psi_o\rangle$)—often referred to as the reference determinant—can often be utilized as an important starting point for other, more-accurate electronic structure methodologies [9, 27–31].

1.3.1 Full Configuration Interaction

One such methodology is Full Configuration Interaction [30, 42] or FCI. Any N-particle antisymmetric wave function can be expressed as a linear combination of orbital wedge products of N orbitals from a complete, orthonormal set of one-particle orbitals $\{\gamma_i\}$. Given the Hartree Fock spin orbitals—a complete, orthonormal set of one-particle orbitals—, the

exact wave function in that basis can thus be represented as

$$|\Psi\rangle = c_o|\Psi_o\rangle + \sum_{i,a} c_a^i \hat{a}_i^\dagger \hat{a}_a|\Psi_o\rangle + \sum_{i,j,a,b} c_{a,b}^{i,j} \hat{a}_i^\dagger \hat{a}_j^\dagger \hat{a}_b \hat{a}_a|\Psi_o\rangle + \cdots \tag{1.47}$$

where the indices $a, b, c, \ldots$ correspond to spin orbitals that are occupied in the Hartree Fock reference state and the indices $i, j, k, \ldots$ correspond to spin orbitals that are unoccupied (or virtual) in the Hartree Fock reference state. Thus, $\sum_{i,a} c_a^i \hat{a}_i^\dagger \hat{a}_a|\Psi_o\rangle$ represents all possible single excitations from the Hartree Fock ground state, $\sum_{i,j,a,b} c_{a,b}^{i,j} \hat{a}_i^\dagger \hat{a}_j^\dagger \hat{a}_b \hat{a}_a|\Psi_o\rangle$ represents all possible double excitations from the Hartree Fock ground state, etc. such that Eq. (1.47) includes the complete basis of Slater determinants relative to the Hartree Fock reference. The FCI wavefunction is completely specified by the unknown set of coefficients ($c_0/c_a^i/c_{a,b}^{i,j}$/etc.) which are probability amplitudes corresponding to each configuration. To determine these coefficients, the Hamiltonian can be represented in the basis of all possible Slater determinants and diagonalized. While this FCI procedure provides the exact solution of the Schrödinger equation for a given basis set, such a diagonalization scales as $O(r!)$ [9] for a basis set composed of r orbitals, which is prohibitive for all but the smallest atoms and molecules.

1.3.2 Truncated Configuration Interaction

To decrease computational expense associated with a Full Configuration Interaction calculation, Eq. (1.47) can be truncated [9, 27–31]. Instead of including all possible configurations, these truncated CI calculations include only a subset. For example, Configuration Interaction Doubles (CID) includes only double excitations; Configuration Interaction Singles Doubles (CISD) includes only single and double excitations; Configuration Interaction Singles Doubles Triples (CISDT) includes single, double, and triple excitations; and so on. The Hamiltonian can then be expressed in the appropriate basis and then diagonalized in this

smaller basis. For example, in the case of CISD, only the Hartree Fock ground state $|\Psi_o\rangle$, the single excitations, and the double excitations are considered, which decreases the computational expense to $O(r^6)$ [9]. While truncated CI methods do decrease the scaling of FCI, they are still limited to systems of relatively small sizes, and they are not size extensive. Further, truncated CI is a single-reference method, which is only accurate in systems where the Hartree Fock ground state contributes significantly to the true ground state (i.e., c_o is large).

1.3.3 Møller-Plesset Perturbation Theory

Another approach to obtain accurate correlation energy at decreased computation expense in to use a perturbative expansion of energy. Specifically, in Møller-Plesset Perturbation Theory (MPPT) [30, 43], traditional Rayleigh-Schrödinger Perturbation Theory ($\hat{H} = \hat{H}_o + \lambda\hat{V}$) is utilized with a reference Hamiltonian given by the Fock Matrix (or $\hat{H}_o = \hat{F}$) and the perturbation Hamiltonian given by $\hat{V} = (\hat{H} - \hat{F})$. While a zeroth-order perturbation theory yields an energy inferior to the Hartree Fock energy and while first-order perturbation yields only the Hartree Fock energy, second-order and higher perturbations increasingly approach the FCI energy. Second-order perturbation theory (MP2) scales as $\mathrm{O}(n^5)$ [9], third-order perturbation theory (MP3) scales as $\mathrm{O}(n^6)$ [9], fourth-order perturbation theory (MP4) scales as $\mathrm{O}(n^7)$ [9], etc. This decreases computational expense relative to FCI, with MP2 even being able to be applied to systems of approximately 100 atoms if implemented efficiently; however, perturbation theory is only accurate for small perturbations and hence fails for strongly-correlated systems. Further, it is again a single-reference methodology.

1.3.4 Coupled Cluster Theory

Another method of interest is the Coupled Cluster approach. In Coupled Cluster Theory [10, 44, 45], we define a cluster operator $\hat{T}$ such that the coupled cluster wave function is

given as the following ansatz:

$$|\Psi_{CC}\rangle = e^{\hat{T}}|\Psi_o\rangle \tag{1.48}$$

where $|\Psi_o\rangle$ is again the Hartree Fock reference wave function. Using the coupled cluster wave function, the electronic Schrödinger equation can be written as

$$\hat{H}e^{\hat{T}}|\Psi_o\rangle = Ee^{\hat{T}}|\Psi_o\rangle. \tag{1.49}$$

By multiplying the left hand side by $e^{-\hat{T}}$ and projecting onto the set of singly-excited, doubly-excited, ..., and m-tuply excited Slater determinants based on the reference where m is the highest-order excitation included in $\hat{T}$, we obtain the following coupled cluster equations:

$$\langle\Psi_o|e^{-\hat{T}}\hat{H}e^{\hat{T}}|\Psi_o\rangle = E \tag{1.50}$$

$$\langle\phi|e^{-\hat{T}}\hat{H}e^{\hat{T}}|\Psi_o\rangle = 0 \tag{1.51}$$

where ϕ is one of the determinants that results from applying the cluster operator on the reference wave function. This set of non-linear equations can then be solved either using the Jacobi method or with an iterative procedure in order to meet the above conditions.

The most commonly-used cluster operator results in the Coupled Cluster Singles and Doubles Ansatz, CCSD:

$$\hat{T}_{SD} = \hat{T}_1 + \hat{T}_2 = \sum_{i,a} T_a^i \hat{a}_i^\dagger \hat{a}_a + \sum_{i,j,a,b} T_{a,b}^{i,j} \hat{a}_i^\dagger \hat{a}_j^\dagger \hat{a}_b \hat{a}_a. \tag{1.52}$$

This CCSD method scales as $O(n^6)$, and other common coupled cluster methods including those that additionally include triples (CCSDT), those that additionally include triples and quadruples (CCSDTQ), etc. have more-expensive computational scaling. Coupled cluster—especially CCSD(T) and higher—is particularly accurate for a single reference method;

however, computational expense does limit system size.

1.3.5 Multi-Reference Approaches

For many chemical processes of contemporary interest, the true electronic ground state is not dominated by the Hartree Fock reference wave function, and, as such, single reference electronic structure methodologies are insufficient. Instead, these so-called strongly-correlated molecular systems require multi-reference approaches.

One typical multi-reference approach involves considering only a subset of all of the possible electrons and orbitals in a particular active space. The active space is usually chosen in order to include electrons and orbitals in the valence shell as well as low-lying virtual orbitals, which are most likely to exhibit fractional occupations, while core orbitals are considered to be fully occupied and high-lying virtual orbitals are considered to fully unoccupied. By limiting the scope of the problem to an active space, a full confiuguration interaction calculation for these relevant electrons and orbitals can be accomplished. This is the broad outline for the Complete Active Space Configuration Interaction (CASCI) method [46], a method that can often be applied to both ground and excited states with a fair degree of accuracy. Further, the orbitals in the active space that undergo the full configuration interaction calculation can be optimized in a self-consistent manner by iteratively performing orbital rotations to minimize energy. This combination of the CASCI method with said orbital rotations leads to the Complete Active Space Self-Consistent Field (CASSCF) method [9, 47]. A limitation of these methodologies, however, is that the number of electrons and orbitals that can be included in the active space is limited as it inherits the exponential scaling of traditional CI approaches, although these methods scale with the number of orbitals in the active space and not the total number of orbitals in a molecular system.

Another common multi-reference method is a reduced density matrix approach, which will be detailed in Chapter 2.

1.3.6 Aside on Scaling in Electronic Structure Methodologies

A summary of the computational scaling for the electronic structure approaches detailed in previous and future sections is shown in Table 1.1. As can be seen, an outstanding challenge in chemical computations is that the cost of highly-accurate *ab initio* methodologies scales prohibitively with system size, making the accurate computation of highly-correlated systems of even moderate size difficult if not infeasible with current methods. Thus, the current literature—as well as several sections of this thesis—is exploring novel techniques—including quantum computing and machine learning—with the goal of decreasing computational expense of electronic structure calculations.

Method	**Scaling with # Basis Functions**
Hartree Fock	$O(r^4)$
MP2	$O(r^5)$
MP3, CISD, CCSD, V2RDM, ACSE	$O(r^6)$
MP4, CCSD(T)	$O(r^7)$
MP5, CISDT, CCSDT	$O(r^8)$
MP6	$O(r^9)$
MP7, CISDTQ, CCSDTQ	$O(r^{10})$
FCI	$O(r!)$

Table 1.1: Summary of computational scaling for various electronic structure methodologies summarized from Refs. [9] and [10].

CHAPTER 2

REDUCED DENSITY MATRIX APPROACHES FOR QUANTUM CHEMISTRY

In the prior chapter, the many-electron wave function was the main variable utilized in computing molecular energies and properties. However, as indistinguishable electrons interact in only a pair-wise fashion, we can reformulate the electronic Hamiltonian given in Eq. (1.4) to

$$\hat{H} = \sum_{i,j,k,l} {}^2\hat{K}^{i,j}_{k,l} \hat{a}^\dagger_i \hat{a}^\dagger_j \hat{a}_l \hat{a}_k \tag{2.1}$$

where

$${}^2\hat{K}(1,2) = \frac{1}{N-1}\left(-\frac{1}{2}\nabla^2_1 - \sum_I \frac{Z_I}{r_{I,1}}\right) + \frac{1}{2}\frac{1}{r_{1,2}} \tag{2.2}$$

is known as the two-electron reduced Hamiltonian. The many-electron electronic energy—which is the expectation value of the Hamiltonian—is thus given by

$$E = \sum_{i,j,k,l} {}^2\hat{K}^{i,j}_{k,l} {}^2\hat{D}^{i,j}_{k,l} = Tr({}^2K {}^2D) \tag{2.3}$$

where ${}^2D$ is the two-electron reduced density matrix (2-RDM) which will be defined in the following section. Reduced density matrix approaches to electronic structure theory, utilize this 2-RDM as the main variable in chemical computation in lieu of the multi-electron wave function [48–62]. Calculating all two-electron properties of a system in this new paradigm often allows us to treat systems demonstrating high correlation at lower computational cost, and such techniques are utilized throughout this dissertation.

2.1 Reduced Density Matrices

The density matrix—which was first introduced by Landau [63] and von Neumann [64] in 1927—for an N-electron wave function $|\Psi(1,2,\ldots,N)\rangle$ is defined as

$$^{N}D(1,2,\ldots,N;1',2',\ldots,N') = |\Psi(1,2,\ldots,N)\rangle\langle\Psi(1',2',\ldots,N')| \tag{2.4}$$

where each integer represents the spatial and spin components of an electron. Integrating Eq. (2.4) over coordinates $k+1$ to N yields a general k-electron reduced density matrix (k-RDM)

$$^{k}D(1,2,\ldots,k;1',2',\ldots,k') = \frac{N!}{(N-k)!}\int \Psi(1,2,\ldots,k,\ldots,N)\Psi^{*}(1',2',\ldots,k',\ldots,N')d(k+1)\cdots dN \tag{2.5}$$

with the matrix elements of this k-RDM in second quantization being given by

$$^{2}D^{i_1,i_2,\ldots,i_k}_{j_1,j_2,\ldots,j_k} = \langle\Psi|\hat{a}^{\dagger}_{i_1}\hat{a}^{\dagger}_{i_2}\cdots\hat{a}^{\dagger}_{i_N}\hat{a}_{j_k}\cdots\hat{a}_{j_2}\hat{a}_{j_1}|\Psi\rangle. \tag{2.6}$$

The normalization of this k-RDM differs depending on convention.

Explicitly, the 1-RDM and 2-RDM—which are used extensively throughout this document—are given by

$$^{1}D^{i}_{j} = \langle\Psi|\hat{a}^{\dagger}_{i}\hat{a}_{j}|\Psi\rangle \tag{2.7}$$

and

$$^{2}D^{i,j}_{k,l} = \langle\Psi|\hat{a}^{\dagger}_{i}\hat{a}^{\dagger}_{j}\hat{a}_{l}\hat{a}_{k}|\Psi\rangle \tag{2.8}$$

with their respective traces being N and $N(N-1)$ by conventional definitions in quantum mechanics.

2.2 N-Representability

Equation (2.3), which formulates electronic energy as a linear functional of the 2-RDM, implies that a variational minimization of energy with respect to the 2-RDM may be a powerful tool for computing accurate molecular energies with far fewer degrees of freedom for a given set of basis orbitals compared to wavefunction methodologies. However, when such computations were initially implemented, optimized energies considerably below the exact ground state energy were obtained [65]. It was later recognized that the variationally-minimized trial 2-RDMs failed to represent physical systems; that is, there was no N-electron density matrix that could yield the trial 2-RDM upon integration [48, 65–67]. To ensure that the 2-RDM is restricted to correspond to an N-electron system, N-representability conditions must be enforced [50, 58, 62, 66]. Specifically, additional constraints must be applied beyond the necessities of a density matrix composed of indistinguishable fermions (i.e., normalization, Hermiticity, antisymmetry under particle exchange, and nonnegative eigenvalues).

2.2.1 Constraints on the 1-RDM

In order to obey the Pauli exclusion principle, the occupations of the 1-RDM must belong to {0,1}, which necessitates that the 1-RDM be positive semidefinite or

$$^1D \succeq 0. \tag{2.9}$$

Similar to the one-particle reduced density matrix, we can additionally define a one-hole reduced density matrix given by

$$^1Q^i_j = \langle \Psi | \hat{a}_i \hat{a}^\dagger_j | \Psi \rangle \tag{2.10}$$

which must also be constrained to be positive semidefinite—or

$$^1Q \succeq 0 \tag{2.11}$$

as the probability of finding a hole in a given orbital must also be nonnegative. These constraints on the one-particle and one-hole matrix together are know as the 1-positivity conditions.

Moreover, for a pure system, the eigenvalues of the 1-RDM are further constrained by the generalized Pauli constraints, which are detailed in References [68] and [69].

2.2.2 Constraints on the 2-RDM

Similar to the 1-RDM, in order to maintain positive probabilities, the two-particle, two-hole, and particle-hole RDMs must be positive semidefinite:

$$^2D \succeq 0 \tag{2.12}$$

$$^2Q \succeq 0 \tag{2.13}$$

$$^2G \succeq 0 \tag{2.14}$$

where the two-hole and particle-hole reduced density matrices are defined as

$$^2Q^{i,j}_{k,l} = \langle \Psi | \hat{a}_i \hat{a}_j \hat{a}^\dagger_l \hat{a}^\dagger_k | \Psi \rangle \tag{2.15}$$

and

$$^2G^{i,j}_{k,l} = \langle \Psi | \hat{a}^\dagger_i \hat{a}_j \hat{a}^\dagger_l \hat{a}_k | \Psi \rangle, \tag{2.16}$$

respectively. These constraints are known as the 2-positivity conditions.

As the one-electron RDM and one-hole RDM are related to the two-electron RDM and the two-hole RDM by contraction—as shown by

$$^1D^i_k = \frac{1}{N-1} \sum_j {}^2D^{i,j}_{k,l} \tag{2.17}$$

and

$$ {}^1Q^i_k = \frac{1}{r-N-1} \sum_j {}^2Q^{i,j}_{k,l} \tag{2.18} $$

where r is the number of orbitals in the one-particle basis set—, the 1-positivity conditions are implied by the 2-positivity conditions. (In fact, this is a general result in that the q-positivity conditions are implied by the p-positivity conditions for $q \leq p$.)

2.3 Variational 2-RDM

The energy of a 2-RDM computed according to Eq. (2.3) subject to the constraints from Sec. 2.2.2 to approximately maintain N-representability can be minimized via use of boundary-point semidefinite programming techniques [48, 54, 70, 71]. This approach is called the Variational 2-RDM approach (V2RDM), and it scales as $O(r^6)$—with active space calculations employing V2RDM techniques demonstrating the ability to effectively capture strong correlation in a large variety of molecules [12, 17, 72–74].

2.4 The Contracted Schrödinger Equation

An alternative to the Variational 2-RDM approach is to directly compute the 2-RDM by projecting the Schrödinger equation onto two-particle space to result in the contracted Schrödinger equation (CSE) [75–87]:

$$ \langle \Psi | \hat{a}^\dagger_i \hat{a}^\dagger_k \hat{a}_l \hat{a}_j \hat{H} | \Psi \rangle = {}^2D^{i,k}_{j,l} E. \tag{2.19} $$

Analogous to how the Schrödinger equation connects the N-particle Hamiltonian and the N-particle wave function, the CSE connects the two-particle reduced Hamiltonian and the 2-RDM; however, the CSE further depends upon both the three-particle and four-particle RDMs, meaning that the CSE can not be directly solved for the 2-RDM without implemen-

tation of both reconstruction and purification.

In reconstruction, the 3-RDMs and 4-RDMs are built from the 2-RDM according to some approximate formulas. Specifically, Ref. [88] details how higher RDMs can be reconstructed from lower RDMs using Schwinger probes such that the reconstruction functionals for the RDMs are given by

$$^1D = {}^1\Delta, \tag{2.20}$$

$$^2D = {}^2\Delta + {}^1\Delta \wedge {}^1\Delta, \tag{2.21}$$

$$^3D = {}^3\Delta + {}^1\Delta^3 + 3^2\Delta \wedge {}^1\Delta, \tag{2.22}$$

$$^4D = {}^4\Delta + {}^1\Delta^4 + 6^2\Delta \wedge {}^1\Delta^2 + 3^2\Delta^2 \tag{2.23}$$

etc. In these equations, ${}^k\Delta$ is the cumulant for the k-RDM, the superscripts indicate the number of times a cumulant should be wedged with itself, and a common approximation to obtain a k-RDM from a $(k-1)$-RDM is to set ${}^k\Delta = 0$ (although other cumulant approximations are in use).

In purification, constraints on the N-representability of the 2-RDM are applied. This purification is crucial for the solutions of the CSE to yield accurate results. See Section 2.2.2 for a discussion on N-representability constraints.

Combining the CSE, N-representability of the 2-RDM, and reconstruction of the 3- and 4-RDMs in a self-consistent iterative algorithm permits the CSE to be directly solved for the 2-RDM, a technique that can be applied to compute molecular energies and properties for a variety of molecular systems [48].

2.5 The Anti-Hermitian Contracted Schrödinger Equations

The contracted Schrödinger equation can be separated into its Hermitian and anti-Hermitian components

$$\langle\Psi|\{\hat{a}_i^\dagger\hat{a}_k^\dagger\hat{a}_l\hat{a}_j, \hat{H} - E\}|\Psi\rangle = 0 \tag{2.24}$$

$$\langle\Psi|[\hat{a}_i^\dagger\hat{a}_k^\dagger\hat{a}_l\hat{a}_j, \hat{H}]|\Psi\rangle = 0 \tag{2.25}$$

which are called the Hermitian CSE (HCSE) and Anti-Hermitian CSE (ACSE), respectively. By introducing a matrix

$${}^2W_{q,s}^{p,r} = {}^2K_{q,s}^{p,r} - {}^2K_{q,s}^{pr,p}, \tag{2.26}$$

both the HCSE and ACSE can be expressed in terms of reduced density matrices with the HCSE being given by [10]

$$\begin{aligned} 0 = \; & 2\sum_{p,r,q,s} {}^2K_{q,s}^{p,r}4D_{j,l,q,s}^{p,r,i,k} \\ & + \sum_{p,r,q} {}^2W_{k,q}^{p,r}3D_{j,l,q}^{p,r,i} + {}^2W_{q,i}^{p,r}3D_{j,l,q}^{p,r,k} + {}^2W_{q,r}^{p,j}3D_{q,r,l}^{i,k,p} + {}^2W_{q,r}^{l,p}3D_{q,r,j}^{i,k,p} \\ & + \sum_{p,q} {}^2W_{i,k}^{p,r}2D_{j,l}^{p,q} + {}^2W_{p,q}^{j,l}2D_{p,q}^{i,k} - E^2D_{j,l}^{i,k} \end{aligned} \tag{2.27}$$

and the ACSE being given by [10]

$$\begin{aligned} 0 = & \sum_{p,q,r} {}^2W_{q,r}^{p,j}3D_{q,r,l}^{i,k,p} + {}^2W_{q,r}^{l,p}3D_{q,r,j}^{i,k,p} - {}^2W_{k,q}^{p,r}3D_{j,l,q}^{p,r,i} - {}^2W_{q,i}^{p,r}3D_{j,l,q}^{p,r,k} \\ & + \sum_{p,q} {}^2W_{p,q}^{j,l}2D_{p,q}^{i,k} - {}^2W_{i,k}^{p,q}2D_{j,l}^{p,q}. \end{aligned} \tag{2.28}$$

Interestingly, the 4-RDM terms of the CSE contribute only to the HCSE—meaning that the Anti-Hermitian CSE only relies upon the 3-RDM, making solving only the anti-Hermitian

component of the CSE for the appropriate 2-RDM and hence two-body molecular properties a particularly attractive prospect. In fact, the direct computation of the 2-RDM from only the ACSE with approximate reconstruction of the 3-RDM from corrected cumulant expansion has been shown to capture between 95% and 100% of the correlation energy for atoms and molecules when compared to FCI with the energetically-minimized 2-RDMs very-nearly satisfying the N-representability conditions [89]. This approach—called the Anti-Hermitian Contracted Schrödinger Equation method—scales as $O(r^6)$ and is competitive with CCSD(T) with the scaling of CCSD.

Note that practical solutions to the ACSE are found through an iterative procedure with the residual and the reduced density matrices being treated as a pair of differential equations. More specifics of this approach can be found in Ref. [90].

CHAPTER 3

CONDENSATION PHENOMENA

From the 1911 discovery of superconductivity [91] to the 1938 observation of superfluidity in liquid helium [92, 93], phenomena which demonstrate the frictionless flow of their constituent particles have been actively researched for over a century. Such superfluid behavior is purely quantum mechanical in nature and has been found to be the result of bosonic particles (or quasi-particles) condensing into single quantum states [94–100]. The superfluidity of bosons—such as in liquid helium [92, 93] and dilute atomic gases [101, 102]—, has seen practical use in the creation of atomic clocks, atomic lasers, and highly-sensitive sensors [103]. However, superconducting behavior—which results from the superfluidity of electrons—is seen as one of the holy grails of modern science. Not only would the frictionless flow of electrons be a boon to the fields of energy transportation and electronics, superconducting magnets—some of the most-powerful electromagnets in modern science—are used in mass spectrometry, magnetic resonance imaging (MRI), particle acceleration, nuclear magnetic resonance (NMR), magnetic separation, and wind mill energy generation [104]. Further, superconducting systems have recently emerged as a powerful platform to act as quantum bits (or qubits) in quantum computers [105]. However, all known superconductors are currently prepared at either too-low a temperature or at too-high a pressure to make practical implementation of superconducting wires feasible on any macroscopic scale. Exciton condensation—a condensate state composed of electron-hole pairs that allows for so-called counterflow superconductivity in bilayer systems [106, 107]—is exciting as excitons being more-tightly bound than Cooper pairs may allow exciton condensates to persist at higher temperatures. However, computational and real-world exploration of exciton condensates are still in their infancy, with the first preparation of an exciton condensate only being accomplished in the mid-2000s [108–112]. A current aim of chemists—both theorists and experimentalists alike—is to identify a room temperature superconductor at ambient

pressures.

Thus, one of the goals of this thesis is to use techniques capable of simulating highly-correlated systems in order to advance the field of condensation phenomena as a whole with a specific emphasis on a novel condensation phase, which we term the "fermion-exciton condensate". This dual condensate demonstrates both particle-particle and particle-hole condensation simultaneously in a single quantum state and may be capable of supporting a hybrid of the properties of superconductors and exciton condensates—as will be explored further in Chapters 10, 11, and 12. To contextualize these chapters as well as Chapters 4-9, which deal with particle-particle and exciton condensation separately, the following primer introduces the basic tenants of Bose-Einstein condensation, fermion-pair condensation, and exciton condensation.

3.1 Bose-Einstein Condensation

Bose-Einstein condensation (BEC) was first proposed by Einstein [113] based on S. N. Bose's 1924 paper [114]. Einstein defined this BEC to be a phase transition associated with the condensation of a macroscopic amount of atoms into the lowest-energy state as a result of quantum statistics. In 1938, London [115] and Tisza [95] identified the superfluid behavior of helium-II [92, 93] to be a manifestation of this condensation. Over the course of the following decades, theoretical frameworks for the understanding of BECs were introduced [116–118], Bose-Einstein condensation was linked to the concept of off-diagonal long range order [119], and critical temperatures for both ideal and non-ideal Bose gases were derived [118]. An introduction to these topics is given in the following sections.

3.1.1 One-Body Density Matrix in Quantum Field Theory

First, let us start by reintroducing the one-particle reduced density matrix (${}^1D$) through use of field operators

$$\hat{\mathbf{\Psi}}(\mathbf{r}) = \sum_v \psi_v(\mathbf{r})\hat{a}_v \tag{3.1}$$

and

$$\hat{\mathbf{\Psi}}^\dagger(\mathbf{r}) = \sum_v \psi_v^*(\mathbf{r})\hat{a}_v^\dagger \tag{3.2}$$

where $\psi_v(\mathbf{r}) = \langle \mathbf{r}|\psi_v\rangle$ and $\psi_v^*(\mathbf{r}) = \langle \mathbf{r}|\psi_v^*\rangle$ are ordinary first-quantization wave functions and where $\hat{a}_v^\dagger$ and $\hat{a}_v$ are conventional second quantization operators that have been discussed in previous chapters. In loose terms, in this framework, the quantum field operators create or annihilate a particle at a given position $\mathbf{r}$ instead of in a given eigenstate v. Note that the commutation relationships for creation and annihilation operators hold in this framework with

$$[\hat{\mathbf{\Psi}}^\dagger, \hat{\mathbf{\Psi}}] = \delta(\mathbf{r} - \mathbf{r'}),\ [\hat{\mathbf{\Psi}}^\dagger, \hat{\mathbf{\Psi}}^\dagger] = [\hat{\mathbf{\Psi}}, \hat{\mathbf{\Psi}}] = 0 \tag{3.3}$$

for bosons.

In terms of these operators, the ${}^1D$ matrix is given by

$${}^1D(\mathbf{r}, \mathbf{r'}) = \langle \hat{\mathbf{\Psi}}^\dagger(\mathbf{r})\hat{\mathbf{\Psi}}(\mathbf{r'})\rangle \tag{3.4}$$

where $\langle \cdots \rangle$ indicates an averaging over all $\mathbf{r}$ and $\mathbf{r'}$. By setting $\mathbf{r} = \mathbf{r'}$, the density of a given state at position $\mathbf{r}$ can be found to be

$$n(\mathbf{r}) = \langle \hat{\mathbf{\Psi}}^\dagger(\mathbf{r})\hat{\mathbf{\Psi}}(\mathbf{r})\rangle = {}^1D(\mathbf{r}, \mathbf{r}) \tag{3.5}$$

which can be rewritten as

$$n(\mathbf{p}) = \langle \hat{\mathbf{\Psi}}^\dagger(\mathbf{p}) \hat{\mathbf{\Psi}}(\mathbf{p}) \rangle = \frac{1}{(2\pi\hbar)^3} \int d\mathbf{R} d\mathbf{s}^1 D \left(\mathbf{R} + \frac{\mathbf{s}}{2}, \mathbf{R} - \frac{\mathbf{s}}{2} \right) e^{-i\mathbf{p}\cdot\mathbf{s}/\hbar} \tag{3.6}$$

to yield the momentum distribution $n(\mathbf{p})$ where $\mathbf{R} = (\mathbf{r} + \mathbf{r}')/2$ and $\mathbf{s} = \mathbf{r}' - \mathbf{r}$. This translation is accomplished by transforming the quantum field operators to the momentum representation

$$\hat{\mathbf{\Psi}}(\mathbf{p}) = \frac{1}{(2\pi\hbar)^{3/2}} \int d\mathbf{r} e^{-i\mathbf{p}\cdot\mathbf{r}/\hbar} \hat{\mathbf{\Psi}}(\mathbf{r}), \tag{3.7}$$

which is a Fourier transformation.

A pure N-body wave function $\Psi_n(\mathbf{r}_1, \ldots, \mathbf{r}_N)$ hence corresponds to a one-body reduced density matrix given by

$${}^1D_n(\mathbf{r}, \mathbf{r}') = N \int d\mathbf{r}_2 \cdots d\mathbf{r}_N \Psi_n^*(\mathbf{r}, \mathbf{r}_2, \ldots, \mathbf{r}_N) \Psi_n(\mathbf{r}', \mathbf{r}_2, \ldots, \mathbf{r}_N). \tag{3.8}$$

For a statistical mixture—a weighted average of the pure eigenstates (Ψ_n) of the Hamiltonian corresponding to an energy E_n and weight e^{-E_n/k_BT}—, the one-body reduced density matrix is given by

$${}^1D(\mathbf{r}, \mathbf{r}') = \frac{1}{Q} \sum_n \left(e^{-E_n/k_BT} \right) {}^1D_n(\mathbf{r}, \mathbf{r}') \tag{3.9}$$

where $Q = \sum_n e^{-E_n/k_BT}$ is the partition function.

3.1.2 BEC and Off-Diagonal Long-Range Order

As a particular example, a uniform, isotropic system of N bosonic particles confined to a box of volume V without any applied external potential is introduced. It can be shown that in the thermodynamic limit ($N, V \to \infty$), the one-body density matrix depends only on $\mathbf{s}$

and can be given according to [118]

$$^1D(\mathbf{s}) = \frac{1}{V}\int d\mathbf{p} n(\mathbf{p}) e^{i\mathbf{p}\cdot\mathbf{s}/\hbar} \tag{3.10}$$

if the density of the system $n = N/V$ remains fixed.

In a system that does not demonstrate Bose-Einstein condensation, the momentum distribution is smooth at low momenta, meaning that Equation (3.10)—and hence the one-electron density—approaches zero when $\mathbf{s} = \mathbf{r}' - \mathbf{r}$ approaches infinity (i.e., at large distances). However, a Bose-Einstein condensate is defined by a macroscopic occupation of the state corresponding to $\mathbf{p} = 0$ such that the momentum distribution is characterized by

$$n(\mathbf{p}) = N_0\delta(\mathbf{p}) + \tilde{n}(\mathbf{p}) \tag{3.11}$$

where $N_0 \propto N$ (the total number of particles). $N_0/N \leq 1$ is the condensate fraction that describes the fraction of the particles in the system that contribute to the condensate phase. Inserting Eq. (3.11) into Eq. (3.10) yields a non-zero one-body density at large distances $^1D(\mathbf{s})_{s\to\infty} \to n_0$ where $n_0 = N_0/V$.

This non-traditional behavior of a Bose-Einstein condensate is termed *off-diagonal long-range order* [117, 119] as it involves the non-diagonal elements ($\mathbf{r} \neq \mathbf{r}'$) of the one-body density. The identification of the condensate fraction and off-diagonal long-range order being necessary results of a Bose-Einstein condensate holds generally for both ideal (i.e., non-interacting) and non-ideal (i.e., interacting) BECs [118]. Further note that the condensate fraction is a function of the temperature of the system and goes to zero above a certain temperature called the critical temperature (T_c) [118].

The long-range order exhibited by the Bose-Einstein condensation is intrinsically linked to the eigenvalues (λ_i) of the one-body density matrix which can be found from the eigenvalue

equation

$$\int d\mathbf{r}'^{1}D(\mathbf{r},\mathbf{r}')\phi_i(\mathbf{r}') = \lambda_i\phi_i(\mathbf{r}) \tag{3.12}$$

or equivalently (in more-traditional notation)

$$^{1}D\phi_i = \lambda_i\phi_i \tag{3.13}$$

where $\{\phi_i\}$ is the set of orthonormal, single-particle eigenstates and $\sum_i \lambda_i = N$—the normalization condition—is satisfied. The eigenvalues λ_i are said to be the single-particle occupation numbers of the eigenstates, which are the natural orbitals [118].

The density matrix can then be rewritten in terms of these eigenfunctions according to

$$^{1}D(\mathbf{r},\mathbf{r}') = \sum_i \lambda_i\phi_i^*(\mathbf{r})\phi_i(\mathbf{r}'), \tag{3.14}$$

which can be further transformed to

$$^{1}D(\mathbf{r},\mathbf{r}') = \lambda_0\phi_0^*(\mathbf{r})\phi_0(\mathbf{r}') + \sum_{i\neq 0} \lambda_i\phi_i^*(\mathbf{r})\phi_i(\mathbf{r}') \tag{3.15}$$

for λ_0 corresponding to the lowest-energy eigenstate, ϕ_0.

For the uniform system discussed in the previous section, the natural orbitals are given by

$$\phi_{p_i}(\mathbf{r}) = \frac{1}{\sqrt{V}}e^{i\mathbf{p}_i\cdot r/\hbar} \tag{3.16}$$

which are plane waves with $\mathbf{p}_i$ determined from boundary conditions. Combining Eqs. (3.6), (3.15), and (3.16), the momentum distribution can be found to be

$$n(\mathbf{p}) = \lambda_0\delta(\mathbf{p}) + \sum_{\mathbf{p}_i\neq 0} \lambda_{\mathbf{p}_i}\delta(\mathbf{p}-\mathbf{p}_i) \tag{3.17}$$

which yields Eq. (3.11) exactly for $\lambda_0 = N_0$ and $\tilde{n}(\mathbf{p}) = \frac{V}{(2\pi\hbar)^3}\lambda_{\mathbf{p}}$ [118]. Thus, the eigenvalue of the reduced density matrix corresponds to the occupation of the lowest-energy state and acts as a signature of the BEC and hence off-diagonal long-range order in a BEC system.

In the general case, the eigenstates of the density matrix are not plane waves and must be determined numerically; however, the above results are general [118]. Therefore, for all bosonic systems, the largest eigenvalue of the one-particle reduced density matrix acts as a signature of Bose-Einstein condensation and corresponds to the occupation of the natural orbital given by the eigenstate corresponding to this largest eigenvalue [117–119].

3.1.3 The Ideal Bose Gas in a Box and the Critical Temperature

The ideal Bose Gas is composed of non-interacting bosons in a cubic box with length L such as those considered in the above sections. The Hamiltonian of such a bosonic system is given according to

$$\hat{H}^{(1)} = \frac{p^2}{2m} \tag{3.18}$$

whose solutions are plane waves such as those given in Eq. (3.16) with energy

$$\epsilon_n = \frac{\mathbf{p}_n^2}{2m} = \frac{\hbar^2\pi^2}{2mL^2}\mathbf{n}^2 \tag{3.19}$$

and momentum

$$\mathbf{p}_n = \frac{2\pi\hbar\mathbf{n}}{L} \tag{3.20}$$

with $\mathbf{n}$ having components $n_x, n_y, n_x \in \{0, \pm1, \pm2, \dots\}$.

These bosons satisfy Bose-Einstein statistics, meaning that the number of particles expected to be in a given state i is

$$\langle n_i \rangle = \frac{1}{e^{\beta(\epsilon_i - \mu)} - 1} \tag{3.21}$$

where ϵ_i is the energy of state i, μ is the chemical potential, and $\beta = 1/k_B T$ [118]. Therefore, the number of particles in the ground state ($\epsilon_i = 0$) of an ideal gas is given by

$$\langle N_{ground} \rangle = \frac{1}{e^{-\beta\mu} - 1}. \tag{3.22}$$

Solving for the chemical potential, which must be less than the lowest system energy for a Bose gas, yields [118]

$$\mu = -k_B T \ln\left(\frac{1}{\langle N_{ground} \rangle} + 1\right). \tag{3.23}$$

As the total number of particles in the system is N, we have the following constraint

$$N = \sum_i \langle n_i \rangle = \sum_i \frac{1}{e^{\beta\epsilon_i} e^{-\beta\mu} - 1} = \sum_i \frac{1}{\left(e^{\beta\epsilon_i}\right)\left(\frac{1}{\langle N_{ground} \rangle} + 1\right) - 1} \tag{3.24}$$

with the energy values ϵ_i given according to Eq. (3.19) such that

$$N = \sum_{n_x, n_y, n_z = 0}^{\infty} \frac{1}{\left(e^{\beta\epsilon_1 (n_x^2 + n_y^2 + n_z^2)}\right)\left(\frac{1}{\langle N_{ground} \rangle} + 1\right) - 1} \tag{3.25}$$

where $\epsilon_1 = \hbar^2 \pi^2 / 2mL^2$ is the energy of the first excited state.

An approximate analytical solution can be obtained by transforming Eq. (3.25) and taking the continuum limit for the excited states, which yields [120]

$$\langle N_{excited} \rangle = \frac{\pi}{4\epsilon_1^{3/2}} \int_0^{\infty} d\epsilon \sqrt{\epsilon} \frac{1}{e^{\beta\epsilon} - 1} = \left(\frac{\pi k_B T}{4\epsilon_1}\right)^{3/2} \zeta_{3/2} \tag{3.26}$$

where μ has been set to zero as $\epsilon^{-\beta\mu} \approx 1$ when $\langle N_{ground} \rangle \gtrsim 1$ (the region of interest) and where $\zeta_{3/2} = \zeta(3/2) \approx 2.61$ using the Riemann Zeta function. This approximation breaks

down when $\langle N_{ground} \rangle \approx 0$ and $\langle N_{excited} \rangle \approx N$ or equivalently when

$$\langle N_{excited} \rangle = \zeta_{3/2} \left(\frac{\pi k_B T}{4\epsilon_1} \right)^{3/2} \approx N. \tag{3.27}$$

Thus, we can define a *critical temperature* T_c such that above this critical temperature a Bose-Einstein condensation is no longer observed, which is characterized according to the equation [120]

$$N = \zeta_{3/2} \left(\frac{\pi k_B T_c}{4\epsilon_1} \right)^{3/2} = 2.612 \left(\frac{m k_B T_c}{8\hbar^2 \pi} \right)^{3/2} V \tag{3.28}$$

or, equivalently, —solving for the critical temperature—

$$T_c = 3.31 \left(\frac{\hbar^2}{k_B m} \right) \left(\frac{N}{V} \right)^{2/3}. \tag{3.29}$$

This allows us to solve for the condensate fraction as follows [120]:

$$\frac{N_0}{N} = \frac{N - \langle N_{excited} \rangle}{N} = 1 - \left(\frac{T}{T_c} \right)^{3/2} \tag{3.30}$$

Note that even for real systems such as helium-IV, this critical temperature predicted for a non-interacting Bose gas is in reasonable agreement with experimental critical temperatures [121].

3.1.4 Brief Discussion of Non-Ideal Bose Condensation

Bose-Einstein condensates of non-interacting bosons are not expected to display the properties that are generally associated with the BEC phase. Specifically, boson-boson interactions lead to superfluidity and prevent the fragmentation of the condensate state into a number of incoherent subsystems [121].

First, let us briefly consider fragmentation of an ideal BEC. As discussed by Noziéres [122], the energetic difference between a system composed of $2N$ momentum $\mathbf{p} = 0$ bosons

and a system composed of N momentum $\mathbf{p}$ and N momentum $-\mathbf{p}$ bosons is proportional to N/L^2 and is hence small to the point of vanishing in the macroscopic limit. By including a repulsive interaction ($v/2 > 0$) between bosons, the system Hamiltonian is

$$\hat{H} = \hat{H}_o + \hat{V} = \sum_{\mathbf{p}} \epsilon_p \hat{\mathbf{\Psi}}^\dagger(\mathbf{p})\hat{\mathbf{\Psi}}(\mathbf{p}) + \frac{v}{2}\sum_{\mathbf{p}} \hat{\mathbf{\Psi}}^\dagger(\mathbf{p}_4)\hat{\mathbf{\Psi}}^\dagger(\mathbf{p}_3)\hat{\mathbf{\Psi}}(\mathbf{p}_2)\hat{\mathbf{\Psi}}(\mathbf{p}_1)\delta^{\mathbf{p}_4+\mathbf{p}_3}_{\mathbf{p}_2+\mathbf{p}_1} \tag{3.31}$$

with the delta function being required to preserve overall momentum. For a fixed number of bosons N_{tot}, the expectation value of the Hamiltonian is given by [121]

$$E_{m,m'} = \langle \phi_{m,m'} | \hat{H} | \phi_{m,m'} \rangle = N_{tot}\epsilon_{\mathbf{p}} + \frac{v}{2}\left(N_{tot}(N_{tot}-1) + 2mm'\right) \tag{3.32}$$

where m describing the number of momentum $+\mathbf{p}$ bosons and m' describing the number of momentum $-\mathbf{p}$ bosons. Thus, for interacting bosons, the energetic difference between a state composed of $2N$ bosons with half $+\mathbf{p}$ and half $-\mathbf{p}$ and a state composed of $2N$ bosons all with $\mathbf{p} = 0$ is given by

$$E_{N,N}(\mathbf{p}) - E_{2N}(\mathbf{0}) = 2N\epsilon_{\mathbf{p}} + vN^2 \tag{3.33}$$

which contains an extensive quantity (vN^2) that persists even in the thermodynamic limit. Therefore, even a small repulsive interaction between bosons is sufficient to prevent the fragmentation possible in the ideal BEC. A similar result can be shown for the prevention of spin fragmentation [121].

Further, superfluidity—which was first explained by Landau in 1941 [123]—is only possible in the presence of interactions between the bosons. Landau's criterion for superfluidity can be written as $v < v_c$ which specifies that if the relative fluid-capillary velocity is smaller

than a certain critical velocity—given by

$$v_c = \min_{\mathbf{p}} \frac{\epsilon(\mathbf{p})}{p} \tag{3.34}$$

where p is the magnitude of the momentum—a persistent, frictionless flow will occur. According to this equation, when $\epsilon(\mathbf{p}) = \mathbf{p}^2/2m$ —as is the case in ideal Bose gases—the critical velocity is equal to zero, which precludes superfluidity in an ideal BEC. However, even weakly-interacting Bose gases fulfil the Landau criterion for superfluidity [118]. See Ref. [124] for a detailed review on the link between Bose-Einstein condensation and superfluidity.

Another difference between ideal and non-ideal Bose gases is the increase in critical temperature observed for systems with a fixed boson density in the infinite size limit [125], which has been explored through use of Monte Carlo calculations [126]. However, in the dilute regime—a regime which encompasses a fair number of condensation phenomena including the BCS limit of the condensation of Cooper pairs—the deviations from the ideal predictions are small [121] and, thus, the ideal critical temperature equation given in Eq. (3.29) can be used to predict critical temperatures of various candidates for real superfluid materials.

3.1.5 Experimental Realizations

Superfluid phenomena—such as the frictionless flow of super-cooled helium-IV—were first observed in the early twentieth century [117]. However, the first "pure" experimental measure of a Bose-Einstein condensate in a laboratory was the 1995 preparation of dilute atomic gas BECs [101, 127]—nearly 70 years after the theoretical framework of BECs was introduced by Bose and Einstein in 1924 [114]. In these dilute atom experiments, Cornell, Weimann, and Ketterle cooled around two thousand atoms of Rubidium-87—using a magneto-optical trap, laser cooling, and evaporative techniques—to below $T_c \approx 170\ nK$ and observed Bose-Einstein condensation of the constituent ^{87}Rb atoms. For this achievement, they shared

the 2001 Nobel Prize in Physics. To verify the creation of such a condensate state, the smaller wavenumbers and hence slower velocities of the ground state atoms were exploited such that if you removed the magnetic trap in which the atoms were prepared, the positions of the atoms after a short amount of time ($t = 100\ ms$) could be measured and used to determine the velocities of the atoms. A macroscopic number of the atoms were observed to have the same, extremely-small velocities (and hence momenta) and were hence confirmed to be in a single quantum state. Over the following decades, the preparation of atomic BECs has become routine with table-top BEC systems being commercially-available. Such readily-prepared systems have been used to study exotic systems including Hawking radiation, create atomic laser and clocks, and act as sensors [103]. However, the cutting edge of BECs is arguably the application of condensation phenomena to quasibosons consisting of pairs of fermions—including the condensation of Cooper pairs and the condensation of excitons, both of which will be explored in the following sections.

3.2 Fermion-Pair Condensation

Fermions are unable to occupy a single one-particle orbital due to the Pauli exclusion principle. However, particle-particle fermion-pair condensation involves the condensation of quasibosonic particle-particle pairs into a single, two-fermion quantum state called a geminal. Due to the resultant superfluidity of the constituent electrons, this condensation—the most well-known class of which is the condensation of Cooper pairs first described by Bardeen, Cooper, and Schrieffer [128]—has been actively studied since the mid-twentieth century in an effort to discover a commercially-viable superconductor, i.e., a condensate capable of forming at ambient pressures and temperatures. Despite this long history, however, the search is ongoing, and a portion of this thesis is dedicated to modelling the highly-correlated fermion-pair condensate phase in an effort to advance this field. As such, the following sections present the basic theory behind fermion-pair condensation.

3.2.1 The Ideal Fermi Gas

The major difference between an ideal Fermi gas and an ideal Bose gas is that fermions obey the Pauli exclusion principle [129], meaning that one-electron spin orbital occupations are bounded by $0 \leq n_i \leq 1$ where i is an index encompassing both the spatial and spin components for a given orbital. The average occupation number of the i^{th} single-particle state of a Fermi gas is characterized by Fermi-Dirac statistics to be

$$\langle n_i \rangle = \frac{1}{e^{\beta(\epsilon_i - \mu)} + 1} = f(\epsilon) \tag{3.35}$$

where μ is the chemical potential, which is constrained by the normalization condition

$$N = \sum_i \langle n_i \rangle. \tag{3.36}$$

Note that the Fermi level (E_F) is determined by the chemical potential of the Fermi gas (μ) and is defined such that $\langle n_i \rangle = 1$ for $\epsilon_i < E_F$ and $\langle n_i \rangle = 0$ for $\epsilon_i > E_F$ at zero Kelvin [28, 118].

In a uniform system of non-interacting particles in a container of volume V, the single-particle orbitals for the Fermi gas—similar to those for a Bose gas—are plane waves given by

$$\phi_{\mathbf{p}} = \frac{1}{\sqrt{V}} e^{i\mathbf{p}\cdot\mathbf{r}/\hbar} \tag{3.37}$$

with energies given by

$$\epsilon_{\mathbf{p}} = \frac{\mathbf{p}^2}{2m} = \frac{h^2\mathbf{k}^2}{8mL^2} \tag{3.38}$$

for a momentum $\mathbf{p}$ that obeys

$$\mathbf{p} = \frac{2\pi\hbar\mathbf{n}}{L} = \hbar\mathbf{k} \tag{3.39}$$

where $\mathbf{n}$ is a vector composed of three components $n_x, n_y, n_z \in \{0, \pm 1, \pm 2, \dots\}$ and where

$k = 2\pi/\lambda$ is the wavenumber.

For this system, the density of states is given by

$$D(\epsilon)d\epsilon = \frac{4\pi V(2m)^{3/2}\epsilon^{1/2}}{h^3}d\epsilon \tag{3.40}$$

which corresponds to the number of electrons in the energy interval $d\epsilon$ with the electron concentration thus being

$$\frac{N}{V} = \frac{1}{V}\int_0^{E_F} D(\epsilon)f(\epsilon)d\epsilon = \frac{8\pi}{3h^3}(2mE_F)^{3/2}. \tag{3.41}$$

By rearranging the above equation, the Fermi energy can be found to be

$$E_F = \frac{1}{2m}\left(\frac{3h^3N}{8\pi V}\right)^{2/3}. \tag{3.42}$$

at zero Kelvin [28].

While this ideal gas model is a good description for a cold, spin-polarized Fermi gas (i.e., a Fermi gas at low temperatures having electrons of only a single spin), systems in which electrons in atoms can occupy different spin states are strongly affected by interactions between electrons. However, the ideas introduced in this section—such as the Fermi energy/level and the density of states—are applicable to the more-complicated, weakly-interacting Fermi gas.

3.2.2 A Brief Aside on the BEC and BCS Limits

Even in dilute gases where the typical range of the two-body forces r_0 is much smaller than the average inter-particle distance d (i.e., $r_0 << d$), the scattering between fermions occupying different spin states is crucial for describing the physics of low-temperature, many-fermion systems [118]. This type of interaction between fermions is essential to understanding the behavior of the system.

A dilute Fermi gas at low temperatures with strong attractive interactions between particles is said to be in the BEC limit and results in a dilute gas of bosonic molecular dimers below the pair-formation crossover temperature [130]. Below the critical temperature in this BEC limit ($T_c = 0.218T_F$, $T_F \equiv$ Fermi temperature), the dimers form a Bose-Einstein condensate and hence exhibit both off-diagonal long-range order and superfluidity; however, the dimers are two-atom molecules interacting in real space and hence act like a traditional condensed Bose gas [130]. On the other hand, a dilute Fermi gas at low temperatures with weak attractive interactions between particles is said to be in the BCS limit and is unstable to the formation of Cooper pairs [131] which leads to superconductivity upon condensation as was first detailed by Ref. [128]. These Cooper pairs—in which atoms pair across the Fermi surface in momentum space—are highly-overlapping spatially and hence can not be considered to be composite bosons. The BEC and BCS limits can be described by the same wave function that changes in a smooth way as the interaction between fermions is tuned without encountering a phase transition—the so-called BEC-BCS crossover [118, 130]. The focus of the following sections will be primarily on the BCS limit as superconductivity is the behavior generally sought in modern scientific inquiry.

3.2.3 A Cooper Pair

A Cooper pair is composed of two electrons that interact via an attractive potential $V(\mathbf{r}_1 - \mathbf{r}_2)$ with their two-electron Schrödinger equation being given by

$$\left[-\frac{\hbar^2 \nabla^2_{\mathbf{r}_1}}{2m} - \frac{\hbar^2 \nabla^2_{\mathbf{r}_2}}{2m} + V(\mathbf{r}_1 - \mathbf{r}_2) \right] \psi(\mathbf{r}_1, \mathbf{r}_2) = E\psi(\mathbf{r}_1, \mathbf{r}_2) \tag{3.43}$$

where $\psi(\mathbf{r}_1, \mathbf{r}_2)$ is the wave function of the Cooper pair. This equation can be translated to

$$\left[-\frac{\hbar^2 \nabla^2_{\mathbf{R}}}{2m^*} - \frac{\hbar^2 \nabla^2_{\mathbf{r}}}{2\mu} + V(\mathbf{r}) \right] \psi(\mathbf{r}, \mathbf{R}) = E\psi(\mathbf{R}, \mathbf{r}) \tag{3.44}$$

where $m^* = 2m$ is the total mass, $\mu = m/2$ is the reduced mass, $\mathbf{r} = \mathbf{r}_1 - \mathbf{r}_2$ is the relative displacement, and $\mathbf{R} = (\mathbf{r}_1 + \mathbf{r}_2)/2$ is the center of mass. As the potential doesn't depend on the center of mass, the Cooper pair wave function should be of the form

$$\psi(\mathbf{r}, \mathbf{R}) = \psi(\mathbf{r}) e^{i\mathbf{K}\cdot\mathbf{R}} \tag{3.45}$$

where the total energy of the system would be $E = E_{\mathbf{R}} + E_{\mathbf{r}}$. The lowest total energy corresponds to $E = E_{\mathbf{r}}$ as $E_{\mathbf{R}} = 0$ for $\mathbf{K} = 0$ when the momentum of the center of mass vanishes.

Thus, the Cooper Pair wave function depends upon the solution of

$$\left[\frac{\hbar^2 \nabla_{\mathbf{r}}^2}{2\mu} + V(\mathbf{r})\right] \psi(\mathbf{r}) = E_{\mathbf{r}} \psi(\mathbf{r}) \tag{3.46}$$

which can be illuminated by taking the Fourier transform to yield [132]

$$\int \frac{d^3k'}{(2\pi)^3} V(\mathbf{k} - \mathbf{k}') \psi(\mathbf{k}') = (E - 2\epsilon_k) \psi(\mathbf{k}) \tag{3.47}$$

with $\epsilon_{\mathbf{k}} = \hbar^2 \mathbf{k}^2 / 2m$ being the free electron energy and setting $E = E_{\mathbf{r}}$. This implies that a bound state between two electrons exists only if the total energy is smaller than the energy of two free electrons ($E < 2\epsilon_k$). An attractive interaction $V(\mathbf{k} - \mathbf{k}') = -V_0$ below the Debye frequency ($\epsilon_{\mathbf{k}'}, \epsilon_{\mathbf{k}} < \hbar\omega_D$) yields a minimum potential of [132]

$$V_{0,min} = \frac{\sqrt{2}\hbar^3 \pi^2}{m^{3/2} \sqrt{\omega_D}} \tag{3.48}$$

for the electrons to be unstable against the formation of a bound pair. Thus, a bound Cooper pair will form only if there is a sufficiently-large attractive potential.

However, in many-body systems, only electrons near the Fermi level "see" the attractive potential such that $V(\mathbf{k} - \mathbf{k}') = -V_0$ for the unoccupied electronic states above the Fermi

level ($\epsilon_{\mathbf{k}'} - E_F, \epsilon_{\mathbf{k}} - E_F < \hbar\omega_D$), which leads to a binding energy given by [132]

$$E_b = 2\omega_D e^{-2/(V_0 D(E_F))} = 2E_F - E > 0 \tag{3.49}$$

where $D(E_F)$ is the density of states at the Fermi level. This positive binding energy for any attractive interaction V_0 indicates that the bound Cooper pair will form no matter how small the interaction. A well-defined Fermi surface that separates occupied and unoccupied electronic states is thus the key property that makes the system unstable against the formation of Cooper pairs for small attractive potentials. This differs from the free electron case that needs a certain minimum potential given in Eq. (3.48).

Note that the energy of this interaction is of the order of $10^{-3}\ eV$ and can hence be easily broken by thermal fluctuations at low temperatures. Further details for this derivation of Cooper pairs can be found in the original 1956 paper [131] as well as some helpful lecture notes [132].

3.2.4 BCS Theory—Many Cooper Pairs

To introduce the model Hamiltonian for BCS theory in second quantization, electron creation and annihilation operators are defined as $\hat{a}^\dagger_{\mathbf{k},\sigma}$ and $\hat{a}_{\mathbf{k},\sigma}$ where the momentum is given by $\mathbf{k}$ and the spin by $\sigma = \uparrow$ or $\downarrow$, which follow all fermionic creation and annihilation commutation relationships. The BCS Hamiltonian is then [128, 133]

$$\hat{H} = \sum_{\mathbf{k},\sigma} \epsilon_{\mathbf{k}} \hat{a}^\dagger_{\mathbf{k},\sigma} \hat{a}_{\mathbf{k},\sigma} + \sum_{\mathbf{k},\mathbf{1}} V_{\mathbf{k}\mathbf{1}} \hat{a}^\dagger_{\mathbf{k},\uparrow} \hat{a}^\dagger_{-\mathbf{k},\downarrow} \hat{a}_{\mathbf{1},\downarrow} \hat{a}_{-\mathbf{1},\uparrow} \tag{3.50}$$

where the first term corresponds to the kinetic energy of the electron and the second term corresponds to an electron-electron interaction.

The Hamiltonian can be diagonalized by doing the linear transformation

$$\hat{a}_{\mathbf{k},\uparrow} = u^*_{\mathbf{k}}\gamma_{\mathbf{k}0} + v_{\mathbf{k}}\gamma^\dagger_{\mathbf{k}1} \tag{3.51}$$

$$\hat{a}_{\mathbf{k},\uparrow} = u^*_{\mathbf{k}}\gamma_{\mathbf{k}0} + v_{\mathbf{k}}\gamma^\dagger_{\mathbf{k}1}, \tag{3.52}$$

and following Bogoliubov's method [134]. Such a treatment yields a gap energy given by [133]

$$\Delta_{\mathbf{k}} = -\sum_{\mathbf{k}'} V_{\mathbf{k}\mathbf{k}'}\langle \hat{a}_{\mathbf{k}',\uparrow}\hat{a}_{\mathbf{k}',\downarrow}\rangle \tag{3.53}$$

where

$$E_{\mathbf{k}} \equiv \sqrt{\epsilon_{\mathbf{k}} + |\Delta_{\mathbf{k}}|} \tag{3.54}$$

with $\epsilon_{\mathbf{k}}$ again being the free electron energy. The gap energy—the energy gap between the superconducting state and normal state—is the order parameter for BCS theory with it arising due to the non-zero energy of the superconducting state with zero kinetic energy [133].

Additionally, from the diagonalized Hamiltonian, the BCS ground state can be obtained to be [133]

$$|\psi_{BCS}\rangle = \prod_{\mathbf{k}} \left(u_{\mathbf{k}} + v_{\mathbf{k}}\hat{a}^\dagger_{\mathbf{k},\uparrow}\hat{a}_{-\mathbf{k},\downarrow}\right)|\emptyset\rangle. \tag{3.55}$$

Further, having both the gap energy and $\gamma_{\mathbf{k}\sigma}$ defined allows for the determination of the critical temperature in the mean field limit to be obtained according to [133]

$$k_B T_c \approx 1.13\hbar\omega_c e^{-1/D(E_F)V}. \tag{3.56}$$

3.2.5 The Two-Particle Reduced Density Matrix and Long Range Order

For fermions, the largest eigenvalue of the one-particle reduced density matrix given by

$$^1D^i_j = \langle \Psi | \hat{a}^\dagger_i \hat{a}_j | \Psi \rangle \tag{3.57}$$

are bound by $0 \leq \lambda \leq 1$ by the Pauli exclusion principle [129] as these eigenvalues correspond to occupation numbers of the natural spin orbitals. Pairs of fermions are capable of forming quasibosonic states, however, with these quasibosons allowed to condense into a single geminal—a particle-particle quantum state analogous to a one-particle orbital. Thus, the eigenvalues of the particle-particle reduced density matrix (^2D) defined by

$$^2D^{i,j}_{k,l} = \langle \Psi | \hat{a}^\dagger_i \hat{a}^\dagger_j \hat{a}_l \hat{a}_k | \Psi \rangle \tag{3.58}$$

are capable of being on the order of N with the largest eigenvalue of the ^2D being constrained to be $\lambda_D \leq N$ for systems of $2N$ or $2N+1$ fermions [135, 136]. In fact, analogous to a large eigenvalue in the one-boson reduced density matrix being indicative of Bose-Einstein condensation, a large eigenvalue in the particle-particle reduced density matrix is indicative of off-diagonal long-range order and is the signature for the condensation of fermion pairs into a single two-particle quantum state [135, 136].

The wave functions introduced by Bardeen, Cooper and Schrieffer [128] and Bogoliubov [134] do contain ODLRO [135], which means that these wavefunctions exhibit eigenvalues of ^2D that exceed the Pauli-like limit of 1. In fact, as proven by Yang's sixth theorem [135], pair occupations of single particle states such as those in the BCS ansatz are required to find a system with the maximal allowed eigenvalue for ^2D. Thus, superconductivity and off-diagonal long range order—and hence a large eigenvalue in the particle-particle reduced density matrix—are inherently linked.

3.2.6 The Antisymmetrized Geminal Powers (AGP) Model

As explained in the previous section, off-diagonal long-range order is obtained from wave functions that inherently pair occupations of single particle states [135]. An alternative way to represent such pairing is to describe an N-electron wave function according to [137]

$$|\Psi_{AGP}\rangle = \left(\hat{G}^{\dagger}\right)^{N/2} |\emptyset\rangle \tag{3.59}$$

where

$$\hat{G}^{\dagger} = \sum \xi_i \hat{a}^{\dagger}_{2i-1} \hat{a}^{\dagger}_{2i} \tag{3.60}$$

is a creation operator for an arbitrary geminal (i.e.,a two-particle function) [138]. In configuration space, this wave function is given by

$$|\Psi_{AGP}(1,2,\ldots,N)\rangle = g^{N}(12\cdots N) = g(1,2) \wedge g(3,4) \wedge \cdots \wedge g(N-1,N) \tag{3.61}$$

where $\wedge$ is the Grassman wedge product which expresses the sum of all products resulting from the antisymmetric permutation of particles and where normalization is implicit. Each geminal is described by

$$g(1,2) = \sum \xi_i \left[\phi_{2i-1}(1)\phi_{2i}(2) - \phi_{2i-1}(2)\phi_{2i}(1)\right] \tag{3.62}$$

where $\{\phi_i\}$ are a set of orthonormal orbitals. It follows that geminals satisfy antisymmetry, i.e., $g(1,2) = -g(2,1)$.

An AGP wave function is said to be extreme when all eigenvalues of the ${}^1D$ are equivalent, which corresponds to geminals of the form

$$g^{ex.}(1,2) = \sum e^{i\theta} \hat{a}^{\dagger}_{2i-1} \hat{a}^{\dagger}_{2i}. \tag{3.63}$$

This extreme geminal corresponds to all ξ_i values being equivalent and may or may not have some global phase θ. The extreme AGP wave function can then be written as

$$|\Psi_{AGP}^{ex.}\rangle = \prod(1 + e^{i\theta}\hat{a}_{2i-1}^{\dagger}\hat{a}_{2i}^{\dagger}) \tag{3.64}$$

and is also known as the BCS wave function [128, 138]. This state is not number-conserving and is instead composed of all possible, paired, evenly-numbered excitations.

The AGP model and the wave functions therein are often useful for electronic structure methods as they include correlations in the geminal expansion. The extreme AGP wave function is of particular interest to this thesis as the upper bound on the largest eigenvalue of ${}^2D$ is approached arbitrarily closely only for the extreme AGP wave function [135, 136, 138]. Thus, the largest number of Cooper pairs occupying the same quantum state is only maximized for a given number of particles in an extreme AGP state. When computationally exploring superconducting states, then, it is essential to consult the AGP states and especially the extreme AGP state.

3.2.7 Experimental Realizations of Superconductors

Superconductors were prepared as early as 1911 [91], although the microscopic principles governing them weren't elucidated until around forty years later [128]. The first experimentally-observed superconductor was liquid mercury, which H. K. Onnes was studying the resistivity of at extremely low temperatures ($T_c \approx 4.15K$) [139]. Since then, the search for higher-temperature superconductors for practical use has led to the vast theoretical and experimental exploration of many classes of systems encompassing pure elements (including allotropes of carbon), organic compounds, cuprates, iron-based systems, heavy fermion superconductors, alloys (such as NbTi), etc. [140]. Still, despite over 100 years of investigation, no currently-known system behaves as a superconductor at both reasonable temperatures and

atmospheric pressures, although a new so-called "room-temperature" superconductor—with critical temperature around 294 Kelvin—has been created under high-pressure conditions of roughly 10,000 times atmospheric pressures—likely still precluding commercial viability [141]. Interestingly, BCS theory is not applicable for a wide array of high-temperature superconductors (with critical temperatures above 30 K), making the development of a new microscopic theory to explain the behavior of such superconductors a current challenge of condensed matter physics.

3.3 Exciton Condensation

The BEC critical temperature equation in Eq. (3.29) demonstrates an inverse relationship with the mass of the bosonic particles. As such, excitons—which are significantly less massive than electron-electron pairs—are expected to condense at higher temperatures than traditional superconductors, especially when the strong electron-hole binding energies that greatly exceed thermal energy at room temperature are considered [112]. However, the recombination of the particles and holes composing an exciton can cause excitonic lifetimes to often be too short to support condensation. As such, separating the electrons and holes of the exciton into distinct layers to prevent recombination is the current focus of the field of exciton condensation, although current condensates of this type still require impractically high magnetic fields, high electric fields, and/or low temperatures. In the following sections, excitons and exciton condensation are introduced with a brief discussion comparing terminology regarding exciton condensation in the literature as well as experimental systems in which exciton condensation has been demonstrated.

3.3.1 An Introduction to Excitons

An exciton is an electron and a hole that are held together as a bound pair via a Coulombic attraction [142] and is hence a quasiboson. In condensed matter physics, a hole is a carrier

of a positive charge that corresponds to the absence of an electron. Unlike Cooper pairs, the strong electrostatic interaction between the negatively-charged electron and the positively-charged hole "holds" the exciton together in real space, making them spatially compact, although the size of an exciton can vary from approximately an Angstom to several hundred Angstroms. Excitons are typically categorized according to their size with so-called "Frenkel" excitons being localized to a single lattice site [143, 144] and so-called "Wannier" excitons (or "Wannier-Mott" excitons) spanning across many lattice sites [145, 146]. Frenkel excitons are typical in organic molecules and materials and have binding energies on the order of one electron volt with radii on the order of ten Angstroms. Wannier excitons are typical to most semiconductors with binding energies on the order of one hundred millielectron volts and radii on the order of one hundred Angstroms [142]. Excitons which lie between the Frenkel and Wannier regimes are typically described by the charge-transfer model with these intermediate-scale excitons being located in spatially-separated regions across some interface—instead of being localized to a single spatial region—and hence exhibiting a non-zero dipole moment [147].

For excitonic systems, the underlying lattice of atoms is treated as a background field with electrons and holes existing as free particles that "orbit" each other analogous to a Rydberg atom [142]. As such, the hydrogenic equations can be almost directly applied to excitonic systems with an adjustment to the reduced mass of the electron and hole system (m^*) —given by

$$\frac{1}{m^*} = \frac{1}{m_e^*} + \frac{1}{m_h^*} \tag{3.65}$$

where m_e^* and m_h^* refer to the electron and hole effective masses—and a modification to the permittivity (ϵ)—to adjust for the electrons and holes not existing in free space but rather in a lattice of atoms—being the only alterations. Specifically, the radius and energy of excitons are given according to

$$r_n = \frac{4\pi\epsilon\epsilon_o n^2\hbar^2}{m^* e^2} = \frac{n^2\epsilon m_e}{m^*} a_o \tag{3.66}$$

and

$$E_n = -\left(\frac{m^*}{m_e \epsilon^2}\right)\frac{R}{n^2} = \frac{R_{ex}}{n^2}, \tag{3.67}$$

respectively, where m_e is the mass of an electron, ϵ_o is the hydrogenic permittivity, e is the charge of an electron, $a_o = 0.529$ Angstroms is the Bohr radius, and $R = 13.6\ eV$ is the Rydberg constant. Note that these excitonic systems are considered metastable, meaning that they have relatively short lifetimes. This short lifetime can be a challenge in experimental realizations of condensations of excitons with approaches to combat this limitation including coupling excitons to light within a cavity to form exciton-polaritons as well as physically separating electrons and holes into distinct layers [112].

Another challenge to the condensation of excitons is the tendency of two excitons to bind to form a biexciton—analogous to the distinction between a free hydrogen atom H and a hydrogen molecular, i.e., the dimer H_2. Delocalization occurs in the low-effective mass limit, which should also favor the formation of the biexciton. Further, low excitonic densities—which favor the BEC limit and increase the critical temperature for superfluidity (see discussion below)—also favor biexciton formation [1]. Thus, it is a bit of a balancing act to increase exciton density enough to disrupt biexciton formation but not so much that the system has left the BEC limit. One way to avoid the formation of biexcitons is to physically separate electrons and holes into distinct layers. Between the prevention of biexcitons and the increase of excitonic lifetimes, these multi-layer systems have been the focus of modern interest when considering possible systems for the experimental and theoretical realization of exciton condensation.

While excitons are unable to carry mass or charge [148], they do carry energy and momentum [106]. Initially, there was a question of the usefulness of condensations of excitons as carrying either mass or charge was seen as being a necessary condition for the creation of a useful superfluid [148]; however, in exciton condensates, there exists the possibility for the frictionless flow of excitation energy [106] as well as counterflow superconductivity in bilayer

exciton condensates with spatially-separated excitons and holes [149].

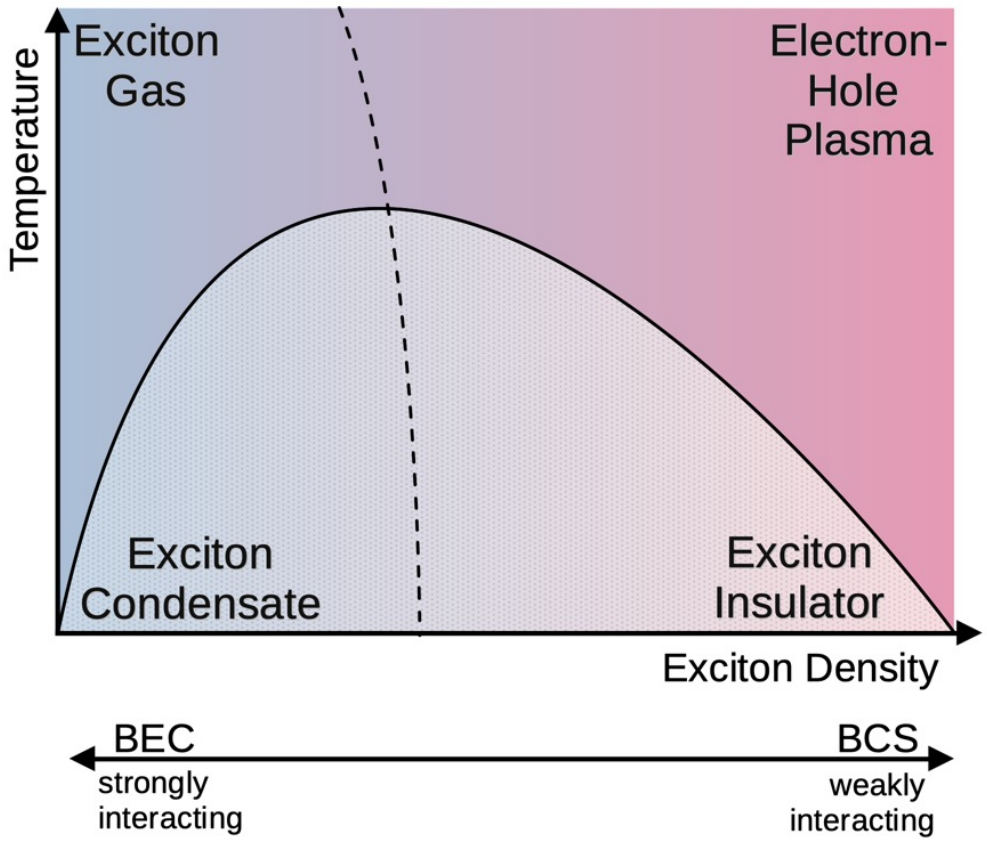

Figure 3.1: A graphic representing the terminology introduced by Refs. [1] and [2] to describe excitonic systems under different limits.

3.3.2 An Aside on Terminology

In this thesis, I utilize the terminology introduced by Comte and Noziéres [1, 2] with respect to the naming conventions with which I refer to various excitonic phases. Specifically, the excitonic phases can be classified according to temperature and the densities of the excitons. A dilute system of excitons at high temperatures is considered to act in a manner similar to a Bose gas and is hence termed an *exciton gas*. Upon cooling of this exciton gas, it can either *crystallize* into a regular lattice of excitons (or biexcitons) or it can undergo *Bose-Einstein condensation* where the excitons (or biexcitons) have condensed into a single quantum state.

Crystallization is likely when $\sigma = m_e^*/m_h^* << 1$; however, when $\sigma \approx 1$, localization of holes is thought to be too energetically-costly and the Bose-Einstein condensate is favored, which is expected to experience BEC-like superfluid behavior. A dense system of excitons at high temperatures, however, overlaps to such a degree that the excitons lose their identity completely, which is better thought of in terms of an *electron-hole plasma* rather than an exciton gas. When this plasma is cooled sufficiently, either *charge density waves*—the dense counterpart of the crystallized state in the dilute limit—or *exciton insulator* states may form. The excitons in the excitonic insulator states are analogous to Cooper pairs in that they are weakly bound and that BCS theory is appropriate for their theoretical description. The transition from dilute to dense systems should be smooth with increasing density slowly causing strongly-interacting bound pairs to evolve towards the loose BCS-like cooperatively-bound pairs. As such, a crossover—and not a phase transition—is expected between the BEC and BCS regimes [1] with a well-defined intermediate regime. In fact, by changing interlayer distances in two-layer systems, the BCS, BEC, and intermediate regimes can all be probed in a single molecular framework by tuning the binding energy between the excitons [150]. Refer to Fig. 3.1 for an overview of the various exciton phases. In this thesis, if large off-diagonal long-range order is noted in the modified particle-hole reduced density matrix without reference to excitonic densities or binding energies, exciton condensation is used as the general term as the ODLRO in this matrix describes the condensation of excitons (particle-hole pairs). This differs somewhat from some literature, which seems to suggest that excitonic insulator should be used for any exciton condensate in a ground state.

In fact, in some portions of the literature, the term exciton insulator is described as a situation in which the binding energy of the excitons exceeds that of the band gap—the energy between the valence band and the conduction band—such that excitons form spontaneously in the ground state without the input of energy [142]. This is an insulator as it opens (i.e., increases) the band gap; in this context, exciton insulator may refer to either the exciton

condensate or exciton insulator or any intermediate phase described by Fig. 3.1—depending on the coupling strength of the excitons—as long as no excitation energy is supplied and the excitons are indeed a ground state phenomenon. Further, some portions of the literature define the BCS and BEC regimes according to whether the excitons exist in semimetals or semiconductors. In this framework, the BCS regime occurs in semimetals (i.e., $E_G < 0$) where interactions are highly-screened and hence weak, and the BEC regime occurs in semiconductors (i.e., $E_G > 0$) where there is strong coupling [151]. This terminology, while consistent with that described in 3.1 in terms of the BEC being strongly interacting and the BCS being weakly interacting, does not connect with the idea of exciton density driving binding energies and is hence distinct. In general, literature in this field has been somewhat confused due to the terminology differences that tend to exist between experimentalists, theorists, and different subfields of condensed matter physics.

3.3.3 Simple Description of the Condensation of Excitons

For an exciton condensate in a semiconductor, the ground state is characterized by the creation operator

$$\psi_0^\dagger = \sum_k \phi_k \hat{a}_k^\dagger \hat{b}_k \tag{3.68}$$

with the N-exciton ground state being given by

$$|\Phi_N^0\rangle = (\psi_0^\dagger)^N |\emptyset\rangle \tag{3.69}$$

where here $\hat{a}^\dagger$ is a creation operator for a conduction electron, $\hat{b}$ is an annihilation operator for a valence electron, $\phi \approx 1/a_0^{3/2}$ is the internal orbital wave function, and $|\emptyset\rangle$ denotes an intrinsic semiconductor with no excitons ($N = 0$). This description of exciton condensation will be explored for a direct gap, isotropic, non-degenerate model with parabolic conduction and valence bands in the mean field limit with the spin degrees of freedom being ignored and

an unscreened Coulomb interaction between free carriers being assumed. Both the dilute (BEC) and dense (BCS) limits will be considered. Then a brief discussion regarding the complications present in more-realistic models will be undertaken. For further mathematical description of exciton condensation, see Refs. [2, 107, 142, 148, 152, 153].

The Keldysh-Kozlov-Kopaev Formulation for Exciton Condensation

As first formulated by Keldysh, Kozlov, and Kopaev [152, 153], for the intrinsic semiconductor reference in which there are no free carriers, the one-electron Hamiltonian of a semiconducting state capable of supporting free electrons and holes is given by

$$\hat{H}_0 = \frac{\hbar^2 k^2}{2m_e^*}\hat{a}^\dagger_{k,\sigma}\hat{a}_{k,\sigma} + \frac{\hbar^2 k^2}{2m_h^*}\hat{b}^\dagger_{k,\sigma}\hat{b}_{k,\sigma} \tag{3.70}$$

where k is the momentum of the electrons and holes that are being counted by their corresponding number operators $\hat{N}_e = \hat{a}^\dagger_{k,\sigma}\hat{a}_{k,\sigma}$ and $\hat{N}_h = \hat{b}^\dagger_{k,\sigma}\hat{b}_{k,\sigma}$. If we ignore interband electron-hole interactions—which are negligible in the BEC limit of dilute excitonic densities—the Coulombic interaction operator is given by

$$\hat{H}_c = \frac{1}{2}V_q\left[\gamma_q\gamma_{-q} - \hat{N}_e - \hat{N}_h\right] \tag{3.71}$$

where

$$\gamma_q = \hat{a}^\dagger_{k+q,\sigma}\hat{a}_{k,\sigma} - \hat{b}_{k-q,\sigma}\hat{b}^\dagger_{k,\sigma}, \tag{3.72}$$

$$V_q = \frac{4\pi e^2}{\kappa q^2}, \tag{3.73}$$

and the self-energy of the electrons and holes are removed. The normalized wave function of the $q = 0$ ground state in momentum space is then given by [1]

$$\phi_{k,0} = \frac{\sqrt{64\pi}}{(1+k)^2} \tag{3.74}$$

in the units of $1/a_0$ and ϵ_0, which is the energy of a single exciton.

If we consider a condensed system of N excitons—where we set $N_e = N_h = N$—at small densities under a mean field approximation, the ground state of the Bose-Einstein condensate of excitons is hence given [1]

$$|\Phi_\lambda^0\rangle = \prod_k e^{\lambda\phi_k \hat{a}_k^\dagger \hat{b}_k}|\emptyset\rangle = \prod_k [1 + \lambda\phi_k \hat{a}_k^\dagger \hat{b}_k]|\emptyset\rangle \tag{3.75}$$

where $\lambda = \sqrt{N}$ fixes the density of excitons. This expression is a special case in the BCS-like ansatz given by

$$|\Phi_\lambda^0\rangle = \prod_k [u_k + v_k \hat{a}_k^\dagger \hat{b}_k]|\emptyset\rangle \tag{3.76}$$

where

$$u_k = 1/\sqrt{1 + |\lambda\phi_k|^2} \approx 1, \tag{3.77}$$

$$v_k = \lambda\phi_k/\sqrt{1 + |\lambda\phi_k|^2} \approx \lambda\phi_k << 1, \tag{3.78}$$

and

$$|u_k|^2 + |v_k|^2 = 1, \tag{3.79}$$

which is a normalization condition. As first recognized by Keldysh and Kozlov [153], Eq. (3.76) can represent a Bose condensation of dilute excitons, and—as discussed by Kohn [148] and Comte [1], Eq. (3.76) can additionally represent an excitonic insulator phase in the limit of a high density of excitons. The shape of $|v_k|^2$ versus $\epsilon_k = \hbar^2 k^2/2m^*$ depicts the internal state of the bound exciton-hole pair [1] with $|v_k|^2$ scaling as a constant shape as a function of N in the dilute limit and with $|v_k|^2$ being a step function in the dense limit with increasing sharpness at increasing densities. The transition between these two limits is smooth, allowing a single wave function to represent the BEC, BCS, and intermediate regimes.

Further, minimizing $\hat{H} - \mu N$ yields additional information regarding the condensates in

each limit. In the BEC (dilute) limit, the chemical potential of an exciton is given by the negative energy of a single bound exciton, $v_{k,0} = \sqrt{N}\phi_{k,0}$, and the condensation parameter is given by [1]

$$\Delta_k = 2(\epsilon_k - \epsilon_0)\phi_k^0\sqrt{N} \tag{3.80}$$

which vanishes in the limit of $N = 0$ for the zeroth order solution. A first order correction to the chemical potential can also be derived to be [1]

$$\delta\mu = \frac{26\pi}{3} N a_0^3 \epsilon_0. \tag{3.81}$$

In the BCS (high-density) limit, the zeroth order solution yields $\Delta = 0$ and a chemical potential equivalent to the Fermi energy ϵ_F. The first order correction yields a value of [1]

$$\Delta = E_c \exp\left\{ -\frac{1}{\sqrt{4\pi e^2 N_0/3k_F^2}} \right\} \tag{3.82}$$

for the condensation parameter where E_c is a cut off energy on the order of the Fermi energy and where this form is similar to the typical BCS weak coupling result. This gap vanishes exponentially when the density approaches infinity. Interestingly, these limiting behaviors for both the chemical potential and the order parameter can be fit with a smoothly-varying function, with interpolation in the intermediate regime allowing for reasonable estimates of these functions for intermediate excitonic densities.

It can be shown that the ground state given in Eq. (3.75) possesses collective excitations that are Bogoliubov modes inside the gap in the dense case but describe center of mass motion of the bound excitons in the dilute case [1], providing a mathematical description consistent with the frictionless flow of exciton pairs in the dilute (BEC) limit below the critical temperature. As for the critical temperature of the condensation of excitons, in the large-N limit, T_c is on the order of Δ, which is exponentially small. In the small-N

limit, however, the critical temperature is given by that of the Bose gas from Eq. (3.29) such that $T_c \propto N^{2/3}$. There is no smooth function allowing for interpolation in the intermediate regime; however, it is typically expected that in between the high-N and low-N limits, the critical temperature should go through some currently-incalculable maximum [1]—likely indicating that this intermediate-N regime would be of interest in the search for high-temperature superconductors.

Qualitative Description of a More-Realistic Model

The major assumptions in the prior section are that both spin and screening effects are ignored and that non-degenerate bands are assumed. With regards to adding spin to the model, the results from above are not much changed in the mean field approximation [2]. Screening, however, makes pairing significantly less efficient and reduces the coupling constant, which decreases the expected critical temperature and hence must be accounted for in any complete treatment of the condensation of excitons [107]. No longer assuming non-degenerate bands would significantly modify the results from above quantitatively, although the qualitative behavior is likely similar [2]. See Ref. [2] for a further discussion of correcting the above model with these more-realistic conditions.

Also note that any impurities in the system—which have additionally been ignored—lead to the reduction of the superfluid density and critical temperature [107]. Further, biexciton formation is not considered in the prior section. Biexciton formation is known to almost-always decrease system energy [107], precluding pure exciton condensation; however, putting excitons and holes into physically-separated layers under certain interlayer distances and m_e^*/m_h^* ratios is known to make the formation of biexcitons undesirable [107]. See Refs. [149, 154] for more details.

3.3.4 Brief Aside on Counterflow Superconductivity

As shown in Refs. [149, 154], bilayer systems which allow for the physical separation of particles and holes support a distinct kind of superconductivity known as counterflow superconductivity. Lozovik and Yudson demonstrate that both the low-density (BEC) condensed states and the high-density (BCS) condensed states are expected to demonstrate superfluidity in such bilayer systems with critical temperatures approaching 100 Kelvin [149]. The result of this superfluidity is nonattenuating currents flowing without friction in opposite directions in each layer corresponding to two-wire electric transmission without dissipation, which would have obvious applications to the fields of energy transport and electronics. See Ref. [149] for the full derivation of the order parameter, the critical current, the critical temperature, and the coherence effects for systems demonstrating counterflow superfluidity.

3.3.5 Modified Particle-Hole Reduced Density Matrix and Long Range Order

Since the condensation of excitons involves particle-hole states, the modified particle-hole reduced density matrix with elements given by

$$ {}^2G^{i,j}_{k,l} = \langle \Psi | \hat{a}^\dagger_i \hat{a}_j \hat{a}^\dagger_l \hat{a}_k | \Psi \rangle \tag{3.83} $$

is the natural matrix to search for ODLRO indicating the condensation of excitons. However, the particle-hole RDM needs to be modified to

$$ {}^2\tilde{G}^{i,j}_{k,l} = {}^2G^{i,j}_{k,l} - {}^1D^i_j \, {}^1D^l_k \tag{3.84} $$

where ${}^1D$ is the one-fermion RDM that has been introduced in previous sections. This modification is done to remove an extraneous ground-state-to-ground-state transition that leads to an extraneous large eigenvalue and obscures relevant particle-hole behavior. Indeed, this

${}^2\tilde{G}$ matrix is still capable of having eigenvalues on the order of N with the largest eigenvalue of this matrix being constrained by $\lambda_G \leq N/2$ for systems of N electrons [155]. In fact, analogous to fermion-pair condensation being observed in the particle-particle RDM, the computational signature of exciton condensation is this largest eigenvalue of the modified particle-hole reduced density matrix (λ_G) exceeding the Pauli-like limit of one. This large λ_G signature of off-diagonal long-range order in the ${}^2\tilde{G}$ matrix—which indicates the condensation of excitons—was initially demonstrated by Garrod and Rosina [155] and then applied to molecular systems by Safaei and Mazziotti [156].

3.3.6 Experimental Realization of the Condensation of Excitons

The condensation of excitons should demonstrate temporal and phase coherence of a single quantum state over distances greater than inter-particle separation. Throughout the course of the last 20 years—in which the condensation of excitons has been experimentally probed—both the systems in which exciton condensation have been explored as well as the experimental signatures utilized to examine excitonic coherence have evolved. In the mid-2000s, some of the first experimental realizations of the condensation of excitons were observed in electronic double layers in a magnetic field [108, 157] and exciton-polariton systems [110, 111, 158–160]. In recent years, theorists and experimentalists alike have shifted focus to layered two-dimensional materials [156, 161–173], although investigation into bulk materials—such as highly-pressurized MoS_2 [174]—and single-layers—such as $ZrTe_2$ ($T_c \approx 180K$) [175]—has not been abandoned. Layered systems, though, create spatially-indirect excitons that hinder the formation of biexcitons and increases excitonic lifetime by preventing the recombination of electrons and holes while additionally allowing the excitonic binding energies to be tuned via interlayer distance [107]. Evidence for exciton condensation has been achieved in such spatially-separated systems including quantum wells formed from two-dimensional structures like semiconductors [166, 176], van der Waal heterostructures

[163, 171, 177, 178], and graphene bilayers [161, 165, 179]. Further, the condensation of microwave photons—which can directly model exciton condensation—has been achieved on a quantum computer [5].

3.3.7 Experimental Signatures of Exciton Condensation

In their 2004 study, Eisenstein et. al. utilized maximum interlayer tunneling, vanishing Hall resistance, and perfect Coulomb drag to provide evidence supporting their claim of creating an exciton condensate in bilayer electronic systems [108, 157]. *Maximum interlayer tunneling* in such systems is expected upon the formation of an exciton condensate due to electron-hole correlations and is characterized by a large highly-resonant peak in the plot of interlayer current (dI/dV) versus applied interlayer voltage (V) at zero voltage [157]. This evidence of exciton condensation was again utilized by Wang et. al. in 2019 [171] where such a peak in interlayer tunneling was able to be observed via electroluminescence due to the recombination of charge-transfer excitons. The *quantum Hall effect* refers to the phenomenon by which a current flowing in the x-direction (I_x) with drag (ρ_{xx}) and with a magnetic field in the z-direction (B) will result in a voltage in the y-direction (V_H) with a corresponding Hall resistance given by $\rho_{xy} = (2\pi\hbar/e^2)(1/v)$. In an exciton condensate system, the longitudinal component of the drag (the friction term) vanishes but a strong V_H develops if equal currents flow in parallel between each layer. However, both the longitudinal and Hall resistances approach zero when the currents in each layer are equivalent in magnitude but have opposite directions. Finally, *perfect Coulomb drag*—which refers to a situation in which a steady transport current in one layer of a bilayer system should be matched by an equal current of holes in the other layer—is used as evidence for the formation of an exciton condensate as excitons within a condensate should act as a unit [180]. Both the vanishing Hall resistance for a counterflow experiment and perfect Coulomb drag are direct evidence for counterflow superconductivity in these bilayer electronic systems. However, electronic double layers are

created upon the application of a magnetic field and appropriate interlayer bias, with such systems hence not being ideal for commercial application. Further, such condensates should arguably not even be considered pure Bose-Einstein condensations of excitons due to the applied voltage causing the system to not be in ground states at equilibrium.

In exciton-polariton systems, many of the hallmarks of the Bose-Einstein condensation of exciton-polaritons have been observed. For example, in 2006, Ref. [110] presented an exciton-polariton system with polarization dependence and *long-range spacial coherence* as well as a very narrow angular distribution of luminescence and thresholding behavior. Again, however, exciton-polaritons aren't ground state phenomena, and the usual concept of Bose-Einstein condensation assumes thermodynamic equilibrium.

Distinct from the previous attempts to characterize exciton condensation behavior is the *momentum-resolved electron energy-loss spectroscopy* (or M-EELs) approach. M-EELs measures both transfered energy and transfered momentum and thus is ideal for providing information about band structures and densities of state [181]. In 2017, Kogar et. al. [178] utilized this tool to probe the Goldstone mode corresponding to translation of the electronic crystal with respect to the atomic lattice. Kogar noted that in a transition metal dichalcogenide this mode falls to zero beneath a given critical temperature, which indicates crystallization of valence electrons into an exciton condensate according to Kogar [178].

Another approach is to consider that a condensation of excitons is predicted to include mixing of the conduction and valence bands and opening of the energetic gap around the Fermi level (E_F) with a corresponding characteristic flattening of the valence band top [1, 174, 175]. In recent years, identification of such features seems to be the favored approach for experimental verification of the condensation of excitons [174, 175, 182]. As an example, in 2019, Ref. [182] utilized *scanning tunneling spectroscopy*—which probes a sample's density of electrons as a function of energy—to identify the opening of the energetic gap between the conduction and valence bands in quantum-confined Sb nanoflakes; however, the

other signatures of an exciton condensate were not probed in this study. In 2021, a theoretical paper examined pre-existing *Raman spectra*—which probes rotational and vibrational modes—for MoS_2 and observed all three of the above features, which they called a Raman fingerprint for exciton condensation [174]. Another similar technique for uniquely identifying exciton condensation is *angle-resolved photoemission spectroscopy* (ARPES), which probes the energies and momenta of electrons in a material. As shown in 2023 by Ref. [175], band mixing, gap opening, and band flattening were all observed using ARPES for single-layer $ZrTe_2$ with a transition temperature of around $180K$.

However, to this day, definitive and uncontroversial experimental evidence for the ground state condensation of excitons has yet to be achieved, making further innovation in experimentally detecting such a state likely necessary. Further, direct evidence for antiparallel superconducting currents indicating counterflow superconductivity has not been realized in ground state systems.

3.4 Teasing the Fermion-Exciton Condensate

In the previous two sections of this chapter, fermion-pair condensates that demonstrate superconductivity and exciton condensates that demonstrate the superfluid flow of the constituent excitons have been discussed. However, as will be shown in Part IV, it is possible for both types of condensates to coexist in a non-trivial manner. Research into such a dual condensate has been a major focus of this thesis, with this author's research providing the first theoretical and computational prediction of the dual condensate, a proposed wave function to describe the condensate, a Hamiltonian that encompasses its physics, and the first preparation of such a condensate. These advances will be detailed in the chapters that comprise Part IV [4, 15, 16]. Recently, Blinov and MacDonald [183] have added to this literature with a distinct Hamiltonian capable of describing dual condensation. While it is hoped that the dual fermion-exciton condensate will exhibit some hybrid of the superfluidity of fermion-pair

condensation and the exciton superfluidity of exciton condensation, the exact properties of such an FEC remains to be explored, and an experimental realization remains to be achieved.

Part II

Exciton Condensation in Molecular Systems

CHAPTER 4

MOLECULAR EXCITON CONDENSATION IN BECHGAARD-LIKE TETRATHIAFULVALENE VAN DER WAALS LAYERED STRUCTURES

Material from: Schouten, A. O., Klevens, J., Sager-Smith, L. M., Xie, J., Anderson, J. S. & Mazziotti, D. A., Potential for exciton condensation in a highly-conductive amorphous polymer. Physical Review Materials, published 2023, 7, 045001.

4.1 Chapter Synopsis

Fifty years after it was initially predicted, exciton condensates—materials in which particle-hole pairs (excitons) form a Bose-Einstein condensate—have been experimentally realized in macroscopically-scaled materials and quantum devices. Here, using large-scale variational calculations, we computationally study *molecular* exciton condensation in layered van der Waal structure systems composed of organic superconductor tetrathiafulvalene (TTF) subunits, exploiting chemical tuneability—including charge and geometry—to maximize the signature of condensate character. These calculations demonstrate that at appropriate interlayer distances—centered around 2.0 Å—and appropriate layer offsets—specifically 0 Å and 3.0 Å—molecular-scale TTF van der Waal structures demonstrate exciton condensation with condensation increasing with both system size and charge. Results indicate that superfluidity in this system and related systems—including van der Waal structures, molecular metals with extended-TTF dithiolate ligands, and Bechgaard salts—likely occurs via an excitonic mechanism tuneable according to system composition, geometry, size, and charge. This study prompts further experimental investigation of the rational design of molecularly-scaled exciton condensates.

4.2 Introduction

The condensation of bosonic particles (or quasiparticles) into a single quantum state has long been an active area of study [97, 101, 113–115, 127, 129] as these condensates manifest macroscopic quantum phenomena such as superfluidity [97, 101, 115, 127], superconductivity [128, 137, 184, 185], and the nondissipative transfer of energy [106, 107]. In more recent years, theoretical and experimental exploration of exciton (particle-hole) condensation—i.e., condensation of bosonic particle-hole pairs into a single quantum state—have become increasingly prominent [4, 5, 107, 112, 156, 178, 179, 186–188] as these relatively-light quasiparticles with comparatively-high binding energies are expected to condense at higher temperatures [112] than traditional superconductivity resulting from the condensation of pairs of fermions (i.e., Cooper electron-electron/particle-particle pairs) [128, 137, 184, 185]. Exciton condensation results in the superfluidity of particle-hole pairs and involves the non-dissipative transfer of energy [106, 107], and—in bilayer systems—can result in so-called counterflow superconductivity [149]. Exciton condensates have been experimentally generated in optical traps with polaritons [109, 110, 158, 189], electronic double layers (EDLs) of semiconductors [180, 186, 187, 190, 191] and graphene [164, 179, 192], van der Waal structures [193, 194], and even photon-hole qubit systems [5].

In this paper we examine the realization of *molecular* exciton condensation—the condensation of excitons in layers or stacks of molecules. Unlike van der Waals structures whose condensates have been tuned in terms of geometric orientation such as twist angles, the assembly of materials from molecules can exploit the much broader tunability of chemistry in terms of chemical substituents, charge, and geometry. While we have shown in previous work that exciton condensation appears computationally in pentacene and hexacene bilayers [156], here we examine the formation of exciton condensation in molecular-scale TTF van der Waal structures (see Fig. 4.3). Tetrathiafulvalene (TTF) has played an instrumental role in the development of organic superconductors as it is highly symmetric, planar, and known to

have considerable π-π alignment and overlap when stacked [3, 195–198, 198]; indeed, the first organic superconductor was composed of a derivative of TTF (specifically, the first Bechgaard salt, $(TMTSF)_2PF_6$ [199]). In fact, the layered nature of these TTF van der Waal structures is reminiscent of a molecular-scaled versions of the stacking seen in the crystalline structures of both single-component molecular metals with extended-TTF dithiolate ligands [197, 200–204]—which can demonstrate superconducting character at high pressures and low temperatures [202, 203]—as well as the class of so-called Bechgaard salts of the form $(TMTTF)_2X$ ($TMTTF$ = tetramethyltetrathiafulvalene) or $(TMTSF)_2X$ ($TMTSF$ = tetramethyltetraselenafulvalene) [3, 198, 199, 201]—which also demonstrate superconducting behavior at low temperatures and high pressures (see the general phase diagram for Bechgaard salts adapted from Ref. [3] and shown in Fig. 4.1).

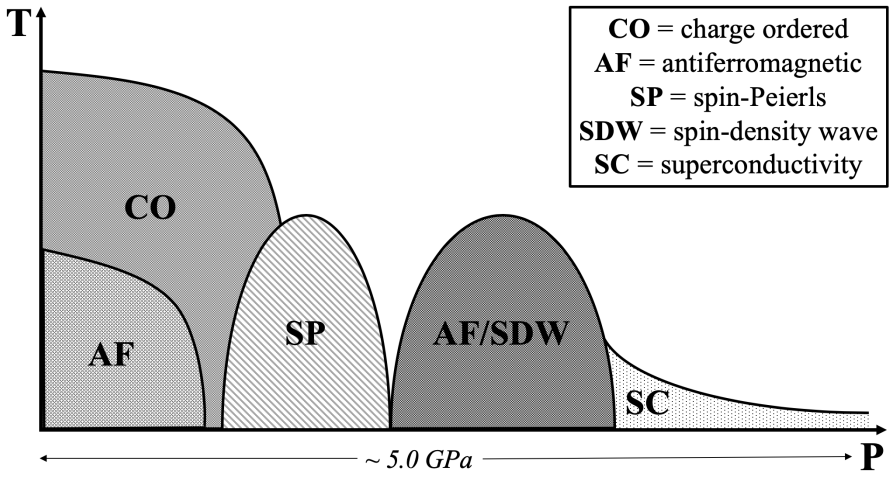

Figure 4.1: The generic phase diagram for TMTSF/TMTTF salts with centrosymmetric anions adapted from Ref. [3] is shown.

Here, for a variety of these Bechgaaard-like van der Waal TTF layered structures, we computationally study the extent of exciton condensation as a function of various interlayer distances, layer-offsets, charges, and numbers of layers, with the signature of exciton condensation being computed as the largest eigenvalue of the modified particle-hole matrix [155, 156] computed from direct variational calculation of the ground-state energies as func-

tionals of the two-electron reduced density matrix (2-RDM). As the primary method for controlling the ground-state properties of layered systems—such as Bechgaard salts—is to control the spacing of layers—through chemical means and/or the application of mechanical pressure—in order to alter orbital overlap [3], we demonstrate that at a range of appropriate interlayer distances between 1.0 and 4.0 Å, molecular-scale TTF structures demonstrate exciton condensation and identify the maximal condensate character as occurring at an interlayer distance of 2.0 Å. Additionally, layer offsets in the range of 0 Å to 4.0 Å were probed with an offset of zero supporting the largest degree of exciton condensate character, although an offset of 3.0 Å was additionally observed as having significant character of exciton condensation. At the optimal interlayer of 2.0 Å and layer offset of 0 Å supporting maximal exciton condensate character, increasing numbers of layers support increasing condensate character with an emergence of multiple islands of condensation (i.e., multiple quantum states containing more than one particle-hole bosonic quasiparticle) with even numbers of layers demonstrating a larger increase in overall excitonic character than their odd counterparts. Moreover, we observe that introducing charge to these molecular systems—consistent with the charged nature of the TTF-analogues in Bechgaard salts [3]—increases the maximum signature of exciton condensation for a given number of layers while retaining trends observed in the neutral system as the number of layers is increased.

Overall, our results suggest that experimental superfluidity in molecular systems composed of TTF layers is likely to occur via an excitonic mechanism with the degree of condensation being tunable through variations in substituents, charge, and geometry. This could illuminate the superconducting mechanism for non-traditional superconductors such as van der Waal structures and Bechgaard salts as well as provide insight on the future rational design of experimental, non-traditional superconductors.

4.3 Signature of Exciton Condensation

In 1924, Einstein and Bose first developed a theoretical framework for an ideal gas of bosons, a "Bose-Einstein" gas. When adequately cooled, these bosonic particles condense into a single, low-energy quantum ground state [113, 114], which results in the emergence of superfluid properties [97, 115].

A quantum signature representing the computational determination of the presence and scope of this so-called Bose-Einstein condensation is given by a large eigenvalue of the one-boson reduced density matrix (RDM) [119], which is expressed as

$$^{1}D^{i}_{j} = \langle \Psi | \hat{b}^{\dagger}_{i} \hat{b}_{j} | \Psi \rangle \tag{4.1}$$

with $|\Psi\rangle$ being an N-boson wave function, with each number demonstrating both the spatial and spin components of the boson, with i, j corresponding to one-boson orbitals in a finite basis set with rank r, and with $\hat{b}^{\dagger}$ and $\hat{b}$ depicting bosonic creation and annihilation operators, respectively. Note that as the eigenvalues of the one-boson RDM can be interpreted as the number of bosons occupying a single bosonic orbital, an eigenvalue exceeding one implies multiple bosons occupy the same quantum state and hence the presence of condensation.

For systems comprised of fermions, however, it is not possible for a macroscopic number of particles to aggregate into a single quantum state [129]. Condensation phenomena in fermionic systems can not occur between correlated fermions but instead comes about due to the correlation of fermion-fermion pairs, which create bosonic quasiparticles that can condense. Condensation of Cooper pairs (i.e., particle-particle pairs) results in the superfluidity of these electron-electron pairs, creating traditional superconductivity [128, 184], the quantum signature of which—independently derived by Yang and Sasaki [135, 136]—is a

large eigenvalue in the particle-particle reduced density matrix (RDM), written as

$$^2D^{i,j}_{k,l} = \langle \Psi | \hat{a}^\dagger_i \hat{a}^\dagger_j \hat{a}_l \hat{a}_k | \Psi \rangle \tag{4.2}$$

with $|\Psi\rangle$ being an N-fermion wave function, with each number demonstrating both the spatial and spin components of the fermion, with i, j, k, l corresponding to one-fermion orbitals in a finite basis set with rank r, and with $\hat{a}^\dagger$ and $\hat{a}$ depicting fermionic creation and annihilation operators, respectively.

Similarly, the condensation of particle-hole pairs (i.e., quasibosonic excitons) into a single quantum state results in exciton condensation. In direct analogy to the large eigenvalue of the particle-particle RDM being a quantum signature for the condensation of particle-particle (Cooper) pairs, one may expect the signature of exciton (particle-hole) condensation to be a large eigenvalue in the particle-hole RDM [148, 155, 156], which is given by

$$^2G^{i,j}_{k,l} = \langle \Psi | \hat{a}^\dagger_i \hat{a}_j \hat{a}^\dagger_l \hat{a}_k | \Psi \rangle. \tag{4.3}$$

However, there exists an extraneous large eigenvalue of the particle-hole RDM corresponding to a ground-state-to-ground-state transition. Thus, a modified particle-hole matrix with this unrelated large eigenvalue removed is constructed [148, 155, 156] and is represented as

$$^2\tilde{G}^{i,j}_{k,l} =^2 G^{i,j}_{k,l} - {}^1D^i_j \, {}^1D^l_k \tag{4.4}$$

We refer to the largest eigenvalue of this modified particle-hole RDM as λ_G and use this eigenvalue as the signature of the extent of exciton condensation throughout the course of our analysis. Note that as the eigenvalues of the modified particle-hole RDM can be interpreted as the number of excitons occupying a single, particle-hole "orbital", a λ_G value exceeding one indicates more than one exciton condensed into the same quantum state and hence the

presence of exciton condensation.

4.4 Results

4.4.1 Initial Exploration of the TTF Bilayer System

Recent scholarship [193, 194] has identified the class of van der Waal layered structures as demonstrating promise for the creation of macroscopically-scaled exciton condensates. In this study, we extrapolate this framework to a molecularly-sized system and use tetrathiafulvalene (TTF)—a molecule known to demonstrate intralayer correlation phenomena [197, 199, 205]—as the subunit composing the structure. The simplest such molecular-scale van der Waal structure is a TTF molecular bilayer. In order to gauge the relative extents of exciton condensation as a result of varying the distances between the two component TTF layers and thus probe a significant range of van der Waal interaction possibilities, interlayer spaces are varied from 1.0 to 4.0 Angstroms, and the signature of condensation, λ_G, is probed in the 6-31g basis using a [12,12] active space.

As can be seen in Fig. 4.2, the TTF bilayer system demonstrates exciton condensation ($\lambda_G > 1$, blue) over a multitude of spacial separations, with the 2.0 Å separation having the maximal signature of exciton condensation—as indicated by the largest eigenvalue. As such, this optimal distance of 2.0 Å is utilized as the interlayer distance throughout all further computations in which other variables are varied. Note that, for completeness, the extent of particle-particle condensation (λ_D, superconductivity) is probed for all systems; however, as can be seen from the pink data in Fig. 4.2, no significant particle-particle condensation is observed.

In order to visualize this excitonic system, we computationally probe the probabilistic location of a hole corresponding to a specified particle location—in a specified atomic orbital—for a given exciton. (See the Appendix for more information.) Specifically, in Fig.

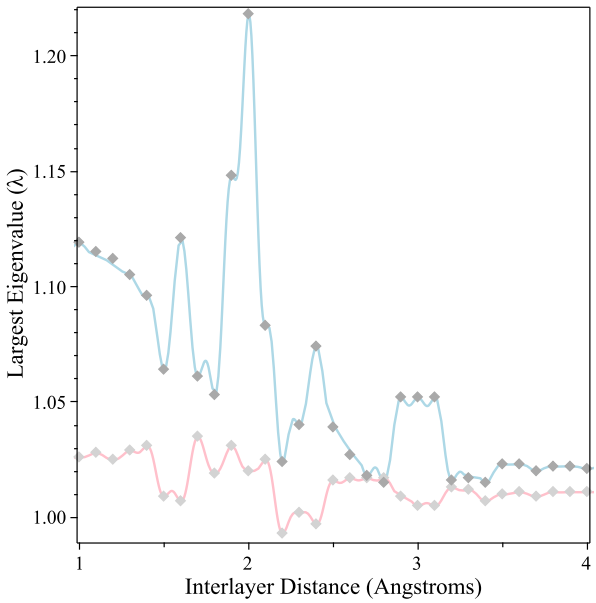

Figure 4.2: The largest eigenvalues of the particle-particle density matrix ($\lambda_D, pink$) and the modified particle-hole density matrix (λ_G, blue) as a function of interlayer distance are given for a bilayer of TTF molecules with no offset.

4.3, for the excitonic mode corresponding to the largest signature of exciton condensation, the probabilistic location of the hole of the exciton (in green and purple) is shown when the particle of the exciton is constrained to $4p_x$ orbital of one of the sulfur atoms (in red). From the image corresponding to the bilayer system, the existence of interlayer (as opposed to intralayer) excitons can be readily observed, indicating a possibility of greater excitonic stability.

4.4.2 Varying Layer Offset

Experimental systems in which TTF-like motifs are stacked—such as the Bechgaard salts [3, 199, 201] and molecular metals with extended-TTF dithiolate ligands [197, 198, 200–204]—tend to have some horizontal offset distance ($d_{off.}$) between layers—in addition to the vertical interlayer distance ($d_{int.}$)—such as the one shown in Fig. 4.4. In order to optimized this offset distance geometric parameter in terms of maximal exciton condensate character,

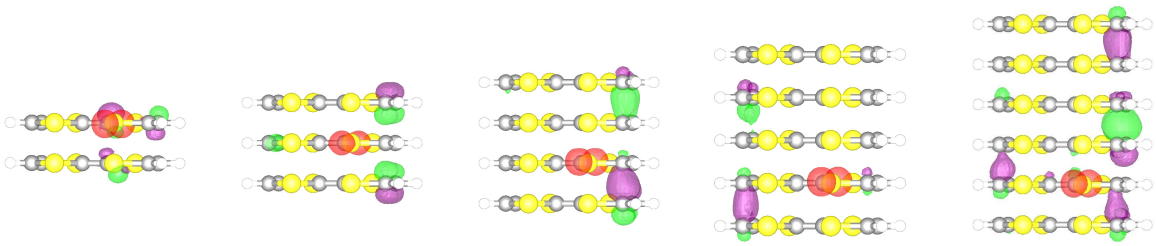

Figure 4.3: Visualization of the exciton where the exciton's particle is constrained to the p_x orbital (shown in red) and where the probabilistic location of the exciton's hole is probed (in green and purple) for the TTF van der Waals structures composed of 2, 3, 4, and 5 layers (pictured from left to right).

we probe the signature of exciton condensate character (λ_G) for the bilayer system—again utilizing the 6-31g basis and a [12,12] active space—across variable interlayer distances and offset parameters, with the significant results of this two-dimensional scan being shown in Figs. 4.2 and 4.5 and with all additional results being reported in the Supplemental Information online.

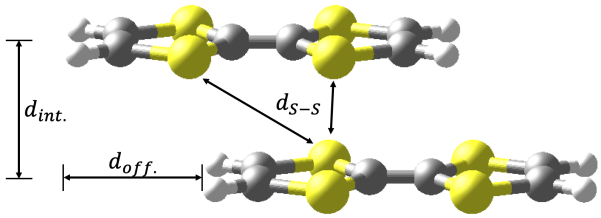

Figure 4.4: A figure demonstrating an offset bilayer system is shown with the interlayer distance ($d_{int.}$), the offset distance ($d_{off.}$), and S-S distances (d_{S-S}) specified.

From our scan across $d_{int.}$ and $d_{off.}$, we note that the largest signature of exciton condensation ($\lambda_G = 1.218$) occurs when there is no offset between layers, with this data already being presented in Fig. 4.2 in the previous section. However, significant exciton condensate character ($\lambda_G = 1.143$) is additionally observed for an offset distance of $d_{off.} = 3.0$ Å in the range of $min(d_{S-S}) \approx 1.8 - 2.2$ Å, as can be seen in Fig. 4.5. Note that in this figure shows the signature of exciton condensation (blue) as a function of the minimum interlayer

$S-S$ distance ($min(d_{S-S})$) as this metric is often the geometric parameter reported in experimental literature [200, 203, 204, 206] and as this value gives a better indication of $\pi-\pi$ overlap. Similar plots for all other offset distances probed are included in the Supplemental Information online, although only the $d_{off.} = 2.5$ and $d_{off.} = 4.0$ offsets demonstrate a signature exceeding $\lambda_G > 1.1$, with these signatures of condensation both being present at S-S distances of approximately 2.0 Å.

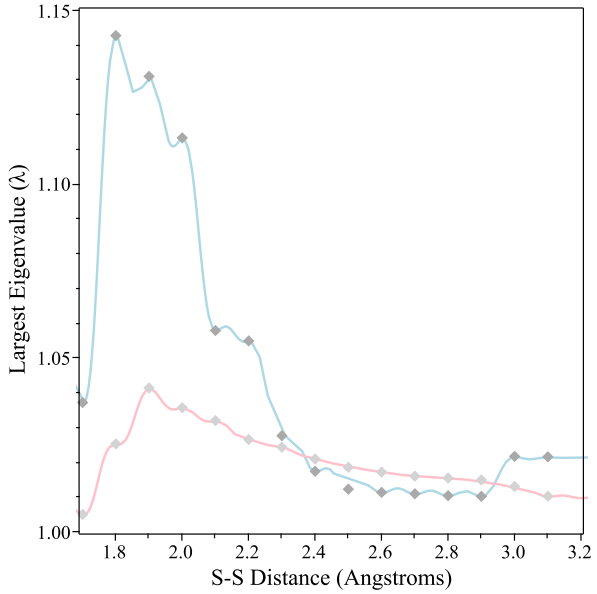

Figure 4.5: The largest eigenvalues of the particle-particle density matrix (λ_D, pink) and the modified particle-hole density matrix (λ_G, blue) as a function of interlayer distance are given for a bilayer of TTF molecules with an offset of 3.0 Å.

4.4.3 Varying the Number of Layers

To explore the behavior of larger van der Waal structure systems and better allow for extrapolated reasoning of excitonic behavior based on system size, we computationally probe the exciton condensate character of multi-layer TTF van der Waals structures composed of two to six TTF layers. As demonstrated in the previous section, the largest degree of exciton condensation is observed for an interlayer distance of 2.0 Å and an offset distance of

0 Å for the bilayer system. Thus, as the number of TTF layers in the systems are varied, the interlayer and offset distances between each layer are fixed to 2.0 Å and 0 Å, respectively, to allow for direct comparison. (Note that for systems composed of 2, 3, 4, 5, and 6 layers, active spaces of [12,12], [18,18], [24,24], [30,30], and [36,36], are utilized with the 6-31g basis set.)

As can be seen in Fig. 4.6, all TTF layered systems probed—from two to six layers—demonstrate character of exciton condensation, evinced by all having an eigenvalue of the modified particle-hole reduced density matrix larger than one. Comparing across all numbers of TTF layers, as the number of even layers increases so does the magnitude of the largest eigenvalue; the same can be said for the odd-layered counterparts, although the magnitude of exciton condensation is lesser for a given system with an odd number of layers than the system one fewer—and hence an even number of—layers.

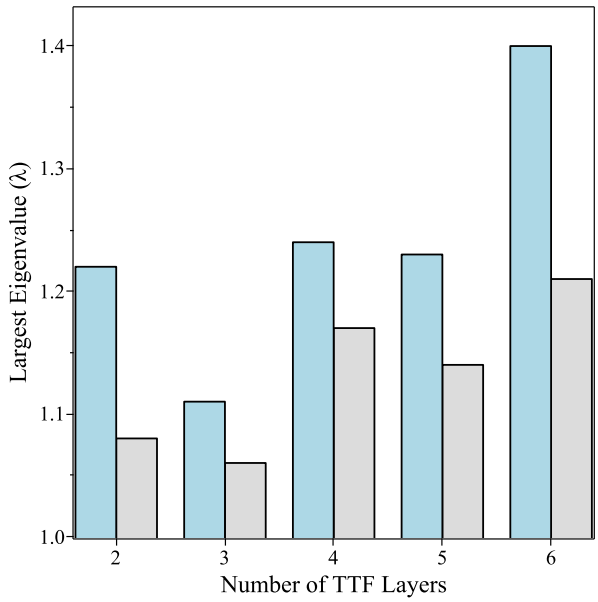

Figure 4.6: The two largest eigenvalues of the modified particle-hole RDM for TTF layered systems of variable numbers of layers separated by 2.0 Å are shown.

Another aspect of interest from Fig. 4.6 is the existence of multiple eigenvalues of the modified particle-hole RDM that exceed one. As the eigenvalues of the modified particle-

hole matrix can be interpreted as the number of excitons occupying a certain two-fermion, particle-hole quantum state, these multiple large eigenvalues indicate that there are multiple quantum states containing more than one exciton bosonic quasiparticle and hence multiple quantum states coexisting with character of exciton condensation. These multiple "islands of condensation" [5] coexist within a given system such that the sum of the eigenvalues exceeding one gives an overall measure of the number of excitons existing in a condensate phase, although the condensate character of these excitons do not exist in a single mode. By this metric, excitonic character increases as the number of layers in the TTF van der Waals structure system is increased with both even and odd numbers of layers supporting this trend. As the superfluidity of excitons is likely reliant on a macroscopic number of them existing within the *same* mode, however, this metric isn't as useful as the signature corresponding to the maximum eigenvalue of the modified particle-hole RDM.

Again, it is an enlightening exercise to visualize the excitonic mode corresponding to the signature of exciton condensation (λ_G) in order to get a sense of the relative delocalization of the excitons in the quantum state corresponding to the largest character of exciton condensation. As can be seen from Fig. 4.3, where the particle location for the exciton with the highest character of condensation is specified to a sulfur $4p_x$ orbital (red) and the corresponding hole location is probed (green and purple), structures of all layer numbers demonstrate significant character of interlayer excitons. By directly comparing the case in which the particle is localized to a sulfur $4p_x$ in the second layer for systems composed of different layers, it is apparent that hole density is delocalized across the entire stack in each case, with the largest delocalization occurring in the six-layer system, which also corresponds to the largest λ_G of the figures shown. As such, this visualization technique seems to allow for a qualitative analysis of exciton condensation via an analysis of delocalization when the same particulate atomic orbitals are compared.

Note that a four-layer calculation of stacked-TTF layers with an interlayer distance

of $d_{int.} = 1.8$ Å, an offset distance of $d_{off.} = 3.0$ Å, and a minimum S-S distance of $min(d_{S-S}) = 1.805$ yields a signature of exciton condensation of $\lambda_G = 1.200$, which verifies that the trend of increasing exciton condensate character with increasing numbers of layers holds for systems demonstrating layer offset as the corresponding bilayer system ($d_{int.} = 1.8$ Å, $d_{off.} = 3.0$ Å, $min(d_{S-S}) = 1.805$) demonstrates a signature of only $\lambda_G = 1.143$.

4.4.4 Varying Charge on the TTF Layers

As seen in recent experimental literature [207, 208], systems composed of TTF—which is strongly electron donating [209]—are often synthesized in a manner in which TTF layers are charged, including in the formation of many Bechgaard salts [3]. As condensation behavior is highly dependent electron and hole densities—and hence the charge of the species—, charge on the TTF layers in each of the van der Waals structures can be modified to optimize the character of exciton condensation. Here we probe the relative signatures of exciton condensation for the four-layer structure system ($d_{int.} = 2.0$ Å, $d_{off.} = 0$ Å, $min(d_{S-S}) = 2.0$ Å)—which demonstrates a large degree of excitonic character for a neutral species—with -1, neutral, $+1$, and $+2$ charges on each TTF layer.

As can be seen from Fig 4.7, as charge is varied from -1 per layer (total charge of -4) to $+2$ per layer (total charge of $+8$), the signature of exciton condensation in the four-layer TTF structure is seen to be at a minimum (although still significantly exceeding one) for the neutral species, with the addition of both positive and negative charge increasing the signature of exciton condensation. Additionally, we note that while negative and positive charge both increase the excitonic character, for the same magnitude of charge (i.e., comparing the structures with overall charges of -4 and $+4$), the addition of positive charge seems to increase the character of excitonic condensation to a slightly higher degree than the addition of negative charge. As increasing positive charge is shown to better increase the character of exciton condensation, syntheses in which each TTF layer has a positive charge

are likely advantageous for experimental realization of molecular-scale exciton condensation.

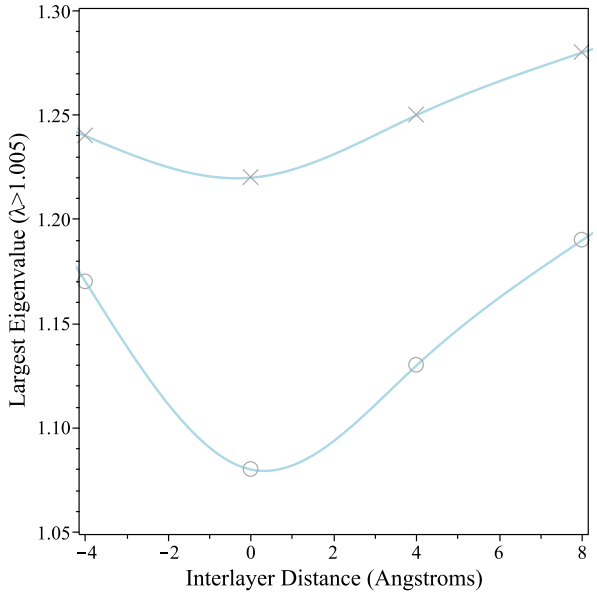

Figure 4.7: The largest (x's) and second largest (o's) eigenvalues of the modified particle-hole matrix for four-layer TTF structures separated by 2.0 Å where charge is varied from −1 per layer (−4 total charge) to +2 per layer (+8 total charge) are shown.

4.5 Discussion and Conclusions

In this study, we theoretically probe the presence and extent of exciton condensation—via the use of a quantum signature—in molecularly-scaled TTF van der Waal structure systems. In order to optimize the character of exciton condensation for such TTF multilayer systems, we analyze the effects of interlayer distance, offset distance, the number of layers, and the charge on each layer. From this investigation, we observe an interlayer distance of 2.0 Å and an offset of 0 Å to be optimal for the support of an exciton condensate, although offsets of $2.5 - 4.0$ Å also demonstrate significant exciton condensate character at minimum S-S distances around 2.0 Å. Additionally, we note the formation of increasing numbers of islands of condensation—in which multiple large eigenvalues indicate the presence of multiple, coexistent exciton condensate modes—as the number of layers is increased.

However, the largest signature of exciton condensation—representing the largest number of excitons condensed into a single quantum state—demonstrates a more nuanced trend; while the signature of exciton condensation increases for structures composed of an even number of layers increases as the system size is increased and while the signature of exciton condensation increases for structures composed of an odd number of layers increases as the system size is increased, odd-layered systems demonstrate lower signatures of exciton condensation relative to the corresponding, even structure with one fewer layer. Finally, the addition of charge is seen to increase the overall signature of exciton condensation with positive charge increasing character to a slightly-larger degree than negative charge of the same magnitude, indicating that positively-charged TTF structures may be beneficial in the experimental search for molecular-scale exciton condensates.

Overall, this study represents an advance in the rational design of exciton condensates. We computationally establish that molecular-scale van der Waal structures—which are highly tunable due to the experimental ability to alter layer geometry and composition—can act as molecularly-scaled exciton condensates with as few as two layers (although condensate character does increase with system size). Additionally, we demonstrate that systems composed of an even number of layers are optimal for practical implementation of molecular-scale condensates, and we note that increasing positive charge promotes a higher degree of exciton condensation as compared to negative and neutral TTF. Such understanding of exciton condensation on a molecular scale could aide not only in the development of macroscopically-scaled materials that demonstrate superfluidity of particle-hole pairs but could also lead to some interesting developments in the fields of molecular-scale electron transport and electronics.

More-complex experimental systems that resemble our simplistic stacked-TTF model include molecular metals with extended-TTF dithiolate ligands and Bechgaard salts, which prompts the question of whether the non-traditional superconductivity observed in such

systems may occur via an excitonic mechanism, with the positive effect of increasing charge on the character of exciton condensation providing additional evidence for such an excitonic mechanism in Bechgaard salts, which contain positively-charged TTF-like motifs. While the offset between layers—such as those present in these experimental systems—did decrease the character of exciton condensation, significant exciton condensate character was observed for offsets in the range of $2.5 - 4.0$ Å at S-S distances centered around 2.0 Å. Moreover, while minimum S-S distances in both classes of stacked-TTF experimental systems tend to be on the order of 3.3−3.7 Å [3, 197, 200, 203, 204, 206, 210, 211], increasing pressure and decreasing temperature—the conditions that yield superconducting character—tend to compress the crystal lattice, decreasing $S - S$ distances in one specific molecular metal to around 2.7 Å for a pressures of 10.7 GPa [200]. Additionally, in the neutral analysis of the TTF stacks ($d_{int.} = 2.0$ Å, $d_{off.} = 0$ Å), exciton condensation was observed in the regime of $3.5 - 3.8$ Å, although at a non-maximal level, which is more-consistent with experimental low-pressure geometric parameters. Overall, this study provides evidence that such molecular metal and Bechgaard salt systems may be observed to exhibit exciton condensate character under high pressure conditions (see Fig. 4.1) or via chemical alterations to decrease interlayer distances (and hence increase $\pi - \pi$ overlap) between the TTF-like layers, which prompts further experimental and theoretical investigation into the excitonic mechanism of superfluidity in such systems.

The flexibility of these molecular-scaled, Bechaard-like, van der Waal structure systems allow for a near-infinite number of modifications, so the development of predictive trends for the extent of condensate behavior by theoriticians is essential for guiding the types of experimental systems that are synthesized and explored in the years to come. This study represents some first steps in understanding and rationalizing exciton condensation in such systems and provides a template for the experimental realization of exciton condensation.

4.6 Appendix

4.6.1 Direct Calculation of the 2-RDM and the Modified G-Matrix

The molecular geometry of tetrathifulvalene (TTF) is obtained via the PubChem database [212], and van der Waal structures of TTF layers are constructed through vertical stacking of these TTF subunits at the specified interlayer distances. The electronic structures of these molecular geometries are then explored through the direct calculation of the 2-RDM, without calculating the many-electron wave function [48–62]. Specifically, the energy of each structure is optimized as a functional of the 2-RDM constrained by the N-representability conditions, which include Hermiticity, anti-symmetry, normalization, and the DQG conditions—i.e., that the particle-particle, hole-hole, and particle-hole RDMs are positive semidefinite—and which are necessary conditions for the 2-RDM to represent an N-electron wave function [50, 58, 62, 66]. In our study, this energetic optimization is conducted in the 6-31g basis with active spaces as specified throughout the text.

4.6.2 Large Eigenvalue of the Modified G-Matrix

The particle-hole RDM is calculated via a direct mapping from the particle-particle RDM given by

$$ {}^2G^{i,j}_{k,l} = \delta^{j1}_{l} D^{i}_{k} + {}^2D^{i,k}_{j,l} \tag{4.5} $$

where ${}^1D$ is the one-fermion RDM which is obtained from the ${}^2D$ via contraction and where δ is the Kronecker delta function. The modified particle-hole reduced density matrix is then obtained via Eq. (4.4), with the eigenvalues ϵ_i and eigenvectors v_i of this matrix being computed through solving the following eigenvalue equation:

$$ {}^2\tilde{G} v_i = \epsilon_i v_i \tag{4.6} $$

The largest eigenvalue (the maximum ϵ_i) is our signature of exciton condensation, which we label λ_G.

4.6.3 Visualization of Excitonic Modes

The visualization of the excitonic modes corresponding to maximum exciton condensate character is accomplished by constraining the location of the excitonic particle to a given atomic orbital and probing the location of the excitonic hole. Through use of the Variational2RDM function in the Quantum Chemistry package in Maple, a matrix expressing the canonical molecular orbitals (columns) in terms of atomic orbitals (rows)—denoted $M_{MO,AO}$—is obtained. This matrix is then manipulated by

$$M_{AO,MO} = (M^T_{MO,AO})^{-1} \tag{4.7}$$

in order to express the atomic orbitals (columns) in terms of the canonical molecular orbitals (rows), and the submatrix of $M_{AO,MO}$ corresponding to the active orbitals is then isolated and denoted as $M^{submat}_{AO,MO}$. The eigenvector of the modified particle-hole reduced density matrix corresponding to the largest eigenvalue, v_{max} is obtained from the spin-adapted ${}^2\tilde{G}$ matrix according to Eq. (4.6) and reshaped into a matrix in the basis of active molecular orbitals, V_{max}. Then,

$$(M^{submat}_{AO,MO})(V_{max})(M^{submat}_{AO,MO})^T \tag{4.8}$$

is performed to result in a matrix in which specified particle atomic orbitals are represented in terms of coefficients corresponding to the hole contributions to other molecular orbitals. Visualization tools in Maple can then be utilized to provide a visual representation of a probabilistic hole location for the specified particle location for a given excitonic mode.

CHAPTER 5

BEGINNINGS OF EXCITON CONDENSATION IN CORONENE ANALOG OF GRAPHENE DOUBLE LAYER

Material from: Sager, L. M., Schouten, A. O., & Mazziotti, D. A., Beginnings of exciton condensation in coronene analog of graphene double layer. The Journal of Chemical Physics, published 2022, 156, 154702.

5.1 Chapter Synopsis

Exciton condensation, a Bose-Einstein condensation of excitons into a single quantum state, has recently been achieved in low-dimensional materials including twin layers of graphene and van der Waals heterostructures. Here we examine computationally the beginnings of exciton condensation in a double layer comprised of coronene, a seven-benzene-ring patch of graphene. As a function of interlayer separation, we compute the exciton population in a single coherent quantum state, showing that the population peaks around 1.8 at distances near 2 Å. Visualization reveals interlayer excitons at the separation distance of the condensate. We determine the exciton population as a function of the twist angle between the two coronene layers to reveal the magic angles at which the condensation peaks. As with previous recent calculations showing some exciton condensation in hexacene double layers and benzene stacks, the present two-electron reduced-density-matrix calculations with coronene provide computational evidence for the ability to realize exciton condensation in molecular-scale analogs of extended systems like the graphene double layer.

5.2 Introduction

Exciton condensation—a Bose-Einstein condensation of particle-hole pairs into a single quantum state—has generated considerable experimental and theoretical interest [4, 5, 12, 107,

112, 164, 165, 178, 179, 179, 180, 186, 186, 187, 187, 188, 190–194, 213] due to the resultant superfluidity [97, 101, 115, 127] of the constituent excitons (particle-hole pairs) allowing for the dissipationless transport of energy [106, 107], which presents the possibility for uniquely energy efficient materials. Further, the greater binding energy and lesser mass of excitonic quasiparticles relative to particle-particle Cooper pairs indicates that exciton condensation should occur at higher temperatures [112] relative to the temperatures at which traditional superconductivity—i.e., the condensation of particle-particle pairs into a single quantum state [128, 137, 184, 185]—occurs.

Exciton condensates, nonetheless, have proven difficult to experimentally observe as excitons often have too short of a lifetime to allow for the simple formation of an exciton condensate; however, recent literature has established bilayer systems as being capable of demonstrating exciton condensation [161–173] likely due to the spatial separation of electrons and holes increasing excitonic lifetimes and causing them to act like oriented electric dipoles whose repulsive interactions prevent the formation of biexcitons and other competing exciton complexes such as electron-hole plasmas [108, 171]. Specifically, van der Waal heterostructures [163, 171, 177, 178] as well as graphene bilayers [161, 165, 179] demonstrate promise in the search for higher-temperature exciton condensate phases, with the tuneability of electronic states afforded by twisting graphene layers relative to each other being particularly of interest in recent literature [167, 173].

Small, molecularly-scaled systems have also been revealed to support exciton condensation via theoretical explorations utilizing a signature of such condensation found in the modified particle-hole reduced density matrix (RDM) [4, 5, 12, 213]. These molecular systems are able to be treated using theoretical approaches at lower computational costs and can be used as an analog for similar larger-scaled systems; moreover, molecular-scaled exciton condensation in and of itself may have potential applications in the design of more energy-efficient molecular-structures and devices. As such, a coronene bilayer system [214, 215]—where each

coronene layer is a seven-benzene-ring patch of graphene—is an ideal candidate for theoretical study of molecularly-scaled condensation phenomena. Exciton condensation in extended graphene bilayers indicate the likelihood that, similarly, coronene bilayers demonstrate correlation consistent with exciton condensation. Conclusions drawn from such a study may prove useful in understanding the mechanism by which exciton condensation occurs in benzene-ring and graphene bilayers in general.

In this paper, we computationally examine the beginnings of exciton condensation in a double layer composed of coronene. Utilizing variational 2-RDM theory [48, 49, 51, 53, 54, 57, 61, 216–220], we explore the largest eigenvalue (λ_G) of the modified particle-hole reduced density matrix ($\tilde{G}$)—which corresponds to the largest population of excitons in a single particle-hole quantum state—for various coronene-bilayer geometries, such that an eigenvalue above the Pauli-like limit of one indicates exciton condensation as more than one exciton is occupying a single state and a larger eigenvalue indicates a higher degree of exciton condensate character. We compare the maximal exciton populations (λ_G) as a function of distance between the layers of coronene and note that, near 2 Å, the population peaks at around 1.8 with interlayer excitons being noted via our visualization technique at this distance. Additionally, exciton populations as a function of twist angle between the two layers are computed in an effort to reveal any "magic angles". Overall, this molecularly-scaled exploration of coronene bilayers provides computational evidence of the beginnings of exciton condensation in molecularly-scaled systems that is related to the condensation found in extended systems like graphene bilayers.

5.3 Theory

Condensation phenomena occur when bosons—or quasibosons—aggregate into a single, low-energy quantum ground state when adequately cooled [113, 114], which results in the emergence of superfluid properties [97, 115]. For traditional bosons, a computational signature

of so-called Bose-Einstein condensation occurs when the largest eigenvalue of the one-boson reduced density matrix (RDM)—expressed as

$$^{1}D^{i}_{j} = \langle \Psi | \hat{b}^{\dagger}_{i} \hat{b}_{j} | \Psi \rangle \tag{5.1}$$

where $|\Psi\rangle$ is an N-boson wave function and $\hat{b}^{\dagger}_{i}$ and $\hat{b}_{i}$ are bosonic creation and annihilation operators for orbital i, respectively—exceeds one [119]. As the eigenvalues of the one-boson RDM correspond to the populations of one-boson orbitals, the largest eigenvalue corresponds to the maximum number of bosons occupying a single quantum state, i.e., the degree of condensation.

However, condensation in fermionic systems occurs via different mechanisms as multiple fermions cannot occupy a single orbital [129]. In traditional superconductivity, superfluidity arises due to correlations within quasibosonic particle-particle (electron-electron, Cooper) pairs, causing the constituent Cooper pairs to flow without friction [128, 184]. The signature of particle-particle condensation is the largest eigenvalue of the particle-particle RDM (2-RDM) [135, 136] given by

$$^{2}D^{i,j}_{k,l} = \langle \Psi | \hat{a}^{\dagger}_{i} \hat{a}^{\dagger}_{j} \hat{a}_{l} \hat{a}_{k} | \Psi \rangle \tag{5.2}$$

where $|\Psi\rangle$ is an N-fermion wave function, where each number demonstrates both the spatial and spin components of the fermion, the indices i, j, k, l correspond to one-fermion orbitals in a finite basis set of rank r, and $\hat{a}^{\dagger}$ and $\hat{a}$ depict fermionic creation and annihilation operators, respectively. The largest eigenvalue of the 2-RDM corresponds to the largest population of a single particle-particle quantum state (called a geminal [66, 135, 136, 221–223]), i.e., the degree of particle-particle condensation.

Similarly, exciton condensation results from particle-hole pairs (excitons) condensing into a single quantum state [106, 107]. The signature of exciton condensation—denoted as λ_G—is a large eigenvalue ($\lambda_G > 1$) of a modified version of the particle-hole reduced density matrix

[148, 155, 213], with elements given by

$$ {}^2\tilde{G}^{i,j}_{k,l} = {}^2G^{i,j}_{k,l} - {}^1D^i_j {}^1D^l_k = \langle\Psi|\hat{a}^\dagger_i\hat{a}_j\hat{a}^\dagger_l\hat{a}_k|\Psi\rangle - \langle\Psi|\hat{a}^\dagger_i\hat{a}_j|\Psi\rangle\langle\Psi|\hat{a}^\dagger_l\hat{a}_k|\Psi\rangle \tag{5.3} $$

where ${}^1D$ is the one-fermion reduced density matrix (1-RDM). After modification—which removes an extraneous ground-state-to-ground-state transition—the largest eigenvalue of the particle-hole RDM corresponds to the number of particle-hole pairs (excitons) that occupy a single particle-hole quantum state and hence signifies presence and extent of exciton condensation.

5.4 Results

Extended graphene bilayer systems have been identified as a major candidate for the creation of macroscopically-scaled exciton condensates [161, 165, 179]. In this study, we extrapolate this framework to a molecularly-sized system and use bilayers of coronene—where each layer is composed of seven, joined benzene rings—in order to probe a molecularly-scaled system whose similarity to graphene bilayers make it both a promising contender for a molecularly-scaled exciton condensate as well as an ideal analogue for exploring the correlation in layers of graphene using a system that can be directly explored by current theoretical techniques for strong electron correlation. As such, we explore relative amounts of correlation in coronene bilayer systems as a function of both interlayer distance and twist angle.

5.4.1 Exciton Population with Distance

To gauge the relative extents of exciton condensation as a result of varying interlayer distances between each layer of coronene and thus probing a significant range of van der Waals interactions between each layer in an attempt to identify an ideal distance for maximal correlation, interlayer spaces are varied from 1.0 Å to 2.5 Å, and the signature of condensation—

λ_G, i.e., the number of excitons condensed into a single particle-hole quantum state—is probed in the STO-6G basis using variational 2-RDM theory with a [24,24] active space.

As can be seen in Fig. 5.1—where the blue data indicates variational 2-RDM complete-active-space self-consistent-field (V2RDM-CASSCF) [24,24] calculations with [X,Y] denotes an active space of X electrons in Y orbitals and the pink data indicates configuration-interaction-based complete-active-space self-consistent-field (CI-CASSCF) [10,10] calculations—coronene bilayer systems demonstrate character of exciton condensation ($\lambda_G > 1$) for a wide variety of interlayer distances with the maximal excitonic populations in the bilayer peaking at 1.824 at 2 Å, although a relatively-wide plateau is noted in the range of 1.8-2.2 Å, indicating that exciton condensation is relatively robust in that region of distances. Distances in the neighborhood of 2.0 Å are hence ideal for the study of exciton condensate phases in bilayer systems composed of coronene, at least for twist angles around 0 degrees.

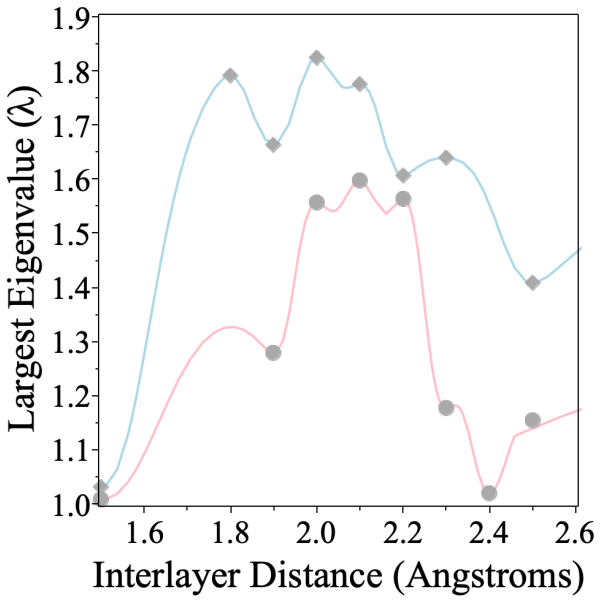

Figure 5.1: A scan over the exciton population in a single coherent quantum state (i.e., the largest eigenvalue of the modified particle-hole RDM) versus the distance between the two coronene layers for V2RDM-CASSCF calculations using a [24,24] active space (blue) and CI-CASSCF calculations using a [10,10] active space (pink). A STO-6G basis is utilized for both calculations.

Figure 5.2 allows for the visualization and comparison of coronene bilayer systems with

differing degrees of excitonic condensation. For the particle-hole wave function associated with the large eigenvalue, we visualize the probability distribution of the hole (gray-violet) for a particle location in a $2p_z$ orbital of one of the symmetrically-equivalent carbon atoms in the interior benzene ring (gold) using the methodology described in 5.6.2 for each geometry. The density cut-off for the probabilistic location of the hole differs between all three visualizations, so the magnitudes of the densities can not be directly compared between computations; however, the general trends in hole density locations can be established. For the 2.0 Å calculation, which shows the maximal excitonic character of the set, the excitonic hole is highly delocalized between both layers, demonstrating a highly correlated interlayer exciton; for the 2.5 Å calculation, an interlayer exciton is still observed, however, the degree of delocalization is highly decreased—with the majority of the hole population being focused on a single layer—, consistent with a lower degree of correlation and a lower signature of condensation; finally, for the 1.0 Å calculation, which does not demonstrate any exciton condensation, the hole's probabilistic location is highly localized with the majority of the population in the same layer as the particle. As such, the delocalization and the interlayer location of the hole seem to be strong indicators of high degrees of exciton condensation and indicate that both factors may be necessary for a condensate to form.

Note that, while the signature of exciton condensation is depressed in the [10,10] CI-CASSCF calculations relative to the [24,24] V2RDM-CASSCF calculations—which is expected as the higher active spaces allow for higher degrees of correlation, which can lead to higher signatures of condensation—the overall trends between the two sets of data are consistent, especially in the region of maximal condensation. As the results are consistent and as the [10,10] calculations are less computationally-expensive, [10,10] CI-CASSCF calculations are used throughout the exploration of the effect of twist angles on the presence and extent of exciton condensation.

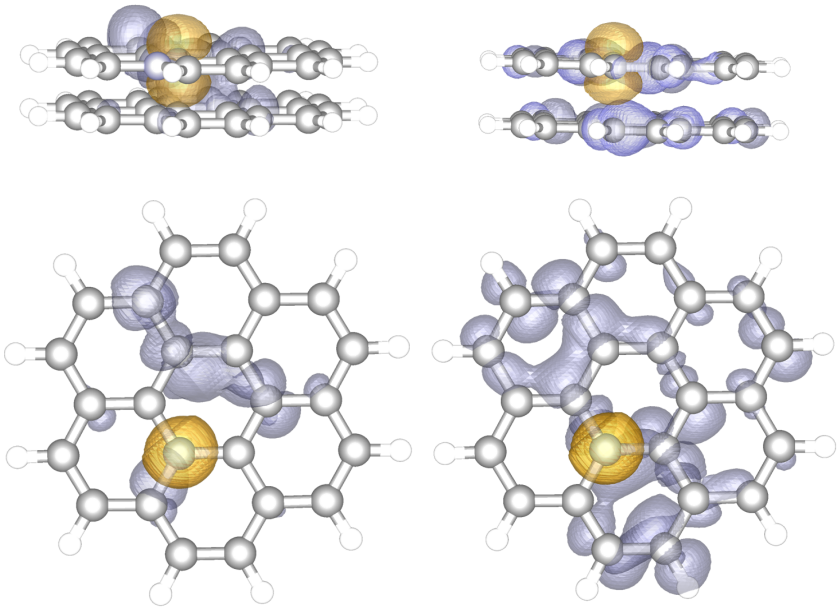

(a) 1.5 Å, $\lambda_G = 1.031$

(b) 2.0 Å, $\lambda_G = 1.824$

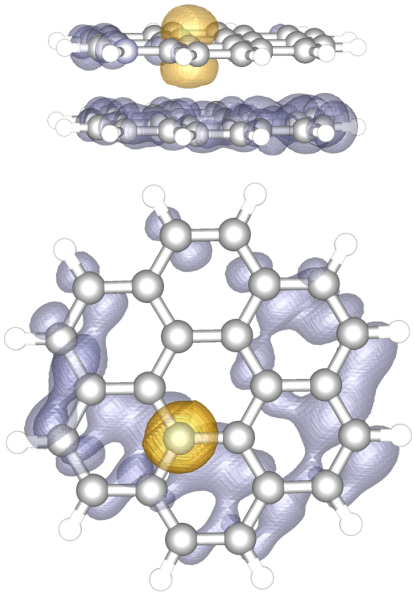

(c) 2.5 Å, $\lambda_G = 1.408$

Figure 5.2: Visualizations of the non-rotated coronene bilayer systems for (a) 1.5 Å, (b) 2.0 Å, and (c) 2.5 Å where the gray-violet represents the probabilistic location of the hole in the particle-hole wave function associated with the large eigenvalue for a particle position in a fixed atomic orbital (gold). Variational 2-RDM calculations with a [24,24] active space and STO-6G basis set are utilized for each visualization.

5.4.2 Exciton Population with Twist Angle

To obtain a more complete understanding of the conditions under which exciton condensation occurs, we explore the effect of rotations between the two layers of coronene on the excitonic population in a single quantum state (i.e., λ_G).

As can be seen from Fig. 5.3a—which scans the exciton population as a function of angles from 0 to 60 degrees, the full range of rotation before an identical configuration is obtained, for coronene bilayer systems with an interlayer distance of 2.0 Å—maximal condensation character is noted in the range of no offset. However, as shown in Fig. 5.3b, the large degree of condensation is relatively stable in the region of small angles, particularly of interest in magic-angle graphene studies [at around 1.1 degrees, [224]], with the largest degree of condensation occurring at 0 degrees but with all angles scanned—from 0 degrees to 2 degrees by 0.5 degrees—the maximal exciton population remains above 1.45.

Additionally, in order to determine whether the optimal interlayer distance is consistent between different twist angles, Fig. 5.2c shows a scan of the degree of condensation versus the distance between the two coronene layers for twist angles of 0 (blue), 15 (pink), and 30 (green) degrees. Interestingly, the optimal interlayer distance for both the 15 and 30 degree twist angles is decreased from 2.0 Å to 1.5 Å, with the 15 degree maximum at 1.5 Å being significantly decreased from that for the unrotated maximum at 2.0 Å and the 30 degree maximum at 1.5 Å being significantly higher—showing a maximal exciton population above two, indicating that more than two excitons are occupying a single quantum state, even using the [10,10] active space with fewer degrees of correlation relative to the [24,24] active space previously used to scan degree of condensation versus interlayer distance for the unrotated bilayer system in the analysis in the preceding section.

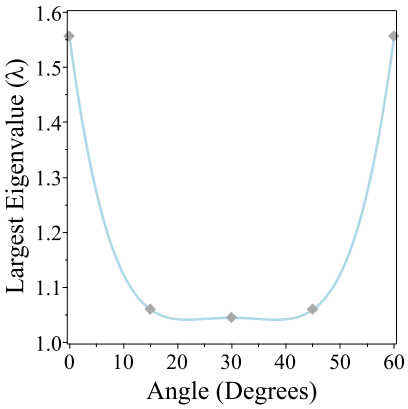

(a) 2.0 Å, Large Angle Scan

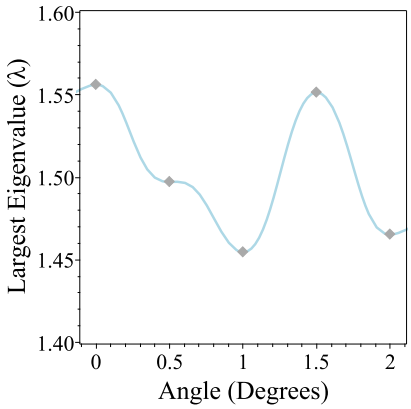

(b) 2.0 Å, Small Angle Scan

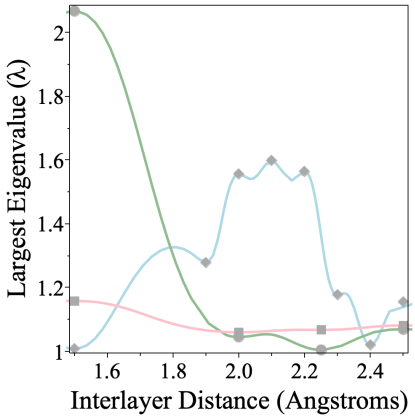

(c) 0(blue)/15(pink)/30(green) Degrees, Distance Scan

Figure 5.3: A scan over the exciton population in a single coherent quantum state (i.e., the largest eigenvalue of the modified particle-hole RDM) versus (a)small or (b)large angle variations are shown in the left-most and middle figure, and a scan over exciton population versus interlayer distance for twist angles of 0 (blue), 15 (pink), and 30 (degrees) is shown in the right-most figure. Activespace SCF calculations with a [10,10] active space with a STO-6G basis are utilized for each plot.

5.5 Discussion and Conclusions

In this study, we theoretically probe the presence and extent of exciton condensation—via the use of a quantum signature measuring the exciton population of a single particle-hole quantum state—for a variety of coronene bilayers. In these coronene bilayer systems—which are molecularly-scaled analogues of extended graphene bilayer systems—, we optimize the excitonic character versus the distance between the bilayers and find excitonic populations

of around 1.8 for interlayer distances around 2.0 Å when the coronene layers have a twist angle of zero degrees; this signature of condensation is seen to be relatively robust in the region of 1.8-2.3 Å, which while shorter than experimental bilayer distances of around 3.0 Å [215], may be attainable using either an appropriate linker or high pressure.

Further, by exploring the effect of the angle of rotation between the two coronene layers (i.e., the twist angle), we discover that for distances around 2.0 Å, the optimal twist angles between the layers are those corresponding to completely-aligned layers (i.e., 0, 60, 120, etc. degrees), although this maximal condensate character is rather robust for small angles around those explored in magic-angle graphene studies [224]. Moreover, by investigating the relationship between interlayer distance and excitonic populations for different twist angles, we note a large dependence on the degree of rotation on the signature of condensation. Specifically, we find the overall highest degree of exciton condensation—with an excitonic population above two in a single quantum state—for a coronene bilayer geometry corresponding to a 30 degree twist angle and a 1.5 Å interlayer distance, which is slightly shorter than a carbon-carbon single bond and hence may not be an experimentally-feasible distance. As such, an experimental exploration of molecular-scaled exciton condensation in coronene bilayer systems should likely focus on untwisted bilayer geometries in the range of 2.0 Å.

Interestingly, our visualization technique in which an exciton—corresponding to the largest degree of condensation—is visualized by plotting a the hole's probabilistic location for a specified particle location, indicates that interlayer excitons may be required in order for the coronene bilayer system to demonstrate exciton condensation. For visualizations with the same specified particle orbital (the $2p_z$ orbital on one of the symmetrically-equivalent carbon atoms in the interior benzene ring), geometries demonstrating character of exciton condensation have clear, delocalized, interlayer excitons. Further, we note that the delocalization of the hole location increases with the increase in excitonic population.

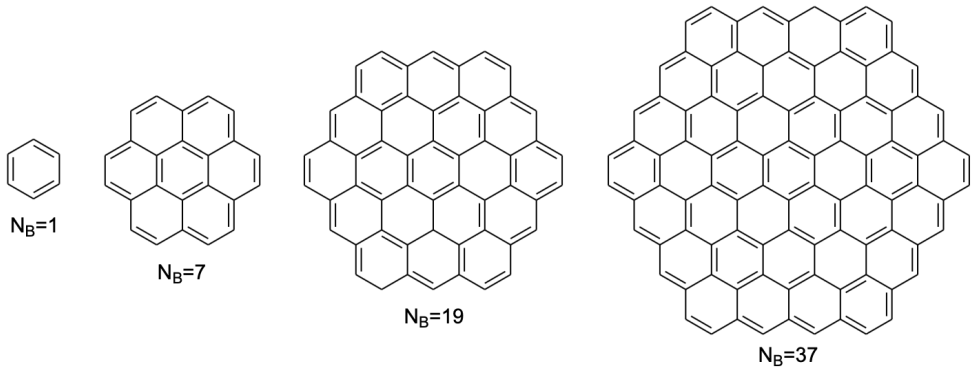

Figure 5.4: The progression of molecular systems in which benzene is completely surrounded by (left to right) zero, one, two, and three complete rows of benzene are shown. These molecules—which have one, seven, nineteen, and thirty-seven constituent benzenes, respectively—would be necessary to extrapolate exciton condensate behavior to the limit of an extended layer of graphene.

An interesting future direction may be the exploration of trends in exciton condensation with system size. Such a study would likely be beneficial in extrapolating smaller-system exciton condensation results to predict behavior of extended system graphene. In prior work, we have indeed explored the relationship between system size—i.e., number of benzene units—in both horizontal bilayer systems including pentacene and hexacene [213] as well as vertically in multilayer, molecular-scale van der Waals stacks composed of benzene subunits with the latter demonstrating an almost-linear increase of condensate character with an increase in the number of layers [12]. In the case of coronene, however, such an extrapolation would prove difficult with current theoretical methodologies robust enough to capture the correlation phenomena inherent to condensation behavior as the natural progression of molecules—shown in Fig. 5.4—rapidly become prohibitively large especially considering double-layer systems.

Another interesting direction would be determination of the temperature dependency of excitonic phenomena. Exciton condensation in coronene is a ground state phenomenon in which multiple constituent particle-hole quasibosons condense into a single quantum state; as such, we would expect it to persist at finite and small temperatures up until some critical

temperature at which thermal energy is sufficient to disrupt the condensation. Determination of critical temperature can be explored theoretically, although the calculation of excited states would be required, which may be an interesting future avenue of exploration.

Overall, this study identifies a candidate for molecular-scale exciton condensation—namely, a bilayer of coronene subunits with twist angles near zero degrees and interlayer separations near 2 Å—, which could have applications involving molecularly-scaled electronic structures and devices. Further, the clear signature of exciton condensation noted for the molecular-scale analogue of a graphene bilayer supports the idea that the interesting electronic phenomena in graphene bilayer systems could be occurring via an excitonic mechanism. The understanding gained throughout this geometric analysis of coronene bilayers illuminates the relationships between twist angle, interlayer distance, and degree of exciton condensation, which increases our understanding of geometric considerations in the design of graphene bilayer-like exciton condensate materials.

5.6 Appendix

We include details of methodology utilized for molecular calculations and visualizations.

5.6.1 Computational Methods

The particle-particle reduced density matrix (2-RDM) for the coronene bilayers is obtained directly from the molecular structure using a variational method [48–50, 53, 54, 225]. Additional constraints allowing the 2-RDM to represent N-particle wave functions—i.e., N-representability conditions—, require the the particle-particle, hole-hole, and particle-hole RDMs all to be positive semi-definite. The STO-6G basis set is used for all coronene bilayer calculations, and the active space utilized is specified throughout the document, with—unless otherwise noted—[24,24] variational 2-RDM CASSCF calculations being utilized for the scan over interlayer distances and [10,10] CI-CASSCF calculations being utilized for the scan over

twist angles.

The 2-RDM obtained directly from the molecular structure is then utilized to construct the particle-hole RDM by the linear mapping given by:

$$ {}^2G^{i,j}_{k,l} = \delta^j_l {}^1D^i_k + {}^2D^{i,k}_{j,l}. \tag{5.4} $$

The modified particle-hole RDM can then be obtained from the particle-hole RDM according to:

$$ {}^2\tilde{G}^{i,j}_{k,l} = {}^2G^{i,j}_{k,l} - {}^1D^i_j {}^1D^l_k. \tag{5.5} $$

The eigenvalues ($\lambda_{G,i}$) and eigenvectors ($\overrightarrow{v}_{G,i}$) of the modified particle-hole matrix are calculated using an eigenvalue optimization:

$$ \tilde{G}\overrightarrow{v}_{G,i} = \lambda_{G,i}\overrightarrow{v}_{G,i} \tag{5.6} $$

where the largest eigenvalue of the modified particle-hole RDM is the signature of condensation that represents the largest exciton population in a single coherent quantum state.

5.6.2 Visualization Technique

The "exciton density" visualization shows the probabilistic hole location as a function of a specific particle location. This information is obtained via a matrix of atomic orbitals in terms of molecular orbitals, $M_{\mathrm{AO,MO}}$, calculated directly from a matrix of molecular orbitals in terms of atomic orbitals, $M_{\mathrm{MO,AO}}$, which is obtained as an output of the direct computation of the 2-RDM:

$$ M_{\mathrm{AO,MO}} = (M^T_{\mathrm{MO,AO}})^{-1}. \tag{5.7} $$

A submatrix corresponding to the active orbitals is isolated from the overall matrix, and the eigenvector of the largest eigenvalue of the modified particle-hole RDM is reshaped as

a matrix in the basis of the active orbital submatrix. The eigenvector matrix, denotes by $V_{\max}$, is then utilized to create

$$(M^{\text{active}}_{\text{AO,MO}})(V_{\max})(M^{\text{active}}_{\text{AO,MO}})^T. \tag{5.8}$$

which is a matrix representing electron atomic orbitals in terms of the corresponding probabilistic hole location, with the resultant coefficients contributing to other orbitals.

Part III

Correlated States on Quantum Devices

CHAPTER 6

QUANTUM COMPUTING FOR MOLECULAR SIMULATION

It has long been heralded that quantum chemistry will greatly benefit from the advent of quantum devices—with quantum computation predicted to increase the speed and accuracy of quantum calculations as well as the size of molecules able to be simulated [226]. As Feynman wrote

> "Nature isn't classical, dammit, and if you want to make a simulation of nature, you'd better make it quantum mechanical, and by golly it's a wonderful problem, because it doesn't look so easy."

This quote provides an excellent rationale for why many in the quantum chemistry community believe using one quantum mechanical object—a quantum computer—to simulate another—an atom or molecule—is the natural approach to take in order to decrease computational expense. In the following chapters, quantum computers will be used to simulate highly-correlated systems that demonstrate condensation behavior. While the research in this thesis does not demonstrate so-called *quantum advantage* over classical simulation—where a quantum device accomplishes a task that is infeasible for a classical computer—, the preparation of these highly-correlated materials allows for another avenue of preparing and probing condensation phenomena. Additionally, the demonstration of long-range order on quantum devices provides the first step towards modeling more-complex highly-correlated states on quantum devices.

To contextualize the following chapters, the basic terminology and techniques involved in both quantum computing and chemical simulation via quantum devices will be detailed along with a brief history of quantum computation and a discussion on simulating fermions on quantum devices. Additional introductory material can be found for the field of quantum computing itself in Refs. [227–235]. Simulating many-body quantum systems on quantum

devices is an emergent field and hence fewer resources introducing the concepts of quantum computation for quantum chemistry exist; however, at least one textbook [236] and several review articles [237–240] can be referenced to provide further information on these topics.

6.1 Brief History of Quantum Computation in Molecular Computation

In 1980, Paul Benioff was the first to introduce a quantum mechanical formulation of a Turing machine [241]; however, Richard Feynman's 1981 keynote lecture at the Physics of Computation conference is generally considered the beginning of the field of quantum computation as a whole and definitely provided the first discussion of molecular simulation on quantum devices [242]. In this lecture, Feynman discussed harnessing quantum physics to build a quantum computer and then harnessing this device to simulate quantum systems too complex to model with classical digital devices [226]. While algorithms for quantum devices [243–245] and possible methodologies for error mitigation [246] were proposed in the 1980's and 1990's, it wasn't until 1997 that the first quantum computer was created [247] and until the early-2000s that algorithms were employed on such devices [242, 248]. From there, the initial quantum chemistry algorithm that utilized quantum computations—the Variational Quantum Eigensolver—was introduced in 2014 [249], with it first being employed to calculate the ground state of a molecule on a real device in 2017 [250]. Since 2016—with IBM creating cloud-accessible quantum devices available to researchers around the world—, the field of quantum computation for molecular simulation has exploded with applications to quantum chemistry ranging from variational eigensolvers to application of the anti-Hermitian Schrödinger equation to open quantum systems to condensation phenomena [5, 6, 10, 13, 16, 237–240].

6.2 Fundamentals of Quantum Computation

6.2.1 The Qubit

A qubit is the basic unit of quantum computing (analogous to the classical bit); the qubit itself is a quantum system in a two-dimensional Hilbert space $\mathbb{C}^2$ whose most-general state is a linear combination of its two basis states—$|0\rangle = \binom{1}{0}$ and $|1\rangle = \binom{0}{1}$, the classical bit states—with an appropriate phase factor ($e^{i\phi}$). The qubit wavefunction is given by

$$|\Psi\rangle = cos\left(\frac{\theta}{2}\right)|0\rangle + e^{i\phi}sin\left(\frac{\theta}{2}\right)|1\rangle = \begin{pmatrix} cos\left(\frac{\theta}{2}\right) \\ e^{i\phi}sin\left(\frac{\theta}{2}\right) \end{pmatrix} \tag{6.1}$$

or more-generally

$$|\Psi\rangle = \alpha|0\rangle + \beta|1\rangle = \binom{\alpha}{\beta} \tag{6.2}$$

for complex coefficients α and β corresponding to the $|0\rangle$ and $|1\rangle$ states that obey the normalization condition $|\alpha|^2 + |\beta|^2 = 1$. Despite a given qubit existing in a quantum superposition at any given time, when the qubit is probed in the computational basis, it will collapse into either the $|0\rangle$ or $|1\rangle$ state with the measurement probabilities being given by $|\alpha|^2$ and $|\beta|^2$, respectively. Practically, this means that a quantum system needs to be prepared and probed multiple times on a quantum device in order to reconstruct the quantum superposition in which the state's qubits exist.

A pure single-qubit wave function can be geometrically represented by a Bloch sphere, which is a unit sphere that contains all possible Bloch vectors of the form

$$\begin{pmatrix} \langle\sigma_x\rangle \\ \langle\sigma_y\rangle \\ \langle\sigma_z\rangle \end{pmatrix} \tag{6.3}$$

where $\langle\sigma_i\rangle$ is the expectation value of one of the *Pauli spin matrices*. These unitary Pauli matrices in the basis of the eigenvectors of the σ_z matrix are defined as

$$\sigma_x = \begin{pmatrix} 0 & 1 \\ 1 & 0 \end{pmatrix}, \ \sigma_y = \begin{pmatrix} 0 & -i \\ i & 0 \end{pmatrix}, \text{ and } \sigma_z = \begin{pmatrix} 1 & 0 \\ 0 & -1 \end{pmatrix} \tag{6.4}$$

with each matrix having $Tr(\sigma_i) = 0$, $|det(\sigma_i)| = 1$, and eigenvalues of ± 1. Commutation and anticommutation relationships for these matrices are given by

$$[\sigma_l, \sigma_j] = 2\epsilon_{l,j,k}\sigma_k \tag{6.5}$$

and

$$\{\sigma_l, \sigma_j\} = 2\delta^l_j I \tag{6.6}$$

where I is the identity matrix and $\epsilon_{l,j,k}$ is the Levi-Civita symbol. In this z-basis, the eigenvectors of σ_x are given by

$$|+x\rangle = \frac{1}{\sqrt{2}}(|0\rangle + |1\rangle) \tag{6.7}$$

$$|-x\rangle = \frac{1}{\sqrt{2}}(|0\rangle - |1\rangle), \tag{6.8}$$

the eigenvectors of σ_y are given by

$$|+y\rangle = \frac{1}{\sqrt{2}}(|0\rangle + i|1\rangle) \tag{6.9}$$

$$|-y\rangle = \frac{1}{\sqrt{2}}(|0\rangle - i|1\rangle), \tag{6.10}$$

and the eigenvectors of σ_z are given by

$$|+z\rangle = |0\rangle \tag{6.11}$$

$$|-z\rangle = |1\rangle \tag{6.12}$$

with the $\pm$ eigenvectors corresponding to the ± 1 eigenvalues. As the Pauli matrices form a complete basis, the Bloch vector uniquely represents the qubit state. Providing a geometric representation of the a qubit by plotting the Bloch vector in a Bloch sphere can sometimes provide a useful visualization of a one-qubit quantum state.

6.2.2 Multi-Qubit States

For an N-qubit system, the quantum state is described by a 2^N-dimensional vector in a $(\mathbb{C}^2)^{\otimes N}$ Hilbert space, which results from the tensor product of the Hilbert spaces of the individual qubits given by

$$|\Psi_{tot.}\rangle = |\Psi_0\rangle \otimes |\Psi_1\rangle \otimes \cdots \otimes |\psi_{N-1}\rangle \tag{6.13}$$

where $|\Psi_{tot.}\rangle$ is the total wave function representing N qubits and where $|\Psi_i\rangle$ refers to the one-qubit wave function—such as that given in Eq. (6.2)—of the i^{th} qubit. Note that in this notation and the notation used throughout the literature on quantum physics, the tensor product is ordered from left to right (where the first qubit q_0 is on the far left and the last qubit q_{N-1} is on the far right), which differs from the right to left ordering that is typical in most quantum computation literature (i.e., IBM Qiskit). This left to right notation of quantum physics is utilized throughout this thesis unless otherwise specified. Further, in instances where all qubits are in a specific state—and not a superposition—the tensor product symbols ($\otimes$) are often dropped in the notation but are still present in actuality. For example, in a three-qubit system, if qubit 0 is in state $|0\rangle$, qubit 1 is in state $|0\rangle$, and qubit

2 is in state $|1\rangle$, the overall state of the system would be represented by $|001\rangle$ which would be equivalent to $\begin{pmatrix}1\\0\end{pmatrix} \otimes \begin{pmatrix}1\\0\end{pmatrix} \otimes \begin{pmatrix}0\\1\end{pmatrix}$.

As an aside on terminology, a multi-qubit system is said to be *entangled* when it can not be decomposed into a tensor product of states. For example,

$$\frac{1}{\sqrt{2}}\left(|00\rangle + |01\rangle\right) = |0\rangle \otimes \frac{1}{\sqrt{2}}\left(|0\rangle + |1\rangle\right) \tag{6.14}$$

is not entangled as it is a product of single particle states, but the Bell state

$$\frac{1}{\sqrt{2}}\left(|00\rangle + |11\rangle\right) \tag{6.15}$$

is entangled because it can not be written as a product of single particle states.

6.2.3 Quantum Gates

Quantum gates refer to norm-preserving unitary operators that act on either one or two qubits. These quantum gates correspond to a matrix representation (U) such that acting the gate on a quantum state—which can be represented by a vector ($|\Psi\rangle$)—is equivalent to the multiplication of the matrix form of the quantum gate by the vector representation of the quantum state or $U|\Psi\rangle$. By applying an appropriate sequence of gates, any quantum state in the $(\mathbb{C}^2)^{\otimes N}$ Hilbert space corresponding to N-qubits should be able to be prepared from the initial state $|\Psi_0\rangle = |0\rangle^{\otimes N}$. Note that physically these gates correspond to experimentally manipulating the quantum system acting as a qubit such that certain quantum devices are capable of only a subset of quantum gates; however, most modern quantum computers are able to accomplish any general unitary transformation via translation of that unitary transformation into a sequence of the gates with which the specific device is equipped.

A single-qubit gate U corresponds to a (2×2) unitary matrix with the general form of

a single-qubit gate being given according to

$$u(\theta,\phi,\lambda) = \begin{pmatrix} cos\frac{\theta}{2} & -e^{i\lambda}sin\frac{\theta}{2} \\ e^{i\phi}sin\frac{\theta}{2} & e^{i(\phi+\lambda)}cos\frac{\theta}{2} \end{pmatrix}. \tag{6.16}$$

All single-qubit gates can be obtained from this general matrix form for certain values of θ, ϕ, and λ. A few important single-qubit gates include the X gate, the Hadamard (H) gate, and the rotation operator gates ($RX,\ RY,\ RZ$). The X gate is given by

$$X = \begin{pmatrix} 0 & 1 \\ 1 & 0 \end{pmatrix} \tag{6.17}$$

and is equivalent to the classical NOT gate in that it maps $|0\rangle$ to $|1\rangle$ and $|1\rangle$ to $|0\rangle$, which is equivalent to a rotation by 180 degrees around the X-axis of the Bloch sphere. The Hadamard gate is given by

$$H = \frac{1}{\sqrt{2}} \begin{pmatrix} 1 & 1 \\ 1 & -1 \end{pmatrix} \tag{6.18}$$

and maps $|0\rangle$ to $|+\rangle = \frac{1}{\sqrt{2}}(|0\rangle + |1\rangle)$ and $|1\rangle$ to $|-\rangle = \frac{1}{\sqrt{2}}(|0\rangle - |1\rangle)$. Finally, the rotation gates are given according to

$$RX(\theta) = \begin{pmatrix} cos\frac{\theta}{2} & -isin\frac{\theta}{2} \\ -isin\frac{\theta}{2} & cos\frac{\theta}{2} \end{pmatrix}, \tag{6.19}$$

$$RY(\theta) = \begin{pmatrix} cos\frac{\theta}{2} & -sin\frac{\theta}{2} \\ sin\frac{\theta}{2} & cos\frac{\theta}{2} \end{pmatrix}, \tag{6.20}$$

and

$$RZ(\lambda) = \begin{pmatrix} -e^{i\lambda/2} & 0 \\ 0 & e^{i\lambda/2} \end{pmatrix}. \tag{6.21}$$

It is known that any two of the above rotations are sufficient to prepare any single qubit state.

A two-qubit quantum gate U corresponds to a (4×4) unitary matrix with the most-common two-qubit gates being the $CNOT$ (or equivalently CX) operator, the CZ operator, and the $SWAP$ operator. The $CNOT$ operator performs the X (i.e., NOT) operation on a second qubit (the target qubit) only if the first qubit (the control qubit) is in the $|1\rangle$ state. The CZ gate is similar; however, it applies the Z operation on the second qubit if the first is in the $|1\rangle$ state. Finally, the $SWAP$ operator swaps two qubits. The matrix representations of these gates are available in Ref. [251]. As the $CNOT$ gate is used extensively throughout this thesis, its form is given here explicitly:

$$CNOT = CX = \begin{pmatrix} 1 & 0 & 0 & 0 \\ 0 & 1 & 0 & 0 \\ 0 & 0 & 0 & 1 \\ 0 & 0 & 1 & 0 \end{pmatrix}. \tag{6.22}$$

As an example on how to apply quantum gates in order to yield a desired quantum state, let us consider how to prepare the $|\phi_+\rangle$ Bell state

$$|\phi_+\rangle = \frac{1}{\sqrt{2}}(|00\rangle + |11\rangle) \tag{6.23}$$

on a quantum computer. Initially, on a quantum device, all qubits are in the $|0\rangle$ state, so for a two-qubit system, the initial state is given by $|00\rangle$. Then, the Hadamard gate can be applied to qubit 0 in order to yield

$$H_0|\Phi_0\rangle = H_0|00\rangle = \frac{|00\rangle + |10\rangle}{\sqrt{2}} \tag{6.24}$$

where H_i represents the Hadamard gate acting on the i^{th} qubit. Then, applying the $CNOT$

gate with qubit 0 acting as the control gate and qubit 1 acting as the target qubit yields

$$C_0^1\left(\frac{|00\rangle+|10\rangle}{\sqrt{2}}\right)=\frac{1}{\sqrt{2}}\left(C_0^1|00\rangle+C_0^1|10\rangle\right)=\frac{|00\rangle+|11\rangle}{\sqrt{2}} \tag{6.25}$$

where C_i^j represents the controlled-NOT gate with control and target qubits i and j, respectively. The overall state preparation can thus be represented as

$$C_0^1 H_0|\psi_0\rangle=\frac{|00\rangle+|11\rangle}{\sqrt{2}} \tag{6.26}$$

where the gates are applied to the system from left to right.

6.2.4 Measurement

To measure a prepared quantum system's quantum state, the state must be projected into the basis of measurement. For quantum computers, this measurement basis is the computational basis of $|0\rangle=|+z\rangle$ and $|1\rangle=|-z\rangle$ where a measurement of the $|+z\rangle$ state corresponds to the non-unitary matrix given by

$$M_{|+z\rangle}=\begin{pmatrix}1 & 0\\ 0 & 0\end{pmatrix} \tag{6.27}$$

and a measurement of the $|-z\rangle$ state corresponds to

$$M_{|+z\rangle}=\begin{pmatrix}0 & 0\\ 0 & 1\end{pmatrix} \tag{6.28}$$

for a single qubit. Practically, for a qubit state prepared M times on a quantum device, the "counts" data is output which specifies the number of times the qubit is observed in the $|0\rangle$ and $|1\rangle$ states—n_0 and n_1, respectively. From this "counts" information, the expectation

value of the Pauli-Z matrix can be determined by

$$\langle \sigma_z \rangle = \frac{n_0 - n_1}{M}. \tag{6.29}$$

The expectation value for the Pauli-X matrix can be attained in an analogous manner if the prepared quantum state is first rotated into the $|+x\rangle/|-x\rangle$ basis through application of the Hadamard gate, as

$$H\sigma_z H = \sigma_x, \tag{6.30}$$

before Eq. (6.29) is evaluated. Similarly, the expectation of the Pauli-Y matrix can be probed by applying the S gate and then the Hadamard gate, as

$$SH\sigma_z HS^\dagger = \sigma_y. \tag{6.31}$$

For a system composed of multiple qubits, the measurements described by Eqs. (6.27) and (6.28) must be applied to every qubit, with up to 2^N possible outcomes of the measurement, which are described by N-length strings of $0s$ and $1s$ for an N-qubit system. The expectation values for all possible permutations of $k = 1$ to $k = N$ strings of the form σ_z^k (i.e., Z_1, Z_1Z_3, $Z_1Z_2Z_4$, etc.) can be evaluated. Further by rotating certain qubits to the X and Y Pauli bases as described in Eqs. (6.30) and (6.31), the expectation values for all possible permutations of Pauli strings given by Z_1, X_2, Z_3X_4, Y_1X_3, $Z_1X_2Y_4$, etc. are able to be calculated. These expectation values can be directly computed from the "counts" data according to [10]

$$\langle P \rangle = \frac{1}{M} \sum_{i=1}^{M} \langle \psi | \hat{P} | \psi \rangle |_i \tag{6.32}$$

for a certain k-qubit Pauli string $\hat{P}$ where $|_i$ denotes the value from the i^{th} measurement.

The variance associated with this measurement is given by [10]

$$Var(P) = \frac{1}{M}\sum_{i=1}^{M}(\langle P^2\rangle - \langle P\rangle^2) = \frac{1}{M}\sum_{i=1}^{M}(1 - \langle P\rangle^2). \tag{6.33}$$

As a specific example, the two-qubit expectation value $\langle Z_0 Z_1\rangle$ can be determined by considering the matrix form of $Z_0 Z_1$, which is given by

$$\begin{pmatrix} 1 & 0 \\ 0 & -1 \end{pmatrix}_0 \otimes \begin{pmatrix} 1 & 0 \\ 0 & -1 \end{pmatrix}_1 = \begin{pmatrix} 1 & 0 & 0 & 0 \\ 0 & -1 & 0 & 0 \\ 0 & 0 & -1 & 0 \\ 0 & 0 & 0 & 1 \end{pmatrix} \tag{6.34}$$

in the $|00\rangle$, $|01\rangle$, $|10\rangle$, $|11\rangle$ basis. This matrix suggest that the expectation value can be obtained by

$$\langle Z_0 Z_1\rangle = \frac{n_{00} - n_{01} - n_{10} + n_{11}}{M} \tag{6.35}$$

with n_{ij} corresponding to the number of times the quantum state was observed to be in the $|ij\rangle$ state in the course of M measurements. Further, the expectation value $\langle X_0 Y_1\rangle$ can be obtained following the above procedure if prior to measurement, qubit 0 is rotated into the X Pauli basis and qubit 1 is rotated into the Y Pauli basis.

Hamiltonians and many objective functions can be expressed in the basis of Pauli strings, and so, in general, we can express the expectation of relevant operators as linear combinations of Pauli terms in the form [10]

$$\hat{O} = \sum_i c_i P_i + \sum_{i,j} c_{i,j} P_i P_j + + \sum_{i,j,k} c_{i,j,k} P_i P_j P_k + \sum_{i,j,k,l} v_{i,j,k,l} P_i P_j P_k P_l + \cdots = \sum_i o_i \hat{P}_i \tag{6.36}$$

where $P_i \in \{I, \sigma_x, \sigma_y, \sigma_z\}$ and $\hat{P}_i$ represents the i^{th} overall Pauli string. Thus, the expectation value of a given operator can be determined by finding the expectation values of all

salient Pauli strings and taking the linear combination of these expectation values according to [10]

$$\langle \hat{O} \rangle = \sum_i o_i \langle \hat{P}_i \rangle. \tag{6.37}$$

Importantly, note that the measurements described above are inherently probabilistic, despite the deterministic nature of the quantum state prepared with a specific set of instructions. For sufficiently large M, the measured expectation value of the Pauli string approaches the exact expectation value corresponding to the prepared quantum state. However, a finite M introduces a probabilistic nature to the results.

6.2.5 Errors on Quantum Computers

Quantum computation has promised to revolutionize the future of technology since the 1980s, yet due to the extreme difficulty in engineering, building, and coding such devices—which results in errors including readout errors, gate noise, and quantum state decoherence—, the promise as of yet remains unrealized [252]. Quantum algorithms have historically assumed systems composed of perfect qubits able to be prepared in any desired state and manipulated with complete precision. While physical systems able to act as higher-quality qubit systems are continually being developed, these physical qubits will not be entirely devoid of imperfections in the near future and hence are too imprecise to act as so-called perfect "logical qubits" in near-term intermediate-scale quantum (NISQ) devices [253]. Therefore, current quantum computing techniques rely on being able to quantify the error of quantum devices as well as having methodologies for correcting for such errors. A description of the types and causes of quantum device errors as well as a brief review of error measurement and mitigation is conducted in the following sections.

Types and Causes of Quantum Device Error

In order for a physical system to act as a logical qubit, each qubit system needs to be kept in perfect isolation from external interferences. This allows the qubit system to maintain coherence while remaining able to strongly interact with the adjacent qubits on the device as is necessary for information processing. Additionally, the isolated qubit system needs to be able to be externally controlled to allow for state preparation and able to be measured by an external probe to allow for results to be obtained in a readable format [254]. Currently, this seemingly contradictory set of criteria is imperfectly realized, leading to three main types of errors that contribute to the deviation of physical qubits from logical qubits: gate noise, readout noise, and decoherence. Note that in the context of quantum computation the term "noise" is used to refer to imperfections in the control of physical qubits [254].

Quantum gates which act on quantum states are operations on a quantum device that correspond to applying a unitary matrix (U) to the vector representation ($|\Psi\rangle$) of quantum states [228]. Multi-qubit quantum gates—the gates prone to the highest rates of error—are well-controlled entangling operations acting on pairs of qubits [254]. For a quantum gate corresponding to a unitary matrix U, a quantum gate error refers to the situation in which the resultant quantum state deviates from $U|\Psi\rangle$. There are two types of gate error—coherent and incoherent gate errors. Coherent gate errors refer to errors that preserve the purity of the input state, i.e. those in which the error can be viewed as a perturbed unitary operation $|\Psi\rangle \rightarrow \tilde{U}|\Psi\rangle$ where $\tilde{U} \neq U$ and are caused by imprecisely-calibrated control of the qubits [228]. Incoherent gate errors, on the other hand, are those that do not preserve the purity of the input state; these errors are caused by imperfect isolation of the qubits from their environment such that the quantum system coevolves with the external degrees of freedom to which it couples [228]. While coherent gate errors can theoretically be decreased by more-precisely calibrating the controls, either a more-isolated quantum device or a robust error-mitigation method is necessary for decreasing the incoherent gate errors [228]. In general,

limiting the number of gates applied—and hence decreasing the gate errors—is optimal for best measurements on quantum devices.

The term readout error refers to transmission line noise that makes the $|0\rangle$ state appear to be the $|1\rangle$ state to a measurement or vice versa. One type of readout error, often referred to as a classical readout bit-flip error, is caused by the probability distributions of the measured physical quantities that correspond to measurement of the $|0\rangle$ and $|1\rangle$ states overlapping, causing a small probability of measuring the opposite value [228, 255]. Additionally, another type of readout error, often referred to as a T1-readout error, is caused by the qubit relaxing/decaying during readout, causing a $|1\rangle$ state to be registered as $|0\rangle$ [228, 255]. Classical readout bip-flip noise can be limited by better-tailoring the optimal readout pulses and/or amplifying the readout signal, while T1-readout error is typically reduced by decreasing the readout pulses relative to the decoherence time [228].

Quantum states are inherently delicate with interactions with external systems often causing the degradation of the quantum state, which is called decoherence [256]. Decoherence is a result of the system interacting with its environment through such means as vibrations, temperature fluctuations, electromagnetic waves, etc., and it destroys the exotic quantum properties of quantum devices [252]. Additionally, the probability of decoherence is known to increase with the size (N) of the qubit state, making larger-scale quantum computations more difficult [254, 256]. While coherence times will likely continue to increase as qubit systems become more and more isolated from their environments, it is likely impossible to completely eliminate quantum decoherence.

Measurement of Quantum Device Error

In order to enumerate the amount of error inherent to a quantum device, one must determine the readout error, single-qubit unitary gate (U2) error, and a CNOT error rate. Determination of the readout error is accomplished in a rather straightforward manner where a large

number of experiments are prepared with the qubit known to be in either the $|0\rangle$ state or the $|1\rangle$ state with immediate measurement after the preparation. The average value of the percentage of $|1\rangle$ states with a $|1\rangle \rightarrow |0\rangle$ error and the percentage of $|0\rangle$ states with a $|0\rangle \rightarrow |1\rangle$ error is reported to be the readout error of the qubit probed [257].

A single qubit ($U2$) error rate is determined via a scalable randomized benchmarking protocol [258]. In this methodology, a sequence of Clifford gates are applied to a given qubit in order to instigate a random walk along points of the Bloch sphere originating at and returning to the $|0\rangle$ state. As the number of Clifford gates is increased in the walk, the probability of the qubit returning to the original $|0\rangle$ state decreases in an exponential manner, eventually saturating at 50%, indicating pure randomness. The $U2$ value is extrapolated from the fit to the exponential decay in probability [257, 258]. Two-qubit (CNOT) gate error rates are obtained in a similar randomized benchmarking technique, replacing the single-qubit Clifford gates with two-qubit analogues [257, 258].

The decoherence times—$T1$, the relaxation time, and $T2$, the dephasing times—are also reported as a measure of the "noise" of a quantum device. These values are determined through measuring the time it takes to decay from an initial state ($|1\rangle$ or $\frac{1}{\sqrt{2}}(|0\rangle - |1\rangle)$) to a final state ($|0\rangle$ or $\frac{1}{\sqrt{2}}(|0\rangle + |1\rangle)$) and fitting to the obtained exponential decay [259]. Note that the error introduced by relatively short decoherence times currently far outweigh the errors introduced by readout and gate noise [260].

The above metrics, however, fail to account for errors caused by interactions with spectator qubits and hence can not accurately be used to naïvely estimate the error of a given measurement or set of measurements on a quantum device. IBM has introduced a single-number metric—called quantum volume—meant to encapsulate the error of a quantum computer in a single value to better account for simultaneous all-qubit interactions; however, while quantum volume allows for easy comparison between devices [261], it does not allow for direct calculation of error given the quantum volume value.

Mitigation of Quantum Device Error

As described in great detail above, near-term quantum computers will likely continue to have relatively high levels of noise. As such, developing methodologies to either correct for these errors or minimize the errors employed in a given algorithm are necessary to employ quantum devices for the foreseeable future. A quantum variation of the classical repetition code for error correction [262] and gathering information from basis state computations to define a matrix to be used to "project" noisy results to error-mitigated results [253] are traditionally employed to minimize the effects of error. Unfortunately, there is a large computational cost to implementing quantum error correction techniques—namely that the large number of qubits or circuits consumed by the implementation of a quantum error correction scheme leaves relatively few qubits available for actual computation [252, 254].

6.3 The Simulation of Fermionic Systems

To simulate many-electron quantum systems on a quantum computer, fermionic statistics must be satisfied. Specifically, the fermionic creation and annihilation operators must obey the following commutation relationships

$$\{\hat{f}_i, \hat{f}_j^\dagger\} = \hat{f}_i \hat{f}_j^\dagger + \hat{f}_j^\dagger \hat{f}_i = \delta_j^i \tag{6.38}$$

and

$$\hat{f}_i^\dagger \hat{f}_j^\dagger + \hat{f}_j^\dagger \hat{f}_i^\dagger = 0 = \hat{f}_i \hat{f}_j + \hat{f}_j \hat{f}_i \tag{6.39}$$

for two spin orbitals i and j where $f_i^{(\dagger)}$ is an annihilation (creation) operator. However, it can be shown that if each qubit is taken to represent one orbital that is either occupied ($|1\rangle$) or unoccupied ($|0\rangle$), $\hat{f}_i \hat{f}_j = \hat{f}_j \hat{f}_i$, $\hat{f}_j^\dagger \hat{f}_i = \hat{f}_i \hat{f}_j^\dagger$, $\hat{f}_i^\dagger \hat{f}_j = \hat{f}_j \hat{f}_i^\dagger$, and $\hat{f}_i^\dagger \hat{f}_j^\dagger = \hat{f}_j^\dagger \hat{f}_i^\dagger$, which is in direct contradiction to the expected fermionic statistics. Thus, other more-complicated

methodologies for encoding fermions on a quantum device are generally required. Three such fermionic encoding techniques are described in the following sections.

6.3.1 The Jordan-Wigner Transformation

The Jordan-Wigner (JW) transformation [263], which is a special example of a Klein transformation, was proposed in order to satisfy the anticommutation relationship $[\hat{w}_i^\dagger, \hat{w}_j] = \hat{w}_i^\dagger \hat{w}_j + \hat{w}_j \hat{w}_i^\dagger = \delta_j^i$. Here, $\hat{w}_p^\dagger$ and $\hat{w}_p$ are the Jordan-Wigner creation and annihilation operators for orbital p, and we are still in Fock space with one qubit representing either an occupied ($|1\rangle$) or unoccupied ($|0\rangle$) orbital. Specifically, the JW creation and annihilation operators are

$$\hat{w}_p^\dagger = \exp\left\{+i\pi \sum_{k=0}^{p-1} \hat{f}_k^\dagger \hat{f}_k\right\} \cdot \hat{f}_p^\dagger \tag{6.40}$$

and

$$\hat{w}_p = \exp\left\{-i\pi \sum_{k=0}^{p-1} \hat{f}_k^\dagger \hat{f}_k\right\} \cdot \hat{f}_p \tag{6.41}$$

where $\hat{f}_p^\dagger$ and $\hat{f}_p$ are our naive creation and annihilation operators with an added phase $\left[\exp\left\{\pm i\pi \sum_{k=0}^{p-1} \hat{f}_k^\dagger \hat{f}_k\right\}\right]$ determined by the number of occupied fermionic qubits "to the left" (i.e., qubits $k = 0, \ldots, p-1$) of the qubit p, the qubit of interest. Taking advantage of the properties of exponents as well as the fact that $\hat{f}_p^\dagger \hat{f}_p \in \{0, 1\}$ and noting that

$$1 - 2\hat{f}_p^\dagger \hat{f}_p = \begin{pmatrix} 1 & 0 \\ 0 & 1 \end{pmatrix}_p - \begin{pmatrix} 0 & 0 \\ 1 & 0 \end{pmatrix}_p \begin{pmatrix} 0 & 1 \\ 0 & 0 \end{pmatrix}_p = \begin{pmatrix} 1 & 0 \\ 0 & -1 \end{pmatrix}_p, \tag{6.42}$$

this phase can be written as

$$\exp\left\{\pm i\pi \sum_{k=0}^{p-1} \hat{f}_k^\dagger \hat{f}_k\right\} = \prod_{k=0}^{p-1} \exp\left\{\pm i\pi \hat{f}_k^\dagger \hat{f}_k\right\} = \prod_{k=0}^{p-1} \left(1 - 2\hat{f}_k^\dagger \hat{f}_k\right) = \prod_{k=0}^{p-1} Z_k. \tag{6.43}$$

Therefore, the Jordan-Wigner mapping for n qubits is given by the following:

$$\hat{w_p^\dagger} = [Z_0 \otimes \cdots \otimes Z_{p-1}] \otimes \hat{f_p^\dagger} \otimes [I_{p+1} \otimes \cdots \otimes I_{n-1}] \tag{6.44}$$

$$\hat{w_p} = [Z_0 \otimes \cdots \otimes Z_{p-1}] \otimes \hat{f_p} \otimes [I_{p+1} \otimes \cdots \otimes I_{n-1}]. \tag{6.45}$$

For example, in a two-qubit system where we define the two qubits to be qubit i and qubit j with qubit i being to the left of qubit j, these JW creation and annihilation operators would be given by

$$\hat{w_i^\dagger} = \hat{f_i^\dagger} \otimes I_j = \frac{1}{2}\left(X_i - iY_i\right) \otimes I_j = \frac{1}{2}\left[X_i \otimes I_j - iY_i \otimes I_j\right], \tag{6.46}$$

$$\hat{w_i} = \hat{f_i} \otimes I_j = \frac{1}{2}\left(X_i + iY_i\right) \otimes I_j = \frac{1}{2}\left[X_i \otimes I_j + iY_i \otimes I_j\right], \tag{6.47}$$

$$\hat{w_j^\dagger} = Z_i \otimes \hat{f_j^\dagger} = Z_i \otimes \frac{1}{2}\left(X_j - iY_j\right) = \frac{1}{2}\left[Z_i \otimes X_j - iZ_i \otimes Y_j\right], \tag{6.48}$$

and

$$\hat{w_j} = Z_i \otimes \hat{f_j} = Z_i \otimes \frac{1}{2}\left(X_j + iY_j\right) = \frac{1}{2}\left[Z_i \otimes X_j + iZ_i \otimes Y_j\right]. \tag{6.49}$$

It can be shown that the Jordan-Wigner transformation satisfies fermionic statistics.

6.3.2 The Parity Basis

In the Jordan-Wigner transformation, the occupation of each qubit is stored locally on a given qubit, but information on parity is completely delocalized across all qubits, leading to linear scaling. Another, equally-valid, approach is to store the parity information locally in the qubit states [264]. This means that qubit p stores the remainder when the sum of the occupation of all electronic states with index $i \leq p$ is divided by two. However, this results in delocalization of information regarding the occupation of each electronic orbital, hence still demonstrating linear scaling.

Specifically, a given qubit j will store

$$q_j = \left[\sum_{k=0}^{j} \hat{f}_k^\dagger \hat{f}_k \right] \%2 \tag{6.50}$$

such that the qubit will be in $|0\rangle$ if the sum of the occupation of the orbitals with all indices $k \leq j$ is even $[(2n)\%2 = 0]$ and in $|1\rangle$ if the sum is odd $[(2n+1)\%2 = 1]$.

The creation and annihilation operators for a system of n orbitals in this parity basis are given by

$$\hat{p}_k^\dagger = \hat{P}_k^+ \otimes (X_{k+1} \otimes \cdots \otimes X_n) \tag{6.51}$$

and

$$\hat{p}_k = \hat{P}_k^- \otimes (X_{k+1} \otimes \cdots \otimes X_n) \tag{6.52}$$

with $\hat{P}_k^+$ and $\hat{P}_k^-$ being defined as

$$\hat{P}_k^+ = |0\rangle\langle 0|_{k-1} \otimes \hat{f}_k^\dagger - |1\rangle\langle 1|_{k-1} \otimes \hat{f}_k = \frac{1}{2} \left[Z_{k-1} \otimes X_k - i I_{k-1} \otimes Y_k \right] \tag{6.53}$$

and

$$\hat{P}_k^- = |0\rangle\langle 0|_{k-1} \otimes \hat{f}_k - |1\rangle\langle 1|_{k-1} \otimes \hat{f}_k^\dagger = \frac{1}{2} \left[Z_{k-1} \otimes X_k + i I_{k-1} \otimes Y_k \right]. \tag{6.54}$$

Note that these creation and annihilation operators depend on the $(k-1)^{th}$ qubit since if qubit $k-1$ is in $|0\rangle$, then qubit k accurately reflects the occupation of k; however, if qubit $k-1$ is in $|1\rangle$, qubit k will have inverted parity compared to the occupation of k. The application of the X Pauli matrix to all qubits with indices greater than k (i.e., $X_{k+1} \otimes \cdots \otimes X_n$) updates the parity for all qubits "to the right" of qubit k.

It can be shown that the Parity Basis satisfies fermionic statistics.

6.3.3 The Bravyi-Kitaev Basis

The Bravyi-Kitaev (BK) Basis [265] balances the locality of the occupation and parity information in order to improve simulation efficiency to the order of $O(log_2 n)$. This is done by using the qubits to store partial sums of occupation numbers according to a specific algorithm that will be further explained below. A qubit j always stores the occupation of the j^{th} orbital, while qubits with odd indices ($j \in (2n+1),\ n \in \mathbb{Z}$) additionally store the occupation information for all orbitals with indices less than or equal to their indices.

In order to understand the specifics of this basis, let us first introduce the recursively-defined BK matrices

$$\beta_{2^{x+1}} = \begin{pmatrix} \beta_{2^x} & \mathbf{0} \\ \mathbf{A} & \beta_{2^x} \end{pmatrix} \tag{6.55}$$

and

$$\beta^{-1}_{2^{x+1}} = \begin{pmatrix} \beta^{-1}_{2^x} & \mathbf{0} \\ \mathbf{A'} & \beta_{2^x} \end{pmatrix} \tag{6.56}$$

where $\beta_1 = \beta_1^{-1} = (1)$ is a 1×1-matrix, $\mathbf{A}$ is a $2^x \times 2^x$ matrix given by

$$\mathbf{A} = \begin{pmatrix} 0 & 0 & \cdots & 0 \\ \vdots & \ddots & \vdots & \vdots \\ 0 & \cdots & 0 & 0 \\ 1 & 1 & \cdots & 1 \end{pmatrix}, \tag{6.57}$$

$\mathbf{A'}$ is a $2^x \times 2^x$ matrix given by

$$\mathbf{A'} = \begin{pmatrix} 0 & \cdots & 0 & 0 \\ \vdots & \ddots & \vdots & \vdots \\ 0 & \cdots & 0 & 0 \\ 0 & \cdots & 0 & 1 \end{pmatrix}, \tag{6.58}$$

and β_n for $2^x < n < 2^{x+1}$ is given by the $n \times n$ segment of $\beta_{2^{x+1}}$ that includes qubits 0 through $n-1$. A qubit i in this basis stores

$$q_i = \left(\sum_j [\beta_n]_{ij} \hat{f}_j^\dagger \hat{f}_j \right) \%2 \tag{6.59}$$

such that transforming an eight orbital example from the occupation basis ($\mathbf{o}$) to the BK basis can be done as follows:

$$\begin{aligned}
[B_8\mathbf{o}]\%2 &= \left[\begin{pmatrix} 1 & 0 & 0 & 0 & 0 & 0 & 0 & 0 \\ 1 & 1 & 0 & 0 & 0 & 0 & 0 & 0 \\ 0 & 0 & 1 & 0 & 0 & 0 & 0 & 0 \\ 1 & 1 & 1 & 1 & 0 & 0 & 0 & 0 \\ 0 & 0 & 0 & 0 & 1 & 0 & 0 & 0 \\ 0 & 0 & 0 & 0 & 1 & 1 & 0 & 0 \\ 0 & 0 & 0 & 0 & 0 & 0 & 1 & 0 \\ 1 & 1 & 1 & 1 & 1 & 1 & 1 & 1 \end{pmatrix} \begin{pmatrix} o_0 \\ o_1 \\ o_2 \\ o_3 \\ o_4 \\ o_5 \\ o_6 \\ o_7 \end{pmatrix} \right] \%2 \\
&= \left[\begin{pmatrix} o_0 \\ o_0 + o_1 \\ o_2 \\ o_0 + o_1 + o_2 + o_3 \\ o_4 \\ o_0 + o_1 + o_2 + o_3 + o_4 + o_5 \\ o_6 \\ o_0 + o_1 + o_2 + o_3 + o_4 + o_5 + o_6 + o_7 \end{pmatrix} \right] \%2.
\end{aligned} \tag{6.60}$$

The creation and annihilation operators for the Bravyi-Kitaev transformation are

$$\hat{k}_i^\dagger = \frac{1}{2} \left[X_{U(i)} \otimes X_i \otimes Z_{P(i)} - i X_{U(i)} \otimes Y_i \otimes Z_{\rho(i)} \right] \tag{6.61}$$

and

$$\hat{k}_i = \frac{1}{2} \left[X_{U(i)} \otimes X_i \otimes Z_{P(i)} + i X_{U(i)} \otimes Y_i \otimes Z_{\rho(i)} \right] \tag{6.62}$$

where $U(i)$ represents the update set of i, $P(i)$ represents the parity set of i, and $\rho(i)$ represents either the parity set ($P(i)$) for qubits with even indices (i-values) or the remainder set ($R(i)$) for qubits with odd indices (i-values). The update set for qubit i ($U(i)$) is the set of qubits with indices $j > i$ such that the j^{th} row of the i^{th} column contains non-zero entries. The parity set for qubit i ($P(i)$) is the set of qubits with indices equal to non-zero entries of the $\pi_n \beta_n^{-1}$ matrix in row i where

$$[\pi_n]_{ij} = \begin{cases} 1, & \text{if } i < j \\ 0, & \text{else} \end{cases}. \tag{6.63}$$

The remainder set for qubit i ($R(i)$) is the set of qubits that belong to the parity set ($P(i)$) but do not belong to the flip set ($F(i)$) where the flip set ($F(i)$) for qubit i contains the column labels of non-zero entries in the i^{th} row of β_n^{-1}.

It can be shown that the Bravyi-Kitaev Basis satisfies fermionic stastistics.

6.4 Quantum Algorithms for Quantum Chemistry

Over the past several years, several algorithms have emerged as potential methodologies for the preparation of molecular eigenstates on a quantum device. Once the molecular eigenstates have been prepared, observables can be measured as described in Section 6.2.4 as long as the observable operators have been transformed to the appropriate Pauli basis. In the following sections, two possible methods for the ground state preparation of a wave function utilizing a quantum computer are briefly summarized: the variational quantum eigensolver (VQE) and the quantum anti-Hermitian Schrödinger equation (qACSE) methodology. Additional information regarding the highly-prominent VQE approach—as well as other common quantum algorithms for quantum chemistry including the adiabatic state preparation algorithm and imaginary time evolution—can be found in Ref. [266]. The qACSE algo-

rithm—which is the approach utilized in this thesis for molecular simulation on quantum devices—is detailed in full in Ref. [267].

6.4.1 The Variational Quantum Eigensolver

The Variational Quantum Eigensolver—first presented by Peruzzo et. al. in 2014 [249]—uses the Variational Principle introduced in Eq. (1.18) to compute an upper bound for the ground state energy of a Hamiltonian. On a classical computer, a variational approach is limited in its accuracy due to the computational costs associated with exactly treating the exponentially-growing wave functions of larger and larger many-electron systems. On a quantum device, however, the variational approach is capable of modelling complex wave function with polynomial scaling, a marked improvement.

Specifically, the variational quantum eigensolver begins with a quantum state parameterized according to a set of variables $\{\theta_i\}$ given by

$$|\psi\rangle = |\psi(\theta)\rangle = U(\theta)|\psi_0\rangle \tag{6.64}$$

where $U(\theta)$ is a unitary matrix and $|\psi_0\rangle$ is the initial state. The minimization is then characterized by

$$E_{VQE} = \min_{\theta} \langle\psi(\theta)|\hat{H}|\psi(\theta)\rangle \tag{6.65}$$

which is iteratively achieved by evaluation of the energy for a given parameter set

$$E(\theta) = \langle\psi(\theta)|\hat{H}|\psi(\theta)\rangle \tag{6.66}$$

with a classical optimization of the parameters θ. For gradient-based approaches, the energy

gradient with respect to each parameter is also required:

$$\frac{dE}{d\theta_i} = \langle \frac{d}{d\theta_i}\psi(\theta)|\hat{H}|\psi(\theta)\rangle + \langle\psi(\theta)|\hat{H}|\frac{d}{d\theta_i}\psi(\theta)\rangle. \tag{6.67}$$

Such an approach has proved to be well-suited for current NISQ architecture, although the approach does appear to be highly dependent on antsatz chosen. For additional information, a recent review of the Variational Quantum Eigensolver is given by Ref. [268].

6.4.2 Quantum Solver for the Anti-Hermitian Contracted Schrödinger Equation

Smart and Mazziotti [267, 269] recently introduced a quantum eigensolver that optimizes a quantum system's ground state energy by solving the anti-Hermitian Contracted Schrödinger equation. Recall that, as described in Sec. 2.5, the ACSE depends upon both the 2-RDM and 3-RDM with the ACSE being closely related to the variational minimization of energy with respect to a series of two-body unitary transformations. It can be shown that the residual of the ACSE approaches zero only as the energy gradient vanishes such that the ACSE can be used to iteratively apply a product of two-body unitary transformations on a reference wave function to find the ground state. Such an approach yields a density matrix given by

$${}^2D^{pq;st}_{n+1} = \langle\Psi_n|e^{-\epsilon_n\hat{A}_n}\hat{a}^\dagger_p\hat{a}^\dagger_q\hat{a}_t\hat{a}_s e^{\epsilon_n\hat{A}_n}|\Psi_n\rangle \tag{6.68}$$

for the $(n+1)^{th}$ iteration where $|\Psi_n\rangle$ is the n^{th}-iteration wave function, $|\Psi_0\rangle$ is the Hartree Fock reference state, ϵ_n is an infinitesimal step, and $\hat{A}_n$ is the residual of the ACSE. Implementing the qACSE can be accomplished by either generating all 2-RDMs on the quantum computer and classically computing $\hat{A}_n$ by classically reconstructing the 3-RDM as described in Chapter 2 or—more-efficiently—by directly computing both the ${}^2D$ and the $\hat{A}_n$ on a quantum device. These approaches are outlined in Refs. [267] and [269].

CHAPTER 7

PREPARATION OF EXCITON CONDENSATE OF PHOTONS ON A 53-QUBIT QUANTUM COMPUTER

Material from: Sager, L. M., Smart, S. E., & Mazziotti, D. A., Preparation of an exciton condensate of photons on a 53-qubit quantum computer. Physical Review Research, published 2020, 2(4), 043205.

7.1 Chapter Synopsis

Quantum computation promises an exponential speedup of certain classes of classical calculations through the preparation and manipulation of entangled quantum states. So far, most molecular simulations on quantum computers, however, have been limited to small numbers of particles. Here we prepare a highly entangled state on a 53-qubit IBM quantum computer, representing 53 particles, which reveals the formation of an exciton condensate of photon particles and holes. While the experimental realization of ground state exciton condensates remained elusive for more than 50 years, such condensates were recently achieved for electron-hole pairs in graphene bilayers and metal chalcogenides. Our creation of ground state photon condensates has the potential to further the exploration of exciton condensates, and this novel preparation may play a role in realizing efficient room-temperature energy transport.

7.2 Introduction

Exciton condensation is defined by the condensation of particle-hole pairs (excitons) into a single quantum state to create a superfluid. The superfluidity of electron-hole pairs—while, by definition, incapable of involving either the frictionless flow of matter or charge—does involve the non-dissipative transfer of energy [106, 107]. As such, understanding and

exploiting the superfluid properties of exciton condensates may be instrumental in the effort to design wires and electronic devices with minimal loss of energy. Consequently, considerable theoretical and experimental investigation has centered on exciton condensation in recent years [107, 112, 156, 178, 179, 186–188].

While excitons form spontaneously in semiconductors and insulators and while the binding energy of the excitons can greatly exceed their thermal energy at room temperature, they recombine too quickly to allow for formation of a condensate in a simple manner. To combat recombination, the coupling of excitons to polaritons—which requires the continuous input of light [110, 112]—and the physical separation of electrons and holes into bilayers—which involves impractically high magnetic fields and/or low temperatures [112, 180, 186, 187, 190]—are employed. Thus, a new, more-practical avenue for the creation of exciton condensates and the study of their properties is desired.

Computation on quantum devices has recently been employed to explore strongly-correlated quantum matter [270], as superconducting circuits allow for precise manipulation of the strongly-interacting qubits to create specified quantum states populated by microwave photons [270–275]. Here we prepare and measure an exciton condensate of photons on a quantum computer. Quantum computation should be particularly adapted to the exploration of exciton condensation as the binary nature of an individual qubit can be interpreted as a site consisting of one fermion and two orbitals; extrapolating, a system of N qubits can be viewed as N degenerate sites each consisting of one fermion and two distinct orbitals. (See Fig. 7.1 for an example of how the $|010\rangle$ qubit state is interpreted in this paradigm). We use such a Hamiltonian of N-fermions in two N-degenerate levels, known as the Lipkin Hamiltonian [225, 276–279] (see SI for details), to prepare a molecular-scale exciton condensate by tuning its interaction parameter to the large-coupling limit. Because each transmon qubit on the quantum computer utilized for this study can be interpreted as an anharmonic oscillator [270–275] whose natural particles are photons (see Ref. [270]), the exciton conden-

sates we construct can be viewed as being comprised of photon-hole pairs condensing into single quantum states—i.e., exciton condensates of photons on a quantum computer.

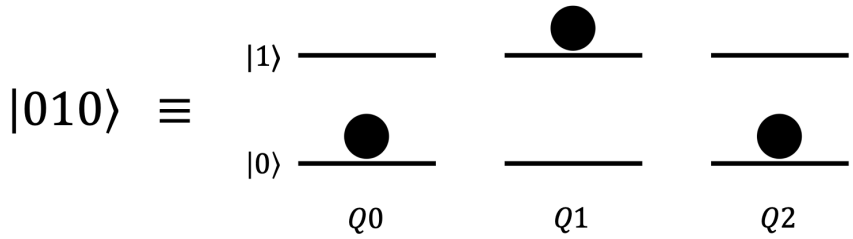

Figure 7.1: A schematic demonstrating the interpretation of the $|010\rangle$ state as three (N) particles in six ($2N$) orbitals in two triply-degenerate (N-degenerate) levels separated by some energetic gap. Each qubit ($Q0, Q1, Q2$) must contain a particle in either the lower $|0\rangle$ or upper $|1\rangle$ level, and only vertical transitions are allowed.

We use the theoretical signature of exciton condensation—derived by Rosina and Garrod [155, 156]—to probe the extent of exciton condensation for a wide range of preparations through simulation and physical quantum computation experiments. From analysis of the natural occupation numbers of these preparations, we establish that prepared states with orbital occupation numbers consistent with the Greenberger-Horne-Zeilinger (GHZ) state—including but not limited to the GHZ state—demonstrate maximal exciton condensation for three qubits. Further, we establish through simulation that for any number of qubits, the GHZ state exhibits maximal character of exciton condensation, demonstrating that the "maximal entanglement" of the GHZ state—for all N—corresponds to the entanglement of particle-hole pairs. Through preparing and probing the GHZ states on quantum devices, character of exciton condensation is experimentally observed in systems composed of up to fifty-three qubits, although decoherence in the higher-qubit systems leads to multiple eigenstates of the particle-hole reduced density matrix (${}^2\tilde{G}$, Eq. (7.3)) demonstrating excitonic character instead of a single, maximally-entangled eigenstate.

Specifically as the GHZ state is prepared here on transmon qubits, the realization of

exciton condensation on the experimental quantum devices of three to fifty-three qubits can be interpreted as the entanglement of photon-hole pairs—i.e., the experimental observation of exciton condensates of photons for systems of three to fifty-three qubits.

7.3 Signature of Exciton Condensation

Condensation phenomena has been an active area of research since 1924 when Einstein and Bose first introduced their ideal "Bose-Einstein" gas [113, 114]. The identical particles comprising this gas—bosons—are able to aggregate into a single quantum ground state when sufficiently cooled [113], which leads to superfluidity of the constituent bosons [97, 115]. In 1940, Pauli established the relationship between spin and statistics, demonstrating that particles with integral spin values (bosons) obey Bose-Einstein statistics and hence may form a condensate [129]. Particles with half-integer spins (fermions), in contrast, must obey the Pauli exclusion principle and are therefore unable to condense into a single quantum state to form a condensate. However, pairs of fermions—forming an overall bosonic state—can condense. In a system of fermionic particles, this pairing can be accomplished through either particle-particle or particle-hole pairing. The condensation of particle-particle pairs into a single quantum state is termed fermion-pair condensation with the resultant superfluidity of fermion pairs causing superconductivity [184]; likewise, the condensation of particle-hole pairs (excitons) into a single quantum state is termed exciton condensation with the resultant superfluidity of exciton pairs causing the nondissipative transfer of energy [107].

In order to computationally probe the presence and extent of condensation behavior, it is useful to establish a calculable, characteristic property. As proven independently by Yang and Sasaki [135, 136], the quantum signature of fermion condensation is associated with a large eigenvalue of the particle-particle reduced density matrix (RDM) with elements given by

$$ {}^2D^{i,j}_{k,l} = \langle \Psi | \hat{a}^\dagger_i \hat{a}^\dagger_j \hat{a}_l \hat{a}_k | \Psi \rangle \tag{7.1} $$

where $|\Psi\rangle$ is an N-fermion wave function, the roman indices correspond to one-fermion orbitals in a finite basis set with rank r, and $\hat{a}^\dagger$ and $\hat{a}$ are fermionic creation and annihilation operators respectively. We denote the largest eigenvalue of the particle-particle RDM as λ_D and use this value as a signature of the extent of fermion pair condensation, with values above one demonstrating condensation.

In analogy to the signature of fermion pair (particle-particle) condensation being a large eigenvalue of the particle-particle RDM, one may assume the quantum signature of exciton (particle-hole) condensation to be a large eigenvalue in the particle-hole RDM [148, 155, 156] with elements given by

$$^2G^{i,j}_{k,l} = \langle\Psi|\hat{a}^\dagger_i\hat{a}_j\hat{a}^\dagger_l\hat{a}_k|\Psi\rangle. \tag{7.2}$$

However, there exist two large eigenvalues for the particle-hole RDM, one of which corresponds to a ground-state-to-ground-state transition (not exciton condensation). In order to eliminate this extraneous large eigenvalue, the modified particle-hole matrix with the ground-state resolution removed

$$^2\tilde{G}^{i,j}_{k,l} =^2 G^{i,j}_{k,l} - {}^1D^i_j\,{}^1D^l_k \tag{7.3}$$

is constructed. Garrod and Rosina [155] have shown that—for an N-fermion system—the eigenvalues of the $^2\tilde{G}$ matrix are zero or one in the non-interacting limit and bounded above by $\frac{N}{2}$ in the limit of strong correlation. We denote the largest eigenvalue of the modified particle-hole RDM as λ_G and use this value as a signature of the presence and extent of exciton condensation.

Note that while we use fermionic creation and annihilation operators to be consistent with the traditional approach to condensation in which particle-particle pairing occurs when two electrons form a Cooper pair and particle-hole pairing occurs when an electron and an electron-hole become paired, bosonic operators can equivalently be employed as a large

eigenvalue in the boson-boson reduced density matrix or a large eigenvalue in the modified boson-hole reduced density matrix would equivalently indicate boson-boson pairs or boson-hole pairs condensing into a single quantum state and hence demonstrating condensation, respectively.

7.4 Results

7.4.1 Condensation with 3 Excitons

Three-qubit systems—which correspond to three fermions in six orbitals [280]—are the smallest systems to possess nontrivial classes of entanglement. Hence, in this study, these minimally-small, three-qubit systems are first thoroughly explored in order to obtain insights on the preparation and characteristics of exciton condensates that are later employed to guide the investigation of larger-qubit systems.

To this end, the three-qubit preparation

$$\begin{aligned} |\Psi\rangle &= C_3^2 R_{y,3}(\theta_3) C_1^2 R_{y,1}(\theta_2) C_1^3 R_{y,1}(\theta_1) |000\rangle \\ &= \alpha|000\rangle + \beta|011\rangle + \gamma|101\rangle + \delta|110\rangle, \end{aligned} \tag{7.4}$$

which—as shown in Ref. [280]—is a minimalistic three-qubit preparation known to effectively span all real, 1-qubit occupations, is utilized to systematically prepare a wide variety of real, three-qubit quantum states. Note that in this preparation, $|000\rangle$ represents the initial all-zero qubit state, C_i^j is a controlled-NOT (CNOT) gate with i control and j target, $R_{y,i}(\theta)$ is a θ- angle rotation about the y-axis of the Bloch sphere on the i^{th} qubit, and α, β, γ, and δ are variables that depend upon θ_1, θ_2, and θ_3.

By scanning over the angles of rotation (θ_1, θ_2, θ_3), we prepare states with all possible, real qubit occupation numbers and hence sweep through all possible correlation phenomena. We then construct the particle-hole RDM [Eq. (7.3)] for each preparation by translating

the expectation values of the creation and annihilation operators to linear combinations of the expectation values of the Pauli X, Y, Z matrices, which can be directly probed on a quantum device. (See the Appendix for a detailed explanation of this process.) By probing λ_G–the largest eigenvalue of the particle-hole RDM–for each of the prepared states, we then determine the extent of exciton condensation for all three-qubit correlation.

Orbital occupation numbers—obtained from the eigenvalues of the one-fermion RDM—are used as a practical coordinate representation in which to visualize λ_G for all electron correlations (all possible occupations). For a three-qubit system, a pure quantum system of three electrons in six orbitals, the requirement that the wave function be antisymmetric for fermionic systems [281, 282] further constrains the eigenvalues of the one-particle reduced density matrix (i.e., the orbital occupations) beyond the traditional Pauli constraints ($0 \leq n_i \leq 1$) [283]. For a three-qubit quantum system, these relevant so-called generalized Pauli constraints are

$$n_5 + n_6 - n_4 \geq 0 \tag{7.5}$$

where

$$n_1 + n_6 = 1 \tag{7.6}$$

$$n_2 + n_5 = 1 \tag{7.7}$$

$$n_3 + n_4 = 1 \tag{7.8}$$

in which each n_i corresponds the natural-orbital occupations ordered from largest to smallest [50, 59, 284–286] .

The three, independent eigenvalues, n_4, n_5, and n_6, can be used as a three-coordinate representation of a given quantum state against the Pauli polytope, the set of all possible occupations according to the Pauli constraints ($0 \leq n_i \leq 1$), as well as the generalized Pauli polytope, the set of all possible occupations according to the generalized Pauli constraint

(Eq. (7.5)). [See Fig. 7.2.]

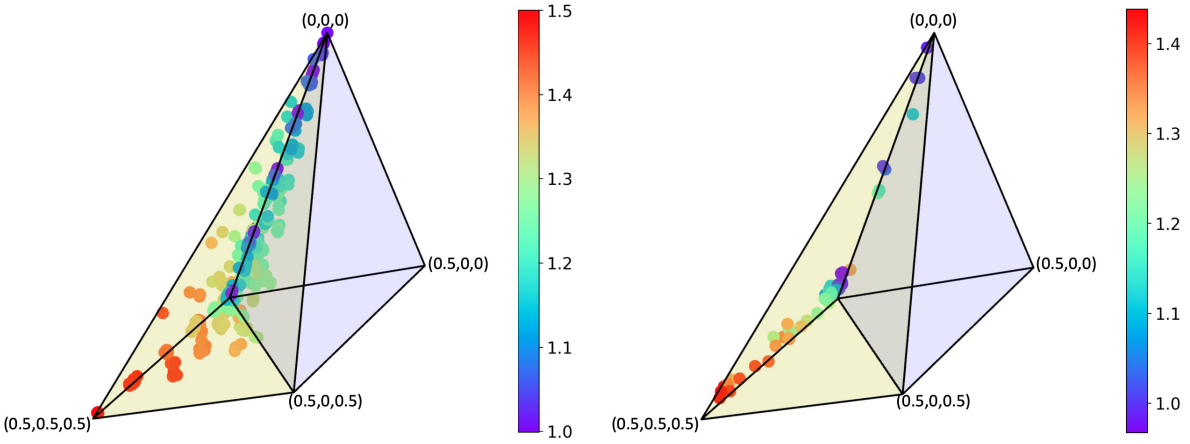

(a) Simulation (b) Mitigated

Figure 7.2: (a) Simulated and (b) experimental data demonstrating that the occupation numbers (n_4, n_5, n_6) of the 1-RDM lie in the generalized Pauli polytope (yellow region) with exciton condensate character (with λ_G increasing from blue to red) emerging as the occupations saturate the vertex $(0.5, 0.5, 0.5)$.

Scatter plots of the occupation numbers for simulated and mitigated, experimental calculations (see Methodology for discussion on error mitigation) are shown in Fig. 7.2 against the Pauli polytope (the combination of the yellow and blue regions allowed by $0 \leq n_i \leq 1$) and the generalized Pauli polytope (only the yellow region allowed by Eq. (7.5)). For the simulated calculations (Fig. 7.2a), possible combinations of angles θ_1, θ_2, and θ_3, varied systematically for $\theta \in \left[0, \frac{\pi}{2}\right]$, are used to prepare quantum states according to Eq. (7.4). Note that the λ_G value associated with the given calculation is represented by the color of the corresponding sphere in the figure with values increasing from blue to red. As can be seen from Fig. 7.2, while the preparations span all orbital occupations consistent with the generalized Pauli constraints and hence all electron correlations, only values approaching the $(n_4, n_5, n_6) = (0.5, 0.5, 0.5)$ corner of the polytope, known to be the occupations of the GHZ state, demonstrate maximal exciton condensation. The mitigated, experimental results shown in Fig. 7.2b in which θ_1 is constrained to either 0 or $\frac{\pi}{2}$ to limit computational expense confirm the simulation results.

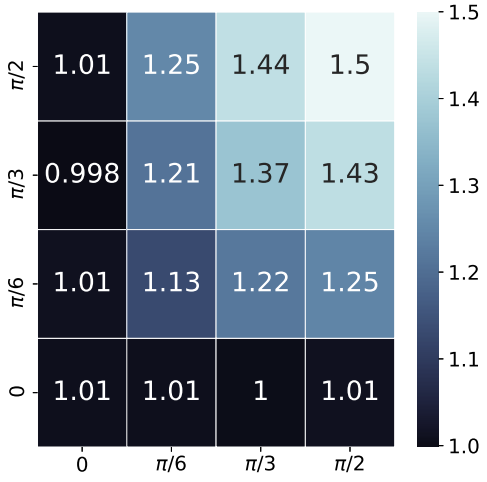

(a) Simulation

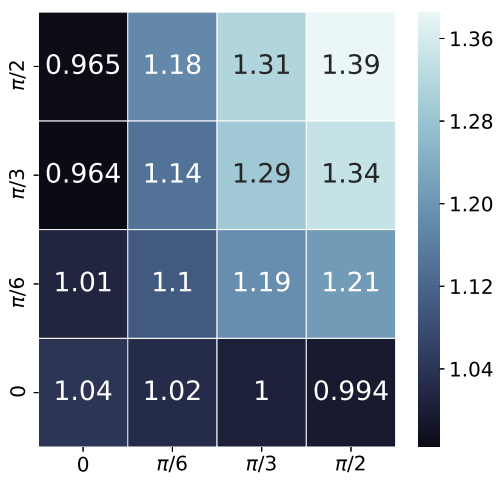

(b) Experimental

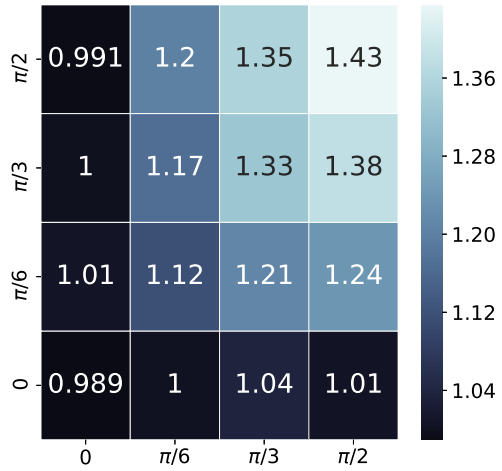

(c) Mitigated

Figure 7.3: The largest eigenvalue λ_G of the modified particle-hole density matrix shown as a function of the preparation angles θ_2 and θ_3 in the range $[0, \frac{\pi}{2}]$ with $\theta_1 = 0$ in Eq. (7.4) for (a) simulated calculations, (b) experimental results, and (c) mitigated, experimental results.

In order to better visualize the variation of exciton condensate character with respect to variation in the preparation of the qubit quantum state, one particular scan of λ_G for the minimalistic three-qubit state preparation is shown in Fig. 7.3 in which the θ_1 value is set to zero and the other angles are varied systematically from 0 to $\frac{\pi}{2}$ with a $\frac{\pi}{6}$ interval.

Table 7.1: Eigenvalue table for the ${}^2\tilde{G}$ matrix for simulated ($\lambda_G^{sim.}$), mitigated experimental ($\lambda_G^{mit.}$), and experimental ($\lambda_G^{exp.}$) GHZ state results.

N	$\lambda_G^{sim.}$	$\lambda_G^{mit.}$	$\lambda_G^{exp.}$
3	1.50	1.44	1.39
4	2.00	1.92	1.80
5	2.50	2.33	2.22
6	3.00	2.70	2.27
7	3.50	—	2.44
8	4.00	—	2.72
9	4.50	—	2.73
10	5.00	—	2.93
11	5.50	—	3.08
12	6.00	—	3.22
13	6.50	—	3.28
14	7.00	—	3.25
15	7.50	—	2.91
16	8.00	—	2.28
22	11.0	—	2.68
28	14.0	—	3.48
34	17.0	—	3.82
41	20.5	—	3.99
47	23.5	—	3.48
53	26.5	—	4.74

In Fig. 7.3, results are given for (a) simulation, (b) experiments without mitigation, and (c) mitigated experiments. Note that these particular scanning parameters are chosen as they well-represent the observed range in λ_G and demonstrate the maximal three-qubit λ_G of $\frac{N}{2} = \frac{3}{2} = 1.5$ for the simulated results. Additionally, note that even the unmitigated, experimental results [(b)] demonstrate a relatively large λ_G of 1.39, a clear demonstration of exciton condensate character despite experimental errors (see the SI for discussion of errors). This large, non-error-corrected signature of exciton condensation shows that exciton condensation is indeed created on the quantum computer and is not an artifact of error correction. The large eigenvalue λ_G and the degree of saturation of the generalized Pauli constraint in Eq. (7.5) are reported in Tables IV through VII and Fig. 1 for many sets of

orbital occupations in the Supporting Information.

7.4.2 Condensation with 3-to-53 Excitons

As shown above, the region of the Pauli polytope associated with the GHZ state, the state described by

$$|\Psi_{GHZ}\rangle = \frac{1}{\sqrt{2}}\left(|0\rangle^{\otimes N} + |1\rangle^{\otimes N}\right) \tag{7.9}$$

for an N-qubit system, demonstrates maximal exciton condensate character for three qubits. While the computations with maximal exciton condensation have occupation numbers consistent with the GHZ state (among other states), the minimalistic preparation used to probe λ_G in the previous section permits only double excitations as shown in Eq. (7.4). As the GHZ state is relatively-easily generalizable to higher-qubit preparations and is hence desirable, a different qubit preparation scheme (Eq. (7.13) in the Appendix) is used to generate the three-qubit GHZ state and verify that the true GHZ state demonstrates exciton condensation. As can be seen in Table 7.1, maximum exciton condensate character ($\frac{N}{2} = \frac{3}{2} = 1.5$) is indeed observed for simulation of the three-qubit GHZ state.

The generalizable qubit preparation of the GHZ for a generic N-qubit state allows for the extension of the above result to larger numbers of qubits, the outcomes of which can be seen in Table 7.1. These results demonstrate that the beginnings of exciton condensation is achieved on quantum computers using 3-to-53 qubits. Note that error mitigation is only feasible for systems with $N \leq 6$ qubits as larger-qubit error mitigation schemes necessitate more circuits than the experimental quantum devices allow. Additionally, to limit computational expense, only real contributions to the reduced density matrices are computed. See the Appendix for specific experimental details and Tables I, II, and III in the Supporting Information for device specifications.

As is apparent from simulated results (Table 7.1 and Fig. 7.4a), the GHZ state for all qubits approaches the maximal value for exciton condensate character of $\frac{N}{2}$. As such, the

GHZ state is expected to demonstrate maximal exciton condensation for a given number of qubits. While the experimental results in Table 7.1 and Fig. 7.4b do not achieve maximal λ_G values, although the error-mitigated results do appear to approach $\frac{N}{2}$, exciton condensation character ($\lambda_G > 1$) is observed for each GHZ state prepared for $N = 3$-to-53 qubits.

The larger deviation from the simulated results observed in the higher-qubit experiments—in which there seems to be a maximal signature of exciton condensation of around $\lambda_G \approx 3$ (Table 7.1 and Fig. 7.4b)— is likely due to the cumulative effects of errors that become increasingly significant as the number of qubits—and hence the number of CNOT gates applied—increases. (See Sec. 6.2.5 for details of gate errors, readout errors, and multi-qubit CNOT errors for the quantum devices employed for experimentation.) These errors seem to prevent the formation of a global excitonic state due to dispersion; however, as the number of qubits is increased, the condensation behavior of the N-qubit system does still increase as is shown in Fig. 7.4c. In these higher-qubit experiments, there are multiple eigenvalues of the ${}^2\tilde{G}$ matrix above one, indicating that there are multiple eigenstates demonstrating character of exciton condensation. The sum of the eigenvalues above one increases in an almost linear fashion as the number of qubits is increased, demonstrating an overall increase in the excitonic nature of the prepared states even if maximal condensation behavior in a single orbital can not be obtained for these higher-qubit experiments due to dispersion.

The GHZ state is often referred to as a "the maximally-entangled state" as it has maximum entanglement entropy [287]; however, there are diverse types of non-equivalent multipartite entanglement. For example, Bose-Einstein condensation, fermion pair condensation, and exciton condensation are all phenomena that occur due to the entanglement of bosons, differing in their signatures and the types of bosons that are entangled. Here we have demonstrated a new characteristic of the maximal entanglement of the GHZ state—namely the maximal entanglement of particle-hole pairs (excitons). Further, the fermion pair condensate character (λ_D) is additionally probed for the GHZ state, and no fermion pair con-

densation is observed ($\lambda_D < 1$). (See Fig. 7.4.) As such, we have shown that the maximal entanglement of the GHZ state does not correspond to the entanglement of particle-particle pairing.

7.5 Discussion and Conclusions

In this study, we have prepared molecular-scale exciton condensates for three- to fifty-three-qubit systems on three quantum computers and verified the presence of the condensation through post-measurement computation of the exciton condensate's quantum signature [155]. The maximal condensate character is observed for the Greenberg-Horne-Zeilinger (GHZ) "maximally-entangled" state, indicating that a characteristic of this maximal entanglement state is the entanglement of particle-hole pairs (excitons). Further, as transmon qubit quantum states [107, 112, 156, 178, 179, 186–188] are experimentally constructed on the quantum devices employed, these exciton condensates corresponding to the GHZ state can be interpreted as exciton condensates of photons—the entanglement of photon-hole pairs. Whether photon-hole pair condensation would have similar properties to those of traditional fermion-hole exciton condensates is unknown, but it seems likely that, as the photons are directly analogous to fermions in a traditional exciton condensate, the superfluidity of photon-hole excitons should allow for the dissipationless flow of energy, which has possible applications in energy transport.

Additionally, the recognition of the GHZ state as an exciton condensate on a quantum computer establishes a new avenue for the creation and characterization of exciton condensates. As the GHZ state can be remotely and reliably constructed and probed through the use of cloud-accessible quantum devices, this preparation of exciton condensation may be more convenient than prior experimental methodologies. Moreover, multi-particle GHZ states have previously been experimentally realized through optical methodologies [288–290], ion traps [291], and even Ising spin models [292], demonstrating that various types of exciton

condensates can be—and indeed have been—prepared. The recognition that such established methodologies for preparation of the GHZ state also demonstrate exciton condensation may advance the search for the creation of convenient, high-temperature, ground state exciton condensation, which may have technological applications.

As quantum devices are created with a larger number of qubits, preparation of these higher-qubit GHZ states would create more macroscopically-scaled exciton condensates of these various compositions, although—as we have demonstrated—unless sufficient effort is done to prevent dispersion, this condensate character will be scattered throughout multiple eigenstates of the particle-hole RDM. Thus, future exploration of the properties of exciton condensates on quantum computers is anticipated, and the creation and characterization of exciton condensates is yet another motivation for the development of low-error quantum devices with macroscopic numbers of qubits.

7.6 Appendix

We include details on the quantum algorithms used to prepare the qubit states presented in the article; the quantum tomography of the modified particle-hole reduced density matrix; the methodology by which error is mitigated; and relevant details on the experimental quantum devices employed.

7.6.1 State Preparations

Two algorithms are utilized in this work to prepare the qubit states.

Minimalistic, Scanning Approach—The first algorithm takes a minimalistic approach to span all valid one-qubit occupation numbers for a three qubit system and is given as follows:

$$|\Psi\rangle = C_3^2 R_{y,3}(\theta_3) C_1^2 R_{y,1}(\theta_2) C_1^3 R_{y,1}(\theta_1) |0\rangle^{\otimes 3}, \tag{7.10}$$

where $R_{y,i}$ refers to rotation of a qubit i about its Bloch sphere's y-axis—which is given by

$$R_{y,i} = \begin{pmatrix} \cos\left(\frac{\theta}{2}\right) & -\sin\left(\frac{\theta}{2}\right) \\ \sin\left(\frac{\theta}{2}\right) & \cos\left(\frac{\theta}{2}\right) \end{pmatrix} \tag{7.11}$$

—and C_i^j is a standard controlled-NOT (CNOT) gate with control and target qubits i and j respectively. Note that the control qubit is rotated prior to the application of the CNOT transformation. Overall, the sequence of transformations in Eq. (7.10) yields a wave function of the form

$$|\Psi\rangle = \alpha|000\rangle + \beta|011\rangle + \gamma|101\rangle + \delta|110\rangle, \tag{7.12}$$

such that α, β, γ, and δ are functions of the input angles (θ_1, θ_2, θ_3) and the 1-RDM contains solely diagonal elements.

The GHZ State—The GHZ State described in Eq. (7.9) is prepared according to

$$|\Psi\rangle = C_{N-1}^N \cdots C_2^3 C_1^2 H_1 |0\rangle^{\otimes N} \tag{7.13}$$

for an N-qubit state where H_i represents the Hadamard gate—which maps $|0\rangle$ to $\frac{|0\rangle+|1\rangle}{\sqrt{2}}$ and $|1\rangle$ to $\frac{|0\rangle-|1\rangle}{\sqrt{2}}$—acting on qubit i. There has been much study on the optimal preparation of the GHZ state for various numbers of qubits [293–296]; in this study, however, the simple algorithm from Ref. [297] for GHZ state preparation is utilized as it is easily implemented and generalizable to any arbitrary number of qubits.

7.6.2 Quantum Tomography of Particle-hole RDM

The modified particle-hole RDM—with elements given by Eq. (7.3)—is obtained through the translation of all of its elements into the bases of Pauli matrices, which are directly probed on the quantum computer.

First, let us focus on the ${}^1D_i^j$ terms of the ${}^2\tilde{G}$ matrix elements. As 1-RDMs simplify to block-diagonal forms with respect to single qubits, there are no non-zero two-qubit 1-RDM terms. In order for a 1-RDM to be non-zero, then, it must be a one-qubit 1-RDM of the form

	$\hat{a}_{p,0}$	$\hat{a}_{p,1}$
$\hat{a}_{p,0}^\dagger$	$\hat{a}_{p,0}^\dagger \hat{a}_{p,0}$	$\hat{a}_{p,0}^\dagger \hat{a}_{p,1}$
$\hat{a}_{p,1}^\dagger$	$\hat{a}_{p,1}^\dagger \hat{a}_{p,0}$	$\hat{a}_{p,1}^\dagger \hat{a}_{p,1}$

(7.14)

for qubit p where $\hat{a}_p^\dagger$ and $\hat{a}_p$ are creation and annihilation operators for qubit p, respectively. Each term of these non-zero, one-qubit 1-RDMs can be written as a linear combination of Pauli matrices. For example, $\hat{a}_{p,0}^\dagger \hat{a}_{p,1}$—which represents the qubit going from state $|1\rangle = \begin{pmatrix} 0 \\ 1 \end{pmatrix}$ to state $|0\rangle = \begin{pmatrix} 1 \\ 0 \end{pmatrix}$—can be written as follows:

$$\hat{a}_{p,0}^\dagger \hat{a}_{p,1} = \begin{pmatrix} 0 & 1 \\ 0 & 0 \end{pmatrix} = \frac{1}{2}\left(X_p + iY_p\right). \tag{7.15}$$

Similarly, the other elements can be represented as shown:

$$\hat{a}_{p,1}^\dagger \hat{a}_{p,0} = \begin{pmatrix} 0 & 0 \\ 1 & 0 \end{pmatrix} = \frac{1}{2}\left(X_p - iY_p\right), \tag{7.16}$$

$$\hat{a}_{p,0}^\dagger \hat{a}_{p,0} = \begin{pmatrix} 1 & 0 \\ 0 & 0 \end{pmatrix} = \frac{1}{2}\left(\hat{I} + Z_p\right), \tag{7.17}$$

$$\hat{a}_{p,1}^\dagger \hat{a}_{p,1} = \begin{pmatrix} 0 & 0 \\ 0 & 1 \end{pmatrix} = \frac{1}{2}\left(\hat{I} - Z_p\right). \tag{7.18}$$

(See the Supporting Information for a discussion on how our representation of creation and annihilation operators corresponds to bosonic and fermionic statistics.)

The expectation value of each matrix element for a given qubit (p) can then be obtained by directly probing the expectation values of X_p, Y_p, and Z_p for a given state preparation.

The overall particle-hole RDM (^2G matrix) can be represented as a $4N \times 4N$ matrix composed of N^2 4×4 sub-matrices of the form

$$\begin{array}{c|cccc} & \hat{a}^\dagger_{q,0}\hat{a}_{q,0} & \hat{a}^\dagger_{q,1}\hat{a}_{q,0} & \hat{a}^\dagger_{q,0}\hat{a}_{q,1} & \hat{a}^\dagger_{q,1}\hat{a}_{q,1} \\ \hline \hat{a}^\dagger_{p,0}\hat{a}_{p,0} & \hat{a}^\dagger_{p,0}\hat{a}_{p,0}\hat{a}^\dagger_{q,0}\hat{a}_{q,0} & \hat{a}^\dagger_{p,0}\hat{a}_{p,0}\hat{a}^\dagger_{q,1}\hat{a}_{q,0} & \hat{a}^\dagger_{p,0}\hat{a}_{p,0}\hat{a}^\dagger_{q,0}\hat{a}_{q,1} & \hat{a}^\dagger_{p,0}\hat{a}_{p,0}\hat{a}^\dagger_{q,1}\hat{a}_{q,1} \\ \hat{a}^\dagger_{p,0}\hat{a}_{p,1} & \hat{a}^\dagger_{p,0}\hat{a}_{p,1}\hat{a}^\dagger_{q,0}\hat{a}_{q,0} & \hat{a}^\dagger_{p,0}\hat{a}_{p,1}\hat{a}^\dagger_{q,1}\hat{a}_{q,0} & \hat{a}^\dagger_{p,0}\hat{a}_{p,1}\hat{a}^\dagger_{q,0}\hat{a}_{q,1} & \hat{a}^\dagger_{p,0}\hat{a}_{p,1}\hat{a}^\dagger_{q,1}\hat{a}_{q,1} \\ \hat{a}^\dagger_{p,1}\hat{a}_{p,0} & \hat{a}^\dagger_{p,1}\hat{a}_{p,0}\hat{a}^\dagger_{q,0}\hat{a}_{q,0} & \hat{a}^\dagger_{p,1}\hat{a}_{p,0}\hat{a}^\dagger_{q,1}\hat{a}_{q,0} & \hat{a}^\dagger_{p,1}\hat{a}_{p,0}\hat{a}^\dagger_{q,0}\hat{a}_{q,1} & \hat{a}^\dagger_{p,1}\hat{a}_{p,0}\hat{a}^\dagger_{q,1}\hat{a}_{q,1} \\ \hat{a}^\dagger_{p,1}\hat{a}_{p,1} & \hat{a}^\dagger_{p,1}\hat{a}_{p,1}\hat{a}^\dagger_{q,0}\hat{a}_{q,0} & \hat{a}^\dagger_{p,1}\hat{a}_{p,1}\hat{a}^\dagger_{q,1}\hat{a}_{q,0} & \hat{a}^\dagger_{p,1}\hat{a}_{p,1}\hat{a}^\dagger_{q,0}\hat{a}_{q,1} & \hat{a}^\dagger_{p,1}\hat{a}_{p,1}\hat{a}^\dagger_{q,1}\hat{a}_{q,1}. \end{array} \tag{7.19}$$

where each element of the matrix is the expectation value of the creation and annhilation operator terms shown. As multi-qubit wave functions are the tensor products of individual qubit wave functions, these four-body terms can be represented as the tensor products of the two-body terms composing them. For example, the matrix element given by $\hat{a}^\dagger_{p,0}\hat{a}_{p,1}\hat{a}^\dagger_{q,1}\hat{a}_{q,1}$ can be written as

$$\begin{aligned} \hat{a}^\dagger_{p,0}\hat{a}_{p,1}\hat{a}^\dagger_{q,1}\hat{a}_{q,1} &= \left(\hat{a}^\dagger_{p,0}\hat{a}_{p,1}\right) \otimes \left(\hat{a}^\dagger_{q,1}\hat{a}_{q,1}\right) \\ &= \left[\frac{1}{2}\left(X_p + iY_p\right)\right] \otimes \left[\frac{1}{2}\left(\hat{I}_q - Z_q\right)\right] \\ &= \frac{1}{4}\left[X_p \otimes \hat{I}_q - X_p \otimes Z_q + iY_p \otimes \hat{I}_q - iY_p \otimes Z_q\right], \end{aligned} \tag{7.20}$$

where $Y_p \otimes Z_q$ is one of nine possible two-qubit tensor products. The Pauli representation of all other matrix elements can be determined using analogous, straightforward methodologies, and the values of these matrix elements are then calculated by probing the expectation values of the two-qubit tensor products of Pauli matrices.

Similarly, the overall modified particle-hole RDM ($^2\tilde{G}$ matrix) can be represented as a $4N \times 4N$ matrix composed of N^2 4×4 sub-matrices. These sub-matrices are identical to

the sub-matrices of the ${}^2G$ matrix with the block modification shown below subtracted off to eliminate the extraneous ground-state-to-ground-state transition:

	$\hat{a}^\dagger_{q,0}\hat{a}_{q,0}$	$\hat{a}^\dagger_{q,1}\hat{a}_{q,0}$	$\hat{a}^\dagger_{q,0}\hat{a}_{q,1}$	$\hat{a}^\dagger_{p,1}\hat{a}_{p,1}$
$\hat{a}^\dagger_{p,0}\hat{a}_{p,0}$	${}^1D_p[0,0]{}^1D_q[0,0]$	${}^1D_p[0,0]{}^1D_q[0,1]$	${}^1D_p[0,0]{}^1D_q[1,0]$	${}^1D_p[0,0]{}^1D_q[1,1]$
$\hat{a}^\dagger_{p,0}\hat{a}_{p,1}$	${}^1D_p[0,1]{}^1D_q[0,0]$	${}^1D_p[0,1]{}^1D_q[0,1]$	${}^1D_p[0,1]{}^1D_q[1,0]$	${}^1D_p[0,1]{}^1D_q[1,1]$
$\hat{a}^\dagger_{p,1}\hat{a}_{p,0}$	${}^1D_p[1,0]{}^1D_q[0,0]$	${}^1D_p[1,0]{}^1D_q[0,1]$	${}^1D_p[1,0]{}^1D_q[1,0]$	${}^1D_p[1,0]{}^1D_q[1,1]$
$\hat{a}^\dagger_{p,1}\hat{a}_{p,1}$	${}^1D_p[1,1]{}^1D_q[0,0]$	${}^1D_p[1,1]{}^1D_q[0,1]$	${}^1D_p[1,1]{}^1D_q[1,0]$	${}^1D_p[1,1]{}^1D_q[1,1]$

(7.21)

Note that ${}^1D_i$ is the RDM for qubit i described in Eq. (7.14) and that ${}^1D_i[a,b]$ is the element of that matrix with matrix coordinates $[a,b]$.

The overall form of the ${}^2\tilde{G}$ matrix is hence

p=0,q=0	p=0,q=1	$\cdots$	p=0,q=N−1
p=1,q=0	p=1,q=1	$\cdots$	p=1,q=N−1
$\vdots$	$\vdots$	$\ddots$	$\vdots$
p=N−1,q=0	p=N−1,q=1	$\cdots$	p=N−1,q=N−1

(7.22)

where each p/q combination represents one of the previously-specified blocks, i.e., the difference of the matrices given in Eqs. (7.19) and (7.21). The largest eigenvalue of this overall matrix is the λ_G value employed throughout this article.

In order to probe the extent of fermion pair condensation, the particle-particle RDM shown in Eq. (7.1) must additionally be constructed. Similar to both the ${}^2G$ and ${}^2\tilde{G}$ matrices, the ${}^2D$ matrix can be represented as a $4N \times 4N$ matrix, and the elements of the ${}^2D$ matrix can be computed according to

$$ {}^2D^{i,j}_{k,l} = \delta^{j}_{l}\,{}^1D^{i}_{k} - {}^2G^{i,l}_{k,j} \tag{7.23} $$

where δ_l^j is a delta function whose value is defined to be one when $i = j$ and otherwise zero and where ${}^1D_k^i$ and ${}^2G_{k,j}^{i,l}$ are the one-particle RDM and the particle-hole RDM whose elements are computed according to Eqs. (7.14)-(7.18) and Eqs. (7.19)-(7.20), respectively. The signature of fermion pair condensation—i.e., λ_D, the largest eigenvalue of the ${}^2D$ matrix—can then be obtained from the particle-particle RDM obtained for a given preparation.

As the states prepared in this study are real wave functions, the imaginary components of the RDMs should be approximately zero within a small range dictated by inherent randomness and by the error of the devices. Therefore, only the five of the possible nine two-qubit expectation values that correspond to real contributions to the RDMs [$\langle X_p \otimes X_q \rangle$, $\langle Y_p \otimes Y_q \rangle$, $\langle Z_p \otimes Z_q \rangle$, $\langle X_p \otimes Z_q \rangle$, and $\langle Z_p \otimes X_q \rangle$] are non-zero and hence essential for construction of the ${}^2\tilde{G}$ matrix. While, for the sake of completeness, the negligibly-small imaginary components are included in the construction of the ${}^2\tilde{G}$ matrix for the low-qubit ($N = 3 - 5$) computations, only real components are included in the ${}^2\tilde{G}$ matrix for higher-qubit ($N = 6 - 15$) computations to lower computational expense.

Error mitigation—A measurement correction fitter for a tensored calibration is employed to mitigate measurement error through use of the "least_squares" method —that constrains the resultant mitigated counts to having physical probabilities—to construct a mitigation filter that can be applied to experimental data [298, 299].

7.6.3 Quantum Device Specifications

Throughout this work, we employ the ibmqx2 (ibmq_5_yorktown) [300], the ibmq_16_melbourne [8], and the ibmq_rochester [301] IBM Quantum Experience devices, which are available online. Unless explicitly stated otherwise, all low-qubit ($N \leq 5$) experiments are conducted using the five-qubit ibmqx2 (ibmq_5_yorktown) device, all midrange-qubit ($5 < N \leq 15$) experiments are conducted using the fifteen-qubit ibmq_16_melbourne device, and all high-qubit ($N > 15$) experiments are conducted using the fifty-three-qubit

ibmq_rochester device. These quantum devices are composed of fixed-frequency transmon qubits with co-planer waveguide resonators [272, 274]. Experimental calibration data and connectivity for these devices are included in the Supporting Information.

7.7 Supplemental Information

7.7.1 The Lipkin Hamiltonian

One of the simplest and most well-known models for exciton condensation is the Lipkin model in the large-coupling regime [225, 276–279]. The Lipkin quasispin model consists of N fermions distributed over two, N-fold degenerate levels with energies $-\epsilon$ and ϵ where the particles have a pairwise "monopole-monopole" interaction with strength V, which scatters the pairs between the two levels. The Hamiltonian for this model is given by

$$\hat{H} = \epsilon \hat{J}_z + \frac{V}{2}\left(\hat{J}^2_{+,-} + \hat{J}^2_{-,+}\right) \tag{SI-1}$$

where

$$\hat{J}_z = \frac{1}{2}\sum_m m \sum_{p=1}^{N} \hat{a}^\dagger_{m,p}\hat{a}_{m,p}, \tag{SI-2}$$

$$\hat{J}_{+,-} = \sum_{p=1}^{N} \hat{a}^\dagger_{+1,p}\hat{a}_{-1,p}, \tag{SI-3}$$

$$\hat{J}_{-,+} = \sum_{p=1}^{N} \hat{a}^\dagger_{-1,p}\hat{a}_{+1,p}, \tag{SI-4}$$

$\hat{a}^\dagger$ and $\hat{a}$ are fermionic creation and annihilation operators, $m(\pm 1)$ denotes the two levels, and ϵ and V are parameters. Note that from this representation, it is apparent that each orbital in the bottom layer has a corresponding orbital in the top layer to which they are particle-hole paired (i.e., only vertical transitions are allowed). Additionally, the parameter V controls the relative importance of of two particle interactions such that a large V indicates

that the two-body part of the Hamiltonian is dominant—the large-coupling limit for which exciton condensation is known to occur.

7.7.2 Bosonic and Fermionic Statistics For One Particle in Two Orbitals Qubit Representation

A single qubit—the analogue to the classical bit on a quantum device—can be represented according to $\cos\left(\frac{\theta}{2}\right)|0\rangle + e^{i\phi}\sin\left(\frac{\theta}{2}\right)|1\rangle$, which can be pictorially depicted by the image of the Bloch sphere shown in Fig. 7.5. The quantum bit is hence a linear combination of the classical bit states, $|0\rangle$ and $|1\rangle$. The classical bit states are represented in vector form as follows.

$$|0\rangle = \begin{pmatrix} 1 \\ 0 \end{pmatrix}$$

$$|1\rangle = \begin{pmatrix} 0 \\ 1 \end{pmatrix}$$

As described in the main text, we view each qubit as being composed of one particle in two particle-hole paired orbitals. As such, if qubit i exists in the $|0\rangle$ state, a particle exists in the orbital which we denote as $i, 0$ and a hole exists in the orbital denoted as $i, 1$. Similarly, if qubit i exists in the $|1\rangle$ state, a particle exists in the orbital which we denote as $i, 1$ and a hole exists in the orbital denoted as $i, 0$. Below, we apply bosonic and fermionic statistics for such a qubit interpretation.

General Bosonic Statistics

Bosons must obey the commutation relationship,

$$[\hat{b}_i, \hat{b}_j^\dagger] = \hat{b}_i\hat{b}_j^\dagger - \hat{b}_j^\dagger\hat{b}_i = \delta_j^i,$$

where $\hat{b}_i^\dagger$ and $\hat{b}_i$ are bosonic creation and annihilation operators for orbital i such they act on a wave function as shown below.

$$\hat{b}_i|i \wedge \psi\rangle = \sqrt{n}|\psi\rangle$$

$$\hat{b}_i^\dagger|\psi\rangle = \sqrt{n+1}|i \wedge \psi\rangle$$

The bosonic commutation relationship can be proven as follows for the case of $i = j$ for qubit p—which exists in a linear combination of $|0\rangle$ and $|1\rangle$, i.e. $|\psi\rangle_p = \cos\left(\frac{\theta}{2}\right)|0\rangle + e^{i\phi}\sin\left(\frac{\theta}{2}\right)|1\rangle$—as can be seen by

$$\hat{b}_{p,0}\hat{b}_{p,0}^\dagger - \hat{b}_{p,0}^\dagger\hat{b}_{p,0} = [2 \times P(|0\rangle) + P(|1\rangle)] - P(|0\rangle) = P(|1\rangle) + P(|0\rangle) = \delta_{p,0}^{p,0} = 1$$

and

$$\hat{b}_{p,1}\hat{b}_{p,1}^\dagger - \hat{b}_{p,1}^\dagger\hat{b}_{p,1} = [2 \times P(|1\rangle) + P(|0\rangle)] - P(|1\rangle) = P(|0\rangle) + P(|1\rangle) = \delta_{p,1}^{p,1} = 1$$

where $P(|0\rangle)$ and $P(|1\rangle)$ are the probabilities of the qubit being in the $|0\rangle$ and $|1\rangle$ respectively.

When $i \neq j$, this bosonic commutation yields the following two relationships, which must be obeyed by bosons.

$$\hat{b}_{p,0}\hat{b}_{p,1}^\dagger - \hat{b}_{p,1}^\dagger\hat{b}_{p,0} = \delta_{p,1}^{p,0} = 0 \Rightarrow \hat{b}_{p,0}\hat{b}_{p,1}^\dagger = +\hat{b}_{p,1}^\dagger\hat{b}_{p,0}$$

$$\hat{b}_{p,1}\hat{b}_{p,0}^\dagger - \hat{b}_{p,0}^\dagger\hat{b}_{p,1} = \delta_{p,0}^{p,1} = 0 \Rightarrow \hat{b}_{p,1}\hat{b}_{p,0}^\dagger = +\hat{b}_{p,0}^\dagger\hat{b}_{p,1}$$

The Bosonic Qubit

In order to establish when a given qubit can be described as bosonic, we first have to determine when it satisfies the bosonic statistics from above. This can be done by representing the

eight possible one-qubit, two-term expectation values as linear combinations of expectation values of the Pauli matrices for the specified qubit. Let's first look at the four previously-established 1-RDM terms (see the Methods section in the main paper).

	$\hat{b}_{p,0}$	$\hat{b}_{p,1}$
$\hat{b}^\dagger_{p,0}$	$\hat{b}^\dagger_{p,0}\hat{b}_{p,0}$	$\hat{b}^\dagger_{p,0}\hat{b}_{p,1}$
$\hat{b}^\dagger_{p,1}$	$\hat{b}^\dagger_{p,1}\hat{b}_{p,0}$	$\hat{b}^\dagger_{p,1}\hat{b}_{p,1}$

These four terms are given by the following four equations and are identical for fermionic and bosonic creation and annihilation operators.

$$\hat{b}^\dagger_{p,0}\hat{b}_{p,1} = \begin{pmatrix} 0 & 1 \\ 0 & 0 \end{pmatrix} = \frac{1}{2}\left(X_p + iY_p\right)$$

$$\hat{b}^\dagger_{p,1}\hat{b}_{p,0} = \begin{pmatrix} 0 & 0 \\ 1 & 0 \end{pmatrix} = \frac{1}{2}\left(X_p - iY_p\right)$$

$$\hat{b}^\dagger_{p,0}\hat{b}_{p,0} = \begin{pmatrix} 1 & 0 \\ 0 & 0 \end{pmatrix} = \frac{1}{2}\left(\hat{I} + Z_p\right)$$

$$\hat{b}^\dagger_{p,1}\hat{b}_{p,1} = \begin{pmatrix} 0 & 0 \\ 0 & 1 \end{pmatrix} = \frac{1}{2}\left(\hat{I} - Z_p\right)$$

Now, let's compare these terms with those from the matrix composed as follows.

	$\hat{b}^\dagger_{p,0}$	$\hat{b}^\dagger_{p,1}$
$\hat{b}_{p,0}$	$\hat{b}_{p,0}\hat{b}^\dagger_{p,0}$	$\hat{b}_{p,0}\hat{b}^\dagger_{p,1}$
$\hat{b}_{p,1}$	$\hat{b}_{p,1}\hat{b}^\dagger_{p,0}$	$\hat{b}_{p,1}\hat{b}^\dagger_{p,1}$

These four terms are given by the following four equations. Note that two of these differ

from their fermionic counterparts (see below) due to the prefactors associated with bosonic creation and annihilation operatures derived from the fact that more than one boson can be created in a given orbital.

$$\hat{b}_{p,0}\hat{b}^{\dagger}_{p,1} = \begin{pmatrix} 0 & 0 \\ 1 & 0 \end{pmatrix} = \frac{1}{2}\left(X_p - iY_p\right) = \hat{b}^{\dagger}_{p,1}\hat{b}_{p,0}$$

$$\hat{b}_{p,1}\hat{b}^{\dagger}_{p,0} = \begin{pmatrix} 0 & 1 \\ 0 & 0 \end{pmatrix} = \frac{1}{2}\left(X_p + iY_p\right) = \hat{b}^{\dagger}_{p,0}\hat{b}_{p,1}$$

$$\hat{b}_{p,0}\hat{b}^{\dagger}_{p,0} = \begin{pmatrix} 2 & 0 \\ 0 & 1 \end{pmatrix} = \frac{1}{2}\left(3\hat{I} + Z_p\right)$$

$$\hat{b}_{p,1}\hat{b}^{\dagger}_{p,1} = \begin{pmatrix} 1 & 0 \\ 0 & 2 \end{pmatrix} = \frac{1}{2}\left(3\hat{I} - Z_p\right)$$

As can be seen from the above, $\hat{b}_{p,0}\hat{b}^{\dagger}_{p,1} = \hat{b}^{\dagger}_{p,1}\hat{b}_{p,0}$ are $\hat{b}_{p,1}\hat{b}^{\dagger}_{p,0} = \hat{b}^{\dagger}_{p,0}\hat{b}_{p,1}$ are always true, which always satisfies the bosonic commutation relationship. **Hence, bosonic statistics are satisfied by all values of θ and ϕ** and no constraints on the preparations are necessary in order to represent bosons using these creation and annihilation operators.

General Fermionic Statistics

Fermions must obey the anticommutation relationship

$$\{\hat{a}_i, \hat{a}^{\dagger}_j\} = \hat{a}_i\hat{a}^{\dagger}_j + \hat{a}^{\dagger}_j\hat{a}_i = \delta^i_j$$

where $\hat{a}^{\dagger}_i$ and $\hat{a}^{\dagger}_i$ are fermionic creation and annihilation operators for orbital i.

The fermionic anticommutation relationship can be proven as follows for the case of $i = j$

for qubit p—which exists in a linear combination of $|0\rangle$ and $|1\rangle$, i.e. $|\psi\rangle_p = \cos\left(\frac{\theta}{2}\right)|0\rangle + e^{i\phi}\sin\left(\frac{\theta}{2}\right)|1\rangle$—as can be seen by

$$\hat{a}_{p,0}\hat{a}^\dagger_{p,0} + \hat{a}^\dagger_{p,0}\hat{a}_{p,0} = P(|1\rangle) + P(|0\rangle) = \delta^{p,0}_{p,0} = 1$$

and

$$\hat{a}_{p,1}\hat{a}^\dagger_{p,1} + \hat{a}^\dagger_{p,1}\hat{a}_{p,1} = P(|0\rangle) + P(|1\rangle) = \delta^{p,1}_{p,1} = 1.$$

When $i \neq j$, this fermionic anticommutation yields the following two relationships, which must be obeyed by fermions.

$$\hat{a}_{p,0}\hat{a}^\dagger_{p,1} + \hat{a}^\dagger_{p,1}\hat{a}_{p,0} = \delta^{p,0}_{p,1} = 0 \Rightarrow \hat{a}_{p,0}\hat{a}^\dagger_{p,1} = -\hat{a}^\dagger_{p,1}\hat{a}_{p,0}$$

$$\hat{a}_{p,1}\hat{a}^\dagger_{p,0} + \hat{a}^\dagger_{p,0}\hat{a}_{p,1} = \delta^{p,1}_{p,0} = 0 \Rightarrow \hat{a}_{p,1}\hat{a}^\dagger_{p,0} = -\hat{a}^\dagger_{p,0}\hat{a}_{p,1}$$

The Fermionic Qubit

In order to establish when a given qubit can be described as fermionic, we first have to determine when it satisfies the fermionic statistics from above. This can be done in a similar manner to that shown for bosonic qubits above. Specifically, let us first look at the four previously-established 1-RDM terms.

	$\hat{a}_{p,0}$	$\hat{a}_{p,1}$
$\hat{a}^\dagger_{p,0}$	$\hat{a}^\dagger_{p,0}\hat{a}_{p,0}$	$\hat{a}^\dagger_{p,0}\hat{a}_{p,1}$
$\hat{a}^\dagger_{p,1}$	$\hat{a}^\dagger_{p,1}\hat{a}_{p,0}$	$\hat{a}^\dagger_{p,1}\hat{a}_{p,1}$

These four terms are given by the following four equations and are identical for fermionic

and bosonic creation and annihilation operators.

$$\hat{a}^{\dagger}_{p,0}\hat{a}_{p,1} = \begin{pmatrix} 0 & 1 \\ 0 & 0 \end{pmatrix} = \frac{1}{2}\left(X_p + iY_p\right)$$

$$\hat{a}^{\dagger}_{p,1}\hat{a}_{p,0} = \begin{pmatrix} 0 & 0 \\ 1 & 0 \end{pmatrix} = \frac{1}{2}\left(X_p - iY_p\right)$$

$$\hat{a}^{\dagger}_{p,0}\hat{a}_{p,0} = \begin{pmatrix} 1 & 0 \\ 0 & 0 \end{pmatrix} = \frac{1}{2}\left(\hat{I} + Z_p\right)$$

$$\hat{a}^{\dagger}_{p,1}\hat{a}_{p,1} = \begin{pmatrix} 0 & 0 \\ 0 & 1 \end{pmatrix} = \frac{1}{2}\left(\hat{I} - Z_p\right)$$

Now, let's compare with the terms from the matrix composed as follows.

	$\hat{a}^{\dagger}_{p,0}$	$\hat{a}^{\dagger}_{p,1}$
$\hat{a}_{p,0}$	$\hat{a}_{p,0}\hat{a}^{\dagger}_{p,0}$	$\hat{a}_{p,0}\hat{a}^{\dagger}_{p,1}$
$\hat{a}_{p,1}$	$\hat{a}_{p,1}\hat{a}^{\dagger}_{p,0}$	$\hat{a}_{p,1}\hat{a}^{\dagger}_{p,1}$

These four terms are given by the following four equations.

$$\hat{a}_{p,0}\hat{a}^{\dagger}_{p,1} = \begin{pmatrix} 0 & 0 \\ 1 & 0 \end{pmatrix} = \frac{1}{2}\left(X_p - iY_p\right) = \hat{a}^{\dagger}_{p,1}\hat{a}_{p,0}$$

$$\hat{a}_{p,1}\hat{a}^{\dagger}_{p,0} = \begin{pmatrix} 0 & 1 \\ 0 & 0 \end{pmatrix} = \frac{1}{2}\left(X_p + iY_p\right) = \hat{a}^{\dagger}_{p,0}\hat{a}_{p,1}$$

$$\hat{a}_{p,0}\hat{a}^{\dagger}_{p,0} = \begin{pmatrix} 0 & 0 \\ 0 & 1 \end{pmatrix} = \frac{1}{2}\left(\hat{I} - Z_p\right) = \hat{a}^{\dagger}_{p,1}\hat{a}_{p,1}$$

$$\hat{a}_{p,1}\hat{a}_{p,1}^{\dagger} = \begin{pmatrix} 1 & 0 \\ 0 & 0 \end{pmatrix} = \frac{1}{2}\left(\hat{I} + Z_p\right) = \hat{a}_{p,0}^{\dagger}\hat{a}_{p,0}$$

Note that from the above, $\hat{a}_{p,0}\hat{a}_{p,1}^{\dagger} = \hat{a}_{p,1}^{\dagger}\hat{a}_{p,0}$ and $\hat{a}_{p,1}\hat{a}_{p,0}^{\dagger} = \hat{a}_{p,0}^{\dagger}\hat{a}_{p,1}$; however, for fermionic statistics, $\hat{a}_{p,0}\hat{a}_{p,1}^{\dagger} = -\hat{a}_{p,1}^{\dagger}\hat{a}_{p,0}$ and $\hat{a}_{p,1}\hat{a}_{p,0}^{\dagger} = -\hat{a}_{p,0}^{\dagger}\hat{a}_{p,1}$ must hold. For this to be resolved, we must have $\hat{a}_{p,0}\hat{a}_{p,1}^{\dagger} = \hat{a}_{p,1}^{\dagger}\hat{a}_{p,0} = 0$ or, equivalently,

$$\mathbf{X_p} = \mathbf{Y_p} = \mathbf{0}$$

In order to represent fermions as particles in this interpretation of qubits and satisfy anticommutation relations, the expectation values of $\hat{a}_{p,0}\hat{a}_{p,1}^{\dagger}$ and $\hat{a}_{p,1}^{\dagger}\hat{a}_{p,0}$ must be zero. As such, the one-qubit expectation values of the X and Y Pauli matrices—which can be directly probed on a quantum device—must be zero for all of our preparations. This has been verified through simulation for both preparations—the minimalistic, scanning approach for three qubits described in Equation (10) and the GHZ state preparation described in Equation (13). For the minimalistic, scanning approach, the simulated expectation values for the Pauli X and Y matrices were in the following ranges: [-0.02, 0.02] and [-0.02, 0.02], respectively. The corresponding expectation value for the Pauli Z matrix for these simulations ranged from -0.03 to 1. Similarly, the range for expectation values for the Pauli X and Pauli Y matrices for simulated GHZ states from 3 to 53 qubits was [-0.03, 0.03] and [-0.04, 0.04] respectively. Note that the expectation value of the Pauli Z matrix for these simulations also centered around zero ([-0.03, 0.03]) as the probability of a given qubit being in the $|0\rangle$ or the $|1\rangle$ state were roughly equivalent.

7.7.3 Confidence Intervals for GHZ State Computations

In order to establish that the λ_G values obtained from post-measurement computation for a given preparation on a specific quantum computer are consistent between measurements,

multiple trials were conducted, and confidence intervals for the resultant samples were calculated according to the methodology described in Sec. 7.7.3. First the optimal number of trials must be established for use in computing the confidence intervals. Ideally, the number of trials will be large enough to accurately obtain the average λ_G value for a given computer and number of qubits but small enough to limit computational expense. To determine the ideal sample size, the several sample sizes for the most-complex computation (that for 53-qubits) were used to establish 95% confidence intervals and these computations were compared.

As can be seen in Fig. 7.6—in which the 95% confidence intervals for the λ_G of 53-qubit GHZ state preparation for differing numbers of trials are shown—, the spread of the confidence interval was relatively small—roughly only five percent of the average value for a sample size of thirty. This indicates that the average value associated with this confidence interval can be interpreted as a characteristic λ_G value associated with the computer (Rochester) and the number of qubits ($N = 53$) probed. Additionally, the average value of λ_G does not seem vary to a significant degree between the sample sizes tested even for this relatively sizeable preparation involving the largest available number of qubits. As such, to minimize computational expense, for the determination of other confidence intervals, a sample size of ten will be utilized.

The 95% confidence intervals for the λ_G values for $N = 3, 4, 5$ for simulation and several different quantum devices are shown for the GHZ state in Fig. 7.7 . As can be seen, despite identical preparations and post-measurement analysis, the character of exciton condensation (λ_G) differ to a statistically-significant degree between computers, likely due to the differing errors associated with each device. However, even for Rochester—the device prone to the largest errors as can be seen from Table III—the confidence intervals are relatively small, which indicates that the λ_G for each individual trial does not vary to an extreme degree (at least for sequential experiments).

Determination of Confidence Intervals

Measurement of the signature of exciton condensation (λ_G) on a given quantum device appears to yield results consistent with a normal distribution. Additionally, due to computational expense, the number of trials (n) for the determination of a given λ_G were relatively low ($n \leq 30$), meaning that both the population average (μ) and the population standard deviation (σ) are unknown. Confidence intervals were hence obtained through use of a family of probability distributions called t distributions. When the mean and standard deviation of a given sample of size n is $\overline{x}$ and s, respectively, then a random variable is defined to be

$$T = \frac{\overline{x} - \mu}{x/\sqrt{n}}. \tag{7.24}$$

This random variable has a corresponding t_ν distribution with $\nu = n - 1$ degrees of freedom. Each of these t_ν distributions is bell-shaped, centered at zero, and has a greater spread than the normal z distribution. As the number of trials (and hence degrees of freedom) increases, the spread of the t_ν distribution decreases to the point that when $\nu \to \infty$, the t_∞ distribution approaches the normal z distribution. If $t_{\alpha,\nu}$ is defined to be the number on the measurement axis of the t_ν distribution to the right of which the area under the curve is α, then the $100(1-\alpha)\%$ confidence interval for the population average (μ) is given by

$$\left(\overline{x} - t_{\alpha/2,\mu} \cdot \frac{s}{\sqrt{n}}, \overline{x} + t_{\alpha/2,\mu} \cdot \frac{s}{\sqrt{n}}\right) \tag{7.25}$$

or, equivalently $\overline{x} \pm t_{\alpha/2,\mu} \cdot \frac{s}{\sqrt{n}}$ [302].

7.7.4 Simulation and Experimentation for Various Test Cases

In order to solidify intuition regarding our methodology, we have supplied various test cases in the following sections. Specifically, we supply information regarding a state with no

entanglement ($|+\rangle^{\otimes N}$), a statistical mixture ($\frac{1}{2}|0\rangle^{\otimes N}\langle 0|^{\otimes N} + \frac{1}{2}|1\rangle^{\otimes N}\langle 1|^{\otimes N}$), $\frac{N}{2}$ independent two-qubit Bell states in overall N-qubit systems, and—finally—a state demonstrating islands of condensation through construction of $\frac{N}{6}$ independent six-qubit GHZ states in overall N-qubit systems. In the first three examples, we don't expect exciton condensation to be observed as—although the two orbitals corresponding to each qubit i (orbitals $i, 0$ and $i, 1$) are particle-hole paired—these preparations do not entangle the qubits. For the final example of $\frac{N}{6}$ independent six-qubit GHZ states, we expect there to be $\frac{N}{6}$ large eigenvalues of the particle-hole reduced density matrix (RDM)—i.e. $\frac{N}{6}$ λ values exceeding one—as $\frac{N}{6}$ entangled subsystems of qubits are prepared.

No Entanglement: $|+\rangle^{\otimes N}$

The $|+\rangle^{\otimes N}$ state for an N-qubit system was prepared by transforming each qubit—initially in the $|0\rangle$ state—to $|+\rangle = \frac{1}{\sqrt{2}}[|0\rangle + |1\rangle]$ through the application of a Hadamard gate. This process is described by

$$|+\rangle^{\otimes N} = H_{N-1} \cdots H_1 H_0 |0\rangle^{\otimes N} \tag{7.26}$$

where H_i is a Hadamard gate on the i^{th} qubit and $|0\rangle^{\otimes N}$ represents the initial all-zero state. The results for the $|+\rangle^{\otimes N}$ state for simulation and experimentation on IBM's Quantum Experience Yorktown (ibmqx2) device for $N = 3, 4, 5$ are shown in Table 7.2. As was expected from the lack of qubit entanglement of the preparation of this state, no eigenvalues significantly exceeding one were observed.

N	Simulation	Yorktown
3	1.00	1.02
4	1.01	1.02
5	1.01	1.02

Table 7.2: Simulated and non-mitigated, experimental λ_G values for the $|+\rangle^{\otimes N}$ state where $N = 3, 4$, and 5 qubits. Experiments were conducted on IBM's Quantum Experience Yorktown (ibmqx2) device.

Statistical Mixture: $\frac{1}{2}|0\rangle^{\otimes N}\langle 0|^{\otimes N} + \frac{1}{2}|1\rangle^{\otimes N}\langle 1|^{\otimes N}$

The statistical mixture of equal proportions of the $|0\rangle^{\otimes N}\langle 0|^{\otimes N}$ and $|1\rangle^{\otimes N}\langle 1|^{\otimes N}$ states were probed by first constructing the modified particle-hole RDM ($^2\tilde{G}$) matrix for the $|0\rangle^{\otimes N}$ initial state and the $|1\rangle^{\otimes N}$ state—prepared by

$$|1\rangle^{\otimes N} = X_{N-1}\cdots X_1 X_0 |0\rangle^{\otimes N} \tag{7.27}$$

where X_i is the X-gate for the i^{th} qubit—, adding these RDM scaled by a factor of $\frac{1}{2}$, and obtaining the eigenvalues of the resultant average modified particle-hole RDM. The results for the these statistical mixtures for simulation and experimentation on IBM's Quantum Experience Yorktown (ibmqx2) device for $N = 3, 4, 5$ are shown in Table 7.3. As was expected from the lack of qubit entanglement of the preparation of this state, no eigenvalues significantly exceeding one were observed.

N	Simulation	Yorktown
3	0.51	0.55
4	0.51	0.55
5	0.51	0.55

Table 7.3: Simulated and non-mitigated, experimental λ_G values for the $\frac{1}{2}|0\rangle^{\otimes N}\langle 0|^{\otimes N} + \frac{1}{2}|1\rangle^{\otimes N}\langle 1|^{\otimes N}$ state where $N = 3, 4$, and 5 qubits. Experiments were conducted on IBM's Quantum Experience Yorktown (ibmqx2) device.

$\frac{N}{2}$ Independent Two-Qubit Bell States in Overall N-Qubit Systems

Two different Bell states were used to construct overall N-qubit systems consisting of $\frac{N}{2}$ independent two-qubit Bell states: specifically, $|\phi^+\rangle = \frac{1}{\sqrt{2}}\left[|00\rangle + |11\rangle\right]$ and $|\psi^+\rangle = \frac{1}{\sqrt{2}}\left[|01\rangle + |10\rangle\right]$. These two-qubit Bell states can be constructed between qubits i and j through use of the following preparations:

$$|\phi^+\rangle = C_i^j H_i |00\rangle \tag{7.28}$$

and

$$|\psi^+\rangle = X_j|\phi^+\rangle = X_j C_i^j H_i|00\rangle \tag{7.29}$$

where C_i^j is a CNOT gate with control qubit i and target qubit j. For each (even) number of qubits, N, three systems were constructed: one composed of $\frac{N}{2}$ independent $|\phi^+\rangle$ states, one composed of $\frac{N}{2}$ independent $|\psi^+\rangle$ states, and one composed of alternating $|\phi^+\rangle$ and $|\psi^+\rangle$ states in the following order $|\phi^+\psi^+\phi^+\psi^+\phi^+\cdots\rangle$. These states were constructed by applying the preparations given in Eqs. (7.28) and (7.29) to the pairs of qubits composing the overall N-qubit systems. For example, for the $N = 6$ $|\phi^+\psi^+\phi^+\rangle$ system, Eq. (7.28) was applied to qubits-pairs $0/1$ and $4/5$, and Eq. (7.29) was applied to the $2/3$ qubit pair. The results for the these composite states for simulation and experimentation on IBM's Quantum Experience Melbourne (ibmq_16_melbourne) device for $N = 4, 6, 8, 10$ are shown in Table 7.4. For the most part, the results align with our intuition in that only one experiment demonstrated an eigenvalue significantly above one. This one outlier—the $N = 10$ $|\psi^+\psi^+\psi^+\psi^+\psi^+\rangle$ with a λ_G of 1.40—is likely a result of error disrupting the preparation of the initial state.

N	State	Simulation	Melbourne
4	$\|\phi^+\phi^+\rangle$	1.02	0.94
4	$\|\psi^+\psi^+\rangle$	1.02	0.94
4	$\|\phi^+\psi^+\rangle$	1.02	0.95
6	$\|\phi^+\phi^+\phi^+\rangle$	1.03	0.93
6	$\|\psi^+\psi^+\psi^+\rangle$	1.02	0.95
6	$\|\phi^+\psi^+\phi^+\rangle$	1.02	0.96
8	$\|\phi^+\phi^+\phi^+\phi^+\rangle$	1.03	0.98
8	$\|\psi^+\psi^+\psi^+\psi^+\rangle$	1.03	0.97
8	$\|\phi^+\psi^+\phi^+\psi^+\rangle$	1.03	0.98
10	$\|\phi^+\phi^+\phi^+\phi^+\phi^+\rangle$	1.04	1.09
10	$\|\psi^+\psi^+\psi^+\psi^+\psi^+\rangle$	1.04	1.40
10	$\|\phi^+\psi^+\phi^+\psi^+\phi^+\rangle$	1.03	1.05

Table 7.4: Simulated and non-mitigated, experimental λ_G values for N-qubit systems composed of $\frac{N}{2}$ independent $|\phi^+\rangle$ and $|\psi^+\rangle$ Bell states where $N = 4, 6, 8$, and 10 qubits. Experiments were conducted on IBM's Quantum Experience Melbourne (ibmq_16_melbourne) device.

$\frac{N}{6}$ Independent Six-Qubit GHZ States in Overall N-Qubit Systems

A six qubit GHZ state on qubits i, j, k, l, p, and q can be prepared using the following gate sequence:

$$C_p^q C_l^p C_k^l C_j^k C_i^j H_i. \tag{7.30}$$

As such, any N-qubit system such that N is a multiple of six can be prepared to have $\frac{N}{6}$ independent GHZ states by independently applying Eq. (7.30) to $\frac{N}{6}$ distinct subsets of qubits. For example, for $N = 18$, three distinct six-qubit GHZ states can be constructed by applying Eq. (7.30) to qubits $0-5$, $6-11$, and $12-17$ independently. This procedure was conducted for $N = 6, 12, 18$, and 24 and was expected to produce one, two, three, and four islands of exciton condensation, respectively, as those are the numbers of independent entangled systems of qubits are prepared in the overall system of N-qubits. The results for the these composite states for simulation and experimentation on IBM's Quantum Experience Rochester (ibmq_rochester) device for $N = 6, 12, 18, 24$ are shown in Table 7.5. As can be seen, for the simulated computations, the number of islands of condensation was consistent with intuition. Additionally, for $N = 12$ and $N = 24$ qubit experiments, multiple eigenvalues distinctly above one were observed, indicating that—even with the error inherent on the "noisy" real-world device employed—multiple large eigenvalues of the particle-hole RDM is consistent with systems composed of distinct, entangled subsystems.

N	# Islands Expected	Simulation	Rochester
6	1	3.00	1.69
12	2	2.97, 3.03	1.16, 1.21
18	3	2.50, 3.00, 3.51	1.20
24	4	2.50, 2.97, 3.03, 3.51	1.15, 1.80, 1.97

Table 7.5: Simulated and non-mitigated, experimental eigenvalues of the ${}^2\tilde{G}$ which exceed one for N-qubit systems composed of $\frac{N}{6}$ independent 6-qubit GHZ States where $N = 6, 12, 18$, and 24 qubits. Experiments were conducted on IBM's Quantum Experience Rochester (ibmq_rochester) device.

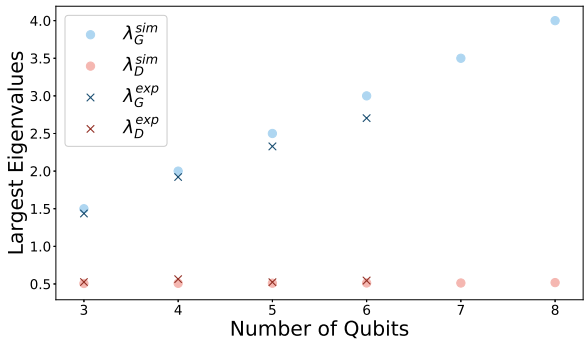

(a) Mitigated

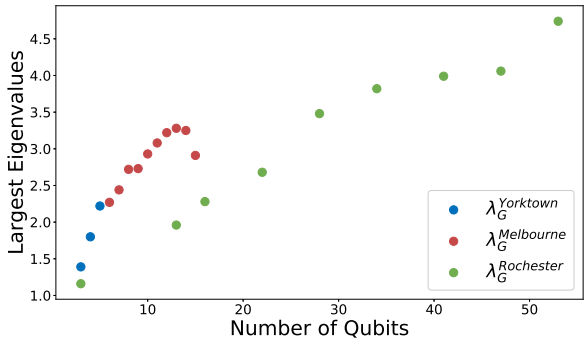

(b) All λ_G

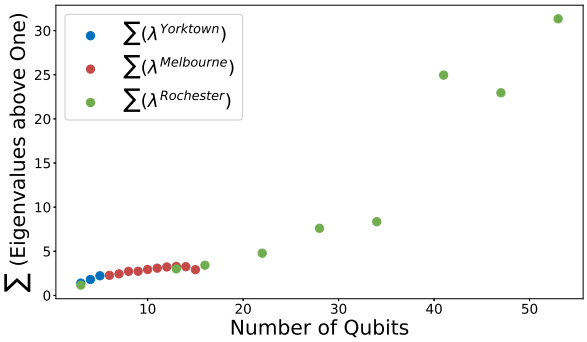

(c) Sum of λs

Figure 7.4: Plots showing (a) the largest eigenvalue of the ${}^2\tilde{G}$ matrix (blue) and the ${}^2D$ matrix(red) for simulated (dots) and all mitigated, experimental ($\times$'s) calculations, (b) the largest eigenvalue of the unmitigated, experimental ${}^2\tilde{G}$ matrix, and (c) the sum of all eigenvalues of the unmitigated, experimental ${}^2\tilde{G}$ matrix demonstrating exciton condensation ($\lambda > 1$) for experiments of N qubits on the Yorktown 5-qubits IBM Quantum Experience device (blue), the Melbourne 15-qubit IBM Quantum Experience device (red), and the Rochester 53-qubit IBM Quantum Experience device (green).

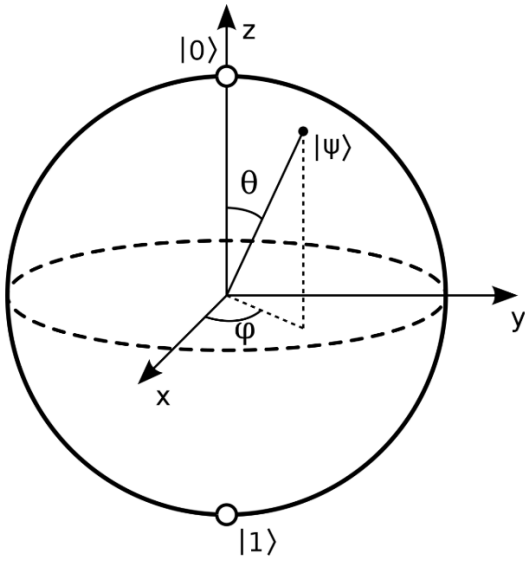

Figure 7.5: A Bloch sphere which represents a qubit is shown.

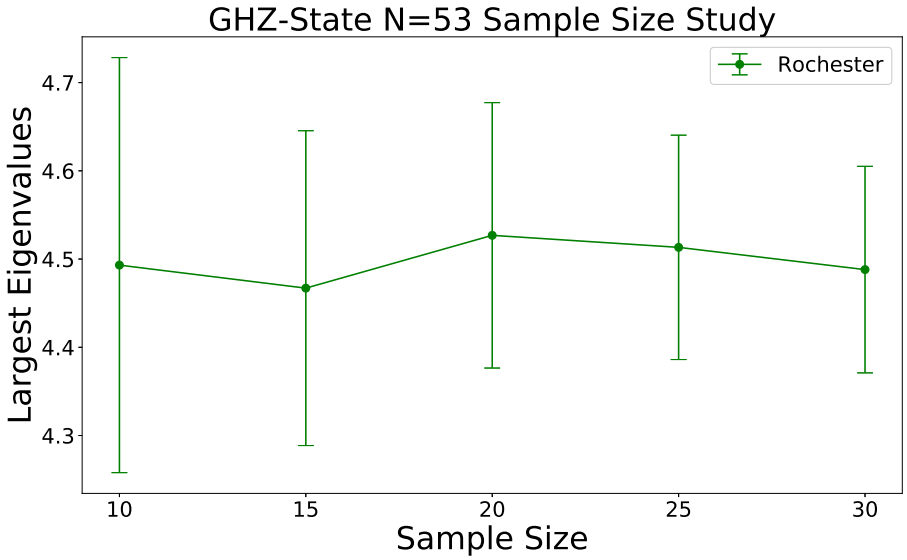

Figure 7.6: The 95% confidence intervals for computed 53-qubit λ_G values obtained from the Rochester 53-qubit IBM Quantum Experience device for the following sample sizes: n=10, 15, 20, 25, 30. Confidence intervals are calculated according to the methodology described in Sec. 7.7.3.

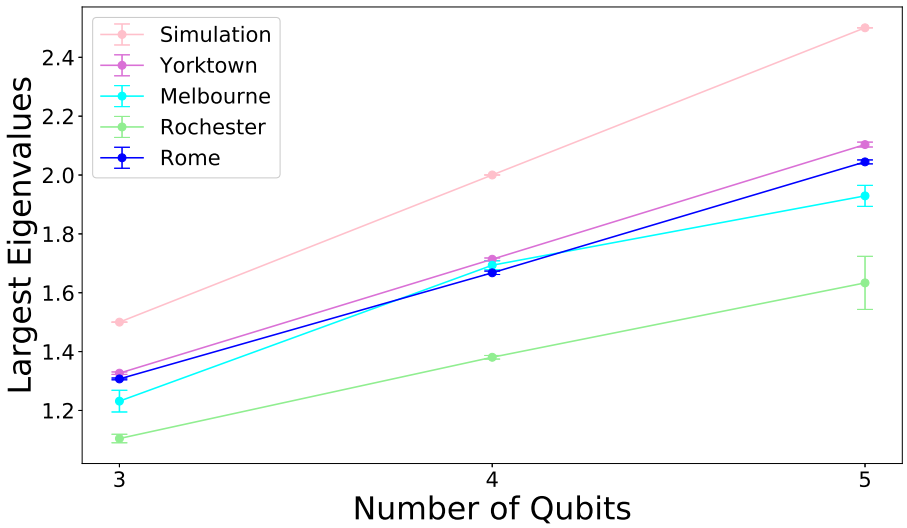

Figure 7.7: The largest eigenvalue of the unmitigated, experimental ${}^2\tilde{G}$ matrix for experiments of N qubits for the GHZ State are shown for simulations (pink) and experiments on the Yorktown 5-qubits IBM Quantum Experience device (violet), the Melbourne 15-qubit IBM Quantum Experience device (teal), the Rochester 53-qubit IBM Quantum Experience device (lime green), and the Rome 5-qubit IBM Quantum Experience device (blue). Confidence intervals are calculated according to the methodology described in Sec. 7.7.3.

CHAPTER 8

QUBIT CONDENSATION FOR ASSESSING EFFICACY OF MOLECULAR SIMULATION ON QUANTUM COMPUTERS

Material from: Sager-Smith, L. M. & Mazziotti, D. A., Qubit condensation for assessing efficacy of molecular simulation on quantum computers. Submitted.

8.1 Chapter Synopsis

Quantum computers may demonstrate significant advantage over classical devices as they are able to exploit a purely quantum-mechanical phenomenon known as entanglement in which a single quantum state simultaneously populates two-or-more classical configurations. However, due to environmental noise and device errors, elaborate quantum entanglement can be difficult to prepare on present-day quantum computers. In this paper, we introduce a metric based on the condensation of qubits to assess the ability of a quantum device to simulate many-electron systems. Qubit condensation occurs when the qubits on a quantum computer condense into a single, highly-correlated, particle-hole state. While conventional metrics like gate errors and quantum volume do not directly target entanglement, the qubit-condensation metric measures the quantum computer's ability to generate an entangled state that achieves non-classical long-range order across the device. To demonstrate, we prepare qubit condensations on various quantum devices and probe the degree to which qubit condensation is realized via post-measurement analysis. We show that the predicted ranking of the quantum devices is consistent with the errors obtained from molecular simulations of H_2 using a contracted quantum eigensolver.

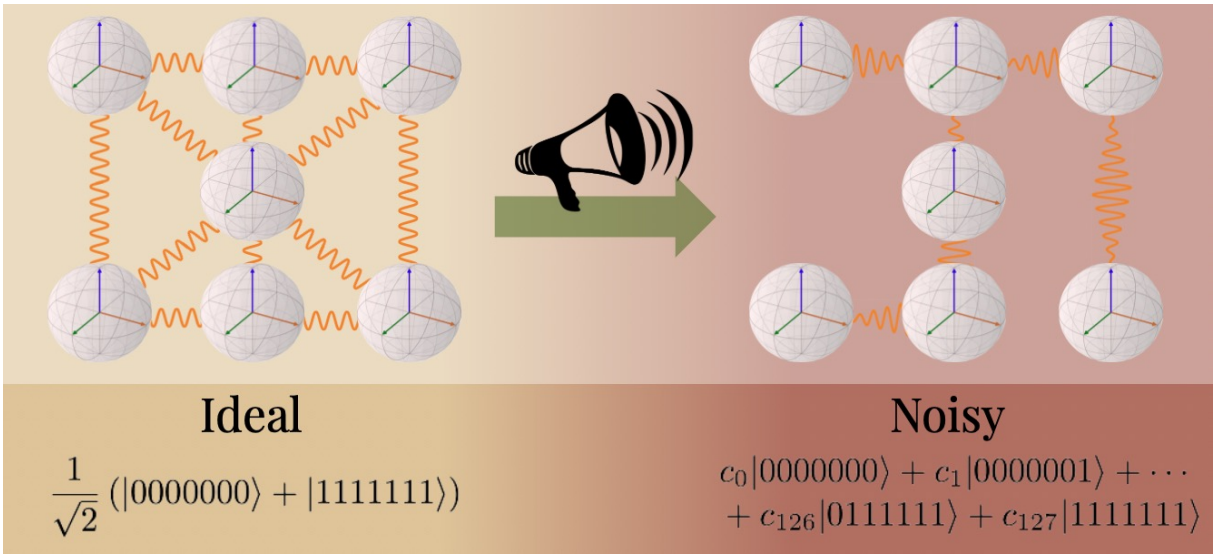

Figure 8.1: A schematic demonstrating noise in a NISQ device disrupting the correlations between a system of seven qubits prepared in the maximally-entangled GHZ state.

8.2 Introduction

Quantum devices have recently emerged as potentially powerful tools for the demonstration of system-wide entanglement and long-range order [5, 6, 266, 303–309], a task that can be difficult or expensive in classic computations. With an ability to simulate large degrees of quantum entanglement—important for the modelling of many chemical processes including those involving transition-metal complexes, energetic degeneracies, solid-state materials, and other systems [310–312]—, quantum devices with quantum chemical algorithms are expected to compete with classical computers and methodologies for chemical computations [313–316].

However, algorithms for the accurate prediction of many-electron molecular energies and properties rely upon the ability of near-term intermediate-scale quantum (NISQ) devices to accurately accomplish state preparations and measurements [254, 307], a requirement whose successful implementation can vary dramatically from device to device. Current NISQ computers are prone to experiencing environmental noise and device errors that disrupt long range order (see Fig. 8.1), often resulting in fragmented islands of correlated qubits instead of system-wide correlation [5], which can make simulating molecular systems difficult.

In this work, we introduce a novel metric for assessing the ability of quantum computers for modelling many-electron molecular systems. By preparing a maximally-correlated qubit condensate state—a state where qubits on a quantum device condense into a single, highly-correlated, particle-hole state—, we directly probe the extent to which a given quantum device can achieve system-wide entanglement and long-range order. Because the modeling of quantum entanglement is what ultimately may separate quantum computers from classical computers, this ability provides a metric for the efficacy of various NISQ devices for the preparation of many-electron quantum systems that may be challenging for classical computers.

Currently, either component-level qubit and gate errors [258, 317, 318] or system-level metrics such as quantum volume (QV) [319, 320] are seen as the conventional means of comparing various quantum devices against each other. While component-level metrics are useful while building quantum systems, they often fail to capture the behavior and errors of large quantum circuits on a given device [321–323]. Thus, a system-level measure such as our metric or QV is desirable. Unlike quantum volume, however, our qubit condensation metric is a specific measure of how well a quantum device can prepare a highly-correlated state, making it a better predictive tool for comparing quantum devices for molecular simulations.

To test qubit condensation as a metric for many-electron quantum simulations, we compute the molecular energy of dihydrogen without error mitigation on several quantum devices using a contracted quantum eigensolver. The predicted ranking of the quantum devices from our qubit condensation analysis—which differs from the order of quantum volumes—is consistent with the errors obtained from the molecular simulation of H_2. Our qubit condensate metric thus directly allows us to compare the accuracy with which NISQ devices are expected to treat many-electron quantum systems, which may aide researchers in the selection of the appropriate quantum device for quantum chemistry applications. Additionally, our metric may provide a measure along which future devices can be optimized in order to improve

their ability to demonstrate quantum long-range order.

8.3 Theory

A measure of the maximal quantum long-range order for the GHZ states that we prepare in this study is the signature of the condensation of particle-hole pairs as the maximal entanglement of the GHZ state corresponds to the maximal entanglement of particle-hole pairs [5]. As such, we first detail the signature of such a qubit condensation, which will be used as a measure of the correlation for the quantum states prepared throughout this study. Further, the quantum solver we utilize to determine uncorrected molecular energies is the quantum anti-Hermitian contracted Schrödinger equation (qACSE) solver; as such, we additionally provide details pertaining to the qACSE.

8.3.1 Signature of Qubit Condensation.

Bose-Einstein condensation occurs when—at sufficiently low temperatures—multiple bosons all condense into a single quantum state [113, 114] and results in superfluidity—i.e., the frictionless flow of the constituent bosons [97, 115]. A computational signature of this type of condensation phenomena is a large eigenvalue in the one-boson reduced density matrix [119] given by

$$^1D^i_j = \langle \Psi | \hat{b}^\dagger_i \hat{b}_j | \Psi \rangle \tag{8.1}$$

where $\hat{b}^\dagger_i$ and $\hat{b}_i$ correspond to creation and annihilation operators for the i^{th} bosonic orbital and where $|\Psi\rangle$ is the full N-boson wave function in a finite basis set. This large eigenvalue corresponds to the largest orbital occupation of a given quantum state such that any eigenvalue above one indicates the beginnings of condensation behavior

As briefly described above, the maximal entanglement of the GHZ states we prepare in this study corresponds to the maximal degree of particle-hole condensation when we

define each qubit to be a two-orbital system composed of a lower- and a higher-energy level corresponding to the $|0\rangle$ and $|1\rangle$ states, respectively. The particles and holes are fermions and thus must obey the Pauli exclusion principle such that they are unable to condense into a single orbital [129]. However, particle-hole pairs are quasi-bosonic and hence can condense into a single particle-hole quantum state which we call a qubit condensate [106, 107].

Similar to the signature of a bosonic condensate being a large eigenvalue of a one-boson RDM, the computational signature of a particle-hole qubit condensate—denoted as λ_G—is a large eigenvalue of the modified particle-hole reduced density matrix given by [148, 155, 156]

$$ {}^2\tilde{G}^{i,j}_{k,l} = {}^2G^{i,j}_{k,l} - {}^1D^i_j\,{}^1D^l_k \tag{8.2} $$

where

$$ {}^2\tilde{G}^{i,j}_{k,l} = \langle\Psi|\hat{a}^\dagger_i\hat{a}_j\hat{a}^\dagger_l\hat{a}_k|\Psi\rangle, \tag{8.3} $$

is the unmodified particle-hole RDM, $\hat{a}^\dagger_i$ and $\hat{a}_i$ correspond to fermionic creation and annihilation operators for the i^{th} fermionic orbital, ${}^1D^i_j$ is an element of the one-fermion RDM corresponding to indices i and j, and $|\Psi\rangle$ is the full N-fermion wave function in a finite basis set. Note that the modification to the particle-hole RDM (${}^2G$) is done in order to remove an extraneous large eigenvalue corresponding to the ground state to ground state transition. Explicitly, a large eigenvalue in the modified particle-hole matrix is a manifestation of the long range order in this matrix and is a measure of entanglement.

For an N-fermion—and hence N-qubit—system, the largest possible signature of condensation is given by

$$ \lambda_G = \frac{N}{2}. \tag{8.4} $$

The GHZ state is expected to demonstrate this maximal degree of condensation on an ideal quantum device [5], and any deviation from this behavior would be due to errors on a given quantum device on which the state is prepared.

8.3.2 Quantum Solver of the Anti-Hermitian Contracted Schrödinger Equation.

Recently, Smart and Mazziotti [267] have introduced a novel quantum eigensolver that optimizes the lowest energy eigenvalue by solving the contracted Schrödinger equation (CSE)—which corresponds to the projection of the Schrödinger equation onto two-particle transitions from the wave function and is given by [75, 78, 79, 84, 324–326]

$$\langle \Psi | \hat{a}_i^\dagger \hat{a}_j^\dagger \hat{a}_l \hat{a}_k \hat{H} | \Psi \rangle = E \; {}^2D_{k,l}^{i,j} \tag{8.5}$$

where ${}^2D$ is the two-particle reduced density matrices, $\hat{a}_i^\dagger$ and $\hat{a}_i$ are, again, fermionic creation and annihilation operators corresponding to the i^{th} orbital, Ψ is the N-electron wave function, and $\hat{H}$ is the system Hamiltonian operator given by

$$\hat{H} = \sum_{p,q,s,t} {}^2K_{s,t}^{p,q} \hat{a}_p^\dagger \hat{a}_q^\dagger \hat{a}_t \hat{a}_s \tag{8.6}$$

where ${}^2K$ is the reduced Hamiltonian matrix comprised of one- and two-electron integrals. Specifically, this quantum eigensolver utilizes the anti-Hermitian part of the CSE—termed the anti-Hermitian CSE or ACSE and is given by [48, 89, 90, 327–331]

$$\langle \Psi | \left[\hat{a}_i^\dagger \hat{a}_j^\dagger \hat{a}_l \hat{a}_k, \hat{H} \right] | \Psi \rangle \tag{8.7}$$

—which depends upon both the 2-RDM and 3-RDM has been utilized to solve for energies and properties of ground and excited state many-electron systems [269, 332–338] with the solution of the ACSE being closely related to the variational minimization of energy with respect to a series of two-body unitary transformations [89, 327, 328]. In fact, the gradient of energy for the two-body unitary transformations is equivalent to the residual of the ACSE, which implies that the residual of the ACSE vanishes if and only if the energy gradient

vanishes. As such, the ACSE can be utilized to iteratively apply a product of two-body unitary transformations on a reference wave function, which defines the quantum ACSE algorithm presented in Refs. [267] and [269]. Specifically, in this framework, the density matrix of the $(n+1)^{th}$ iteration (${}^2D_{n+1}$) is given by

$$ {}^2D^{pq;st}_{n+1} = \langle \Psi_n | e^{-\epsilon_n \hat{A}_n} \hat{a}^\dagger_p \hat{a}^\dagger_q \hat{a}_t \hat{a}_s e^{\epsilon_n \hat{A}_n} | \Psi_n \rangle \tag{8.8} $$

where $|\Psi_n\rangle$ is the wave function that corresponds to the n^{th} iteration with the initial wave function corresponding to the Hartree Fock state $|\Psi_0\rangle$, where ϵ_n is an infinitesimal step, and where $\hat{A}_n$ is an anti-Hermitian operator that can be set to the residual of the ACSE [267, 328] from Eq. (8.7) such that the residual is related to the energy gradient according to

$$ \langle \Psi_n | \left[\hat{a}^\dagger_i \hat{a}^\dagger_j \hat{a}_l \hat{a}_k, \hat{H} \right] | \Psi_n \rangle \tag{8.9} $$

Thus, the choice of $\hat{A}_n$ chooses a search direction that maximizes the change in energy for small ϵ_n. Note that in our implementation of the qACSE, we generate all 2-RDMs on the quantum computer and compute $\hat{A}_n$ by classically reconstructing the 3-RDM with $O(r^6)$ cost where r is the rank of the one-electron basis set. A potentially more-efficient manner for the direct computation of $\hat{A}_n$ on a quantum device has been introduced [267], however, this approach is not utilized for this study.

Note that while many error mitigation techniques have been utilized for the qACSE approach—such as those presented in Ref. [269]—, as this study proposes an approach for comparing NISQ quantum hardware's current utility for computation of many-electron systems rather than aiming to determine absolute energies of such systems, error mitigation techniques are not performed—allowing for the more-direct comparison of each device against all others.

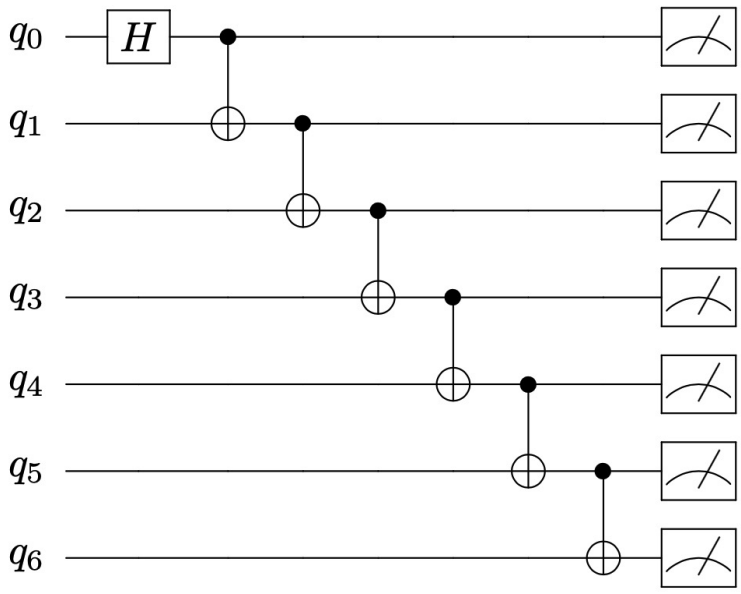

Figure 8.2: A schematic demonstrating the quantum state preparation that yields the seven-qubit GHZ state described by Eq. (8.10) with $N = 7$—where H represents the Hadamard gate and where two-qubit CNOT gates are represented such that the control qubit is specified by a dot connected to a target qubit represented by $\bigoplus$.

8.4 Results

To demonstrate the accuracy with which specific quantum computers can construct highly-correlated quantum states, we first prepare the "maximally-entangled" [287] N-qubit GHZ states (which are equivalently referred to as the Schrödinger's cat states) described by

$$|\Psi\rangle = \frac{1}{\sqrt{2}}\left(|0\rangle^{\otimes N} + |1\rangle^{\otimes N}\right) \tag{8.10}$$

—where $|i\rangle^{\otimes N}$ represents the tensor product of the state $|i\rangle$ for qubits $q[0]$ through $q[N-1]$—on several of IBM's seven-qubit quantum devices. The quantum state preparation for a seven-qubit GHZ state is shown in Fig. 8.2, and details on this quantum state preparation are presented in the Experimental.

As demonstrated in Ref. [5], a characteristic of the GHZ state is the maximal entanglement of particle-hole pairs when each qubit is interpreted as as a site consisting of one

particle and two orbitals. Hence, an N-qubit GHZ state should demonstrate qubit condensation, namely a large eigenvalue of the modified particle-hole reduced density matrix (${}^2\tilde{G}$) given by $N/2$ where N is the number of qubits and hence the number of particles. Any deviation from this expected value on a real quantum device, then, must be the result of errors in preparing and measuring the GHZ state on a given system. Therefore, measurement of the signature of qubit condensation for an N-qubit GHZ state on a given quantum device can serve as a measurement of the accuracy of that quantum device for preparing a highly-correlated quantum state—the types of quantum states that will be required when utilizing quantum devices to compute energies and properties of highly-correlated molecular systems.

To this end, we have prepared GHZ states composed of three to seven qubits on several of IBM's seven-qubit quantum devices—specifically, ibm_lagos (QV=32), ibm_perth (QV=32), and ibmq_jakarta (QV=16). As can be seen in Figure 8.3, the graph of the signature of qubit condensation (λ_G) versus the number of qubits (N) for an ideal quantum device—such as IBM's QASM simulator that models a "perfect" quantum computer using classically-computed probabilities—should be a line nearly-exactly described by Equation (8.4) (i.e., with slope $m = 0.5$) with any deviation resulting from sampling errors that approach zero as the number of samples (or "shots") is increased.

The real devices, however, do not exhibit such ideal behavior. While the plots of λ_G vs. N for real systems still appear linear, their slopes deviate from the expected value of 0.5 with this deviation demonstrating an overall decrease in the signature in qubit condensation for larger numbers of qubits. The signature of qubit condensation for a three-qubit subsystem as well as the slope associated with each real quantum system are shown in Table 8.1. The λ_G value for the three-qubit subsystem—with three being the smallest number of qubits capable of demonstrating condensation behavior (i.e., $\lambda_G > 1$)—indicates that all three real-world quantum devices are capable of supporting qubit condensation—a highly-correlated

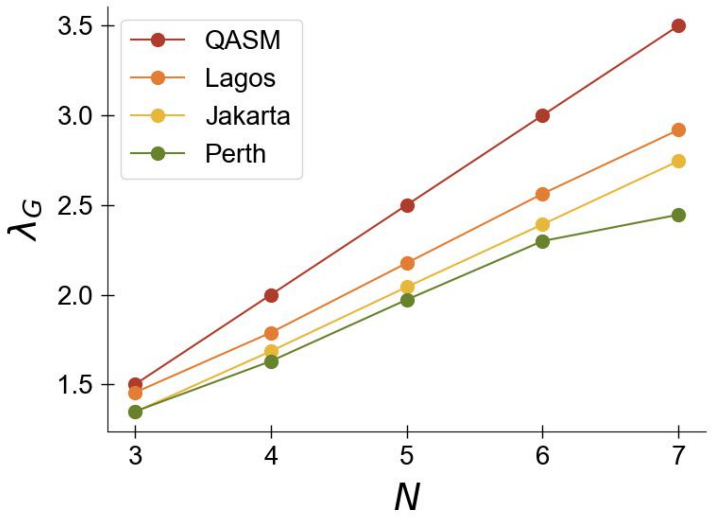

Figure 8.3: The graph of the signature of qubit condensation (λ_G) for an N-qubit GHZ state versus the number of qubits (N) for a QASM simulator (red), ibm_lagos (orange), ibmq_jakarta (yellow), and ibm_perth (green). The associated slopes as well as the λ_G corresponding to the three qubit (i.e., $N = 3$) GHZ state for each device in this plot is specified in Table 8.1.

phenomena—at small numbers of qubits, although the difference in the specific values does signify that even at this small number of qubits certain devices demonstrate more noise than others. Specifically, Lagos best matches the expected value of $3/2 = 1.5$ with Jakarta and Perth showing much more notable deviations. On the other hand, this metric is specific to the three-qubit subsystem, does not sufficiently differentiate Jakarta and Perth, and the relative values between devices may not accurately reflect errors across the full seven-qubit quantum computers.

However, the slope of the lines for the λ_G vs. N plots for each device gives a metric for how the degree of the highly-correlated qubit condensation phenomena in the N-qubit GHZ state scales as N increases—with a slope approaching the ideal value of 0.5 indicating excellent preparation of larger, highly-entangled states and slopes significantly diminished from 0.5 indicating large degrees of device error for the preparation of correlated states. As this metric corresponds to the preservation of correlation, we propose to utilize it to diagnose

Device	$\mathbf{m}\,(\lambda_{\mathbf{G}})$	$\lambda_{\mathbf{G}}^{(\mathbf{N=3})}$	$\mathbf{m}\,(\mathbf{S_e})$	QV
QASM Simulator	0.500	1.500	0.000	—
Lagos	0.370	1.455	0.357	32
Jakarta	0.351	1.346	0.405	16
Perth	0.286	1.349	0.527	32

Table 8.1: A table summarizing the slope of λ_G vs. N for an N-qubit GHZ state on a simulator and three experimental devices as well as the λ_G value for a three-qubit GHZ state on each device, the slope of Shannon entropy versus N for an N-qubit GHZ state on each device, and the quantum volume of each device.

the relative efficacy of NISQ devices for the many-electron quantum calculations that heavily depend upon the accurate modeling of high degrees of correlation. As can be seen from Table 8.1, using this metric, one would predict that Lagos (with $m = 0.370$) would support the most-accurate quantum chemical calculations followed by Jakarta ($m = 0.351$) with Perth ($m = 0.286$) being the least accurate by a significant margin.

To verify these predictions for the relative ability of different quantum devices to support the accurate computation of energies of many-electron quantum systems, we compare the non-error mitigated calculation of the energy of a multi-electron quantum system across all devices. Explicityly, we utilize the quantum anti-Hermitian Contracted Schrödinger Equation (qACSE) solver introduced in Ref. [267] to compute the ground state energy of dihydrogen (H_2) with an internuclear distance of 1 Åand utilizing the minimal Slater-type orbital STO-6G basis on each quantum system of interest. Note that on the quantum computer, the dihydrogen molecule is represented in the qACSE algorithm by a two-qubit compact mapping that can be compressed to a one-qubit mapping through the application of appropriate tapering (as described in Ref. [269]).

As shown in Fig. 8.4, both one-qubit and two-qubit mappings were utilized to compute the energy of dihydrogen on each of the three seven-qubit quantum devices where Fig. 8.4 displays the energy at each iteration in the solution of the qACSE. No attempts were made at error mitigation as we aren't interested in accurately determining the energy of dihydrogen

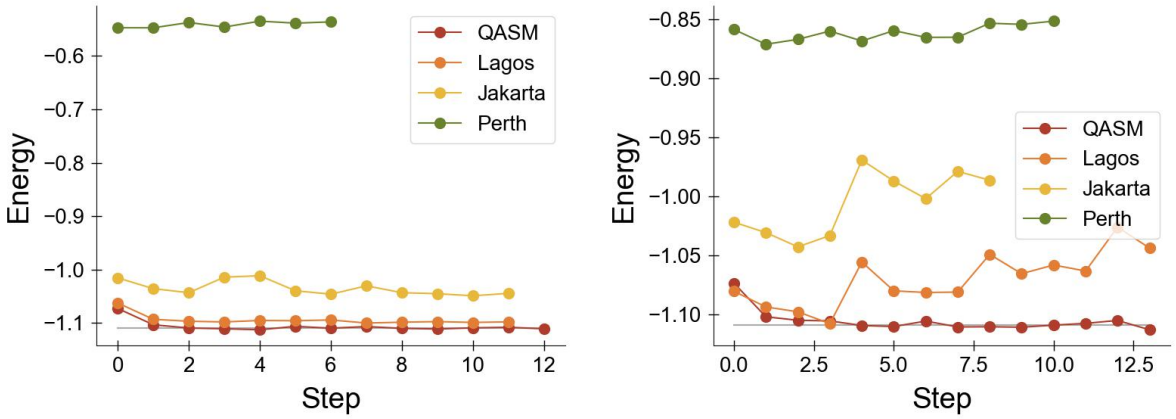

(a) 1Q Non-Shifted

(b) 2Q Non-Shifted

Figure 8.4: For H_2 with an internuclear distance of 1 Å, the energy at each iteration in the solution of the ACSE utilizing the STO-6G basis on a QASM simulator (red), ibm_lagos (orange), ibmq_jakarta (yellow), and ibm_perth (green) are shown for (a) the one-qubit and two-qubit calculations where the grey line is the expected FCI energy and where the shift corresponds to correcting the zeroth iteration to the Hartree Fock energy and shifting the entire trajectory by this correction.

but rather we are interested in using the deviations from the expected energy to confirm the our predictions of which NISQ devices would be better for accurate calculations of molecular systems. For both the one-qubit (1Q, Fig. 8.4(a)) and two-qubit (2Q, Fig. 8.4(b))—where QASM is a simulator that demonstrates ideal behavior and where the grey line represents the exact FCI energy for H_2—, it is clear that Lagos supports the most-accurate computation of H_2's energy followed by Jakarta with Perth being a distant third—which is exactly what we predicted with our proposed metric.

Finally, we compare our metric for determination of appropriate NISQ devices for the computation of many-electron chemical systems against two previously-established metrics for determination of the capabilities of quantum systems. The first metric, quantum volume [319, 320], was introduced by IBM in Ref. [320] to compare the capabilities of NISQ devices, and the quantum volumes for the devices employed in this study are provided in Table 8.1. The quantum volume gives a quantitative measure to the largest random circuit of equal width and depth that the computer successfully implements such that systems with high fi-

delity, high connectivity, and a high number of possible gates have higher quantum volumes. However, many devices which may behave in vastly different ways have the same quantum volume—making this metric only somewhat useful for differentiating between devices. Further, it is not clear that QV directly applies to the ability of a given device to support high degrees of correlation as needed for molecular simulation. In fact, in this instance, using quantum volume as a metric one would predict Perth to be better-able to compute the energy of dihydrogen relative to Jakarta, which is not consistent with the results in Fig. 8.4. Hence, our metric is better able to predict the behavior of NISQ devices in terms of viability for many-electron calculations than quantum volume.

The second metric of interest is the one based on the slope of the plot of Shannon entropy versus number of qubits for N-qubit GHZ states proposed by Hunt et. al. in Ref. [339]. As can be seen in Fig. 8.5, we have constructed figures of Shannon entropy (S_e) versus number of qubits (N) for each quantum device employed in this study. (Specifics regarding the calculation of Shannon entropy are included in the Experimental.) We then obtained the slopes of these plots, which are given in Table 8.1 with the extent to which slopes deviate from the expected value of zero being a possible metric for a quantum computer's error. Using this criteria, then, one would expect Lagos to be the most-accurate quantum system, followed by Jakarta and then Perth—which agrees with both the qACSE results and additionally the metric we propose. While our qualitative predictions agree with those from Hunt's metric, the Shannon entropy is derived from the diagonal elements of the N-qubit density matrix and hence doesn't directly probe the correlation between pairs of qubits. As the measurement of correlation is essential for the accurate computation of many-electron quantum systems, our metric—the slope of λ_G vs. N—which does directly probe two-body correlation through probing the modified particle-hole density matrix may be better suited for differentiating between NISQ devices for quantum-chemical simulations.

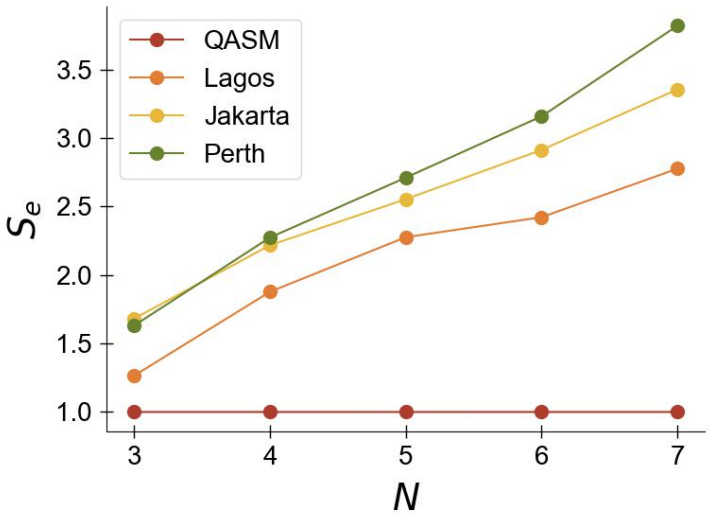

Figure 8.5: The graph of Shannon entropy (S_e) for an N-qubit GHZ state versus the number of qubits (N) for a QASM simulator (red), ibm_lagos (orange), ibmq_jakarta (yellow), and ibm_perth (green). The assocated slopes for each device are shown in Table 8.1.

8.5 Conclusions

Here we introduce a novel metric for benchmarking near-term intermediate-scale quantum devices focused on the ability of such quantum systems to reliably prepare and probe a maximally-entangled quantum system. As quantum chemical systems of interest often display high degrees of quantum long range order, such a benchmark is taken to be predictive of the efficacy with which a given quantum device can simulate a many-electron atom or molecule. Specifically, we utilize the signature of the maximally-entangled GHZ state—i.e., the largest eigenvalue of the modified particle-hole RDM (λ_G) which should ideally approach $N/2$ for a N-qubit GHZ state. This signature can either be utilized as a singular metric that can quantify the "loss" of correlation for a given subsystem of qubits, or—as we have proposed—one can construct a plot of λ_G versus N for a given device in order to determine the slope of the resultant linear fit. This slope of λ_G versus N is then a metric that describes the ability of an entire quantum system to maintain quantum long range order—the closer to 1/2, the more-accurately the quantum device is capable of accurately preparing

and measuring highly correlated systems.

Using this metric, we then benchmark three of IBM's NISQ quantum devices, and, from this analysis, we predict Lagos to be best-suited for calculating molecular energies and properties followed by Jakarta and then Perth. By directly computing the energy of dihyrogen using the qACSE solver outlined in Ref. [267], we verify this prediction by identifying that the dihydrogen energy is best computed by Lagos followed by Jakarta with Perth being the least accurate—just as our metric forecasts. Of note is that if one were to utilize quantum volume as the metric by which such a prediction were made, Lagos and Perth would be expected to demonstrate roughly-equivalent accuracy for computing chemical properties with Jakarta—having the lowest quantum volume—being the least accurate.

Comparing to the more established benchmark of quantum volume, our proposed metric not only allows for more-granular discernment in comparing devices with the same quantum volume (as the slope values are less likely to be identical), but additionally overcomes a shortcoming of quantum volume—namely that quantum volume doesn't necessarily directly probe metrics related to the preparation of molecular systems which may limit its applicability to prescribing which quantum computers are "best" for such applications. By directly corresponding to a measurement of entanglement, the slope of λ_G versus N allowed us to correctly identify that, although Perth has a higher quantum volume than Jakarta, Jakarta is the better system for modelling molecular systems.

One aspiration of quantum computing since the days of Feynman [226] has been the achievement of quantum advantage over traditional classical computing for the simulation of atoms and molecules. As the construction of the wave function on a classical system scales exponentially with the number of orbital-based configurations and—in principle—quantum computers offer the possibility of nonexponential scaling, such an advantage may be obtained as quantum algorithms and *especially* hardware mature. In order to obtain quantum advantage, however, highly-correlated molecular systems need to be modelled on real-world

devices in an accurate manner—a feat that is difficult on modern NISQ devices for complex state preparations and more than a few qubits. The benchmark that we propose—in addition to allowing for the comparison of current quantum systems—may act as a metric along which future devices can be improved in order to better demonstrate quantum long range order and hence may serve as an aide in the search for quantum advantage in molecular simulations.

8.6 Appendix

We include relevant details on the quantum algorithm utilized to prepare the N-qubit GHZ states presented in this article; the quantum tomography of the particle-hole reduced density matrix; the determination of average Shannon entropies; the quantum anti-Hermitian Schrödinger equation; and the experimental quantum devices employed.

8.6.1 GHZ state preparation

See Section 7.6.1 for details regarding the GHZ state preparation.

8.6.2 Quantum tomography of the particle-hole RDM

See Section 7.6.2 for details regarding the quantum tomography of the particle-hole reduced density matrix.

8.6.3 Determination of Shannon entropy

Shannon entropy (S_e) is determined according to

$$S_e = -\sum_{j=1}^{2^N} p_j log_2(p_j) \tag{8.11}$$

where p_j corresponds to the probability of the system to be in the specific j^th quantum state of the 2^N possible quantum states for an N-qubit state preparation. These probabilities correspond to the diagonal elements of the full N-qubit density matrix, ${}^2D$. In the case of a two-qubit system, there are 2^2 or four possible states ($|00\rangle$, $|01\rangle$, $|10\rangle$, and $|11\rangle$) with the diagonal elements corresponding to $\hat{a}^\dagger_{0,0}\hat{a}_{0,0}\hat{a}^\dagger_{1,0}\hat{a}_{1,0}$, $\hat{a}^\dagger_{0,0}\hat{a}_{0,0}\hat{a}^\dagger_{1,1}\hat{a}_{1,1}$, $\hat{a}^\dagger_{0,1}\hat{a}_{0,1}\hat{a}^\dagger_{1,0}\hat{a}_{1,0}$, and $\hat{a}^\dagger_{0,1}\hat{a}_{0,1}\hat{a}^\dagger_{1,1}\hat{a}_{1,1}$. These diagonal elements can again be translated into a linear combination of Pauli matrices. For example, $\hat{a}^\dagger_{0,0}\hat{a}_{0,0}\hat{a}^\dagger_{1,1}\hat{a}_{1,1}$ can be written as

$$\begin{aligned}\hat{a}^\dagger_{0,0}\hat{a}_{0,0}\hat{a}^\dagger_{1,1}\hat{a}_{1,1} &= \left(\hat{a}^\dagger_{0,0}\hat{a}_{0,0}\right)\otimes\left(\hat{a}^\dagger_{1,1}\hat{a}_{1,1}\right)\\ &= \left[\frac{1}{2}\left(I_0+Z_0\right)\right]\otimes\left[\frac{1}{2}\left(I_1-Z_1\right)\right]\\ &= \frac{1}{4}\left[I_0\otimes I_1+Z_0\otimes I_1-I_0\otimes Z_1-Z_0\otimes Z_1\right].\end{aligned} \tag{8.12}$$

The element can then be computed from the appropriate linear combination of the expectation values of Z_0, Z_1, and $Z_0\otimes Z_1$. This methodology can be generalized to the other elements in the case of a two-qubit quantum system and further generalized to an N-qubit system.

8.6.4 Determination of energy via the qACSE

To compute the molecular energy of dihydrogen (H_2) with an internuclear distance of 1 Angstrom using the $STO-6G$ basis, we implement the quantum Anti-Hermitian Schrödinger Equation method—a quantum solver of contracted eigenvalue equations introduced in Ref. [267] with the technique to reduce the number of qubits by tapering being detailed in Ref. [269]. The quantum computations were done by using the electron integrals from a full configuration interaction calculation performed via use of the pySCF package. In particular, we perform both the one-qubit and two-qubit calculations under the Jordan Wigner transformation.

8.6.5 Quantum device specification

Throughout this work, we employ ibm_lagos, ibm_perth, and ibmq_jakarta IBM Quantum Experience devices, which are available online. These quantum devices are composed of fixed-frequency transmon qubits with co-planer waveguide resonators [272, 274]. Device specifications are detailed at IBM's Quantum Experience Website [340]. The Python package QISKIT [251] was used to interface with the devices. Each measurement for the calculation of λ_G and S_e were performed with 2^{13} shots, and each measurement for in the qACSE method was performed with 20,000 shots.

CHAPTER 9

COOPER-PAIR CONDENSATES WITH NONCLASSICAL LONG-RANGE ORDER ON QUANTUM DEVICES

Material from: Sager, L. M. & Mazziotti, D. A., Cooper-pair condensates with nonclassical long-range order on quantum devices. Physical Review Research, published 2022, 4(1), 013003.

9.1 Chapter Synopsis

An important problem in quantum information is the practical demonstration of non-classical long-range order on quantum computers. One of the best known examples of a quantum system with non-classical long-range order is a superconductor. Here we achieve Cooper-like pairing of qubits on a quantum computer, which can be interpreted as superconducting or superfluid states via a Jordan-Wigner mapping. We rigorously confirm the quantum long-range order by measuring the large $O(N)$ eigenvalue of the two-electron reduced density matrix. The demonstration of maximal quantum long-range order is an important step towards more complex modeling of phenomena with significant quantum long-range order on quantum computers such as superconductivity and superfluidity.

9.2 Introduction

Phenomena like superconductivity and superfluidity arise from a Bose-Einstein-like condensation of fermion pairs into a quantum state with large non-classical long-range order [96, 107, 128, 137, 156, 178, 179, 184, 185, 187, 341–351]. Recently, quantum computers have emerged as potentially powerful calculators of correlated quantum systems [5, 266, 270, 303–306, 352–355], which foreshadows the potential emergence of a significant advantage of quantum computers over classical computers for certain classes of problems—a phenomenon known as

quantum advantage [316, 356, 357]. Here, we prepare and measure Cooper-like pairs of qubit particles on a transmon-qubit quantum computer. As the distinction between bosonic and fermionic statistics is lost as a result of a Jordan-Wigner mapping, condensations of Cooper-like qubit pairs can be interpreted as fermion-pair condensations, which can represent superconducting (or superfluid) states.

In this study, qubit particles—which are hard-core bosons— are entangled into Cooper-like bosonic pairs (see Fig. 9.1) to form superconducting-like states—extreme antisymmetrized geminal power (AGP) wave functions [5, 66, 119, 135, 136, 138, 156, 358–362]. As originally shown by Yang [135] and Coleman [66, 138, 363], such states are extreme in the set of two-electron reduced density matrices (2-RDM), exhibiting the largest possible eigenvalue of the 2-RDM on the order of the number N of electrons $O(N)$ that represents the maximum possible number of Cooper pairs in a common two-electron (geminal) eigenfunction of the 2-RDM. We use tomography on the quantum computer to measure a subblock of the 2-RDM [138, 364, 365] (see Eq. (9.9)) containing the large eigenvalue. Diagonalization of this subblock on a classical computer produces the large eigenvalue and confirms the preparation of the extreme states with maximal non-classical (off-diagonal) long-range order (ODLRO) [135, 363]. Even though the extreme AGP functions are expressible as projections of product wave functions [66, 138], they have contributions from an exponentially scaling number of orbital-product configurations (see Fig. 9.2). Moreover, the measurement of the large eigenvalue of the 2-RDM is applicable to confirming non-classical long-range order in a much richer set of quantum states. Because a necessary criterion for the modeling of superconductors (superfluids) on the quantum computer is the ability to capture the ODLRO, its demonstration provides a first step towards modeling more-complex superconducting (superfluid) materials.

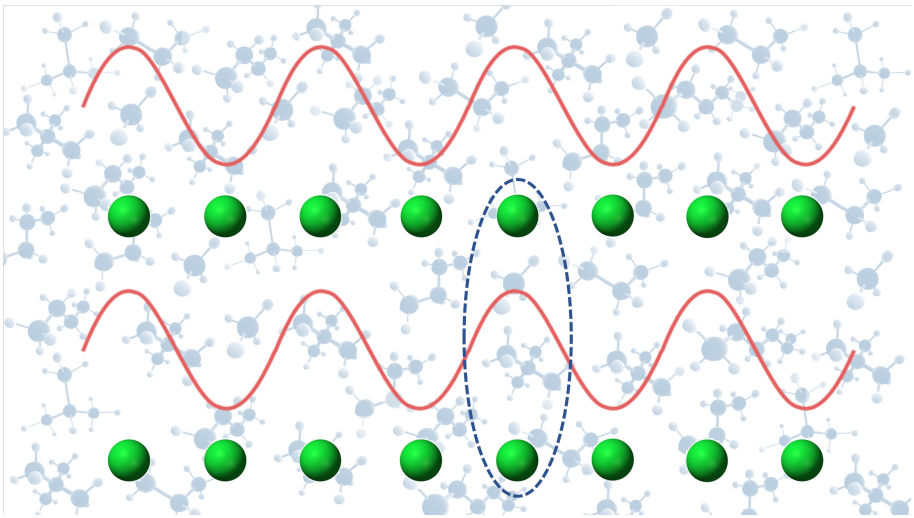

Figure 9.1: A schematic demonstrating the interpretation of the Cooper pairing of qubit particles to create an overall Cooper-like paired state in a quantum system.

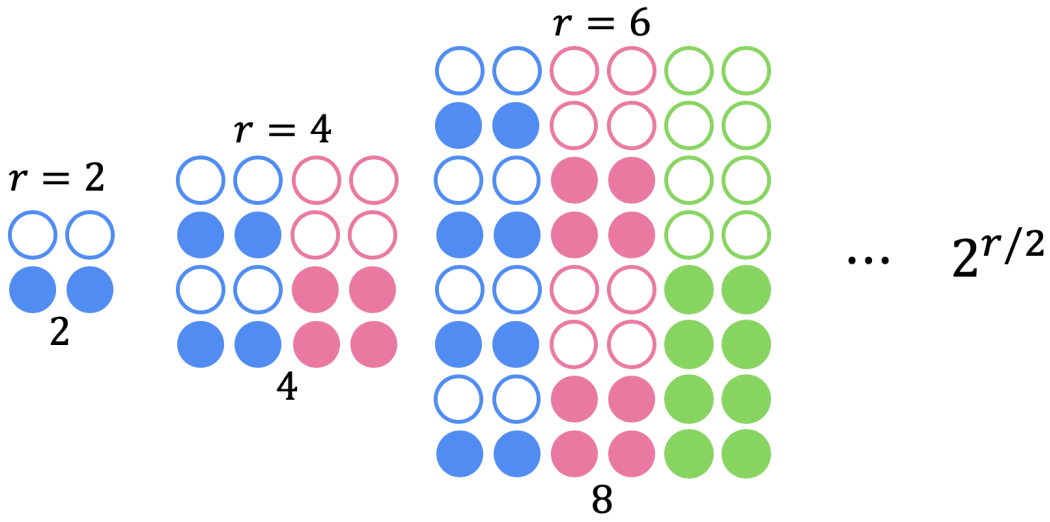

Figure 9.2: A schematic demonstrating the possible configurations (i.e., each row) for a given number r of qubits where a filled circle indicates the $|1\rangle$ state which corresponds to an occupied orbital and an unfilled circle represents the $|0\rangle$ state which corresponds to an unoccupied orbital.

9.3 Theory

9.3.1 The wave function:

The superconducting-like state on the quantum computer is prepared by entangling pairs of qubits into Cooper-like bosonic states. Consider the creation of a state with a Cooper pair of electrons, an extreme geminal [66, 137, 138, 358], from the vacuum state

$$|g\rangle = \sum_{j} e^{i\theta} \hat{a}^{\dagger}_{\bar{j}} \hat{a}^{\dagger}_{j} |\varnothing\rangle \tag{9.1}$$

where j and $\bar{j}$ are the indices of the paired orbitals ϕ_j and $\phi_{\bar{j}}$, the sum over j is taken with respect to all pairs, and θ is an arbitrary global phase. If we represent each orbital by a qubit with the $|0\rangle$ state representing an unfilled orbital and the $|1\rangle$ state representing a filled orbital, we can use a specific Klein transformation [366] known as the Jordan-Wigner mapping [263]

$$\hat{a}^{\dagger}_{j} = e^{i\pi \sum_{k=1}^{j-1} \sigma_k^+ \sigma_k^-} \sigma_j^+ \tag{9.2}$$

to map the fermionic operators in Eq. (9.1) to qubit operators to obtain

$$|g\rangle = \sum_{j} e^{i\theta} e^{i\pi \sum_{k=1}^{\bar{j}-1} \sigma_k^+ \sigma_k^-} \sigma_{\bar{j}}^+ e^{i\pi \sum_{k=1}^{j-1} \sigma_k^+ \sigma_k^-} \sigma_j^+ |\varnothing\rangle. \tag{9.3}$$

If the paired orbital indices j and $\bar{j}$ are selected to be consecutive integers in the range $[1, r]$ where r is the total number of orbitals, then the Jordan-Wigner mappings in Eq. (9.3) simplify to a negative global phase which we can cancel by selecting $\theta = \pi$ to obtain

$$|g\rangle = \sum_{j} \sigma_{\bar{j}}^+ \sigma_j^+ |\varnothing\rangle. \tag{9.4}$$

Hence, the extreme geminal of the Cooper pair $|g_{j\bar{j}}\rangle$ of electrons can be represented as two-qubit excitations without approximation. The difference between the fermion and qubit statistics, typically included through an explicit many-qubit Jordan-Wigner mapping , disappears from the pairing of the orbitals to generate an extreme geminal. Moreover, the explicit details of the pairing of the particles is contained within the unspecified orbitals ϕ_j and $\phi_{\bar{j}}$. Consequently, the extreme geminal can physically represent Cooper pairing of electrons in a superconductor or a superfluid in addition to representing even the Cooper-like pairing of qubit particles (hard-core bosons) [367] which are paraparticles [368, 369].

The N-electron extreme AGP wave function $|\Psi^N_{\text{AGP}}\rangle$ for even N can be generated from the wedge product of the extreme geminal with itself $N/2$ times [66, 138, 358, 370]

$$|\Psi^N_{\text{AGP}}\rangle = |g(12)\rangle \wedge |g(34)\rangle \wedge ... \wedge |g((N-1)N)\rangle \tag{9.5}$$

where the wedge $\wedge$ denotes the sum of all products resulting from the antisymmetric permutation of the particles. We can also consider a wave function $|\Psi_{\text{AGP}}\rangle$, also known as a Bardeen-Cooper-Schrieffer (BCS) wave function [128], that is a linear combination of the $|\Psi^N_{\text{AGP}}\rangle$ for all N which is expressible as a product state

$$|\Psi_{\text{AGP}}\rangle = \prod_{j=1}^{r/2} (1 + e^{i\theta} \hat{a}^\dagger_{2j} \hat{a}^\dagger_{2j-1}) |\varnothing\rangle. \tag{9.6}$$

Using the Jordan-Wigner transformation and simplifying as above, we can generate the AGP state in Eq. (9.6) with the qubit excitation operators

$$|\Psi_{\text{AGP}}\rangle = \prod_{j=1}^{r/2} (1 + \hat{\sigma}^+_{2j} \hat{\sigma}^+_{2j-1}) |\varnothing\rangle, \tag{9.7}$$

which can also be cast as the tensor multiplication of $r/2$ distinct extreme geminals (or the

$|\Phi^+\rangle$ Bell states [371])

$$|\Psi_{\text{AGP}}\rangle = \bigotimes_{j=1}^{r/2} \frac{1}{\sqrt{2}} \left[|00\rangle_{2j,2j-1} + |11\rangle_{2j,2j-1} \right] \tag{9.8}$$

where j specifies the pair index and adjacent qubits with qubit indices $2j-1$ and $2j$ paired by definition. This state, which is composed of substates with all possible, paired, even-numbered excitations, can be prepared on a quantum device according to the general gate sequence given in Eq. (9.12). Figure 9.3 shows the specific $r = 4$ preparation.

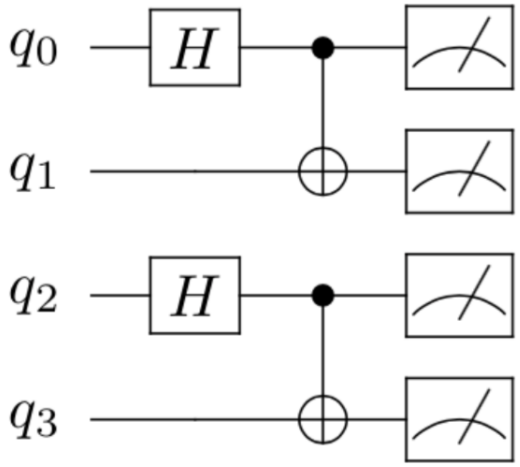

Figure 9.3: A schematic demonstrating the quantum state preparation for the $r = 4$ AGP wave function given in Eq. (9.8) where H represents the Hadamard gate which maps $|0\rangle$ to $(|0\rangle + |1\rangle)/\sqrt{2}$ and $|1\rangle$ to $(|0\rangle - |1\rangle)/\sqrt{2}$ and where each pair of qubits is connected via a standard controlled-NOT (CNOT) gate with control $\bullet$ and target $\oplus$.

On the quantum computer, the extreme AGP state is physically composed of Cooper-like pairs of qubits. Because the phase changes from the fermionic statistics are lost in the pairing—as seen in the above fermionic encoding of the qubits, the extreme state rigorously represents not only entangled pairs of qubits but also Cooper pairs of electrons that are entangled in superconducting or superfluid states. Moreover, the state can represent any physical model for pairing as the precise nature of the pairing (i.e. the pairing of electrons in

physical space or in momentum space) is contained in the paired orbitals ϕ_j and $\phi_{\bar{j}}$, which are left unspecified. All pairing states have fundamental entanglement and order properties that are independent of the physical definition of the orbitals. The non-classical long-range order of the extreme AGP state can be assessed from the number of Cooper pairs in the same extreme geminal, which is determinable from the largest eigenvalue of the 2-RDM [66, 135, 136].

9.3.2 The Signature of Non-Classical Off-Diagonal Long-Range Order (ODLRO)

In order to measure whether the experimentally-prepared quantum state and/or the number-conserving substates—which are all possible, even eigenstates of the number operator (Eq. (9.27)) that can be projected out from the overall ensemble quantum state according to the methodology presented in 9.6.3—demonstrate off-diagonal long-range order, we conduct quantum tomography (see 9.6.2 and 9.6.3) to probe directly the presence and extent of ODLRO . To determine the presence and degree of this long-range order for a specified quantum state, it is useful to establish a calculable, characteristic property [5, 66, 119, 135, 136, 138, 156, 359]. Such a signature of ODLRO is a large eigenvalue in the 2-RDM, which we denote as λ_D [135, 136]. As this large eigenvalue corresponds to the number of Cooper-like qubit pairs occupying the same two-qubit geminal (which is directly analogous to the one-qubit orbital), any λ_D value exceeding the Pauli-like limit of one is indicative of ODLRO [66, 135, 136].

While the entire 2-RDM can be measured by quantum tomography, only the following subblock of the 2-RDM [138, 364, 365] is required due to the block diagonal structure of the 2-RDM of the AGP wave function

$$ {}^2D^{j\bar{j}}_{k\bar{k}} = \langle \Psi_{\mathrm{AGP}} | \hat{a}^\dagger_j \hat{a}^\dagger_{\bar{j}} \hat{a}_{\bar{k}} \hat{a}_k | \Psi_{\mathrm{AGP}} \rangle \tag{9.9} $$

where $j/\bar{j}$ and $k/\bar{k}$ represent paired fermions, which are given by $j = 2m/\bar{j} = 2m - 1$ and $k = 2n/\bar{k} = 2n - 1$ for integers m, n in the framework of the AGP wave function. After Jordan-Wigner transformation to the qubit representation, we can equivalently represent this block of the 2-RDM in terms of the qubit excitation operators as

$$^2D^{j\bar{j}}_{k\bar{k}} = \langle \Psi_{\mathrm{AGP}} | \hat{\sigma}^\dagger_j \hat{\sigma}^\dagger_{\bar{j}} \hat{\sigma}_{\bar{k}} \hat{\sigma}_k | \Psi_{\mathrm{AGP}} \rangle. \tag{9.10}$$

For fixed number N of electrons, if the 2-RDM is normalized to $N(N-1)$ as in second quantization, the maximum eigenvalue for even N is bounded from above by N as shown by Yang [135] and Sasaki [136]. Moreover, for a finite rank of r orbitals, this bound can be further tightened [66, 138] to

$$\lambda_D \leq N \left(1 - \frac{N-2}{r} \right). \tag{9.11}$$

While the thermodynamic limit is not reached until $r \to \infty$, even for finite r, as long as $N \geq 4$, the 2-RDM exhibits a large eigenvalue that represents the non-classical long-range order associated with Cooper pairing. The 2-RDM from the non-number conserving extreme AGP state $|\Psi_{\mathrm{AGP}}\rangle$ also exhibits a large eigenvalue, representing an average of the Cooper pairs in each of the fixed-N extreme AGP states (i.e., the number-conserving substates). The number-conserving blocks of the 2-RDM with even particle numbers—i.e., 2-RDMs of zero, two, four, ..., $r-2$, and r particles for an r-qubit system—can be determined from the non-number conserving state via post-measurement analysis (see 9.6.3). Analysis on the presence and extent of ODLRO (measured via λ_D) of both the overall entangled state ($|\Psi\rangle$) and the number-conserving substates is conducted for various numbers r of total qubits in the following sections.

9.4 Results

The extreme non-number conserving AGP state is prepared for both simulation utilizing IBM's QASM simulator (ibmq_qasm_simulator) and an experimental quantum device for all even-numbered qubit systems from $r = 0$ to $r = 14$. Post-measurement computation of the quantum signature of off-diagonal long-range order (λ_D) is then employed to probe the presence and extent of ODLRO for these overall states. As can be seen in Figure 9.4, the signature of ODLRO increases as the number r of qubits comprising the system is increased, and—for QASM simulation— ODLRO is observed (i.e., $\lambda_D > 1$) for all prepared states with $r \geq 8$. While the experimental results deviate from QASM simulation due to the noisy nature of near-term quantum devices [254] (see 9.6.4 and 9.6.6), experimental systems with $r = 12$ and $r = 14$ qubits did demonstrate ODLRO. Further, the trend of the extent of ODLRO increasing as the number of qubits comprising the system increases holds for the experimental results, which is promising for future benchmarking of quantum computers through the preparation of extreme AGP states with larger number of qubits as well as efforts to probe more macroscopically-scaled materials demonstrating ODLRO on quantum devices.

As the non-number conserving extreme AGP state is an ensemble composed of number-conserving substates, the large eigenvalue associated with the ODLRO of the ensemble state is the ensemble average of the substates. By definition, then, the long-range order of the ensemble is less than that of the substate with the largest degree of ODLRO, which is expected to occur around the center of the number distribution $N \approx r/2$.

Additionally, real-world materials demonstrating ODLRO such as superconductors should conserve particle number. It is hence beneficial to probe the number-conserving substates that comprise the overall entangled state in order to both isolate the ODLRO behavior of the number-conserving substates and to more-closely model real-world materials.

By projecting out a specific number of particles from the results obtained for overall en-

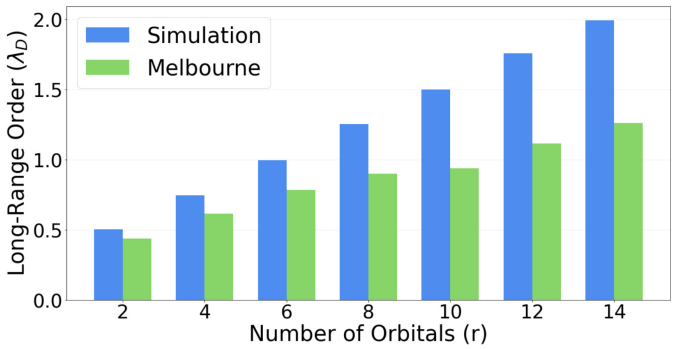

Figure 9.4: The λ_D values for the overall ensemble state preparation for QASM simulation and experimental melbourne results.

tangled state (see 9.6.3), we can probe the behavior and properties of the number-conserving substates. Specifically, as is shown in Fig. 9.5, the extent of ODLRO (λ_D) for each number-conserving state can be isolated from the overall r-qubit preparation described in Eq. (9.8). As can be seen from the QASM simulation results, all number-conserving substates with $2 < N < r$ demonstrate ODLRO ($\lambda_D > 1$) where $N = 2$ fails to demonstrate condensation behavior as the maximum signature of condensation is $N/2$ for even N-particle systems [135, 136] and where $N = r$ fails to demonstrate condensation behavior as this substate describes the state in which all orbitals are fully occupied with no entanglement—i.e., the single Slater determinant $|1\rangle^{\otimes r}$—and is hence expected to have a maximum eigenvalue of $\lambda_D = 1$.

Further, the signature of condensation seems to follow a bell curve centered around $(r+2)/2$ such that maximum ODLRO is observed at half filling for $N = (r+2)/2$ if $(r+2)/2$ is even and for both $N = (r+2)/2 - 1$ and $(r+2)/2 + 1$ if $(r+2)/2$ is odd. Again, the extent of ODLRO is lesser for the experimental results for all particle-conserving states due to experimental error; however, the qualitative trends described for QASM simulation hold in general although the bell curve does demonstrate a slight negative (right-modal) skew, implying that the quantum computer does not exactly treat the particle and hole statistics symmetrically. Importantly, ODLRO is clearly observed for $r = 14$ experimental results for

particle numbers $N \geq 6$. Note that although only results for the largest-qubit preparation $r = 14$ are shown, all data is included in Table 9.2; the trends in the $r = 14$ data hold for the lower-qubit results, and additionally, the $r = 14$ qubit data demonstrates the largest signature of off-diagonal long-range order as the largest λ_D value for a fixed N increases as the number r of qubits is increased.

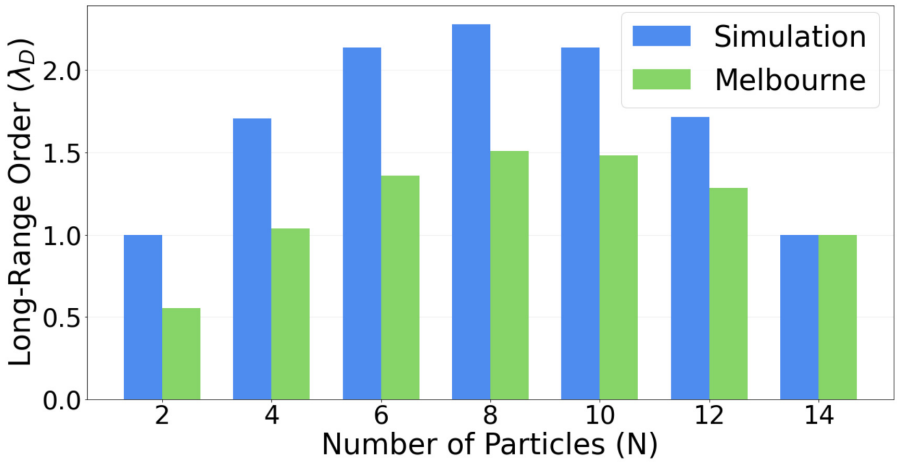

Figure 9.5: The λ_D values for the number-conserving substates of rank $r = 14$ for QASM simulation and experimental melbourne results.

9.5 Conclusions

Here we prepare superconducting-like states from the Cooper pairing of qubits on a transmon quantum computer—where each qubit is composed of a microwave phonon in an anharmonic well potential. Using the Jordan-Wigner mapping between fermions and qubits, we rigorously show that the prepared states are equally valid representations of condensations of Cooper pairs of fermions, bosons, or qubits. Hence, such Cooper-pair-based condensations and their associated non-classical long-range order are independent of the particle statistics. Moreover, the prepared states are also independent of the physical details of the paired orbitals, and consequently, are representative of superconducting, superfluid, or other pairing states. The

studied states are known as extreme AGPs because they exhibit the maximum degree of non-classical (off-diagonal) long-range order as determined by the number of Cooper pairs in the same geminal state, which is equal to the largest eigenvalue of the 2-RDM [66, 135–138, 360, 363]. We measure a subblock of the 2-RDM [138, 364, 365] on the quantum computer and compute its largest eigenvalue on a classical computer. We observe large eigenvalues both for the non-particle conserving extreme AGP state and the particle-conserving extreme AGP substates. The large eigenvalues confirm the preparation of these extreme AGP states, which are the only states to exhibit the largest possible eigenvalues [138], as well as the generation of maximum non-classical long-range order.

The upper bound on the largest eigenvalue of the 2-RDM, $\lambda_D = N$, is technically only reached in the thermodynamic limit of $r \to \infty$. However, as seen in Eq. (9.11), the large eigenvalue is rapidly approached with increasing r as the fraction of Cooper pairs that are removed from the condensate due to finite size effects scales as $1/r$. Consequently, the quantum long-range order as well as its associated entanglement begin to appear for the range of r ($r \leq 14$) explored in the present study. On both IBM's QASM simulator and an IBM quantum computer, we observe that the large eigenvalue follows the expected bell curve with respect to r. The known value for the maximum eigenvalue of the extreme AGP state provides a clear metric for not only confirming the presence of the extreme state and its long-range order but also benchmarking the fidelity with respect to noise of both current and future quantum computers.

An aspirational goal of quantum computing is to achieve a quantum advantage over traditional classical computing for the solution of a significant problem. One such area of chemistry and physics, which traces back to the original proposal of Feynman [226], is the simulation of molecules on quantum computers. The construction of the wave function on a classical computer scales exponentially in the number of orbital-based configurations. In principle, the quantum computer offers the possibility of preparing and measuring quantum

states with non-exponential scaling. In the present case, the extreme AGP wave function is a product state composed of a product of extreme geminals (or Bell states). Consequently, the maximum degree of non-classical long-range order, at least as measured by the largest eigenvalue of the 2-RDM, can be achieved with polynomial cost on both classical and quantum computers. The extreme AGP states, nonetheless, provide an intriguing reference for the exploration of more complicated states demonstrating large ODLRO (i.e., demonstrating large eigenvalues) that cannot be easily expressed as product-state wave functions. From this perspective, the present work of preparing and measuring superconducting-like states from Cooper pairs of qubits on a quantum computer provides an initial step towards investigating more complicated condensates of Cooper pairs—with potential future applications to the study of both superconducting materials and simulation.

9.6 Appendix

We include details on the quantum algorithms used to prepare the qubit states presented in the article; the quantum tomography of the particle-particle reduced density matrix for both the overall non-number conserving state as well as number-conserving substates; a description of noise on near-term quantum devices; an analysis of errors by comparing simulated and experimental joint probabilities of occupation; relevant details on the experimental quantum backends employed; full results obtained from ibmq_qasm_simulation, ibmq_16_melbourne, ibmq_5_yorktown, ibmq_santiago, and ibmq_rochester; and information regarding the state preparation fidelity.

9.6.1 State Preparations

The overall quantum state is composed of all pairwise even excitations of the $r/2$ individually-paired qubits. This preparation is accomplished by

$$|\Psi\rangle = \left[\prod_{p=0}^{r/2-1} C_{2p}^{2p+1} H_{2p}\right] |0\rangle^{\otimes r} \tag{9.12}$$

where $|0\rangle^{\otimes r}$ is the initial quantum state in which all qubits are in their ground state (i.e., all orbitals are unoccupied), p represents the index of each of the possible $r/2$ adjacent, paired qubits, H_i is the Hadamard gate acting on Qi, and C_i^j is a CNOT gate with Qi and Qj acting as the control and target qubits, respectively. Application of the gate sequence given in Eq. (9.12)—represented pictorially for $r = 4$ in Fig. 9.3— produces the AGP wave function described by Eq. (9.8).

9.6.2 Quantum Tomography for the Particle-Particle RDM

While the full particle-particle RDM has elements given by

$${}^2D_{k,l}^{i,j} = \langle\Psi|\hat{a}_i^\dagger \hat{a}_j^\dagger \hat{a}_k \hat{a}_l|\Psi\rangle \tag{9.13}$$

for all possible combinations of one-boson spin orbitals indexed by i, j, k, and l in a finite basis state with rank r, the large eigenvalue, λ_D, is contained within the subblock of the 2-RDM given by [66, 138]

	$\hat{a}_1\hat{a}_0$	$\hat{a}_3\hat{a}_2$	$\cdots$	$\hat{a}_{r-2}\hat{a}_{r-1}$
$\hat{a}_0^\dagger\hat{a}_1^\dagger$	$\hat{a}_0^\dagger\hat{a}_1^\dagger\hat{a}_1\hat{a}_0$	$\hat{a}_0^\dagger\hat{a}_1^\dagger\hat{a}_3\hat{a}_2$	$\cdots$	$\hat{a}_0^\dagger\hat{a}_1^\dagger\hat{a}_{r-2}\hat{a}_{r-1}$
$\hat{a}_2^\dagger\hat{a}_3^\dagger$	$\hat{a}_2^\dagger\hat{a}_3^\dagger\hat{a}_1\hat{a}_0$	$\hat{a}_2^\dagger\hat{a}_3^\dagger\hat{a}_3\hat{a}_2$	$\cdots$	$\hat{a}_2^\dagger\hat{a}_3^\dagger\hat{a}_{r-2}\hat{a}_{r-1}$
$\vdots$	$\vdots$	$\vdots$	$\ddots$	$\vdots$
$\hat{a}_{r-2}^\dagger\hat{a}_{r-1}^\dagger$	$\hat{a}_{r-2}^\dagger\hat{a}_{r-1}^\dagger\hat{a}_1\hat{a}_0$	$\hat{a}_{r-2}^\dagger\hat{a}_{r-1}^\dagger\hat{a}_3\hat{a}_2$	$\cdots$	$\hat{a}_{r-2}^\dagger\hat{a}_{r-1}^\dagger\hat{a}_{r-2}\hat{a}_{r-1}$

(9.14)

and, hence, only this portion of the matrix is constructed. Note that $\hat{a}_i^\dagger$ and $\hat{a}_i$ are creation and annihilation operators for orbital i (and thereby qubit Qi), which can be represented in matrix form as

$$\hat{a}_i^\dagger = \begin{pmatrix} 0 & 0 \\ 1 & 0 \end{pmatrix}_i \tag{9.15}$$

and

$$\hat{a}_i = \begin{pmatrix} 0 & 1 \\ 0 & 0 \end{pmatrix}_i \tag{9.16}$$

such that each creation operator creates a particle in an empty orbital i—takes a qubit i from $|0\rangle$ to $|1\rangle$—and each annihilation operator kills a particle in a filled orbital i—takes a qubit i from $|1\rangle$ to $|0\rangle$—where

$$|0\rangle = \begin{pmatrix} 1 \\ 0 \end{pmatrix} \tag{9.17}$$

and

$$|1\rangle = \begin{pmatrix} 0 \\ 1 \end{pmatrix} \tag{9.18}$$

After construction of the subblock of the 2-RDM corresponding to the large eigenvalue (${}^2D_{\text{s.b.}}$), the signature of off-diagonal long-range order—λ_D—is then obtained by solving the eigenvalue equation

$${}^2D_{\text{s.b.}}v_i^D = \epsilon_i^D v_i^D \tag{9.19}$$

with the signature corresponding to the largest ϵ_i^D value.

Tomography via Pauli Expectation Values

The subblock of the 2-RDM containing the large eigenvalue (i.e., Eq. (9.14)) can be obtained via translation of each of its elements into the bases of Pauli matrices, the expectation values of which can be directly probed on a quantum device. Specifically, the creation and annihilation operators can be rewritten as

$$\hat{a}_i^\dagger = \frac{1}{2}\left(X_i - iY_i\right) \tag{9.20}$$

and

$$\hat{a}_i = \frac{1}{2}\left(X_i + iY_i\right) \tag{9.21}$$

with diagonal elements being given by

$$\begin{aligned}
\hat{a}_j^\dagger \hat{a}_{j+1}^\dagger \hat{a}_{j+1} \hat{a}_j &= (\hat{a}_j^\dagger \hat{a}_j)(\hat{a}_{j+1}^\dagger \hat{a}_{j+1}) \\
&= \frac{1}{16}\left(X_j - iY_j\right)\left(X_j + iY_j\right)\left(X_{j+1} - iY_{j+1}\right)\left(X_{j+1} + iY_{j+1}\right) \\
&= \frac{1}{4}\left(I_j - Z_j\right)\left(I_{j+1} - Z_{j+1}\right) \\
&= \frac{1}{4}\left(1 - Z_j - Z_{j+1} + Z_j Z_{j+1}\right)
\end{aligned} \tag{9.22}$$

and off-diagonal elements being given by

$$\hat{a}_j^\dagger \hat{a}_{j+1}^\dagger \hat{a}_{k+1} \hat{a}_k = \frac{1}{16} \left(X_j - iY_j\right) \left(X_{j+1} - iY_{j+1}\right) \left(X_{k+1} + iY_{k+1}\right) \left(X_k + iY_k\right)$$
$$\frac{1}{16}(X_j X_{j+1} X_k X_{k+1} + iX_j X_{j+1} X_k Y_{k+1} + iX_j X_{j+1} Y_k X_{k+1} - X_j X_{j+1} Y_k Y_{k+1}$$
$$-iX_j Y_{j+1} X_k X_{k+1} + X_j Y_{j+1} X_k Y_{k+1} + X_j Y_{j+1} Y_k X_{k+1} + iX_j Y_{j+1} Y_k Y_{k+1}$$
$$-iY_j X_{j+1} X_k X_{k+1} + Y_j X_{j+1} X_k Y_{k+1} + Y_j X_{j+1} Y_k X_{k+1} + iY_j X_{j+1} Y_k Y_{k+1}$$
$$-Y_j Y_{j+1} X_k X_{k+1} - iY_j Y_{j+1} X_k Y_{k+1} - iY_j Y_{j+1} Y_k X_{k+1} + Y_j Y_{j+1} Y_k Y_{k+1}) \tag{9.23}$$

Therefore, each 2-RDM matrix element can be obtained by directly probing the expectation values of four-qubit tensor products of Pauli matrices.

As all wave functions prepared in this study are real, the 2-RDM should consist of only real-valued elements; hence, all imaginary components of 2-RDM elements should approach zero within a small range dictated by randomness inherent to quantum systems as well as error on the device employed. Therefore, only eight of the sixteen four-qubit expectation values corresponding to real contributions to a given 2-RDM element are nonzero and hence necessary for the determination of the subblock of the 2-RDM; thus, to lower computational expense, only these real values are used to construct the 2-RDM subblock where tomography via Pauli expectation values is conducted (as is consistent with previous analysis conducted in a manner similar to that described in Ref. [5]).

Tomography via Direct Computation of the wave function

As can be observed from Eq. (9.8), the phase angle of all qubits in the AGP wave function are known to be uniformly zero. As such, knowledge of the probabilities with which each of the possible 2^r basis states ($|\eta_i\rangle$) for an r-qubit calculation are sampled out of the 81,920 times (8192 per trial) a given state is prepared and probed is sufficient information to completely construct the wave function ($|\Psi\rangle$). Specifically, the wave function takes the form of a vector

(using traditional qubit vector notation [372]) with each element of the wave function $|\Psi_i\rangle$ corresponding to the basis state $|\eta_i\rangle$ being given by

$$|\Psi_i\rangle = +\sqrt{p(\eta_i)} = +\sqrt{|\langle\eta_i|\Psi\rangle|^2} = +|\langle\eta_i|\Psi\rangle| \tag{9.24}$$

which is the positive square root of the probability ($p(\eta_i)$) with which the corresponding qubit basis state is measured.

Each individual element of the matrix shown in Eq. (7.19) is then computed from the appropriate expectation value $\langle\Psi|\hat{a}_j^\dagger\hat{a}_{j+1}^\dagger\hat{a}_{k+1}\hat{a}_k|\Psi\rangle$ for the wave function in vector form obtained for a given state preparation. The operator $\hat{a}_j^\dagger\hat{a}_{j+1}^\dagger\hat{a}_{k+1}\hat{a}_k$ can be represented as a $2^r \times 2^r$ matrix according to

$$\begin{aligned}\hat{a}_j^\dagger\hat{a}_{j+1}^\dagger\hat{a}_{k+1}\hat{a}_k = &\left[\bigotimes_{a=1}^{j-1}\begin{pmatrix}1 & 0\\ 0 & 1\end{pmatrix}_a\right]\otimes\begin{pmatrix}0 & 0\\ 1 & 0\end{pmatrix}_j\otimes\begin{pmatrix}0 & 0\\ 1 & 0\end{pmatrix}_{j+1}\\ &\left[\bigotimes_{b=j+2}^{k-1}\begin{pmatrix}1 & 0\\ 0 & 1\end{pmatrix}_b\right]\otimes\begin{pmatrix}0 & 1\\ 0 & 0\end{pmatrix}_k\otimes\begin{pmatrix}0 & 1\\ 0 & 0\end{pmatrix}_{k+1}\left[\bigotimes_{c=k+2}^{r}\begin{pmatrix}1 & 0\\ 0 & 1\end{pmatrix}_c\right]\end{aligned} \tag{9.25}$$

which is the tensor product of the creation and annihilation operators in matrix form (Eqs. (9.15) and (9.16)) corresponding to the appropriate qubits $(j, j+1, k, k+1)$ and identity matrices for each spectator qubit. The expectation value can thus be computed directly via Matrix-Vector multiplication.

Comparing this method for the tomography of the subblock of the 2-RDM corresponding to the large eigenvalue (${}^2D^{\Psi}_{\text{s.b.}}[i,j]$) to the tomography obtained via the expectation values of the Pauli matrices (${}^2D^{P}_{\text{s.b.}}[i,j]$) yields Euclidean distances between the two matrices—

represented mathematically as

$$\sqrt{\sum_{i=0}^{r/2-1}\sum_{j=0}^{r/2-1}\left({}^{2}D^{P}_{\text{s.b.}}[i,j]-{}^{2}D^{\Psi}_{\text{s.b.}}[i,j]\right)^{2}} \tag{9.26}$$

—of $[r=2:0.001, r=4:0.004, r=6:0.003, r=8:0.005, r=10:0.007, r=12:0.009]$ for IBMQ QASM simulation, which indicates that any difference between the two methods is caused by inherent randomness in the absence of error. Indeed, if the QASM simulator is used, no difference is observed between the two methodologies. On the error-prone melbourne experimental device, the Euclidean distances for the $r=2$ and the $r=8$ calculations are $[r=2:0.015, r=8:0.338]$, which is likely due to a large degree of error on the quantum device, which increases with the number of qubits (and hence the number of two-qubit gates) involved. In fact, for the same number of qubits, the Euclidean distances between ${}^{2}D^{P}_{\text{s.b.}}[i,j]$ and the ideal, expected ${}^{2}D_{\text{s.b.}}$ matrix is $[r=2:0.063, r=8:0.541]$ and that between ${}^{2}D^{\Psi}_{\text{s.b.}}[i,j]$ and ${}^{2}D_{\text{s.b.}}$ is $[r=2:0.048, r=8:0.372]$, showing that the Euclidean distance between the two is on the same order or significantly smaller than the distance between each and the ideal. If anything, the direct wave function methodology seems to provide a slight mitigation of errors, likely due to the smaller number of circuits run as only one circuit per trial for the direct wave function is necessary while multiple circuits per trial must be run in order to obtain the expectation values of the Pauli matrices.

Note that to decrease computational expense—especially in terms of the isolation of the number-conserving substates as explained in the following section—in this paper, we implement the tomography via the direct computation of the wave function.

9.6.3 Isolation of Number-Conserving Components

The number-conserving substates are eigenfunctions of the number operator,

$$\hat{N} = \sum_{q=0}^{N-1} \hat{a}_q^\dagger \hat{a}_q = \sum_{q=0}^{N-1} \frac{1 - Z_q}{2} \tag{9.27}$$

where Z_q is the Pauli Z gate corresponding to qubit q. Therefore, each substate is composed of a definite number of particles (i.e., qubits in the $|1\rangle$ state) such that, for example, an overall $r = 6$ AGP wave function

$$\begin{aligned} |\Psi_{\text{AGP}}^{6,\text{full}}\rangle = \frac{1}{2\sqrt{2}}[&|000000\rangle + |000011\rangle + |001100\rangle + |110000\rangle \\ &+|111100\rangle + |110011\rangle + |001111\rangle + |111111\rangle] \end{aligned} \tag{9.28}$$

which has contributions from basis states with $N = 0$, $N = 2$, $N = 4$, and $N = 6$ particles can be decomposed into the following substates that are eigenfunctions of the number operator and hence have a definite number of particles:

$$|\Psi_{\text{AGP}}^{6,0}\rangle = |000000\rangle, \tag{9.29}$$

$$|\Psi_{\text{AGP}}^{6,2}\rangle = \frac{1}{\sqrt{3}}[|000011\rangle + |001100\rangle + |110000\rangle], \tag{9.30}$$

$$|\Psi_{\text{AGP}}^{6,4}\rangle = \frac{1}{\sqrt{3}}[|111100\rangle + |110011\rangle + |001111\rangle], \tag{9.31}$$

and

$$|\Psi_{\text{AGP}}^{6,6}\rangle = |111111\rangle. \tag{9.32}$$

In general, the overall AGP wave function is constructed from its number-conserving substates according to

$$|\Psi_{\mathrm{AGP}}^{r,\mathrm{full}}\rangle = \left(\frac{1}{\sqrt{2}}\right)^{r/2} \left[\sum_{i=0}^{r/2} \sqrt{\binom{r/2}{i}} |\Psi_{\mathrm{AGP}}^{r,2i}\rangle\right] \tag{9.33}$$

The density matrices associated with the number-conserving substates (${}^2D_{r,N}$) are able to be isolated as shown in the following sections such that the signature of ODLRO, λ_D, can be attained for subblocks of the 2-RDM specific to each substate in addition to the signature of the overall non-particle-conserving AGP state with contributions from each of the number-conserving substates.

Tomography via Pauli Expectation Values

As can be extrapolated from Eq. (9.33), the full density matrix (${}^2D_{r,\mathrm{full}}$) obtained as shown using tomography via Pauli expectation values in 9.6.2 can be represented as a sum of the density matrices for each of the individual substates (${}^2D_{r,N}$) with elements given according to

$$\begin{aligned}\left({}^2D_{r,\mathrm{full}}\right)_{k,l}^{i,j} &= \left(\frac{1}{2}\right)^{r/2} \left[\sum_{i=0}^{r/2} \binom{r/2}{i} \left({}^2D_{r,2i}\right)_{k,l}^{i,j}\right] \\ &= \langle \Psi_{r,\mathrm{full}} | \hat{a}_i^\dagger \hat{a}_j^\dagger \hat{a}_l \hat{a}_k | \Psi_{r,\mathrm{full}} \rangle \end{aligned} \tag{9.34}$$

This relationship alone is insufficient to solve for the number-conserving density matrices in terms of the full density matrix. Instead, we introduce the number operator from Eq. (9.27) to define a new matrix with elements given by

$${P1}_{k,l}^{i,j} = \langle \Psi | \hat{a}_i^\dagger \hat{a}_j^\dagger \hat{a}_l \hat{a}_k \hat{N} | \Psi \rangle \tag{9.35}$$

The elements of this new matrix can be obtained by again directly computing the expectation values of Pauli matrices in a manner directly analogous to that described in 9.6.2 with the creation and annihilation operators in the basis of Pauli matrices being written as shown in Eqs. (9.15) and (9.16) and the number operator being written as shown in Eq. (9.27). Thus, each element can be expressed as

$$\hat{a}_j^\dagger \hat{a}_{j+1}^\dagger \hat{a}_{k+1} \hat{a}_k \hat{N} = \frac{1}{32} \sum_{q=0}^{r} \left(X_j - iY_j\right) \left(X_{j+1} - iY_{j+1}\right) \left(X_{k+1} + iY_{k+1}\right) \left(X_k + iY_k\right) \left(1 - Z_q\right) \tag{9.36}$$

so that the expectation values of four- and five-qubit Pauli expressions—such as $X_j Y_{j+1} X_{k+1} Y_k$ and $X_j Y_{j+1} X_{k+1} Y_k Z_q$—can be directly probed on the quantum device in order to compute the each element of the P_1 matrix.

Each element of the P_1 matrix can additionally be represented as the following linear combination of number-conserving density matrices (${}^2D_{r,N}$)

$${P_1}_{k,l}^{i,j} = \left(\frac{1}{2}\right)^{r/2} \left[\sum_{i=0}^{r/2} \binom{r/2}{i} \left[(2i)^1\right] \left({}^2D_{r,2i}{}_{k,l}^{i,j}\right)\right] \tag{9.37}$$

Similarly, other matrices can be defined with elements

$${P_x}_{k,l}^{i,j} = \langle \Psi | \hat{a}_i^\dagger \hat{a}_j^\dagger \hat{a}_l \hat{a}_k \hat{N}^x | \Psi \rangle \tag{9.38}$$

which can be additionally be represented according to

$${P_x}_{k,l}^{i,j} = \left(\frac{1}{2}\right)^{r/2} \left[\sum_{i=0}^{r/2} \binom{r/2}{i} \left[(2i)^x\right] \left({}^2D_{r,2i}{}_{k,l}^{i,j}\right)\right] \tag{9.39}$$

Obtaining ${}^2D_{r,\text{full}}$, P_1, P_2, etc. directly from probing expectation values of Pauli matrices and solving the system of linear equations described by Eqs. (9.34), (9.37), and (9.39) for

the individual number-conserving density matrices (${}^2D_{r,N}$) allows for the computation of the signature of ODLRO (λ_D) corresponding to each of the number-conserving substates.

As can be readily observed, this methodology for obtaining the number-conserving substates quickly becomes prohibitively expensive as system size is increased. As such, this study relies on the methodology presented in the following section.

Tomography via Direct Computation of the wave function

wave functions corresponding to each individual number-conserving substate can be determined from the probability information obtained from a quantum device in a manner analogous to how the full AGP wave function is prepared as described in 9.6.2. Specifically, for a specific possible, even value of $N \in \{0, 2, 4, \ldots, r\}$, each element of the number-conserving wave function ($|\Psi_i^{r,N}\rangle$) in the basis of the 2^r possible stated ($|\eta_i\rangle$) can be obtained according to

$$|\Psi_i^{r,N}\rangle = \begin{cases} 0 & if\ \hat{N}|\eta_i\rangle \neq N|\eta_i\rangle \\ +|\langle\eta_i|\Psi\rangle| & if\ \hat{N}|\eta_i\rangle = N|\eta_i\rangle \end{cases} \tag{9.40}$$

whereby if the basis state $|\eta_i\rangle$ contains N particles (i.e., has N qubits in the $|1\rangle$ state), the element of the number-conserving wave function ($|\Psi_i^{r,N}\rangle$) corresponding to that basis state is identical to that from the full wave function ($|\Psi_i\rangle$); however, if the basis state $|\eta_i\rangle$ doesn't contain N particles, $|\Psi_i^{r,N}\rangle$ is set to zero. The resulting number-conserving wave function is then normalized to one.

The signature of ODLRO (λ_D) can then be obtained directly from the number-conserving wave function in the manner described in 9.6.2. Note that this projection can act as a form of error mitigation as contributions from bases corresponding to odd-numbered basis states—and indeed all basis states not corresponding to the number of particles of interest—are omitted. Additionally note that for QASM simulation, this methodology for isolating the number-conserving substates from the data obtained from the quantum device yields

identical results within sampling error to the methodology presented in 9.6.3 while being significantly less computationally expensive. As such, tomography via direct computation of the wave function is employed in this study.

9.6.4 Description of Noise on Near-Term Quantum Devices

Three main classes of errors lead to the deviation of physical qubits from the idealized logical qubits: namely, gate noise, readout noise, and decoherence. Quantum gate noise/error refers to a situation where the application of a unitary gate $\hat{U}$ to a quantum state $|\Psi\rangle$ yields a result that deviates from $\hat{U}|\Psi\rangle$. This class of error is caused by either imprecisely calibrated control of the qubits and/or imperfect isolation of qubits from their environment, and the overall gate error increases with the number of gates applied. Readout noise/error refers to transmission line noise that makes the $|0\rangle$ state appear to be $|1\rangle$ or vice versa; it can be caused by the probability distributions of the measured physical quantities that correspond to the $|0\rangle$ and $|1\rangle$ states overlapping and/or the qubit decaying during readout. Decoherence involves interactions with external systems (vibrations, temperature fluctuations, electromagnetic waves, etc.) leading to the degradation of the quantum state prepared on quantum devices. As both the number of gates applied to a system—and hence gate noise—and decoherence tend to increase with system size (r), larger-scale quantum computations often involve more and more error [254]. See the Supplemental Information of Ref. [5] for a more thorough exploration of error on near-term quantum devices.

9.6.5 Analysis of Errors Via Joint Probabilities of Occupation

Comparing the results obtained from the simulated and experimental Melbourne data illustrates the error associated with the Melbourne device. The probability of a given orbital (i.e. qubit) being occupied if the orbital with index 0 (i.e., Q0) is occupied was computed for all combinations of total orbitals (qubits, r) and particles ($|1\rangle$ qubit states, N), and the results

for $N = 2$ are shown in Tab. 9.1 in order to comment on relative error based on system size (r). Note that all other joint probabilities for Melbourne and QASM simulation are given in Tabs. 9.2 and 9.3, respectively.

As can be seen from the joint probability data in Tab. 9.1, simulated results exactly demonstrate the orbital (qubit) pairing that we program into the system as the only possible two-particle orientation with Q0 being occupied should be to have Q1 simultaneously occupied. However, due to errors on Melbourne, this ideal behavior is not exactly recreated on the experimental quantum device. Specifically, the joint probability of occupying Q0 and Q1 is not unity and seems to decrease with increasing system size. Additionally, the joint probability of Q0 and Qi where $i \neq 0, 1$ should be zero as is seen in QASM simulation; however, the experimental data demonstrates that other double-excitations are contributing to the overall two-particle substate, indicating error in either state preparation or measurement. Overall, the error associated with noisy near-term quantum computers decreases the signature of ODLRO, indicating less ODLRO character for the experimentally-prepared states than predicted by QASM simulation. In order to best construct and probe entangled states on quantum computers, then, errors on real-world devices need to be minimized.

r,N	$\lambda_D^{sim.}$	Probability of Occupation if Particle on Q0 (sim.)
2, 2	0.502	[x, 1.000]
4, 2	0.745	[x, 1.000, 0.000, 0.000]
6, 2	0.996	[x, 1.000, 0.000, 0.000, 0.000, 0.000]
8, 2	1.253	[x, 1.000, 0.000, 0.000, 0.000, 0.000, 0.000, 0.000]
10, 2	1.500	[x, 1.000, 0.000, 0.000, 0.000, 0.000, 0.000, 0.000, 0.000, 0.000]
12, 2	1.755	[x, 1.000, 0.000, 0.000, 0.000, 0.000, 0.000, 0.000, 0.000, 0.000, 0.000, 0.000]
14, 2	1.991	[x, 1.000, 0.000, 0.000, 0.000, 0.000, 0.000, 0.000, 0.000, 0.000, 0.000, 0.000, 0.000, 0.000]
r,N	$\lambda_D^{mel.}$	Probability of Occupation if Particle on Q0 (mel.)
2, 2	0.437	[x, 1.000]
4,2	0.616	[x, 0.972, 0.014, 0.014]
6,2	0.783	[x, 0.946, 0.013, 0.010, 0.013, 0.018]
8,2	0.898	[x, 0.831, 0.016, 0.039, 0.027, 0.031, 0.037, 0.018]
10,2	0.937	[x, 0.856, 0.024, 0.011, 0.011, 0.019, 0.017, 0.024, 0.010, 0.027]
12,2	1.116	[x, 0.678, 0.067, 0.019, 0.036, 0.026, 0.046, 0.041, 0.026, 0.031, 0.012, 0.017]
14,2	1.261	[x, 0.784, 0.026, 0.009, 0.009, 0.009, 0.004, 0.043, 0.013, 0.022, 0.039, 0.030, 0.009, 0.004]

Table 9.1: The joint probability of the occupation numbers of other orbitals (qubits) if the first orbital ($Q0$) is filled for QASM simulation (sim.) and ibmq_16_melbourne results.

9.6.6 Experimental QASM Simulator and Quantum Device Specifications

Throughout this work, we have employed QASM simultator [373] and Melbourne [8] IBM Quantum Experience devices, which are available online. The QASM simulator is a general-purpose simulator that emulates execution of quantum circuits in either an ideal manner (i.e., with only sampling error) or subject to highly-configurable noise modeling; in this study, all reported QASM results are ideal. The ibmq_16_melbourne device is composed of fixed-frequency transmon qubits with co-planer waveguide resonators [272, 274]. Experimental calibration data and connectivity for this device—as well as that for other devices employed in obtaining supplemental data—is given in Tablels 9.4-9.7.

9.6.7 State Preparation Fidelity

To provide a metric on which to judge the degree to which the expected state preparation was prepared on the quantum devices employed, we include the state preparation fidelity given by [374]

$$\mathcal{F}(\Psi_{\text{ideal}}, \Psi_{\text{exp.}}) = |\langle \Psi_{\text{ideal}} | \Psi_{\text{exp.}} \rangle|^2 \tag{9.41}$$

where $|\Psi_{\text{ideal}}\rangle$ is the wave function corresponding to the result of applying the unitary obtained from the matrix form of the state preparation given in Eq. (9.12) to the all-zero initial state $\left(\bigotimes_{p=0}^{r-1} |0\rangle \right)$ and is hence the ideal expected outcome for a given state preparation on a device with no error and where $|\Psi_{\text{exp.}}\rangle$ represents the wave function obtained from the quantum device. The state preparation fidelities for ibmq_16_melbourne and QASM simulation are reported in Tabs. 9.2 and 9.3.

9.6.8 Additional Device Data

While only data from QASM simulation and the ibmq_16_melbourne quantum device are presented, additional data for ibmq_5_yorktown, ibmq_santiago, and ibmq_rochester are

r	N	λ_D	$\mathcal{F}$	Probability of Occupation if Particle in Q0
	all	0.437	0.924	[x, 0.930]
2	0	0.000	1.000	N/a
	2	1.000	1.000	[x, 1.000]
	all	0.616	0.788	[x, 0.92, 0.476, 0.472]
4	0	0.000	1.000	N/a
	2	0.971	0.971	[x, 0.972, 0.014, 0.014]
	4	1.000	1.000	[x, 1.000, 1.000, 1.000]
	all	0.783	0.658	[x, 0.920, 0.484, 0.483, 0.424, 0.438]
	0	0.000	1.000	N/a
6	2	0.923	0.916	[x, 0.946, 0.013, 0.010, 0.013, 0.018]
	4	1.250	0.916	[x, 0.974, 0.569, 0.563, 0.444, 0.449]
	6	1.000	1.000	[x, 1.000, 1.000, 1.000, 1.000, 1.000]
	all	0.898	0.466	[x, 0.842, 0.436, 0.476, 0.498, 0.487, 0.549, 0.494]
	0	0.000	1.000	N/a
8	2	0.788	0.777	[x, 0.831, 0.016, 0.039, 0.027, 0.031, 0.037, 0.018]
	4	1.230	0.728	[x, 0.871, 0.311, 0.348, 0.351, 0.341, 0.410, 0.368]
	6	1.291	0.791	[x, 0.928, 0.599, 0.630, 0.698, 0.692, 0.743, 0.710]
	8	1.000	1.000	[x, 1.000, 1.000, 1.000, 1.000, 1.000, 1.000, 1.000]
	all	0.937	0.303	[x, 0.897, 0.475, 0.401, 0.452, 0.541, 0.483, 0.448, 0.384, 0.462]
	0	0.000	1.000	N/a
	2	0.631	0.624	[x, 0.856, 0.024, 0.011, 0.011, 0.019, 0.017, 0.024, 0.010, 0.027]
10	4	1.084	0.500	[x, 0.898, 0.282, 0.217, 0.241, 0.332, 0.294, 0.263, 0.193, 0.281]
	6	1.280	0.498	[x, 0.928, 0.525, 0.446, 0.517, 0.624, 0.541, 0.495, 0.422, 0.502]
	8	1.211	0.606	[x, 0.958, 0.761, 0.697, 0.776, 0.860, 0.784, 0.740, 0.682, 0.742]
	10	1.000	1.000	[x, 1.000, 1.000, 1.000, 1.000, 1.000, 1.000, 1.000, 1.000, 1.000]
	all	1.116	0.269	[x, 0.820, 0.486, 0.417, 0.479, 0.512, 0.558, 0.482, 0.420, 0.491, 0.502, 0.490]
	0	0.000	1.000	N/a
	2	0.647	0.626	[x, 0.678, 0.067, 0.019, 0.036, 0.026, 0.046, 0.041, 0.026, 0.031, 0.012, 0.017]
12	4	1.130	0.478	[x, 0.763, 0.237, 0.156, 0.213, 0.244, 0.295, 0.236, 0.171, 0.239, 0.229, 0.216]
	6	1.404	0.445	[x, 0.840, 0.407, 0.327, 0.425, 0.453, 0.507, 0.432, 0.347, 0.418, 0.428, 0.416]
	8	1.450	0.485	[x, 0.889, 0.600, 0.533, 0.619, 0.650, 0.688, 0.597, 0.531, 0.616, 0.644, 0.633]
	10	1.288	0.616	[x, 0.944, 0.805, 0.763, 0.790, 0.821, 0.868, 0.796, 0.767, 0.820, 0.811, 0.817]
	12	1.000	1.000	[x, 1.000, 1.000, 1.000, 1.000, 1.000, 1.000, 1.000, 1.000, 1.000, 1.000, 1.000]
	all	1.261	0.193	[x, 0.893, 0.389, 0.320, 0.588, 0.491, 0.507, 0.599, 0.499, 0.514, 0.548, 0.538, 0.459, 0.464]
	0	0.000	1.000	N/a
	2	0.555	0.535	[x, 0.784, 0.026, 0.009, 0.009, 0.009, 0.004, 0.043, 0.013, 0.022, 0.039, 0.030, 0.009, 0.004]
	4	1.038	0.375	[x, 0.840, 0.100, 0.069, 0.205, 0.135, 0.175, 0.273, 0.211, 0.215, 0.241, 0.252, 0.139, 0.146]
14	6	1.358	0.326	[x, 0.869, 0.229, 0.167, 0.440, 0.310, 0.351, 0.478, 0.360, 0.380, 0.418, 0.413, 0.287, 0.300]
	8	1.510	0.335	[x, 0.906, 0.382, 0.302, 0.616, 0.506, 0.529, 0.641, 0.510, 0.519, 0.575, 0.563, 0.472, 0.478]
	10	1.483	0.402	[x, 0.933, 0.576, 0.497, 0.794, 0.715, 0.699, 0.760, 0.665, 0.683, 0.700, 0.688, 0.648, 0.640]
	12	1.282	0.561	[x, 0.963, 0.789, 0.741, 0.907, 0.879, 0.864, 0.875, 0.805, 0.820, 0.829, 0.829, 0.843, 0.856]
	14	1.000	1.000	[x, 1.000, 1.000, 1.000, 1.000, 1.000, 1.000, 1.000, 1.000, 1.000, 1.000, 1.000, 1.000, 1.000]

Table 9.2: All eigenvalue (λ_D) information for the non-number-conserving overall state (all) and the number-conserving substates are given with state preparation fidelities ($\mathcal{F}$) and joint probability of occupation numbers of other orbitals (qubits) if the first orbital ($Q0$) is filled for ibmq_16_melbourne.

provided in Tabs. 9.8-9.10.

r	N	λ_D	$\mathcal{F}$	Probability of Occupation if Particle in Q0
	all	0.502	1.000	[x, 1.000]
2	0	0.000	1.000	N/a
	2	1.000	1.000	[x, 1.000]
	all	0.745	1.000	[x, 1.000, 0.506, 0.506]
4	0	0.000	1.000	N/a
	2	1.000	1.000	[x, 1.000, 0.000, 0.000]
	4	1.000	1.000	[x, 1.000, 1.000, 1.000]
	all	0.996	1.000	[x, 1.000, 0.491, 0.491, 0.497, 0.497]
	0	0.000	1.000	N/a
6	2	1.000	1.000	[x, 1.000, 0.000, 0.000, 0.000, 0.000]
	4	1.333	1.000	[x, 1.000, 0.494, 0.494, 0.506, 0.506]
	6	1.000	1.000	[x, 1.000, 1.000, 1.000, 1.000, 1.000]
	all	1.253	1.000	[x, 1.000, 0.505, 0.505, 0.498, 0.498, 0.506, 0.506]
	0	0.000	1.000	N/a
8	2	1.000	1.000	[x, 1.000, 0.000, 0.000, 0.000, 0.000, 0.000, 0.000]
	4	1.499	1.000	[x, 1.000, 0.334, 0.334, 0.331, 0.331, 0.335, 0.3358]
	6	1.500	1.000	[x, 1.000, 0.671, 0.671, 0.657, 0.657, 0.673, 0.673]
	8	1.000	1.000	[x, 1.000, 1.000, 1.000, 1.000, 1.000, 1.000, 1.000]
	all	1.500	1.000	[x, 1.000, 0.499, 0.499, 0.499, 0.499, 0.502, 0.502, 0.490, 0.490]
	0	0.000	1.000	N/a
	2	1.000	1.000	[x, 1.000, 0.000, 0.000, 0.000, 0.000, 0.000, 0.000, 0.000, 0.000]
10	4	1.598	1.000	[x, 1.000, 0.233, 0.233, 0.274, 0.274, 0.263, 0.263, 0.230, 0.230]
	6	1.798	1.000	[x, 1.000, 0.519, 0.519, 0.481, 0.481, 0.499, 0.499, 0.500, 0.500]
	8	1.600	1.000	[x, 1.000, 0.743, 0.743, 0.760, 0.760, 0.758, 0.758, 0.739, 0.739]
	10	1.000	1.000	[x, 1.000, 1.000, 1.000, 1.000, 1.000, 1.000, 1.000, 1.000, 1.000]
	all	1.755	1.000	[x, 1.000, 0.518, 0.518, 0.499, 0.499, 0.508, 0.508, 0.502, 0.502, 0.509, 0.509]
	0	0.000	1.000	N/a
	2	1.000	1.000	[x, 1.000, 0.000, 0.000, 0.000, 0.000, 0.000, 0.000, 0.000, 0.000, 0.000, 0.000]
12	4	1.664	1.000	[x, 1.000, 0.228, 0.228, 0.205, 0.205, 0.184, 0.184, 0.181, 0.181, 0.202, 0.202]
	6	1.997	1.000	[x, 1.000, 0.410, 0.410, 0.376, 0.376, 0.389, 0.389, 0.432, 0.432, 0.393, 0.393]
	8	1.997	1.000	[x, 1.000, 0.615, 0.615, 0.590, 0.590, 0.619, 0.619, 0.567, 0.567, 0.609, 0.609]
	10	1.666	1.000	[x, 1.000, 0.792, 0.792, 0.810, 0.810, 0.802, 0.802, 0.793, 0.793, 0.802, 0.802]
	12	1.000	1.000	[x, 1.000, 1.000, 1.000, 1.000, 1.000, 1.000, 1.000, 1.000, 1.000, 1.000, 1.000]
	all	1.991	1.000	[x, 1.000, 0.494, 0.494, 0.497, 0.497, 0.501, 0.501, 0.506, 0.506, 0.500, 0.500, 0.494, 0.494]
	0	0.000	1.000	N/a
	2	1.000	0.999	[x, 1.000, 0.000, 0.000, 0.000, 0.000, 0.000, 0.000, 0.000, 0.000, 0.000, 0.000, 0.000, 0.000]
	4	1.707	1.000	[x, 1.000, 0.134, 0.134, 0.167, 0.167, 0.149, 0.149, 0.205, 0.205, 0.167, 0.167, 0.177, 0.177]
14	6	2.137	1.000	[x, 1.000, 0.334, 0.334, 0.332, 0.332, 0.315, 0.315, 0.330, 0.330, 0.359, 0.359, 0.331, 0.331]
	8	2.278	1.000	[x, 1.000, 0.508, 0.508, 0.477, 0.477, 0.514, 0.514, 0.518, 0.518, 0.482, 0.482, 0.502, 0.502]
	10	2.138	1.000	[x, 1.000, 0.649, 0.649, 0.679, 0.679, 0.684, 0.684, 0.669, 0.669, 0.675, 0.675, 0.644, 0.644]
	12	1.713	1.000	[x, 1.000, 0.835, 0.835, 0.864, 0.864, 0.835, 0.835, 0.818, 0.818, 0.813, 0.813, 0.835, 0.835]
	14	1.000	1.000	[x, 1.000, 1.000, 1.000, 1.000, 1.000, 1.000, 1.000, 1.000, 1.000, 1.000, 1.000, 1.000, 1.000]

Table 9.3: All eigenvalue (λ_D) information for the non-number-conserving overall state (all) and the number-conserving substates are given with state preparation fidelities ($\mathcal{F}$) and joint probability of occupation numbers of other orbitals (qubits) if the first orbital ($Q0$) is filled for QASM simulation.

Table 9.4: Calibration data for "Yorktown"

Device:	ibmqx2 ("Yorktown")						
Calibration Date:	09/10/20						
Version:	2.0.0						
Gate time (ns):	71.1						
Qubit:		0	1	2	3	4	
	T2 (μs)	24.6	24.8	90.8	41.5	45.0	
	f (GHz)	5.28	5.25	5.03	5.29	5.08	
	T1 (μs)	46.7	40.1	60.2	60.9	73.3	
	Gate Error (10^{-3})	0.99	1.94	0.59	0.49	0.52	
	Readout Error (10^{-3})	65.2	41.6	29.2	17.0	30.8	
Multi-Qubit:		0,1	0,2	1,2	2,3	2,4	3,4
	Error (10^{-3})	20.9	14.7	22.2	15.3	15.0	13.7

Table 9.5: Calibration data for "Santiago"

Device:	ibmq_santiago ("Santiago")					
Calibration Date:	09/10/20					
Version:	2.0.0					
Gate time (ns):	561.78					
Qubit:		0	1	2	3	4
	T2 (μs)	149.2	86.3	100.8	108.1	123.2
	f (GHz)	4.83	4.62	4.82	4.74	4.82
	T1 (μs)	74.0	190.2	138.2	161.5	106.9
	Gate Error (10^{-3})	0.32	0.18	0.19	0.19	0.20
	Readout Error (10^{-3})	22.6	12.1	8.8	10.9	7.5
Multi-Qubit:		0,1	1,2	2,3	3,4	
	Error (10^{-3})	10.5	7.8	5.8	5.4	

Table 9.6: Calibration data for “Melbourne”

Device:	ibmq_16_melbourne (“Melbourne”)																					
Calibration Date:	09/02/20																					
Version:	2.0.0																					
Gate time (ns):	53.3																					
Qubit:		0	1	2	3	4	5	6	7	8	9	10	11	12	13	14						
	T2 (µs)	95.6	56.0	87.9	16.5	63.1	37.7	77.4	14.4	101.6	30.9	92.3	24.9	68.8	34.4	64.6						
	f (GHz)	5.11	5.24	5.04	4.89	5.02	5.07	4.93	4.98	4.75	4.97	4.94	5.00	4.76	4.97	5.01						
	T1 (µs)	73.7	56.0	63.1	66.7	59.1	20.3	72.5	38.0	108.6	44.5	64.5	14.6	71.9	32.2	45.8						
	Gate Error (10^{-3})	0.64	1.03	0.64	0.50	0.80	3.16	1.19	1.66	0.76	1.48	2.00	50.90	0.83	2.14	0.61						
	Readout Error (10^{-3})	27.8	34.3	25.2	89.1	38.7	43.9	33.1	66.0	55.4	78.3	72.9	268.3	159.3	80.1	50.7						
Multi-Qubit:		0,1	0,14	1,2	1,13	2,3	2,12	3,4	3,11	4,5	4,10	5,6	5,9	6,8	7,8	8,9	9,10	10,11	11,12	12,13	13,14	
	Error (10^{-3})	19.9	28.1	12.0	45.8	25.5	38.8	17.1	1000.0	26.2	27.8	58.3	32.8	28.4	34.3	39.4	39.7	1000.0	1000.0	22.5	35.7	

Table 9.7: Calibration data for “Rochester”

Device:	ibmq_rochester (“Rochester”)																				
Calibration Date:	2/26/20																				
Version:	1.2.0																				
Gate time (ns):	53.3																				
Qubit:		0	1	2	3	4	5	6	7	8	9	10	11	12	13	14	15	16	17	18	19
	T2 (µs)	77.9	48.3	61.1	78.3	59.2	74.6	63.8	32.9	53.2	55.4	73.5	56.8	67.8	66.7	64.7	26.0	46.7	11.2	43.4	47.0
	f (GHz)	4.92	5.08	5.00	5.05	4.94	5.05	5.05	4.93	5.03	4.97	5.06	4.93	5.05	4.95	5.07	4.87	5.08	4.99	5.06	5.02
	T1 (µs)	51.0	41.8	54.2	49.3	51.9	53.0	46.6	56.4	45.8	44.3	59.4	64.6	57.3	53.9	54.9	50.5	36.6	47.6	51.2	62.6
	Gate Error (10^{-3})	0.88	1.24	4.48	3.74	1.16	1.61	1.43	13.95	8.85	1.80	0.88	1.47	1.96	2.06	0.74	0.95	0.61	1.18	1.09	1.19
	Readout Error (10^{-3})	76.9	210.6	129.4	133.1	47.5	256.3	61.9	361.2	312.5	103.8	61.9	152.5	145.0	280.6	98.8	63.7	341.9	66.3	34.4	85.6
		20	21	22	23	24	25	26	27	28	29	30	31	32	33	34	35	36	37	38	39
	T2 (µs)	84.6	38.0	14.5	42.3	37.8	58.2	18.1	66.6	63.3	14.7	27.8	86.6	69.7	76.2	32.0	22.6	11.5	50.7	50.7	45.4
	f (GHz)	4.89	5.14	4.90	4.96	4.88	4.97	5.02	4.99	5.02	5.00	5.13	4.96	5.15	5.21	4.97	5.05	5.03	5.17	4.91	5.05
	T1 (µs)	65.4	48.1	54.0	79.1	62.0	61.2	48.8	54.0	55.6	63.9	31.2	66.2	47.2	58.8	55.0	61.4	50.1	51.6	79.1	55.5
	Gate Error (10^{-3})	0.64	4.13	1.12	1.54	1.25	0.69	1.73	1.92	0.85	2.05	3.77	1.12	2.59	1.10	1.11	2.95	4.21	1.07	0.96	1.06
	Readout Error (10^{-3})	17.5	87.5	130.0	335.0	35.6	175.0	56.3	121.3	196.3	26.2	353.8	171.3	58.1	65.0	38.7	209.4	25.6	171.3	195.6	125.0
		40	41	42	43	44	45	46	47	48	49	50	51	52							
	T2 (µs)	79.6	35.3	83.7	46.3	48.1	57.0	60.9	63.8	89.4	50.2	31.1	47.8	57.9							
	f (GHz)	5.06	5.05	4.99	5.07	4.98	5.09	5.03	5.07	4.97	5.07	4.96	5.13	5.04							
	T1 (µs)	53.4	51.0	45.2	51.7	64.4	44.5	51.8	57.2	68.4	46.5	60.9	59.5	54.5							
	Gate Error (10^{-3})	1.76	1.87	0.62	1.05	0.90	1.00	1.46	0.86	1.38	0.88	0.90	8.12	5.01							
	Readout Error (10^{-3})	121.9	446.3	36.9	197.5	103.8	154.4	243.8	161.9	28.1	345.6	104.4	110.6	266.3							
Multi-Qubit:		0,1	0,5	1,2	2,3	3,4	4,6	5,9	6,13	7,8	7,16	8,9	9,10	10,11	11,12	11,17	12,13	13,14	14,15	15,18	16,19
	Error (10^{-3})	63.0	54.1	32.9	60.5	48.4	39.2	31.6	1000.0	1000.0	1000.0	1000.0	35.7	24.2	51.0	20.5	1000.0	46.3	80.9	35.1	22.7
		17,23	18,27	19,20	20,21	21,22	21,28	22,23	23,24	24,25	25,26	25,29	26,27	29,36	30,31	30,39	31,32	32,33	33,34	34,35	34,40
	Error (10^{-3})	40.1	39.4	20.8	32.8	69.4	38.2	59.2	36.4	38.8	45.2	73.1	33.6	75.4	1000.0	1000.0	39.4	31.5	37.6	38.9	33.3
		35,36	36,37	37,38	38,41	39,42	40,46	41,50	42,43	43,44	44,45	44,51	45,46	46,47	47,48	48,49	48,52	49,50			
	Error (10^{-3})	56.2	92.7	58.8	1000.0	38.7	40.8	1000.0	28.0	28.0	1000.0	134.6	1000.0	29.2	19.8	31.4	49.4	29.7			

r	N	λ_D	Probability of Occupation if Particle on Q0
2	all	0.460	[x, 0.902]
	0	0.000	N/a
	2	1.000	[x, 1.000]
4	all	0.658	[x, 0.900, 0.486, 0.493]
	0	0.000	N/a
	2	0.957	[x, 0.983, 0.006, 0.011]
	4	1.000	[x, 1.000, 1.000, 1.000]

Table 9.8: All eigenvalue information for the non-number-conserving overall state (all) and the number-conserving substates are given with joint probability of occupation numbers of other orbitals (qubits) if the first orbital ($Q0$) is filled for ibmq_5_yorktown.

r	N	λ_D	Probability of Occupation if Particle on Q0
2	all	0.429	[x, 0.959]
	0	0.000	N/a
	2	1.000	[x, 1.000]
4	all	0.669	[x, 0.964, 0.506, 0.508]
	0	0.000	N/a
	2	0.998	[x, 0.997, 0.001, 0.002]
	4	1.000	[x, 1.000, 1.000, 1.000]

Table 9.9: All eigenvalue information for the non-number-conserving overall state (all) and the number-conserving substates are given with joint probability of occupation numbers of other orbitals (qubits) if the first orbital ($Q0$) is filled for ibmq_santiago.

r	N	λ_D	Probability of Occupation if Particle on Q0
2	all	0.339	[x, 0.690]
	0	0.000	N/a
	2	1.000	[x, 1.000]
4	all	0.490	[x, 0.687, 0.507, 0.511]
	0	0.000	N/a
	2	0.779	[x, 0.785, 0.114, 0.101]
	4	1.000	[x, 1.000, 1.000, 1.000]
6	all	0.673	[x, 0.771, 0.514, 0.522, 0.501, 0.497]
	0	0.000	N/a
	2	0.727	[x, 0.720, 0.088, 0.099, 0.042, 0.051]
	4	1.071	[x, 0.853, 0.548, 0.552, 0.526, 0.520]
	6	1.000	[x, 1.000, 1.000, 1.000, 1.000, 1.000]
8	all	0.746	[x, 0.751, 0.504, 0.484, 0.469, 0.495, 0.519, 0.497]
	0	0.000	N/a
	2	0.514	[x, 0.549, 0.075, 0.076, 0.088, 0.087, 0.076, 0.049]
	4	0.921	[x, 0.740, 0.389, 0.374, 0.355, 0.373, 0.399, 0.370]
	6	1.015	[x, 0.851, 0.689, 0.668, 0.645, 0.686, 0.734, 0.727]
	8	1.000	[x, 1.000, 1.000, 1.000, 1.000, 1.000, 1.000, 1.000]
10	all	0.898	[x, 0.819, 0.483, 0.536, 0.465, 0.432, 0.508, 0.515, 0.477, 0.455]
	0	0.000	N/a
	2	0.515	[x, 0.608, 0.053, 0.072, 0.045, 0.050, 0.042, 0.050, 0.042, 0.038]
	4	0.966	[x, 0.759, 0.293, 0.342, 0.254, 0.237, 0.288, 0.300, 0.279, 0.249]
	6	1.163	[x, 0.847, 0.518, 0.578, 0.494, 0.446, 0.555, 0.564, 0.514, 0.485]
	8	1.108	[x, 0.925, 0.751, 0.785, 0.751, 0.707, 0.795, 0.801, 0.752, 0.735]
	10	1.000	[x, 1.000, 1.000, 1.000, 1.000, 1.000, 1.000, 1.000, 1.000, 1.000]
12	all	0.974	[x, 0.846, 0.518, 0.534, 0.568, 0.555, 0.426, 0.422, 0.469, 0.447, 0.476, 0.474]
	0	0.000	N/a
	2	0.361	[x, 0.565, 0.056, 0.040, 0.052, 0.048, 0.044, 0.032, 0.028, 0.016, 0.073, 0.044]
	4	0.831	[x, 0.743, 0.222, 0.234, 0.314, 0.305, 0.192, 0.202, 0.182, 0.172, 0.215, 0.221]
	6	1.103	[x, 0.833, 0.443, 0.473, 0.519, 0.501, 0.350, 0.354, 0.378, 0.357, 0.394, 0.398]
	8	1.165	[x, 0.898, 0.654, 0.673, 0.671, 0.665, 0.534, 0.521, 0.617, 0.585, 0.592, 0.588]
	10	1.024	[x, 0.946, 0.850, 0.854, 0.823, 0.841, 0.752, 0.733, 0.849, 0.816, 0.763, 0.773]
	12	1.000	[x, 1.000, 1.000, 1.000, 1.000, 1.000, 1.000, 1.000, 1.000, 1.000, 1.000, 1.000]
14	all	0.909	[x, 0.529, 0.561, 0.487, 0.551, 0.545, 0.536, 0.515, 0.432, 0.451, 0.538, 0.539, 0.487, 0.485]
	0	0.000	N/a
	2	0.149	[x, 0.093, 0.155, 0.052, 0.031, 0.000, 0.062, 0.103, 0.103, 0.155, 0.062, 0.103, 0.031, 0.052]
	4	0.580	[x, 0.302, 0.311, 0.224, 0.161, 0.155, 0.260, 0.204, 0.235, 0.230, 0.280, 0.276, 0.175, 0.188]
	6	0.905	[x, 0.436, 0.436, 0.367, 0.374, 0.366, 0.405, 0.379, 0.333, 0.354, 0.439, 0.438, 0.338, 0.335]
	8	1.036	[x, 0.546, 0.589, 0.517, 0.599, 0.600, 0.573, 0.548, 0.446, 0.449, 0.556, 0.568, 0.504, 0.507]
	10	1.032	[x, 0.665, 0.713, 0.635, 0.802, 0.797, 0.711, 0.696, 0.582, 0.604, 0.720, 0.698, 0.691, 0.686]
	12	0.945	[x, 0.778, 0.850, 0.823, 0.943, 0.925, 0.873, 0.859, 0.764, 0.778, 0.838, 0.831, 0.866, 0.873]
	14	1.000	[0, 1.000, 1.000, 1.000, 1.000, 1.000, 1.000, 1.000, 1.000, 1.000, 1.000, 1.000, 1.000, 1.000]

Table 9.10: All eigenvalue information for the non-number-conserving overall state (all) and the number-conserving substates are given with joint probability of occupation numbers of other orbitals (qubits) if the first orbital ($Q0$) is filled for ibmq_rochester.

Part IV

The Fermion-Exciton Condensate

CHAPTER 10

POTENTIAL COEXISTENCE OF EXCITON AND FERMION PAIR CONDENSATIONS

Material from: Sager, L. M., Safaei, S., & Mazziotti, D. A., Potential coexistence of exciton and fermion pair condensations. Physical Review B, published 2020, 101(8), 081107.

10.1 Chapter Synopsis

An extensive theoretical and experimental investigation has been conducted on fermion-pair condensation and exciton condensation as distinct classes of Bose-Einstein-like condensation. In this study, the existence of a fermion-exciton condensate—a single quantum state in which the characters of both fermion-pair and exciton condensates coexist—is established computationally in the low-particle-number (N) limit and theoretically in the large-N thermodynamic limit. The trade-off between the fermion-pair and excitonic character of the fermion-exciton condensate is shown to be elliptic in nature. The possibility that the properties of fermion-exciton condensates could be a hybrid of the properties of fermion-pair condensates and exciton condensates is discussed, and future experimental and computational exploration of this class of condensate, which may potentially be realizable in a bilayer of superconductors, is anticipated.

10.2 Introduction

Ample experimental and theoretical investigation has centered around particle-particle fermion pair condensation (hereafter referred to as fermion pair condensation) [128, 137, 184, 185] and particle-hole fermion pair condensation (hereafter referred to as exciton condensation) [107, 156, 178, 179, 186–188]. Fermion pair condensates—the most familiar of which include

the class of Bardeen-Cooper-Schrieffer (BCS) superconductors [128]—occur when particle-particle pairs condense into a single quantum state to create a superfluid. For condensates of Cooper (electron) pairs, the superfluidity of the electrons cause the material through which they flow to be both a perfect conductor and a perfect diamagnet [184]. Similarly, exciton condensates involve the condensation of particle-hole pairs (excitons) into a single quantum state to create a superfluid. The superfluidity of the electron-hole pairs—while incapable of involving either the flow of matter or charge by definition—does involve the nondissipative transfer of energy [106, 107]. Exciton condensates have been experimentally observed in optical traps with polaritons [109, 110, 158, 189] and the electronic double layers of semiconductors [180, 186, 187, 190, 191] and graphene [164, 179, 192].

In order to combine the frictionless transfer of electrons of fermion pair condensates and the frictionless transfer of energy of exciton pair condensates, it may be beneficial to explore a system composed of both fermion pair and excitonic condensations. Both condensates are known to exist in systems designed to use exciton condensates to mediate the creation of Cooper pairs at higher temperatures [375, 376] (allowing for higher temperature fermion pair condensation). However, this coexistence of fermion pair and excitonic condensation occurs in two adjacent systems that interact with one another (such as a superconducting ring deposited around a semiconductor microcavity [376]) instead of existing in a joint fermion-exciton condensate state. As such, the properties of each condensate exist separately from one another instead of creating a system with the combined properties of both.

In this study, we address the possible coexistence of a fermion-exciton condensate that contains both fermion pair condensation and exciton condensation in a single quantum state (see Fig. 10.1). To this end, we use the theoretical signatures of fermion pair condensation—independently discovered by Yang [135] and Sasaki [136]—and exciton condensation—derived by Garrod and Rosina [155, 156]—to explore the fermion pair and exciton character of a small system and to develop a model wave function for macroscopic fermion-exciton condensation.

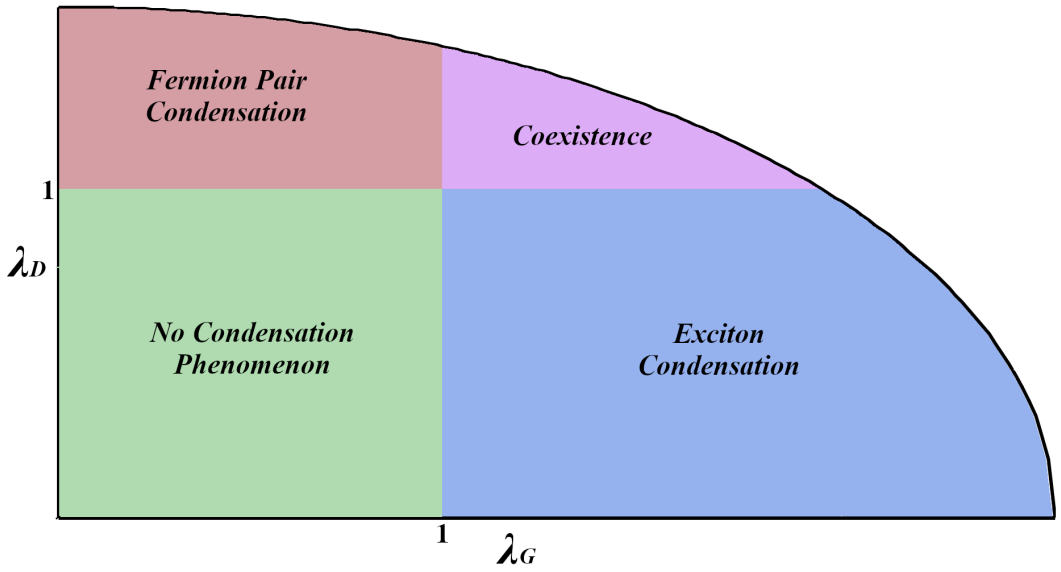

Figure 10.1: A figure demonstrating the elliptic trade-off between the signatures of fermion pair condensation, λ_D, and exciton condensation, λ_G, is shown.

10.3 Theory

Bosons, which are not bound by the Pauli exclusion principle due to their integer spin values, are able to condense into a single, lowest-energy orbital. A signature of this so-called Bose-Einstein condensation is a large eigenvalue of the one-boson reduced density matrix [119] with elements given by

$$^1D^i_j = \langle \Psi | \hat{b}^\dagger_i \hat{b}_j | \Psi \rangle \tag{10.1}$$

where $|\Psi\rangle$ is defined to be a N-boson wave function, each number represents both spatial and spin components of the boson, i, j correspond to one-boson orbitals in a finite basis set with rank r, and $\hat{b}^\dagger$ and $\hat{b}$ are bosonic creation and annihilation operators respectively.

Fermions, however, have half-integer spins and must obey the Pauli exclusion principle. Hence, the occupation of a given spin orbital must be either zero or one, and the one-fermion reduced density matrix (1-RDM) must have eigenvalues bounded above by one. For

fermion condensation to occur, pairs of fermions (creating a bosonic state) must condense into a single two-electron function [66, 135, 136, 221]; this two-electron analogue to the one-electron orbital is referred to as a geminal [222, 223]. The signature of fermion condensation is hence related to the two-fermion reduced density matrix (2-RDM) with elements given by

$$^2D^{i,j}_{k,l} = \langle \Psi | \hat{a}^\dagger_i \hat{a}^\dagger_j \hat{a}_k \hat{a}_l | \Psi \rangle \tag{10.2}$$

where $|\Psi\rangle$ is a N-fermion wave function, each number represents both spatial and spin components of the fermion, i, j, k, l correspond to one-fermion orbitals in a finite basis set with rank r, and $\hat{a}^\dagger$ and $\hat{a}$ are fermionic creation and annihilation operators respectively. In fact, Yang [135] and Sasaki [136] have independently demonstrated that a large eigenvalue of the 2-RDM (above the bound of one from the Pauli exclusion principle) is a signature of fermion pair condensation. Additionally, Sasaki [136] has proven that the eigenvalues of the 2-RDM are bounded by N for systems of $2N$ or $2N + 1$ fermions in the limit of strong correlation.

Analogous to fermion-fermion condensation into a single particle-particle function, exciton condensation is the condensation of particle-hole pairs (excitons) into a single particle-hole function. By comparison, one may hence expect a signature of exciton condensation to be a large eigenvalue in the particle-hole RDM [148, 155, 156] with elements given by

$$^2G^{i,j}_{k,l} = \langle \Psi | \hat{a}^\dagger_i \hat{a}_j \hat{a}^\dagger_l \hat{a}_k | \Psi \rangle \tag{10.3}$$

similar to the large eigenvalue of the fermionic 2-RDM for fermion pair condensation. However, there are two large eigenvalues of the particle-hole RDM with one corresponding to a ground-state-to-ground-state projection, not excitonic condensation [155]. To eliminate the extraneous large eigenvalue, we construct a modified particle-hole matrix with the ground-

state resolution removed with elements

$$ {}^2\tilde{G}^{i,j}_{k,l} = {}^2G^{i,j}_{k,l} - {}^1D^i_j {}^1D^l_k \tag{10.4} $$

which we denote as the ${}^2\tilde{G}$ matrix. While in the noninteracting limit, the eigenvalues of the ${}^2\tilde{G}$ matrix are zero or one, Garrod and Rosina have shown that the eigenvalue of the ${}^2\tilde{G}$ matrix is bounded by $\frac{N}{2}$ for an N-electron system in the limit of strong correlation [155]. This bound also describes the maximum number of excitons in a condensate.

10.4 Results

Unconstrained Calculations—In order to determine whether there is possible coexistence of exciton character and fermion pair character, general N-fermion wave functions in $r = 2N$ orbitals were constructed, and the coefficients of the wave functions were then optimized with respect to the signatures of fermion pair condensation (λ_D) and exciton condensation (λ_G). Specifically, multiobjective optimization was performed on $|\Psi\rangle$ with respect to a variable λ_{DG}, which depends on the largest eigenvalues of the ${}^2\tilde{G}$ matrix (λ_G) and the ${}^2D$ matrix (λ_D) according to

$$ \lambda_{DG} = w_G(\lambda_G - \lambda^o_G)^2 - (1 - w_G)\lambda_D \tag{10.5} $$

where w_G describes the weight given to the optimization of the largest eigenvalue of ${}^2\tilde{G}$ to the specified eigenvalue provided (λ^o_G) and where λ_D is left unconstrained. This optimization was conducted through use of a sequential quadratic programming (SQP) algorithm [377, 378] with gradients computed by second-order centered finite differences [379].

To visualize the entirety of λ_D versus λ_G space, we systematically varied the weight (w_G) and the specified eigenvalue of ${}^2\tilde{G}$ (λ^o_G). These visualizations for three and four electrons ($N = 3$ and $N = 4$) can be seen in Figs. 10.2a and 10.2b. The λ_D versus λ_G space for each case was then fit with a characteristic ellipse that defines the maximum λ_D for a given λ_G

and whose equation is given by

$$\left(\frac{\lambda_D - \gamma_D^{\min}}{\gamma_D^{\max} - \gamma_D^{\min}}\right)^2 + \left(\frac{\lambda_G - \gamma_G^{\min}}{\gamma_G^{\max} - \gamma_G^{\min}}\right)^2 = 1 \tag{10.6}$$

where the maximum eigenvalues of the ${}^2D$ and ${}^2\tilde{G}$ matrices are bounded by $\lambda_D \in [\gamma_D^{\min}, \gamma_D^{\max}]$ and $\lambda_G \in [\gamma_G^{\min}, \gamma_G^{\max}]$ respectively and where these maxima ($\gamma^{\max}$) and minima ($\gamma^{\min}$) were obtained from the previously-described scan over λ_D versus λ_G space.

Such elliptical nature of the boundary of the convex set of 2-RDMs when projected onto two dimensions has been previously observed in the context of quantum phase transitions [380–382].

Fig. 10.2a shows that for the case of three electrons in six orbitals ($N = 3$, $r = 6$), the eigenvalues of the ${}^2D$ matrix lie in the range $\lambda_D \in [0.5, 1]$, and the eigenvalues of the ${}^2\tilde{G}$ matrix lie in the range $\lambda_G \in [1, 1.5]$. As explained in the Theory section, strong fermion pair correlation is only seen when λ_D exceeds one; hence, for the $N = 3$ case, fermion pair condensation is not observed. However, exciton condensation—seen when λ_G exceeds one—can be obtained for this system. In fact, maximum exciton condensation ($\lambda_G = \frac{3}{2} = 1.5$) can be achieved. Thus, while exciton and fermion pair condensation can not coexist for the $N = 3$ case (as fermion pair condensation is not achievable), this small system can be used to further explore the properties of exciton condensation in future works.

Fig. 10.2b shows that for the case of four electrons in eight orbitals ($N = 4$, $r = 8$), the eigenvalues of the ${}^2D$ matrix lie in the range $\lambda_D \in [0.5, 1.5]$, and the eigenvalues of the ${}^2\tilde{G}$ matrix lie in the range $\lambda_G \in [0.7, 2]$. Therefore, both excitonic and fermion pair condensation can be observed as both λ_G and λ_D exceed one for certain $N = 4$ calculations. Interestingly, there is indeed a region in λ_D versus λ_G space where both eigenvalues surpass one, demonstrating the simultaneous existence of exciton and fermion pair condensations. However, as is apparent from the elliptical nature of the fit, there is a trade-off between

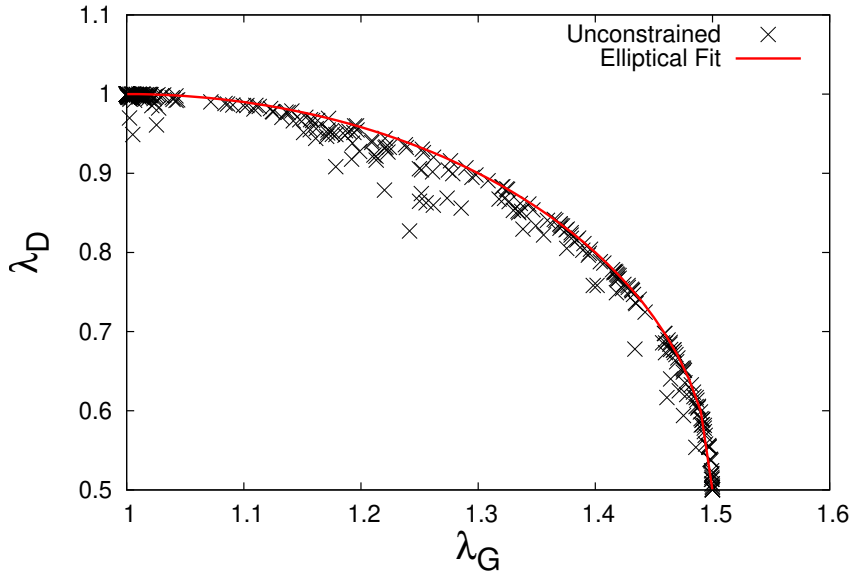

(a) N=3

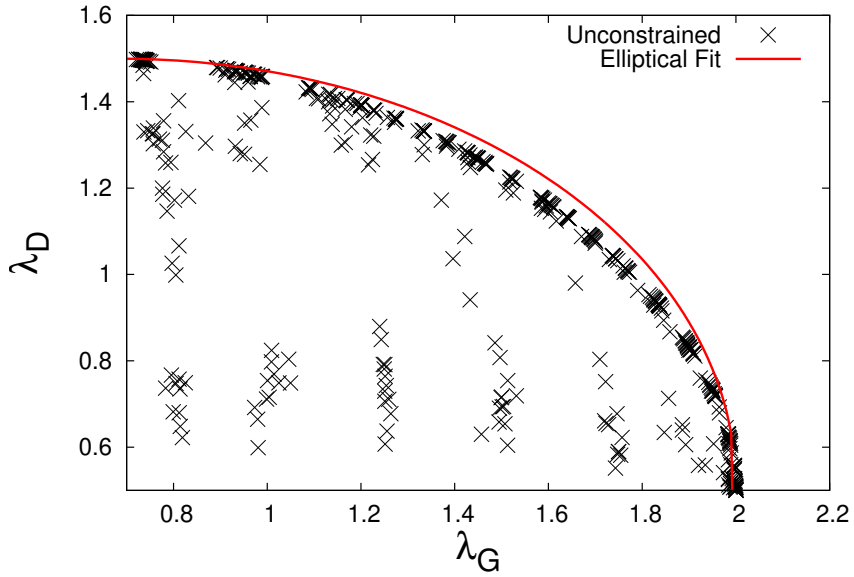

(b) N=4

Figure 10.2: Plots showing scans of λ_D versus λ_G are shown for unconstrained optimizations with a characteristic elliptical fit for the (a) $N = 3$ and (b) $N = 4$ cases.

the ability of the model system to exhibit high exciton character (a large λ_G) and high fermion pair character (a large λ_D). This compromise between the two behaviors is shown schematically in Fig. 10.1 and can be rationalized through analysis of the pairing behavior

of the r orbitals shown in Fig. 10.3.

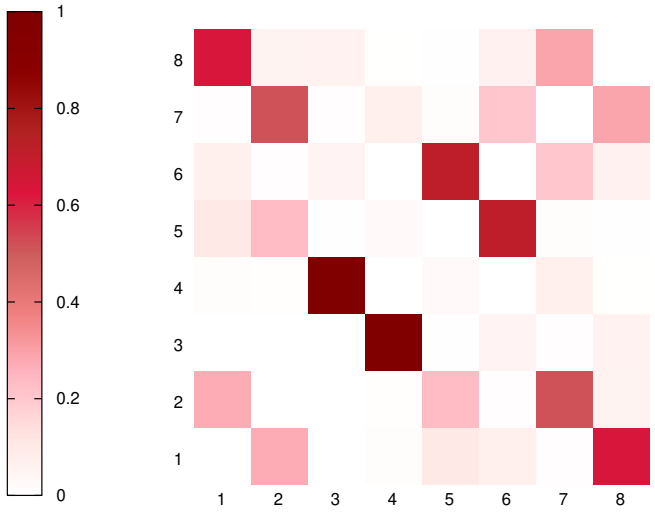

(a)

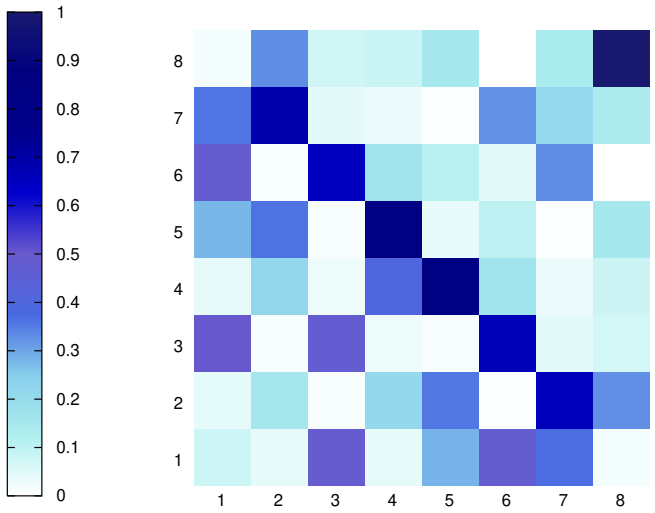

(b)

Figure 10.3: Visualizations of the (a) particle-particle pairs (red) and the (b) particle-hole pairs (blue) for optimizations of an $N = 4$ calculation demonstrating both exciton and fermion pair condensation (λ_G=1.52, $\lambda_D = 1.22$) are shown. Note that the darker the shade of each color, the greater the extent of particle-particle/particle-hole pairing between orbitals. The units of pair character are dimensionless.

Since excitons are particle-hole pairs and fermion pairs are particle-particle pairs, the existence of an excitonic relationship between orbitals should preclude a fermionic relationship between the same orbitals and vice versa. Figs. 10.3a and 10.3b present the fermion-paired orbitals (red) and the exciton-paired orbitals (blue) respectively for an unconstrained $N = 4$ calculation which demonstrated simultaneous fermion pair and excitonic condensation (λ_G=1.52, $\lambda_D = 1.22$). Note that the darker the shade of each color, the greater the extent of particle-particle (red) or particle-hole (blue) pairing between the corresponding orbitals in the matrix plots. As can be seen from Fig. 10.3a, the orbital pairs with the largest particle-particle character are {1,8}, {3,4}, and {5,6}, and as can be seen from Fig. 10.3b, the orbital pairs with the largest particle-hole character are {1,3}, {2,7}, {3,6}, and {4,5}. As expected, there is no overlap between strong fermion pair particle-particle orbital pairing and strong exciton particle-hole orbital pairing. These figures thereby confirm the apparent trade-off between exciton and fermion pair character explicitly given by Eq. (10.6) and observed in Fig. 10.2b.

Note that despite the trade-off, neither the excitonic nor fermion pair character is trivial. Both are delocalized across almost every pair of orbitals as can be seen by the scarcity of white squares in Figs. 10.3a and 10.3b. As such, the coexistence of fermion pair and excitonic character seems to be enmeshed in a significant manner.

Macroscopic Limit—To explore fermion-exciton condensation behavior for a macroscopic number of fermions ($N \to \infty$), we first introduce model Hamiltonians known to exhibit fermion pair condensation and exciton condensation separately—the extreme Antisymmetrized Geminal Powers (AGP) Hamiltonian ($\hat{H}_A$) [66, 138, 383] and the Lipkin Hamiltonian ($\hat{H}_L$) [276–279, 324], respectively. (See references for details.) As the extreme AGP model demonstrates maximal fermion condensation [138], there must exist a wave function that corresponds to $\hat{H}_A$—$|\Psi_A\rangle$—whose largest eigenvalue of particle-particle RDM

(λ_D) approaches the maximal limiting value or

$$Tr\left(\hat{d}\hat{d}^T|\Psi_A\rangle\langle\Psi_A|\right) = \lambda_D^{(A)} = N \tag{10.7}$$

for systems of $2N$ or $2N+1$ fermions [136, 138] where $\hat{d}$ is the eigensIntate of ${}^2D$ corresponding to λ_D. Similarly, there must be a wave function that corresponds to $\hat{H}_L$—$|\Psi_L\rangle$—whose largest eigenvalue of the modified particle-hole RDM (λ_G) approaches the maximal limiting value or

$$Tr\left(\hat{g}\hat{g}^T|\Psi_L\rangle\langle\Psi_L|\right) = \lambda_G^{(L)} = \frac{N}{2} \tag{10.8}$$

for systems of N fermions [155] where $\hat{g}$ is the eigenstate of ${}^2\tilde{G}$ corresponding to λ_G.

Let the model wave function of the fermion-exciton condensate be given by the entanglement of the AGP and Lipkin wave functions,

$$|\Psi_{FEC}\rangle = \frac{1}{\sqrt{2}}\left(|\Psi_A\rangle \pm |\Psi_L\rangle\right). \tag{10.9}$$

For this wave function, an eigenvalue of the particle-particle RDM corresponding to the eigenstate $\hat{d}$ is given by

$$\begin{aligned} Tr\Bigg[\hat{d}\hat{d}^T\Big(&\frac{1}{2}|\Psi_A\rangle\langle\Psi_A| + \frac{1}{2}|\Psi_L\rangle\langle\Psi_L| \\ &\pm \frac{1}{2}|\Psi_A\rangle\langle\Psi_L| \pm \frac{1}{2}|\Psi_L\rangle\langle\Psi_A|\Big)\Bigg] = \lambda_D^{(FEC)}. \end{aligned} \tag{10.10}$$

From Eq. (10.7), the contribution to $\lambda_D^{(FEC)}$ from $|\Psi_A\rangle\langle\Psi_A|$ would be $\lambda_D^{(A)}$; additionally, as the extreme AGP model does not support exciton condensation, the contribution of $|\Psi_L\rangle\langle\Psi_L|$ to the eigenvalue must satisfy the Pauli bounds of $0 \leq \lambda_D^{(L)} \leq 1$. Limits on the cross terms can be obtained by representing the positive, semi-definite matrix $\hat{d}\hat{d}^T$ in the $|\Psi_A\rangle/|\Psi_L\rangle$

basis:

$$\begin{pmatrix} \langle\Psi_A|\hat{d}\hat{d}^T|\Psi_A\rangle & \langle\Psi_A|\hat{d}\hat{d}^T|\Psi_L\rangle \\ \langle\Psi_L|\hat{d}\hat{d}^T|\Psi_A\rangle & \langle\Psi_L|\hat{d}\hat{d}^T|\Psi_L\rangle \end{pmatrix} = \begin{pmatrix} \lambda_D^{(A)} & x \\ x & \lambda_D^{(L)} \end{pmatrix} \succcurlyeq 0. \tag{10.11}$$

As the determinant of this matrix must be greater than or equal to zero, the maximum contribution of the cross terms is

$$\lambda_D^{(A)}\lambda_D^{(L)} - x^2 \geq 0 \Rightarrow x \leq \sqrt{\lambda_D^{(A)}\lambda_D^{(L)}} \leq \sqrt{\lambda_D^{(A)}}. \tag{10.12}$$

Inserting the lower-bound values into Eq. (10.12) yields

$$\lambda_D^{(FEC)} \geq \frac{1}{2}\lambda_D^{(A)} - \sqrt{\lambda_D^{(A)}} = \frac{N}{2} - \sqrt{N} \tag{10.13}$$

for 2N or 2N+1 fermions. Thus, as the number of fermions gets arbitrarily large ($N \to \infty$), $\lambda_D^{(FEC)}$ is simultaneously large.

Through an analogous derivation, it can be shown that an eigenvalue of the particle-hole RDM corresponding to the eigenstate $\hat{g}$ is given by

$$\lambda_G^{(FEC)} \geq \frac{1}{2}\lambda_G^{(L)} - \sqrt{\lambda_G^{(L)}} = \frac{N}{4} - \sqrt{\frac{N}{2}} \tag{10.14}$$

for a system of N fermions. Thus, as the number of fermions gets arbitrarily large ($N \to \infty$), $\lambda_G^{(FEC)}$ is simultaneously large.

As an entanglement of the AGP and Lipkin wave functions demonstrates simultaneous large eigenvalues of ${}^2D$ and ${}^2\tilde{G}$, $|\Psi_{FEC}\rangle$ does indeed represent a fermion-exciton condensate in this macroscopic limit.

10.5 Discussion and Conclusions

In this study, we have theoretically observed the coexistence of both fermion pair and exciton condensation in a single quantum state: a fermion-exciton condensate. This concurrent character is not disparate; rather, the fermion pair and excitonic character are entwined in a highly non-trivial manner. Still, there does appear to be an inherent trade-off between fermion pair and excitonic character following an elliptic relationship, which precludes the simultaneous presence of maximum fermion pair and maximum excitonic condensation. However, as the number of electrons (N) is increased, the length of the major and minor axes of the ovular fit increase, causing the compromise between characters to become less and less stark.

We have also demonstrated that the wave function corresponding to the entanglement of the extreme Antisymmetrized Geminal Powers (AGP) model wave function—known to demonstrate fermion pair condensation—and the Lipkin model wave function—known to demonstrate exciton condensation—exhibits simultaneously large signatures of fermion pair condensation and exciton condensation in the macroscopic limit. As such, this model wave function can be used to explore macroscopic fermion-exciton condensates.

As described in the Introduction, a significant motivation for investigating fermion-exciton condensates is the possible hybridization of the properties of both fermion pair condensates and exciton condensates. A material that combines the superconductive nature of fermion pair condensation [128, 137] with the dissipationless transport of energy of excitonic condensation [107, 186, 187] would have obvious applications in energy transport and electronics. Now that the coexistence of fermion pair and excitonic character in a fermion-exciton condensate has been computationally established, further theoretical and experimental studies are needed. There are certainly many open questions regarding the formation, the properties, the applications, and the stability of fermion-exciton condensates that need to be explored in the following years.

CHAPTER 11

SIMULTANEOUS FERMION AND EXCITON CONDENSATIONS FROM A MODEL HAMILTONIAN

11.1 Chapter Synopsis

Fermion-exciton condensation in which both fermion-pair (i.e. superconductivity) and exciton condensations occur simultaneously in a single coherent quantum state has recently been conjectured to exist. Here, we capture the fermion-exciton condensation through a model Hamiltonian that can recreate the physics of this new class of highly-correlated condensation phenomena. We demonstrate that the Hamiltonian generates the large-eigenvalue signatures of fermion-pair and exciton condensations for a series of states with increasing particle numbers. The results confirm that the dual-condensate wave function arises from the entanglement of fermion-pair and exciton wave functions, which we previously predicted in the thermodynamic limit. This model Hamiltonian—generalizing well-known model Hamiltonians for either superconductivity or exciton condensation—can explore a wide variety of condensation behavior. It provides significant insights into the required forces for generating a fermion-exciton condensate, which will likely be invaluable for realizing such condensations in realistic materials with applications from superconductors to excitonic materials.

11.2 Introduction

Model Hamiltonians are theoretical tools that are often useful in simulating the key physics associated with large-scale, highly-correlated systems. They are capable of modeling an

array of quantum phases and many-body phenomena such as phase transitions [384–388], superconductivity [128, 383, 389–391], quantum magnetism [392–395], exciton condensation [276, 277, 279, 396–399], lattice-like systems [400, 401], etc. Additionally, model Hamiltonians which encompass nontrivial physics are often useful as benchmarks for theoretical tools such as many-body approximations [389, 402–404].

Condensation phenomena—which are inherently highly-correlated—have a long history of being computationally studied through the lens of model Hamiltonians as traditional band theory is inaccurate for such highly-entangled materials [5, 128, 276, 389, 390, 405, 406]. Specifically, superconductors—materials in which fermion-fermion (Cooper/electron-electron) pairs aggregate into a single quantum state, resulting in the superfluidity of the fermion-fermion pairs—are often explored through use of the Pairing-Force (PF) Hamiltonian [383, 389–391], which is additionally referred to as the Standard Reduced Bardeen-Cooper-Schrieffer (BCS) Hamiltonian [128, 362, 407]. This Hamiltonian is a simple representation of superconductivity as it describes a system with bound Cooper (or Cooper-like particle-particle) pairs interacting in an attractive manner with the holes they leave behind in a Fermi sea with the high-correlation limit of this Hamiltonian resulting in well-known, number-projected BCS wave functions [390, 408]. Similarly, exciton condensation—in which particle-hole (exciton) pairs condense into a single quantum state resulting in the superfluidity of the composite excitons [106]—can be modeled according to the Lipkin-Meshkov-Glick (LMG) Hamiltonian, which is often simply referred to as the Lipkin model [5, 276, 277, 279, 324, 396–399]. This Hamiltonian is a highly-degenerate system in which partnered orbitals are inherently particle-hole paired and whose strongly-correlated form results in ground states that demonstrate character of exciton condensation.

Here, we introduce a model Hamiltonian that is capable of capturing fermion-exciton condensation, a new class of highly-correlated condensation phenomena in which both fermion-pair and exciton condensations coexist in a single quantum state. We demonstrate such coex-

istent condensate character by calculating the quantum signatures of fermion-pair [135, 136] and exciton [155, 156] condensations (see Sec. 11.3 and Appendix 11.6.1) for systems of even particle numbers ranging from $N = 4$ to $N = 10$ particles in $r = 2N$ orbitals. These fermion-exciton condensates are shown to be described by wave functions which are entanglements of wave functions from BCS-like superconductivity and Lipkin-like exciton condensation—consistent with our prior predictions for the large-N thermodynamic limit [4] as well as those we observed experimentally on a quantum device [309].

Our determination of a model Hamiltonian that supports fermion-exciton condensation provides information regarding the nature of the forces necessary to generate such systems—an invaluable first step in the realization of real-world systems that support such dual condensation of excitons and fermion-fermion pairs, which may demonstrate some sort of hybrid of the properties of superconductors and exciton condensates and hence have applications in energy transport and electronics. The extent of these different phases and the transitions between these phases can also be studied. Moreover, our Hamiltonian provides an important reference in order to determine whether a given many-body approximation is capable of measuring dual condensate character.

11.3 Theory

11.3.1 Fermion-Pair Condensation

Superconductivity results from the condensation of bosonic fermion-fermion pairs [113, 114, 128, 184] into a single geminal—a two-fermion function directly analogous to the one-fermion orbital [66, 135, 136, 221–223]—at temperatures below a certain critical temperature. This condensation of fermion-pairs results in the superfluidity (i.e., frictionless flow) of the constituent particle-particle pairs [97, 115, 128, 184]; if the fermionic pairs are composed of electrons (i.e., Cooper pairs), then these superfluid electron-electron pairs demonstrate su-

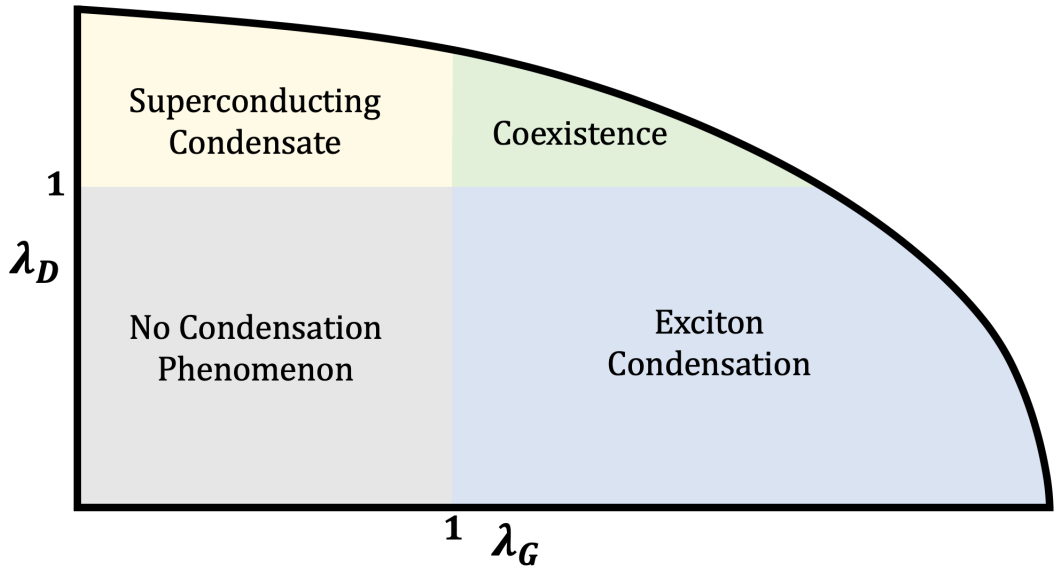

Figure 11.1: A figure of the condensate phase diagram in the phase space of the signatures of particle-particle condensation, λ_D, and exciton condensation, λ_G, is shown.

perconductivity.

As was first demonstrated by Yang [135] and Sasaki [136], a computational signature of such superconducting states is a large eigenvalue in the particle-particle reduced density matrix (2-RDM), whose elements are given by

$$^2D^{i,j}_{k,l} = \langle \Psi | \hat{a}^\dagger_i \hat{a}^\dagger_j \hat{a}_l \hat{a}_k | \Psi \rangle \tag{11.1}$$

where $|\Psi\rangle$ is an N-fermion wave function and where $\hat{a}^\dagger_i$ and $\hat{a}_i$ are fermionic creation and annihilation operators for orbital i, respectively. As eigenvalues of the 2-RDM can be interpreted as the occupations of the two-fermion geminals [138], when the largest eigenvalue of the 2-RDM—the signature of particle-particle condensation, represented by λ_D—exceeds the Pauli-like limit of one ($\lambda_D > 1$), multiple fermion-fermion pairs occupy a single geminal and hence superconducting character is observed. This signature is known to directly probe the presence and extent of non-classical (off-diagonal) long-range order [221]. (See the Appendix for more details on how the signature of superconductivity, λ_D, was computed.)

The Pairing-Force (PF) model [383, 389–391]—also called the Standard Reduced Bardeen-Cooper-Schrieffer (BCS) model [128, 362, 407]—is known to exhibit superconducting character in the strong correlation limit and hence achieve a large λ_D. The Hamiltonian for the PF model is given in second quantization by

$$\mathcal{H}_{PF} = \frac{1}{2} \sum_{\sigma=\uparrow,\downarrow} \sum_{p=1}^{N} \epsilon_p \hat{a}^{\dagger}_{p,\sigma} \hat{a}_{p,\sigma} - G \sum_{p=1}^{N} \sum_{q=1}^{N} \hat{a}^{\dagger}_{p,\uparrow} \hat{a}^{\dagger}_{p,\downarrow} \hat{a}_{q,\downarrow} \hat{a}_{q,\uparrow} \tag{11.2}$$

where p is a quantum number that represents a pair of orbitals denoted as $p,\uparrow$ and $p,\downarrow$ with the same energy, where the energies (ϵ_p) are considered to be known, and where the parameter G is a constant that tunes the strength of the pairwise interactions. Note that in the limit of strong correlation ($G >> \epsilon_p$), maximal superconducting character—$\lambda_D = \frac{N}{2}\left(1 - \frac{N-2}{r}\right)$ [66, 138]—is observed.

11.3.2 Exciton Condensation

Directly analogous to superconductivity resulting from bosonic particle-particle pairs condensing into a single particle-particle function, exciton condensation results from the condensation of particle-hole pairs (i.e., excitons) into a single particle-hole function below a certain critical temperature, which results in the superfluidity of the excitons [106, 107]. Exciton condensates, while difficult to realize experimentally, have been observed in systems composed of polaritons (excitons coupled to photons) [110, 112, 409] and in two-dimensional structures such as semiconductors [176], graphene bilayers [161, 179, 224], and van der Waals heterostructures [163, 171, 177, 178].

The signature of exciton condensation—denoted as λ_G—is similarly analogous to that for fermion-pair condensation; the presence and extent of exciton condensate character can be measured from the largest eigenvalue of a modified particle-hole reduced density matrix

given by [148, 155, 156]

$$ {}^2\tilde{G}^{i,j}_{k,l} = {}^2G^{i,j}_{k,l} - {}^1D^i_j {}^1D^l_k = \langle\Psi|\hat{a}^\dagger_i\hat{a}_j\hat{a}^\dagger_l\hat{a}_k|\Psi\rangle - \langle\Psi|\hat{a}^\dagger_i\hat{a}_j|\Psi\rangle\langle\Psi|\hat{a}^\dagger_l\hat{a}_k|\Psi\rangle \tag{11.3} $$

where ${}^1D$ is the one-fermion reduced density matrix (1-RDM). Note that this modification removes the extraneous large eigenvalue from a ground-state-to-ground-state transition such that a signature above one ($\lambda_G > 1$) is indicative of exciton condensation. (See the Appendix for more details on how the signature of exciton condensation, λ_G was computed.) This computational signature has been utilized to study exciton condensation is possible in quantum and molecular systems [4, 5, 156, 309, 410].

One model known to achieve a large λ_G value and hence exhibit exciton condensate character in the limit of a large correlation is the Lipkin quasispin model [276, 277, 279, 396–399]. The N-fermion Lipkin quasispin model consists of two energy levels $\left\{-\frac{\epsilon}{2}, \frac{\epsilon}{2}\right\}$, each containing N energetically-degenerate states. The second-quantized Hamiltonian can be expressed as [279]

$$ \begin{aligned} \mathcal{H}_L = &\frac{\epsilon}{2}\sum_{\sigma=\pm1}\sigma\sum_{p=1}^{N}\hat{a}^\dagger_{\sigma,p}\hat{a}_{\sigma,p} \\ &+\frac{\gamma}{2}\sum_{\sigma=\pm1}\sum_{p,q=1}^{N}\hat{a}^\dagger_{+\sigma,p}\hat{a}_{-\sigma,p}\hat{a}^\dagger_{-\sigma,q}\hat{a}_{+\sigma,q} \\ &+\frac{\lambda}{2}\sum_{\sigma=\pm1}\sum_{p,q=1}^{N}\hat{a}^\dagger_{+\sigma,p}\hat{a}^\dagger_{+\sigma,q}\hat{a}_{-\sigma,q}\hat{a}_{-\sigma,p} \end{aligned} \tag{11.4} $$

where $\sigma = \pm1$ and $p = 1, 2, \ldots, N$ are quantum numbers that completely characterize the system in which p describes the site number labelling the N states in a given level and σ represents the upper $(+1)$ or lower (-1) energy levels, respectively. Note that in this model, the λ term allows for double excitations and de-excitations, and the γ term allows for a single particle to be scattered up while another is simultaneously scattered down; as a result, in the

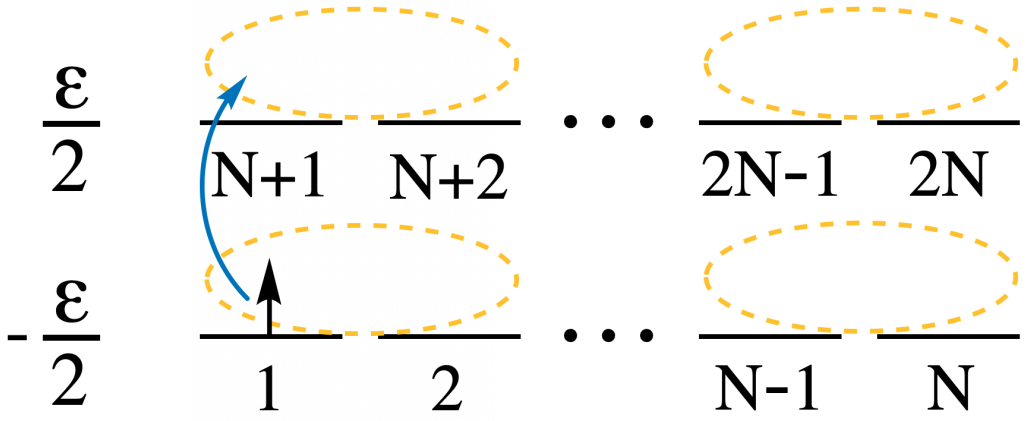

Figure 11.2: A pictorial representation of the model Hamiltonian we introduce in which there are two N-degenerate energy levels—with energies $-\frac{\epsilon}{2}$ and $\frac{\epsilon}{2}$—with double excitations and de-excitations, scattering in which one particle is de-excited while another is simultaneously excited, and a pair-wise interaction term between sites $2j-1$ and $2j$ for $j \in \{1, 2, \ldots, N\}$ (yellow circles) is shown. Note that the Lipkin-like excitations must occur within a site ($p \leftrightarrow p+N$, blue arrow).

Lipkin model, only even excitations are allowed, and only one particle may occupy a given site (i.e., have a specific quantum number p) such that each site in the lower level is particle-hole paired with the corresponding site in the upper level. By having the terms correlating orbitals in the Hamiltonian (λ, γ) be sufficiently larger than the energy term (i.e., in the limit of high correlation), maximal exciton condensation—$\lambda_G = \frac{N}{2}$ [155]—can be obtained for $\lambda = \gamma$.

11.3.3 Fermion-Exciton Condensation

A fermion-exciton condensate is a single quantum state that simultaneously demonstrates character of superconductivity and exciton condensation, i.e., both signatures of condensation—the largest eigenvalue of the particle-particle RDM (Eq. (11.1)) and the largest eigenvalue of the modified particle-hole RDM (Eq. (11.3))—are simultaneously large ($\lambda_D, \lambda_G > 1$). [4].

To gain insight into such fermion-exciton condensates, here we propose a model system that is capable of demonstrating simultaneous fermion-pair and exciton condensate character.

In this model, we introduce the pairwise interaction from the Pairing-Force model into the scaffolding of the Lipkin model; thus, the model keeps the structure of the Lipkin model in which N particles occupy two N-degenerate energy levels ($-\frac{\epsilon}{2}$ and $\frac{\epsilon}{2}$) with allowed double excitations on two sites (λ) and simultaneous scattering of a particle up on one site and down on another (γ)—where Lipkin-like sites are now given as orbitals p and $p+N$; however, we additionally pair adjacent orbitals—orbitals $2j-1$ and $2j$ for $j \in \{1, 2, \ldots, N\}$—via the PF parameter, G. (See Fig. 11.2.) The Hamiltonian for this model is thus given by

$$\begin{aligned}
\mathcal{H} = &-\frac{\epsilon}{2}\sum_{i=1}^{N}\hat{a}_i^\dagger\hat{a}_i + \frac{\epsilon}{2}\sum_{i=1}^{N}\hat{a}_{i+N}^\dagger\hat{a}_{i+N} \\
&+\frac{\lambda}{2}\sum_{p=1}^{N}\sum_{q=1}^{N}\hat{a}_p^\dagger\hat{a}_q^\dagger\hat{a}_{q+N}\hat{a}_{p+N} + \frac{\lambda}{2}\sum_{p=1}^{N}\sum_{q=1}^{N}\hat{a}_{p+N}^\dagger\hat{a}_{q+N}^\dagger\hat{a}_q\hat{a}_p \\
&+\frac{\gamma}{2}\sum_{p=1}^{N}\sum_{q=1}^{N}\hat{a}_{p+N}^\dagger\hat{a}_q^\dagger\hat{a}_{q+N}\hat{a}_p + \frac{\gamma}{2}\sum_{p=1}^{N}\sum_{q=1}^{N}\hat{a}_p^\dagger\hat{a}_{q+N}^\dagger\hat{a}_q\hat{a}_{p+N} \\
&-G\sum_{j=1}^{N}\sum_{k=1}^{N}\hat{a}_{2j-1}^\dagger\hat{a}_{2j}^\dagger\hat{a}_{2k}\hat{a}_{2k-1}
\end{aligned} \tag{11.5}$$

in second quantization, with a given set of parameters $(\epsilon, \lambda, \gamma, G)$ directly determining the extent of fermion-pair and exciton condensation (λ_D and λ_G, respectively) of the ground state corresponding to this model Hamiltonian.

While this model Hamiltonian is not the first to combine the pairwise interaction from the Pairing-Force model with the Lipkin model, the model Hamiltonian introduced by Plastino and coworkers causes direct competition between particle-particle and particle-hole correlations and hence proves incapable of demonstrating a fermion-exciton condensate phase (see Appendix 11.6.2) [411–413]. Conversely, due to our introduction of the Pairing-Force interactions between adjacent orbitals instead of orbitals in the same Lipkin-like site, particle-particle and particle hole pairing can coexist and hence fermion-pair-exciton (FEC) states can be achieved as is shown in the results that follow.

11.4 Results

11.4.1 The Minimal FEC

As the authors have previously demonstrated [4], a system with as few as $N = 4$ particles in $r = 8$ orbitals can support formation of a fermion-exciton condensate. As such, we first fully explore such a minimalistic FEC system. The ground state of the FEC Hamiltonian that we have introduced—Equation (11.5)—for four particles has contributions from only ten of the seventy (rCN) possible configurations. Of these ten basis states, there are only five distinct classes composed of degenerate orientations—see Fig. 11.3—that allow for the direct computation of a matrix-form of the Hamiltonian in a minimal basis state. The five basis states are defined by three quantum numbers, $x, y, bool$, where the first indicates the number of particles excited to the upper energy level (x), the second indicates the number of BCS-like pairs (number of times both $2j-1$ and $2j$ are occupied, y), and the third is a boolean that indicates whether the configuration is "Lipkin"-like in the regard that no two orbitals representing a "Lipkin" site (denoted as p and $p+N$, see the blue arrow in Fig. 11.3) are dually occupied or dually unoccupied.

Utilizing the basis shown in Fig. 11.3—$|0,2,T\rangle$, $|2,2,F\rangle$, $|2,2,T\rangle$, $|2,0,T\rangle$, and $|4,2,T\rangle$—the Hamiltonian from Eq. (11.5) can be represented by

$$\mathcal{H}_4 = \begin{pmatrix} -2\epsilon - 2G & -G\sqrt{2} & \frac{2\lambda-2G}{\sqrt{2}} & 2\lambda & 0 \\ -G\sqrt{2} & -2G+2\gamma & -2G & 0 & -G\sqrt{2} \\ \frac{2\lambda-2G}{\sqrt{2}} & -2G & -2G & 2\gamma\sqrt{2} & \frac{2\lambda-2G}{\sqrt{2}} \\ 2\lambda & 0 & 2\gamma\sqrt{2} & 2\gamma & 2\lambda \\ 0 & -G\sqrt{2} & \frac{2\lambda-2G}{\sqrt{2}} & 2\lambda & 2\epsilon - 2G \end{pmatrix} \tag{11.6}$$

where each term—corresponding to the interaction between two classes of basis states, $|i\rangle$ and $|j\rangle$—is obtained from programmatically generating all sets of second-quantization creation

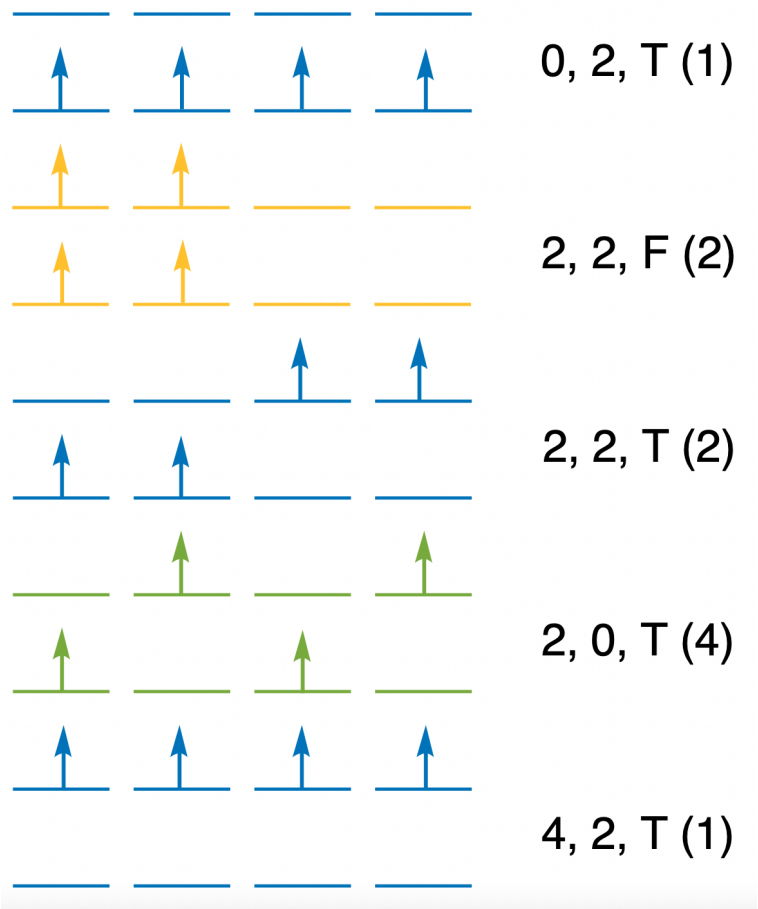

Figure 11.3: Configurations representing each of the five classes of non-zero basis states for the FEC Hamiltonian for $N, r = 4, 8$ are shown where each label $x, y, bool$ represents the number of particles excited to the upper N-degenerate energy level (x), the number of BCS-like pairs (y), and whether the configuration is consistent with the Lipkin model ($bool$), where the degeneracy of each class of states is given in parenthesis, and where green, yellow, and blue configurations represent that the corresponding states are consistent with only the Lipkin Hamiltonian, only the Pairing-Force Hamiltonian, or both Lipkin and PF Hamiltonians, respectively.

and annihilation operators in Eq. (11.5), taking the expectation value for each combination of pairs of configurations in classes $|i\rangle$ and $|j\rangle$, summing the results, and normalizing by dividing by the square root of the number of configurations for both $|i\rangle$ and $|j\rangle$. For example, if $|i\rangle = |2, 2, F\rangle = (|1, 2, 5, 6\rangle + |3, 4, 7, 8\rangle)/\sqrt{2}$ and $|j\rangle = |2, 2, T\rangle = (|1, 2, 7, 8\rangle + |3, 4, 5, 6\rangle)/\sqrt{2}$,

the Hamiltonian term would be given by

$$\begin{aligned}
&\frac{(\langle 1,2,5,6| + \langle 3,4,7,8|)}{\sqrt{2}}\mathcal{H}_4\frac{(|1,2,7,8\rangle + |3,4,5,6\rangle)}{\sqrt{2}} \\
&= \frac{1}{2}[\langle 1,2,5,6|\mathcal{H}_4|1,2,7,8\rangle + \langle 1,2,5,6|\mathcal{H}_4|3,4,5,6\rangle \\
&+\langle 3,4,7,8|\mathcal{H}_4|1,2,7,8\rangle + \langle 3,4,7,8|\mathcal{H}_4|3,4,5,6\rangle] \qquad (11.7)
\end{aligned}$$

Fig. 11.4a scans over the signatures of condensation—λ_D and λ_G—for the ground state of the Hamiltonian in Eq. (11.6) by systematically varying the parameters ϵ, λ, γ, and G where the yellow BCS x's represent ground states in which the PF Hamiltonian is implemented (i.e., $\lambda = \gamma = 0$), the blue Lipkin x's represent states in which the Lipkin Hamiltonian is implemented (i.e., $G = 0$), and where the green FEC x's represent states with character of both PF and Lipkin Hamiltonians. As this figure demonstrates, the largest degree of superconducting character (the largest λ_D) is indeed observed in the BCS limit of the FEC Hamiltonian (when $G >> \epsilon,\ \lambda = \gamma \approx 0$), and the largest degree of exciton condensate character (the largest λ_G) is observed in the Lipkin limit of the FEC Hamiltonian ($\lambda \approx \gamma >> \epsilon,\ G \approx 0$). However, neither the BCS nor Lipkin limits of the Hamiltonian is capable of demonstrating a dual fermion-exciton condensate as λ_D and λ_G only simultaneously exceed the Pauli-like limit of one when the full FEC Hamiltonian from Eq. (11.5) is implemented including both BCS-like (G) and Lipkin-like (λ, γ) terms.

Our model FEC Hamiltonian, however, is capable of demonstrating a wide variety of dual condensate character as a variety of input parameters lead to ground state configurations in which both λ_G and λ_D simultaneously exceed one. Additionally, the λ_D and λ_G values obtained by scanning over the Hamiltonian parameters (in Fig. 11.4a) demonstrate an elliptic nature consistent with the convex nature of 2-RDMs projected onto a two-dimensional space [380–382] that matches predictions for a FEC that these authors first presented in Ref. [4]. This elliptic boundary as well as the density of points in the zone corresponding to fermion-

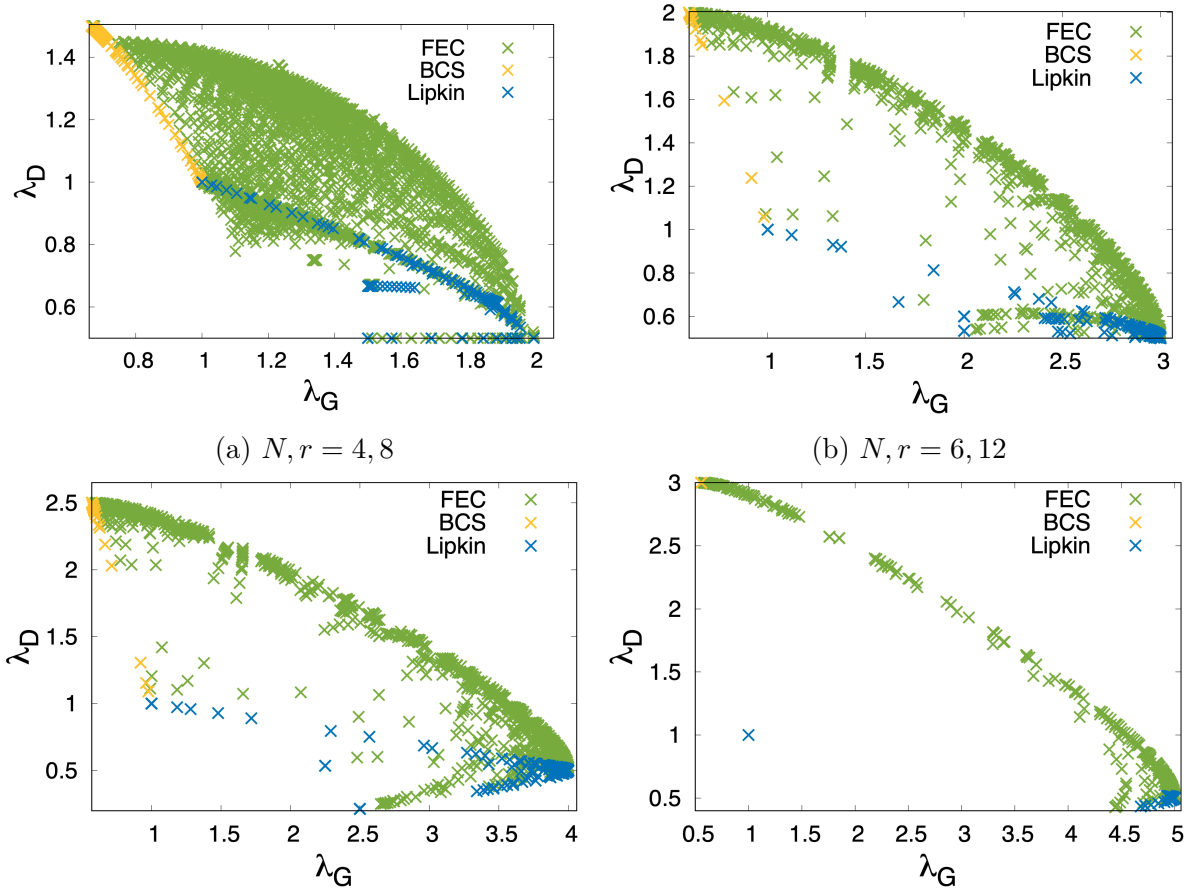

(a) $N, r = 4, 8$

(b) $N, r = 6, 12$

(c) $N, r = 8, 16$

(d) $N, r = 10, 20$

Figure 11.4: Plots of λ_G versus λ_D where parameters in the FEC Hamiltonian are systematically varied are shown for systems involving (a) $N = 4$, (b) $N = 6$, (c) $N = 8$, and (d) $N = 10$ particles in $r = 2N$ orbitals.

exciton condensate character indicate that the FEC model Hamiltonian introduced here is capable of spanning the entirety of the FEC region of λ_D versus λ_G space (i.e., $\lambda_D, \lambda_G > 1$).

In Ref. [4], these authors theoretically establish that in the thermodynamic limit, a possible wave function demonstrating fermion-exciton condensation can be obtained by entangling wave functions that separately demonstrate superconducting character ($|\Psi_D\rangle$ with large λ_D) and exciton condensate character ($|\Psi_G\rangle$ with large λ_G) according to

$$|\Psi_{FEC}\rangle = \frac{1}{\sqrt{2 - |\Delta|}} \left(|\Psi_D\rangle - \mathrm{sgn}(\Delta) |\Psi_G\rangle \right), \tag{11.8}$$

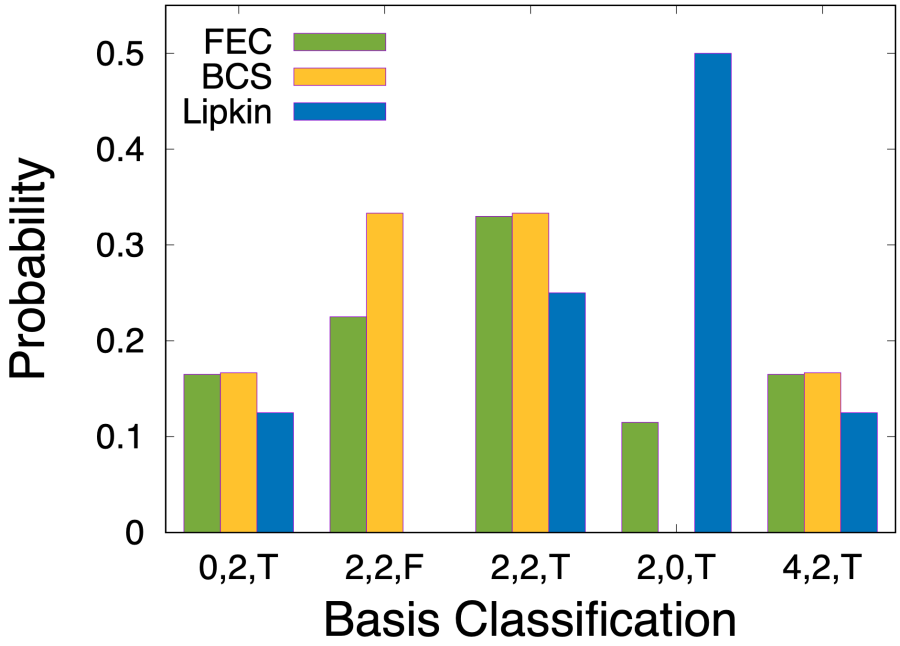

Figure 11.5: The probabilities corresponding to each of the five classes of basis states (see Fig. 11.3) consistent with the FEC Hamiltonian for $N, r = 4, 8$ are shown where green, yellow, and blue bars correspond to the lowest eigenstate of the Lipkin Hamiltonian, the Pairing-Force Hamiltonian, and FEC Hamiltonian, respectively.

where $\Delta = 2\langle\Psi_D|\Psi_G\rangle$. In Fig. 11.5 occupation probabilities for each of the five classes of basis states consistent with the $N, r = 4, 8$ FEC Hamiltonian that contribute to a BCS wave function (yellow, $\epsilon, \lambda, \gamma, G = 0, 0, 0, 0.7$, $\lambda_D = 1.50$, $\lambda_G = 0.67$), a Lipkin wave function (blue, $\epsilon, \lambda, \gamma, G = 0, -0.5, -0.5, 0$, $\lambda_D = 0.50$, $\lambda_G = 2.00$), and a FEC wave function (green, $\epsilon, \lambda, \gamma, G = 0, -0.5, -0.5, 0.7$, $\lambda_D = 1.31$, $\lambda_G = 1.32$) are given. From this data, it can be observed that the FEC wave function does indeed appear to be an entanglement of the individual BCS and Lipkin wave functions for the case of $N = 4$; this is consistent with the theoretical result in the thermodynamic limit.

11.4.2 Higher-Particle FECs

In order to observe trends related to system size, we employ the methodologies used to explore the $N, r = 4, 8$ model system and extrapolate to systems composed of $N = 6, 8, 10$ particles in $r = 12, 16, 20$ orbitals. Figures summarizing the signatures of superconducting character (λ_D) and exciton condensate character (λ_G) obtained for the ground state wave functions of these larger model Hamiltonians can be seen in Figs. 11.4b-11.4d. Similar to the results from the $N = 4$ data, elliptic fits spanning the maximal signature of superconducting character observed for the BCS wave function to the maximal signature of exciton condensate character for the Lipkin wave function with a large variety of parameters supporting dual fermion-exciton condensation. Note that as the size of the system increases from $N = 6$ to $N = 8$ to $N = 10$, the number of classes of degenerate, non-zero basis states as well as the number of basis states composing each class increase from 8 classes with a total of 44 non-zero basis states to 14 classes with a total of 230 non-zero basis states to 20 classes with a total of 1212 non-zero basis states. As such, the relative sparsity of the computations in λ_D versus λ_G as system size is increased is due to fewer computations being run with larger increments between each of the parameters as they are varied.

To demonstrate how the classes of non-zero basis states vary as system size is increased, Fig. 11.6—which shows the occupation probabilities for each of the fourteen classes of basis states consistent with the $N, r = 8, 16$ FEC Hamiltonian that contribute to a BCS wave function (yellow, $\epsilon, \lambda, \gamma, G = 0, 0, 0, 0.9$, $\lambda_D = 2.50$, $\lambda_G = 0.57$), a Lipkin wave function (blue, $\epsilon, \lambda, \gamma, G = 0, -0.5, -0.5, 0$, $\lambda_D = 0.50$, $\lambda_G = 4.00$), and a FEC wave function (green, $\epsilon, \lambda, \gamma, G = 0, -0.5, -0.5, 0.9$, $\lambda_D = 2.06$, $\lambda_G = 1.87$)—is included. Note that due to an increase in the possible complexity, two more quantum numbers are added to describe a few of the classes of basis states; specifically, ζ and τ are added to $x, y, bool, \zeta, \tau$ where ζ corresponds to the number of times BCS-like pairs are "stacked" into the same site such that orbitals $2j - 1$, $2j$, $2j - 1 + N$, and $2j + N$ are all occupied and where τ corresponds to the

number of diagonal configurations in which either $2j-1/2j+N$ or $2j-1+N/2j$ are both occupied where $2j-1$ and $2j$ are adjacent, BCS-paired orbitals. A few configurations with the necessary quantum numbers specified for $N=8$ are included in Fig. 11.7.

As can be seen from Fig. 11.6, the groundstate wave function for the $N=8$ FEC Hamiltonian no longer simply contains elements of the BCS wave function and the Lipkin wave function naively entangled together. Specifically, while the $|4,4,F,1,2\rangle$ class of basis states does include BCS-paired particles (see Fig. 11.7), it does not include the maximal number of BCS-paired particles, which appears to be a necessary condition for non-zero occupation of the ground state for the BCS Hamiltonian. However, this class of basis states can interact with other BCS-like and Lipkin-like classes of basis states. Explicitly, $|4,4,F,1,2\rangle$ interacts with $|2,4,F\rangle$ via $\frac{\lambda}{2}\hat{a}_p^\dagger\hat{a}_q^\dagger\hat{a}_{q+N}\hat{a}_{p+N}$; $|4,4,F,1\rangle$ via $\frac{\lambda}{2}\hat{a}_p^\dagger\hat{a}_{q+N}^\dagger\hat{a}_q\hat{a}_{p+N}$; $|6,4,F\rangle$ via $\frac{\lambda}{2}\hat{a}_{p+N}^\dagger\hat{a}_{q+N}^\dagger\hat{a}_q\hat{a}_p$; and $|2,2,T\rangle$ via $-G\hat{a}_{2j-1}^\dagger\hat{a}_{2j}^\dagger\hat{a}_{2k}\hat{a}_{2k-1}$, which does further entangle the Lipkin-like configurations and BCS-like configurations in a non-trivial manner. As such, while the interaction between the BCS-like classes of basis states and Lipkin-like classes of basis states in the formation of the FEC ground state wave function is not as clear-cut or simple as in the $N=4$ case, the $N=8$ FEC wave function is still an entanglement of BCS-like and Lipkin-like terms.

A representative configuration as well as the relevant quantum numbers for all classes of basis states for the $N=6$, $N=8$, and $N=10$ FEC Hamiltonians is given in the Supplemental Information.

11.5 Discussion and Conclusions

In this study, we introduce a model Hamiltonian that successfully demonstrates the physics associated with both fermion-pair condensation and exciton condensation, as well as encompassing the phase space consisting of systems in which fermion-pair condensation and exciton condensation are simultaneously realized—a phenomenon which we term fermion-

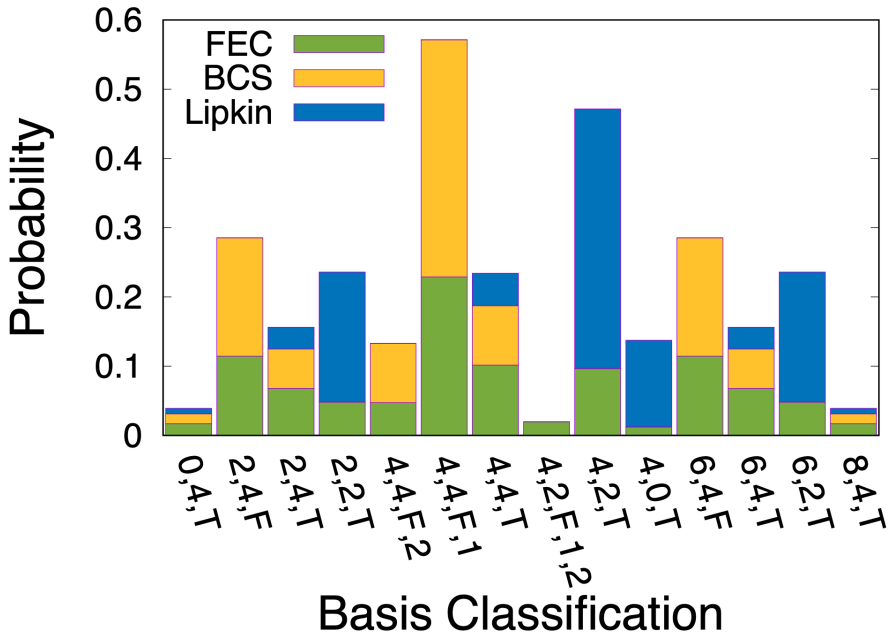

Figure 11.6: The probabilities corresponding to each of the fourteen classes of basis states consistent with the FEC Hamiltonian for $N, r = 8, 16$ are shown where green, yellow, and blue bars correspond to the lowest eigenstate of the Lipkin Hamiltonian, the Pairing-Force Hamiltonian, and FEC Hamiltonian, respectively. Each label $x, y, bool, \zeta, \tau$ represents the number of particles excited to the upper N-degenerate energy level (x), the number of BCS-like pairs (y), whether the configuration is consistent with the Lipkin model ($bool$), the number of times BCS-like pairs are "stacked" into the same site (ζ), and the number of times a diagonal configuration occur in which either $2j - 1/2j + N$ or $2j - 1 + N/2j$ are simultaneously occupied where $2j - 1$ and $2j$ are adjacent, paired orbitals (τ). These values act as quantum numbers that define the degenerate classes of non-zero basis functions composing the ground state to the FEC Hamiltonian.

exciton condensation (FEC). Applying this model to systems composed of $N = 4, 6, 8, 10$ particles in $r = 2N$ orbitals, we confirm this fermion-exciton condensate character for a wide variety of ground state wavefunctions corresponding to a diverse range of input parameters in the model Hamiltonian, additionally verifying the prediction made in prior investigation [4] that the wavefunction of a fermion-exciton condensate is an entanglement of wavefunctions of exciton condensates and fermion-pair condensates.

The introduction of our model Hamiltonian that supports fermion-exciton condensation advances our understanding of the forces and orbital correlations necessary for the experi-

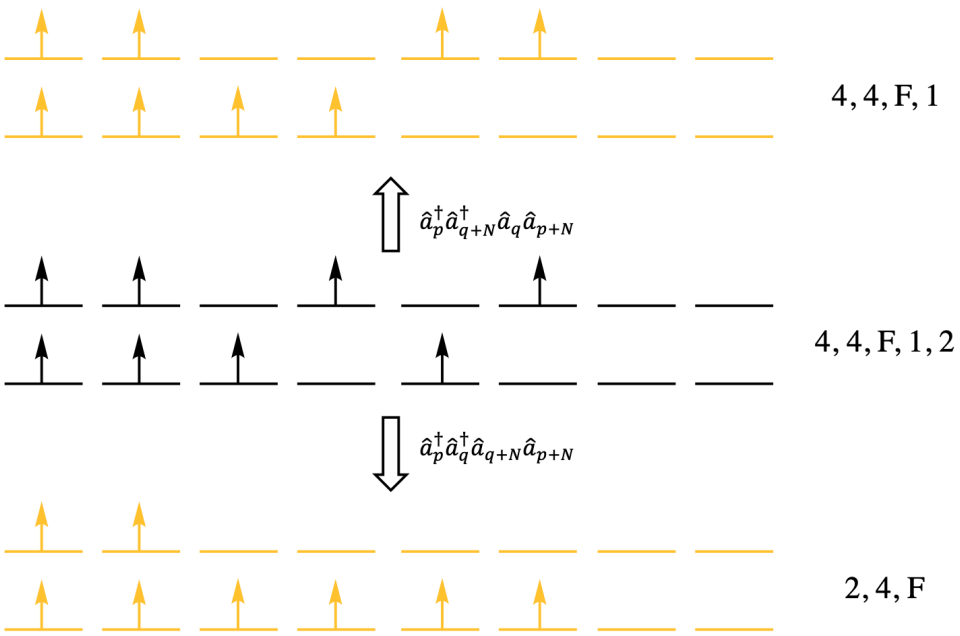

Figure 11.7: Configurations representing how the Lipkin-like double excitation term (λ) and scattering term (γ) in the FEC Hamiltonian relate the $|4, 4, F, 1, 2\rangle$ basis state for $N, r = 8, 16$ to BCS-like basis states.

mental construction of FEC states in real-world materials—important insights in the search for real-world materials exhibiting fermion-exciton condensate character. Depending on the interpretation of the Hamiltonian elements, this could have ramifications for fields such as traditional and molecularly-scaled electronics, spin systems, and nuclear physics.

Specifically, if the orbitals in the Hamiltonian are interpreted as spin orbitals, fermion-exciton condensates simultaneously demonstrate the condensation of Cooper into a single particle-particle quantum state and the condensation of electron-hole pairs into a single particle-hole quantum state; thus, superfluid Cooper pairs—resulting in superconductivity—and superfluid excitons—which are associated with the dissipationless flow of energy [106, 107]—should both be present to a certain extent in FEC systems, maybe demonstrating some hybridization of the properties of superconductors and exciton condensates, which may be relevant to the fields of energy transport and electronics in both macroscopic materials and molecular-scaled systems.

Alternatively, the two Lipkin-like N-degenerate levels can be interpreted as being representative of specific spin states such that the upper level is spin up and the lower level is spin down or vice versa. This interpretation is most-consistent with $\epsilon = 0$—which does demonstrate FEC states for a wide variety of input parameters—, although in a magnetic field the different spin states could be separated by some non-zero energy. In this framework, the Lipkin-like terms could represent simultaneous double spin flips that are either aligned (λ) or misaligned (γ), and the pairwise Pairing-Force term could be seen as a favorable interaction between adjacent particles demonstrating the same spin.

Moreover, as both particle-particle (consistent with the Pairing-Force Hamiltonian) and particle-hole (consistent with the Lipkin Hamiltonian) are utilized in the field of nuclear physics to display the essential properties of the nuclear interaction [414–416], we can interpret our FEC Hamiltonian in this framework. In this interpretation, the particles being created and annihilated are nucleons such that the Lipkin terms are associated with the interaction of nucleons within a valence shell (γ), the mixing of particle-hole excitations with the valence configurations, and excitations of a nucleon from one valence shell to another having an energetic penalty (ϵ) [414, 416]. Additionally, in this interpretation, the PF pairwise interaction is associated with the short-range portion of the nuclear interaction [414, 415].

Overall, this model Hamiltonian is capable of demonstrating a wider array of collective behavior than either the Lipkin or the Pairing-Force models. Such a Hamiltonian will have a vast degree of applications and will be beneficial for the exploration—and for benchmarking computational methodologies for the treatment of—the nontrivial physics of real-world material and chemical systems.

11.6 Appendix

11.6.1 Determination of Signatures of Condensation

To determine the largest eigenvalue of the particle-particle RDM (${}^2D$, see Eq. (11.1)—i.e., λ_D, the signature of superconducting character—, only the following $N \times N$ subblock of the full 2-RDM containing the large eigenvalue must be computed and diagonalized [138, 364, 365]

	$\hat{a}_0\hat{a}_1$	$\hat{a}_2\hat{a}_3$	$\cdots$	$\hat{a}_{r-2}\hat{a}_{r-1}$
$\hat{a}_0^\dagger\hat{a}_1^\dagger$	$\hat{a}_0^\dagger\hat{a}_1^\dagger\hat{a}_0\hat{a}_1$	$\hat{a}_0^\dagger\hat{a}_1^\dagger\hat{a}_2\hat{a}_3$	$\cdots$	$\hat{a}_0^\dagger\hat{a}_1^\dagger\hat{a}_{r-2}\hat{a}_{r-1}$
$\hat{a}_2^\dagger\hat{a}_3^\dagger$	$\hat{a}_2^\dagger\hat{a}_3^\dagger\hat{a}_0\hat{a}_1$	$\hat{a}_2^\dagger\hat{a}_3^\dagger\hat{a}_2\hat{a}_3$	$\cdots$	$\hat{a}_2^\dagger\hat{a}_3^\dagger\hat{a}_{r-2}\hat{a}_{r-1}$
$\vdots$	$\vdots$	$\vdots$	$\ddots$	$\vdots$
$\hat{a}_{r-2}^\dagger\hat{a}_{r-1}^\dagger$	$\hat{a}_{r-2}^\dagger\hat{a}_{r-1}^\dagger\hat{a}_0\hat{a}_1$	$\hat{a}_{r-2}^\dagger\hat{a}_{r-1}^\dagger\hat{a}_2\hat{a}_3$	$\cdots$	$\hat{a}_{r-2}^\dagger\hat{a}_{r-1}^\dagger\hat{a}_{r-2}\hat{a}_{r-1}$

(11.9)

where, again, $\hat{a}_i^\dagger$ and $\hat{a}_i$ are to creation and annihilation operators corresponding to the orbital with index i. Each element of this subblock of the 2-RDM is the expectation value $\langle\Psi|\hat{a}_{2j-1}^\dagger\hat{a}_{2j}^\dagger\hat{a}_{2k}\hat{a}_{2k-1}|\Psi\rangle$ obtained by programmatically applying the appropriate creation and annihilation operators to each pair of non-zero basis states composing the previously-obtained ground state wave function of the Hamiltonian. As an example, for the $N, r = 4$ computations, there are ten non-zero basis elements composing five distinct classes ($|0,2,T\rangle$, $|2,2,F\rangle$, $|2,2,T\rangle$, $|2,0,T\rangle$, $|4,2,T\rangle$) that are used to construct the Hamiltonian (see the Result section). The ground-state wave function is obtained in terms of these classes with a structure given by

$$\begin{aligned}|\Psi\rangle = v_{0,2,T}|0,2,T\rangle + v_{2,2,F}|2,2,F\rangle + v_{2,2,T}|2,2,T\rangle \\ +v_{2,0,T}|2,0,T\rangle + v_{4,2,T}|4,2,T\rangle\end{aligned} \tag{11.10}$$

where each of the classes is a weighted linear combination of the basis states composing it, i.e,

$$|2,0,T\rangle = \frac{|1,3,6,8\rangle + |1,4,6,7\rangle + |2,3,5,8\rangle + |2,4,5,7\rangle}{\sqrt{4}} \tag{11.11}$$

Thus, $\langle\Psi|\hat{a}^{\dagger}_{2j-1}\hat{a}^{\dagger}_{2j}\hat{a}_{2k}\hat{a}_{2k-1}|\Psi\rangle$ is a sum of all expectation values of the form

$$v_{c_1}v_{c_2}\langle c_1|\hat{a}^{\dagger}_{2j-1}\hat{a}^{\dagger}_{2j}\hat{a}_{2k}\hat{a}_{2k-1}|c_2\rangle \tag{11.12}$$

where c_1 and c_2 refer to each of the distinct classes of non-zero basis states and where these expectation values are sums over

$$\frac{v_{b_1}v_{b_2}}{N(c_{b_1})N(c_{b_2})}\langle b_1|\hat{a}^{\dagger}_{2j-1}\hat{a}^{\dagger}_{2j}\hat{a}_{2k}\hat{a}_{2k-1}|b_2\rangle \tag{11.13}$$

where b_1 and b_2 are the basis states composing each class, where $N(c_{b_1})$ refers to the size of the class to which basis b_1 belongs, and where all possible combinations of basis states are analyzed.

Note that only $\epsilon = 0$ calculations were run for the $N, r = 10, 20$ scan such that site symmetry allowed the entire matrix to be constructed from three distinct types of elements, which lowered computational expense; these element types are as follows: $\hat{a}^{\dagger}_{2j-1}\hat{a}^{\dagger}_{2j}\hat{a}_{2j}\hat{a}_{2j-1}$, $\hat{a}^{\dagger}_{2j-1}\hat{a}^{\dagger}_{2j}\hat{a}_{2k}\hat{a}_{2k-1}$, and $\hat{a}^{\dagger}_{2j-1}\hat{a}^{\dagger}_{2j}\hat{a}_{2j\pm N}\hat{a}_{2j-1\pm N}$.

The signature of superconductivity (λ_D) is then computed from the $N \times N$ subblock of the 2-RDM according to the eigenvalue equation

$${}^2Dv^i_D = \epsilon^i_D v^i_D \tag{11.14}$$

with the signature corresponding the largest eigenvalue (the maximum ϵ^i_D).

The portion of the particle-hole RDM (${}^2G$) associated with a large eigenvalue is composed of sub-matrices of the form

	$\hat{a}_q^\dagger \hat{a}_q$	$\hat{a}_{q+N}^\dagger \hat{a}_q$	$\hat{a}_q^\dagger \hat{a}_{q+N}$	$\hat{a}_{q+N}^\dagger \hat{a}_{q+N}$
$\hat{a}_p^\dagger \hat{a}_p$	$\hat{a}_p^\dagger \hat{a}_p \hat{a}_q^\dagger \hat{a}_q$	$\hat{a}_p^\dagger \hat{a}_p \hat{a}_{q+N}^\dagger \hat{a}_q$	$\hat{a}_p^\dagger \hat{a}_p \hat{a}_q^\dagger \hat{a}_{q+N}$	$\hat{a}_p^\dagger \hat{a}_p \hat{a}_{q+N}^\dagger \hat{a}_{q+N}$
$\hat{a}_p^\dagger \hat{a}_{p+N}$	$\hat{a}_p^\dagger \hat{a}_{p+N} \hat{a}_q^\dagger \hat{a}_q$	$\hat{a}_p^\dagger \hat{a}_{p+N} \hat{a}_{q+N}^\dagger \hat{a}_q$	$\hat{a}_p^\dagger \hat{a}_{p+N} \hat{a}_q^\dagger \hat{a}_{q+N}$	$\hat{a}_p^\dagger \hat{a}_{p+N} \hat{a}_{q+N}^\dagger \hat{a}_{q+N}$
$\hat{a}_{p+N}^\dagger \hat{a}_p$	$\hat{a}_{p+N}^\dagger \hat{a}_p \hat{a}_q^\dagger \hat{a}_q$	$\hat{a}_{p+N}^\dagger \hat{a}_p \hat{a}_{q+N}^\dagger \hat{a}_q$	$\hat{a}_{p+N}^\dagger \hat{a}_p \hat{a}_q^\dagger \hat{a}_{q+N}$	$\hat{a}_{p+N}^\dagger \hat{a}_p \hat{a}_{q+N}^\dagger \hat{a}_{q+N}$
$\hat{a}_{p+N}^\dagger \hat{a}_{p+N}$	$\hat{a}_{p+N}^\dagger \hat{a}_{p+N} \hat{a}_q^\dagger \hat{a}_q$	$\hat{a}_{p+N}^\dagger \hat{a}_{p+N} \hat{a}_{q+N}^\dagger \hat{a}_q$	$\hat{a}_{p+N}^\dagger \hat{a}_{p+N} \hat{a}_q^\dagger \hat{a}_{q+N}$	$\hat{a}_{p+N}^\dagger \hat{a}_{p+N} \hat{a}_{q+N}^\dagger \hat{a}_{q+N}$.

(11.15)

tiled in the following manner:

p=0,q=0	p=0,q=1	$\cdots$	p=0,q=$\frac{N}{2}-1$
p=1,q=0	p=1,q=1	$\cdots$	p=1,q=$\frac{N}{2}-1$
$\vdots$	$\vdots$	$\ddots$	$\vdots$
p=$\frac{N}{2}-1$,q=0	p=$\frac{N}{2}-1$,q=1	$\cdots$	p=$\frac{N}{2}-1$,q=$\frac{N}{2}-1$

(11.16)

In order to remove the ground-state-to-ground-state transition (to form the modified particle-hole RDM, ${}^2\tilde{G}$, see Eq. (11.3)),

	$\hat{a}_q^\dagger \hat{a}_q$	$\hat{a}_{q+N}^\dagger \hat{a}_q$	$\hat{a}_q^\dagger \hat{a}_{q+N}$	$\hat{a}_{p+N}^\dagger \hat{a}_{p+N}$
$\hat{a}_p^\dagger \hat{a}_p$	${}^1D_p[0,0]{}^1D_q[0,0]$	${}^1D_p[0,0]{}^1D_q[0,1]$	${}^1D_p[0,0]{}^1D_q[1,0]$	${}^1D_p[0,0]{}^1D_q[1,1]$
$\hat{a}_p^\dagger \hat{a}_{p+N}$	${}^1D_p[0,1]{}^1D_q[0,0]$	${}^1D_p[0,1]{}^1D_q[0,1]$	${}^1D_p[0,1]{}^1D_q[1,0]$	${}^1D_p[0,1]{}^1D_q[1,1]$
$\hat{a}_{p+N}^\dagger \hat{a}_p$	${}^1D_p[1,0]{}^1D_q[0,0]$	${}^1D_p[1,0]{}^1D_q[0,1]$	${}^1D_p[1,0]{}^1D_q[1,0]$	${}^1D_p[1,0]{}^1D_q[1,1]$
$\hat{a}_{p+N}^\dagger \hat{a}_{p+N}$	${}^1D_p[1,1]{}^1D_q[0,0]$	${}^1D_p[1,1]{}^1D_q[0,1]$	${}^1D_p[1,1]{}^1D_q[1,0]$	${}^1D_p[1,1]{}^1D_q[1,1]$

(11.17)

is subtracted off from each segment defined by p and q where the one-particle density matrix (${}^1D$) is given by

	$\hat{a}_p$	$\hat{a}_{p+N}$
$\hat{a}_p^\dagger$	$\hat{a}_p^\dagger \hat{a}_p$	$\hat{a}_p^\dagger \hat{a}_{p+N}$
$\hat{a}_{p+N}^\dagger$	$\hat{a}_{p+N}^\dagger \hat{a}_p$	$\hat{a}_{p+N}^\dagger \hat{a}_{p+N}$

(11.18)

The signature of exciton condensation (λ_G) is then obtained from the eigenvalue equation

$$^2\tilde{G}v_G^i = \epsilon_G^i v_G^i \tag{11.19}$$

with the signature corresponding the largest eigenvalue (the maximum ϵ_G^i).

Again, for the $N, r = 10, 20,\ \epsilon = 0$ calculations, site symmetry was utilized to decrease computational expense. Only sub-matrices corresponding to diagonal sub-matrices $p = q$, sub-matrices for BCS-paired orbitals $p = 2j - 1,\ q = 2j$, and for unpaired orbitals $p = 2j - 1,\ q \neq p \neq 2j$ needed to be computed.

11.6.2 Plastino's Model

In literature that dates back to the 1960s and continues to this day, Plastino and coworkers [411–413] explore a model Hamiltonian that adds a pairing-force term to the Lipkin model in the context of nuclear physics. Introducing the Plastino pairing-force term to the Lipkin Hamiltonian from Eq. (11.4)—which allows for slightly more flexibility than the formulation given in the Plastino literature as that literature is concerned only with the double excitation/de-excitation (λ) term and omits the scattering term (γ)—yields the following model Hamiltonian:

$$\begin{aligned}
\mathcal{H}_P = &-\frac{\epsilon}{2}\sum_{i=1}^{N}\hat{a}_i^\dagger\hat{a}_i + \frac{\epsilon}{2}\sum_{i=1}^{N}\hat{a}_{i+N}^\dagger\hat{a}_{i+N} \\
&+\frac{\lambda}{2}\sum_{p=1}^{N}\sum_{q=1}^{N}\hat{a}_p^\dagger\hat{a}_q^\dagger\hat{a}_{q+N}\hat{a}_{p+N} + \frac{\lambda}{2}\sum_{p=1}^{N}\sum_{q=1}^{N}\hat{a}_{p+N}^\dagger\hat{a}_{q+N}^\dagger\hat{a}_q\hat{a}_p \\
&+\frac{\gamma}{2}\sum_{p=1}^{N}\sum_{q=1}^{N}\hat{a}_{p+N}^\dagger\hat{a}_q^\dagger\hat{a}_{q+N}\hat{a}_p + \frac{\gamma}{2}\sum_{p=1}^{N}\sum_{q=1}^{N}\hat{a}_p^\dagger\hat{a}_{q+N}^\dagger\hat{a}_q\hat{a}_{p+N} \\
&-G\sum_{p=1}^{N}\sum_{q=1}^{N}\hat{a}_{p+N}^\dagger\hat{a}_p^\dagger\hat{a}_q\hat{a}_{q+N}
\end{aligned} \tag{11.20}$$

While the form of this Hamiltonian is similar to the one we introduce in Eq. (11.5), the difference is the orbitals which the pairing-force term (G) causes to be correlated in Cooper-like pairs. Specifically, while our model Hamiltonian pairs adjacent qubits (see Fig. 11.2), the Plastino Hamiltonian pairs orbitals with on the same Lipkin-like cite in different layers (i.e., stacked orbitals p and $p + N$).

In order to determine whether the Plastino Hamiltonian is capable of probing fermion-exciton condensate character—where λ_D and λ_G simultaneously exceed the Pauli-like limit of one and hence character of both fermion-pair condensation and exciton condensation are observed in a single quantum state—, a systematic scan over the input parameters of the Hamiltonian $(\epsilon, \lambda, \gamma, G)$ is conducted. As can in seen by Fig. 11.8 where the blue pluses represent the Lipkin model Hamiltonian, the yellow pluses represent the PF BCS-like Hamiltonian, and the green x's represent the Plastino Hamiltonian, while Plastino's Hamiltonian is capable of reproducing all Lipkin states accessible by the Lipkin model and states that demonstrate fermion-pair condensation, no dual condensate character is observed from the Plastino model as the region in which both λ_D and λ_G exceed one is not probed within this model.

In fact, there is direct competition between the particle-hole and particle-particle pairing between Lipkin-like sites which results in each type of pairing "driving" the system toward radically different states with the magnitudes of the coupling constants causing a transition between the Lipkin-like and BCS-like states favored by the different interactions. Conversely, because the particle-particle and particle-hole pairing in the model we introduce do not occur between the same orbitals, they can coexist, allowing for a much larger possible range of λ_D versus λ_G including the region demonstrating a fermion-exciton condensate.

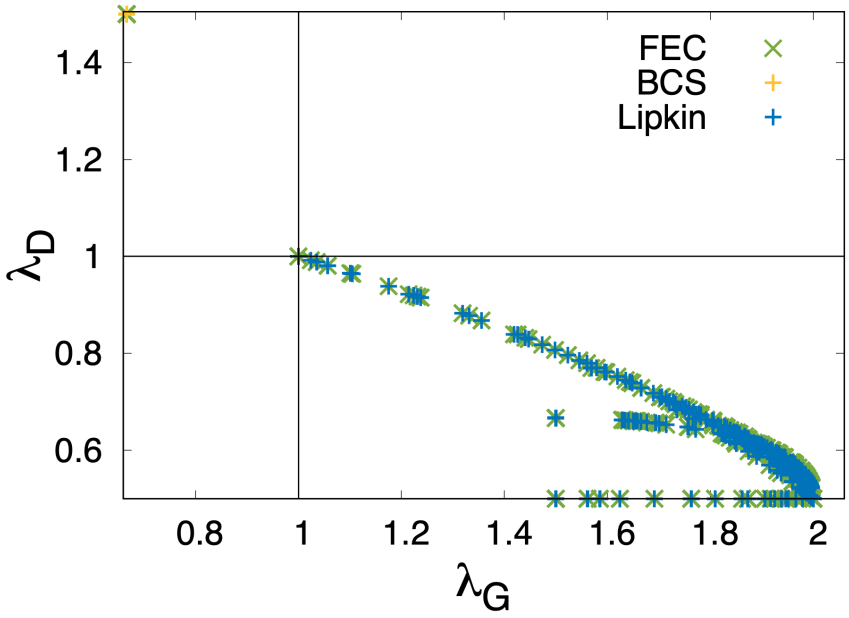

Figure 11.8: A plot of λ_G versus λ_D where parameters in the Plastino Hamiltonian are systematically varied for $N = 4$ particles in $r = 8$ orbitals is shown.

11.6.3 Supplemental Configurations

Configurations representing each of the classes of non-zero basis states for the FEC Hamiltonian for six electrons in twelve orbitals; eight electrons in sixteen orbitals; and ten electrons in twenty orbitals are—similar to Fig. 11.3—are given in Figs. 11.9-11.11.

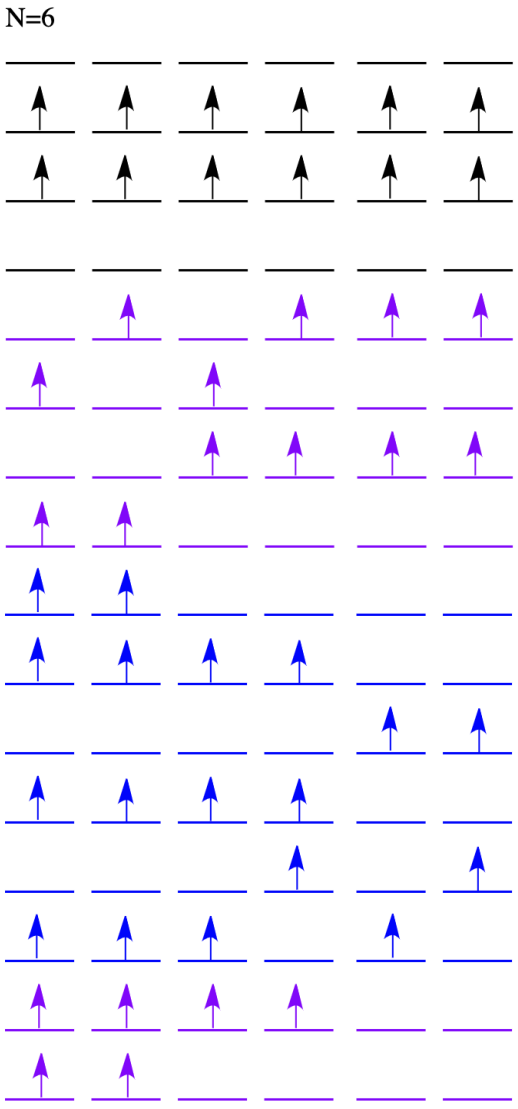

Figure 11.9: Configurations representing each of the eight classes of non-zero basis states for the FEC Hamiltonian for $N, r = 6, 12$ are shown. From top to bottom, the quantum numbers for each state are given by $|x, y, bool\rangle = |0, 3, T\rangle$,$|6, 3, T\rangle$, $|4, 1, T\rangle$, $|4, 3, T\rangle$, $|2, 3, F\rangle$, $|2, 3, T\rangle$, $|2, 1, T\rangle$, $|4, 3, F\rangle$, which represent the number of particles excited to the upper N-degenerate energy level (x), the number of BCS-like pairs (y), and whether the configuration is consistent with the Lipkin model ($bool$).

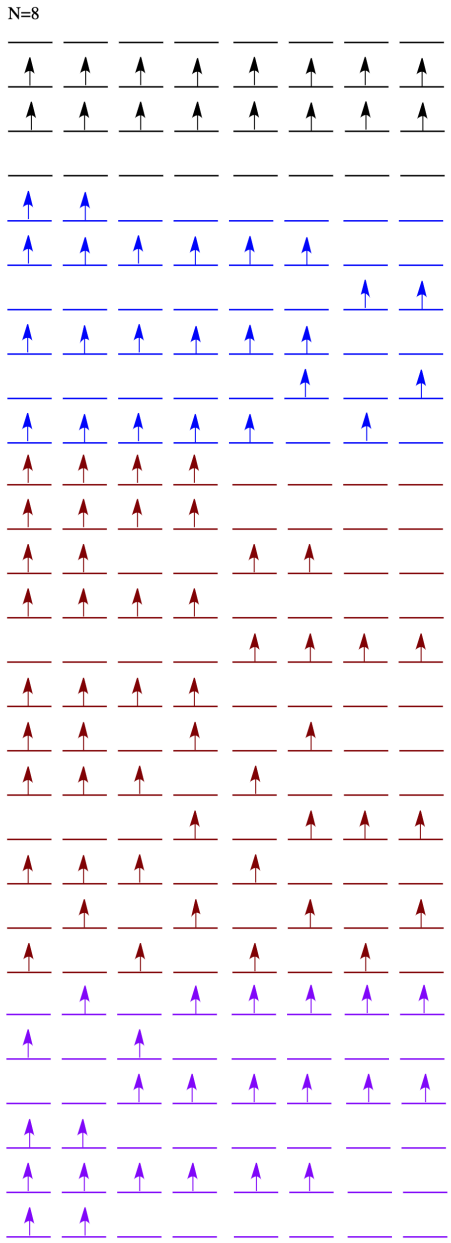

Figure 11.10: Configurations representing each of the fourteen classes of non-zero basis states for the FEC Hamiltonian for $N, r = 8, 16$ are shown. From top to bottom, the quantum numbers for each state are given by $|x, y, bool, (\zeta, \tau)\rangle = |0, 4, T\rangle$, $|8, 4, T\rangle$, $|2, 4, F\rangle$, $|2, 4, T\rangle$, $|2, 2, T\rangle$, $|4, 4, F, 2\rangle$, $|4, 4, F, 1\rangle$, $|4, 4, T\rangle$, $|4, 2, F, 1, 2\rangle$, $|4, 2, T\rangle$, $|4, 0, T\rangle$, $|6, 2, T\rangle$, $|6, 4, T\rangle$, $|6, 4, F\rangle$, which represent the number of particles excited to the upper N-degenerate energy level (x), the number of BCS-like pairs (y), and whether the configuration is consistent with the Lipkin model (*bool*); ζ and τ are additional quantum numbers to clarify a few basis states where ζ corresponds to the number of times BCS-like pairs are "stacked" into the same site such that orbitals $2j - 1$, $2j$, $2j - 1 + N$, and $2j + N$ are all occupied and where τ corresponds to the number of diagonal configurations in which either $2j - 1/2j + N$ or $2j - 1 + N/2j$ are both occupied where $2j - 1$ and $2j$ are adjacent, BCS-paired orbitals.

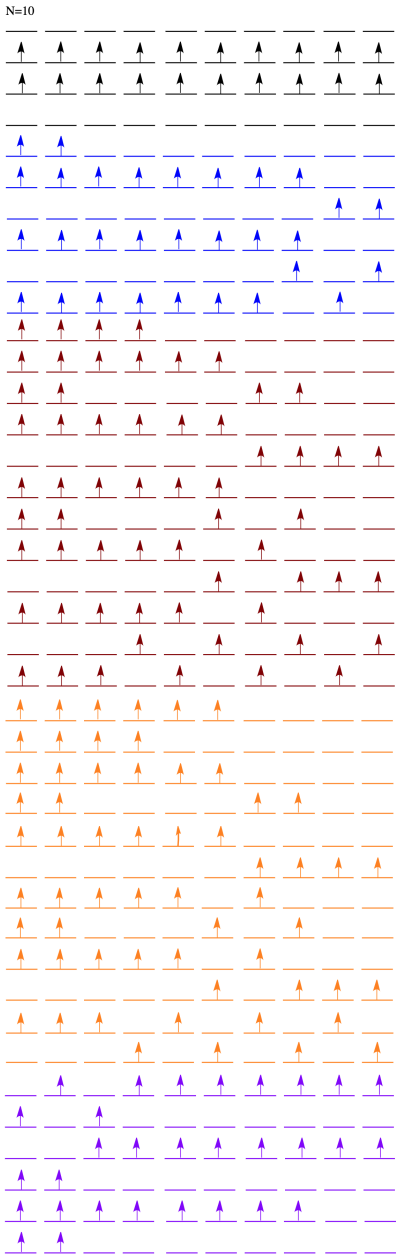

Figure 11.11: Configurations representing each of the twenty classes of non-zero basis states for the FEC Hamiltonian for $N, r = 10, 20$ are shown. From top to bottom, the quantum numbers for each state are given by $|x, y, bool, (\zeta, \tau)\rangle = |0, 5, T\rangle$, $|10, 5, T\rangle$, $|2, 5, F\rangle$, $|2, 5, T\rangle$, $|2, 3, T\rangle$, $|4, 5, F, 2\rangle$, $|4, 5, F, 1\rangle$, $|4, 5, T\rangle$, $|4, 3, F, 1, 2\rangle$, $|4, 3, T\rangle$, $|4, 1, T\rangle$, $|6, 5, F, 2\rangle$, $|6, 5, F, 1\rangle$, $|6, 5, T\rangle$, $|6, 3, F, 1, 2\rangle$, $|6, 3, T\rangle$, $|6, 1, T\rangle$, $|8, 3, T\rangle$, $|8, 5, T\rangle$, $|8, 5, F\rangle$, which represent the number of particles excited to the upper N-degenerate energy level (x), the number of BCS-like pairs (y), and whether the configuration is consistent with the Lipkin model ($bool$); ζ and τ are additional quantum numbers to clarify a few basis states where ζ corresponds to the number of times BCS-like pairs are "stacked" into the same site such that orbitals $2j-1$, $2j$, $2j-1+N$, and $2j+N$ are all occupied and where τ corresponds to the number of diagonal configurations in which either $2j-1/2j+N$ or $2j-1+N/2j$ are both occupied where $2j-1$ and $2j$ are adjacent, BCS-paired orbitals.

CHAPTER 12

ENTANGLED PHASE OF SIMULTANEOUS FERMION AND EXCITON CONDENSATIONS REALIZED

Material from: Sager, L. M. & Mazziotti, D. A., Entangled phase of simultaneous fermion and exciton condensations realized. Physical Review B, published 2022, 105(12), L121105.

12.1 Chapter Synopsis

Fermion-exciton condensates (FECs)—computationally- and theoretically-predicted states that simultaneously exhibit character of superconducting states and exciton condensates—are novel quantum states whose properties may involve a hybridization of superconductivity and the dissipationless flow of energy. Here, we exploit prior investigations of superconducting states and exciton condensates on quantum devices to identify a tuneable quantum state preparation entangling the wave functions of the individual condensate states. Utilizing this state preparation, we prepare a variety of fermion-exciton condensate states on quantum computers—realizing strongly-correlated FEC states on current, noisy intermediate-scale quantum devices—and verify the presence of the dual condensate via post-measurement analysis. This confirmation of the previously-predicted condensate state on quantum devices as well as the form of its wave function motivates further theoretical and experimental exploration of the properties, applications, and stability of fermion-exciton condensates.

12.2 Introduction

It may be possible to create materials that conduct both electric current and exciton excitation energy through the realization a single quantum state that simultaneously demonstrates properties of two different condensates—one composed of "Cooper" (particle-particle) pairs

and the other composed of excitons (particle-hole pairs) [4]. Bose-Einstein condensation allows for multiple bosons aggregating in a single quantum state [113, 114] at sufficiently low temperatures, resulting in the superfluidity of the constituent bosons [97, 115]. A superconducting quantum phase is created upon the condensation of pairs of fermions into a single quantum state, which results in the frictionless flow of the constituent particle-particle pairs [128, 184]. Significant theoretical and experimental investigation [6, 96, 107, 128, 137, 156, 178, 179, 184, 185, 187, 341–351, 417] has centered on superconductors in an effort to determine a commercially-viable material supporting superconductivity at sufficiently high temperatures. However, the relatively low energy of the Cooper pairs [128, 184] cause them to become unstable, reverting to traditional conductors above a critical temperature too low for commercial applications.

One avenue towards higher-temperature condensate phases has been an examination of condensations composed of particle-hole pairs (excitons) in a single quantum state, which can carry exciton excitation energy without resistance [106, 107]. Excitons are more-tightly bound than Cooper pairs, meaning that the condensation of excitons can persist at higher temperatures than those at which superconductors form, although the natural recombination of particles and holes is a cause of experimental difficulties in creating stable, high-temperature, ground-state exciton condensates. As such, much recent literature has explored the characteristics of exciton condensation as well as established various methodologies for overcoming the problem of annihilation upon recombination [5, 107, 112, 156, 178, 179, 186–188]. Specifically, exciton condensates have been observed in optical traps with polaritons [109, 110, 158, 189], the electronic double layers of semiconductors [180, 186, 187, 190, 191] and graphene [164, 179, 192], and in systems composed of transition metal chalcogenides [169, 171, 178, 418–420].

Here, we present an entangled quantum phase of matter in which a superconductor and an exciton condensate coexist in a single quantum state—a fermion-exciton condensate (FEC).

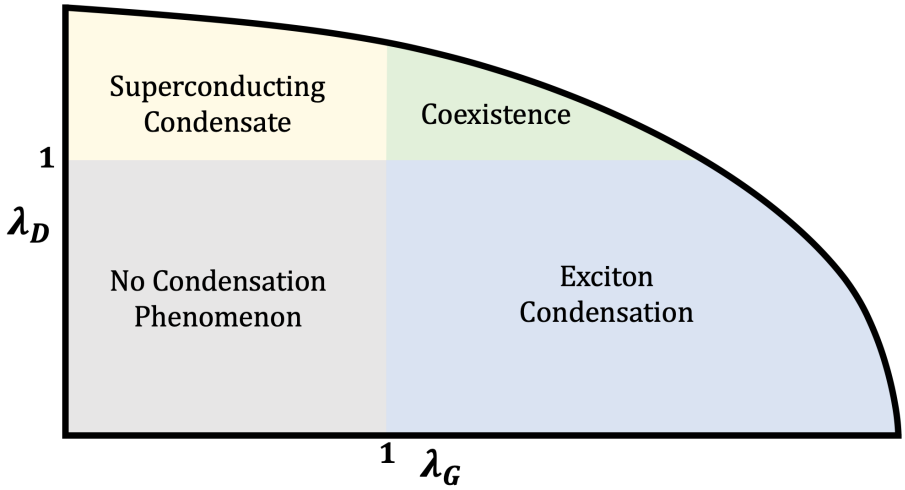

Figure 12.1: A figure of the condensate phase diagram in the phase space of the signatures of particle-particle condensation, λ_D, and exciton condensation, λ_G,—previously presented as Fig. 1 in Ref. [4]—is shown.

We leverage the ability of quantum computation to explore strongly correlated phenomena [270–275] as well as prior investigation [5, 6] to prepare a variety of fermion-exciton condensate states on quantum devices via a tuneable quantum state preparation—verifying the presence of the condensate state through probing the signatures of particle-particle (λ_D) [135, 136] and exciton (λ_G) [155, 156] condensations. Our results not only confirm the existence of a new class of condensates, they verify the theoretical prediction of the form of the wave function of the FEC as well as the phase diagram of the states (see Fig. 12.1). These results suggest that such condensates can potentially be prepared in physical systems such as twisted graphene bilayers in which forces favoring exciton condensation and superconducting, respectively, are in fierce competition.

Note that while both particle-particle and exciton condensates are known to exist in systems designed to use exciton condensates to mediate the creation of Cooper pairs at higher temperatures [375, 376], this coexistence of fermion pair and excitonic condensation occurs in two adjacent systems that interact with one another [376] instead of existing in a joint FEC state.

12.3 Theory

12.3.1 Signatures of Condensation

Condensation occurs when multiple bosons aggregate into a single quantum state [113, 114] at temperatures below a certain critical temperature, resulting in the superfluidity of the constituent bosons [97, 115]. In a condensation of particle-particle pairs, pairs of fermions condense into a single geminal, a two-fermion function directly analogous to a one-fermion orbital [66, 135, 136, 221–223], resulting in the frictionless flow of the particle-particle pairs [128, 184]. As established by Yang [135] and Sasaki [136], a computational signature of such superconducting states—denoted as λ_D—is a large eigenvalue ($\lambda_D > 1$) of the particle-particle reduced density matrix (2-RDM) with elements given by

$$ {}^2D^{i,j}_{k,l} = \langle \Psi | \hat{a}^\dagger_i \hat{a}^\dagger_j \hat{a}_l \hat{a}_k | \Psi \rangle \tag{12.1} $$

where $|\Psi\rangle$ is an N-fermion wave function and where $\hat{a}^\dagger_i$ and $\hat{a}_i$ are fermionic creation and annihilation operators for orbital i, respectively. This signature directly probes the presence and extent of non-classical (off-diagonal) long-range order [221].

Exciton condensation, similarly, results from the condensation of particle-hole pairs (excitons) condensing into a single quantum state [106, 107]. A computational signature of exciton condensation—denoted as λ_G—is a large eigenvalue ($\lambda_G > 1$) of a modified version of the particle-hole reduced density matrix [148, 155, 156], with elements given by

$$ {}^2\tilde{G}^{i,j}_{k,l} = {}^2G^{i,j}_{k,l} - {}^1D^i_j \, {}^1D^l_k = \langle \Psi | \hat{a}^\dagger_i \hat{a}_j \hat{a}^\dagger_l \hat{a}_k | \Psi \rangle - \langle \Psi | \hat{a}^\dagger_i \hat{a}_j | \Psi \rangle \langle \Psi | \hat{a}^\dagger_l \hat{a}_k | \Psi \rangle \tag{12.2} $$

where ${}^1D$ is the one-fermion reduced density matrix (1-RDM). Note that this modification removes the extraneous large eigenvalue from a ground-state-to-ground-state transition.

See the Methods section of the Supplemental Information for specifics of how the signa-

tures of superconductivity (λ_D) and exciton condensation (λ_G) are obtained from the result data of a given quantum state preparation.

12.3.2 Fermion-Exciton Condensate

A fermion-exciton condensate is a quantum state in which character of both particle-particle condensation and exciton condensation coexist [4]; thus, a fermion-exciton condensate exhibits simultaneous large eigenvalues of the particle-particle and modified particle-hole RDMs—i.e., $\lambda_D, \lambda_G > 1$. As we have previously theoretically established in the thermodynamic limit [4], a fermion-exciton condensate should result from the entanglement of a wave function exhibiting superconductivity, $|\Psi_D\rangle$, with a wave function exhibiting exciton condensation, $|\Psi_G\rangle$), mathematically represented as

$$|\Psi_{FEC}\rangle = \frac{1}{\sqrt{2 - |\Delta|}} \left(|\Psi_D\rangle - \text{sgn}(\Delta)|\Psi_G\rangle\right), \tag{12.3}$$

where $\Delta = 2\langle\Psi_D|\Psi_G\rangle$ [4].

From our previous work [4], we note that a fermion-exciton condensate state is accessible in systems as small as four fermions ($N = 4$) in eight orbitals ($r = 8$), and from our investigations of condensate behavior on quantum devices, wave functions demonstrating maximal particle-particle condensation [6] and maximal exciton condensation [5], individually, have been identified, prepared, and probed on quantum devices for $N = 4, r = 8$ systems. Using the forms of these wave functions, we construct a state preparation that allows for the entanglement of the non-zero elements of the separate condensates, which is shown in Fig. 12.2. The input angles (θ_1, θ_2) are then optimized to generate a fermion-exciton condensate with character of each (i.e., a dual maximization of λ_D and λ_G).

See the Methods section of the Supplemental Information for details of state preparations using both the bosonic representation of a qubit—in which each qubit is interpreted as a

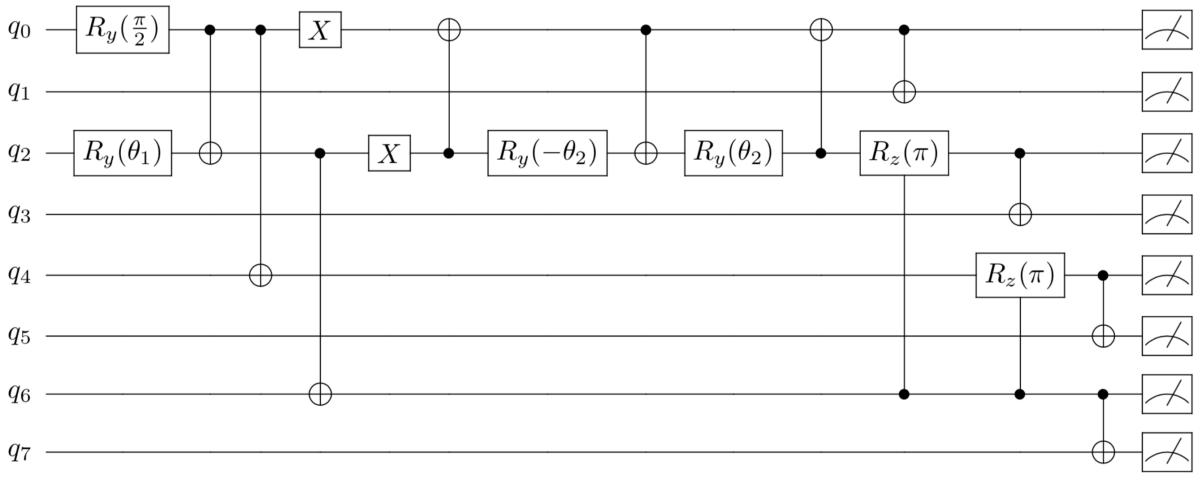

Figure 12.2: A schematic demonstrating the fermionic quantum state preparation that yields an entanglement of the non-zero elements of the separate particle-particle and particle-hole condensates [5, 6], where R_y and R_z represent rotations about the y and z axes of the Bloch sphere and where two-qubit gates are represented such that the control qubit is specified by a dot connected to the target qubit, which is specified by the appropriate gate. The wave function that results from this state preparation is given in the Supplemental Information. Note that the condensate character—and hence the signatures of condensation λ_G, λ_D—are varied by scanning over input angles (θ_1, θ_2).

two-fermion geminal—and the fermionic representation of a qubit—in which each qubit is interpreted as a one-fermion orbital—as well as the optimization procedure for the input angles. Also note that—as in Ref. [6]—in our fermionic preparation, the pairing of qubits causes the usual difference between fermion and qubit statistics to disappear and hence allows for the direct representation of electron pairs on the quantum computer.

12.4 Results

Using the bosonic state preparations with input angles that span the region exhibiting dual condensate character, we prepare a fermion-exciton condensate on a five-qubit quantum device [7]. As can be seen in Fig. 12.3a, with the blue x's representing device data before any error mitigation, various input angles yield quantum states with the signatures of both superconductor (λ_D) and exciton condensate (λ_G) character simultaneously exceeding the

Pauli-like bound of one. Moreover, as statistical analysis was conducted with the average and standard deviation determined from a sample size of ten trials per state preparation, these large eigenvalues are not spurious; rather, they are statistically-significant within one standard deviation. Further, for several of these unmitigated, experimental fermion-exciton condensates, the signature of condensation persists within two standard deviations. (See the Supplemental Information for the standard deviation ranges of the signatures of condensation.) Note that divergence from the maximal dual condensate character predicted for these input angles (i.e., the degree to which the reported data deviates from points along the elliptical fit) is likely due to preparation and readout errors on this noisy intermediate-scale quantum (NISQ) computer [252–254, 256]. (See the Supplemental information for device error specifications.)

As is shown in Fig. 12.3b, using the fermionic state preparation on a noisier, fifteen-qubit quantum device [8] fails to realize a fermion-exciton condensate before error mitigation. Further, as shown in Table 12.1 which presents the λ_D and λ_G values for a range of preparations simulated using four noise models that simulate errors consistent with real-world quantum device backends, this fermionic preparation would likely not yield fermion-exciton condensates on even the newer and less-error-prone Montreal and Mumbai quantum computers. Likely, the four additional two-qubit, CNOT gates introduced into the fermionic state preparation—relative to the bosonic state preparation—introduce sufficient error to the quantum state such that the degree that condensate character is decreased or lost altogether. This is further evidenced by both simulated Montreal and Mumbai being capable of demonstrating dual condensate behavior indicative of a fermion-exciton condensate for the bosonic state preparation and by simulated Melbourne demonstrating higher signatures of condensation for the bosonic preparation relative to the fermionic preparation.

In order to use NISQ devices to better-model these fermion-exciton condensate phases, we introduce an error mitigation scheme. As can be seen in the Methods section of the

Supplemental Information, the state preparations should yield quantum states with only six of the qubit basis states contributing to the overall wave function. Any contribution from states other than these six basis states are unexpected and are directly caused by error on the quantum devices (or simulators) employed. As such, we perform an error mitigation technique in which we project contributions from the qubit basis states that are not expected to contribute to zero and renormalize the resultant wave function. As can be seen in Fig. 12.3 and Table 12.1, using this error mitigation technique improves results from both the fermionic and bosonic preparations. Specifically—as can be readily observed from the green x's representing the mitigated, projected results in Fig. 12.3—, this projection technique leads to values approximating the ideal dual existence of excitonic and fermionic behavior along the elliptical fit, allowing us to prepare and probe ideal fermion-exciton condensates despite significant amounts of error on the NISQ quantum devices.

One interesting aside is that—for both the raw and projected data—the trade-off between character of a superconductor and that of an exciton condensate first noted in Ref. [4] is also observed here. This trade-off appears to be elliptic in nature—consistent with the convex nature of the 2-RDMs when projected onto two dimensions [380–382]—even for the noisy, non-mitigated Santiago results, and nearly the exact elliptic fit established in Ref. [4] is observed when the contributions from the components that should not contribute are projected to zero. (See Ref. [4] for additional details.) This trade-off is significant as it precludes a fermion-exciton condensate with maximal condensate character of both particle-particle and exciton condensations. However, as the trade-off is elliptic in nature and as the maximal λ_D and λ_D values increase with system size (N), the lengths of the major and minor axes of the elliptical fit will increase as the size of the system is increased, causing the trade-off to become less and less stark.

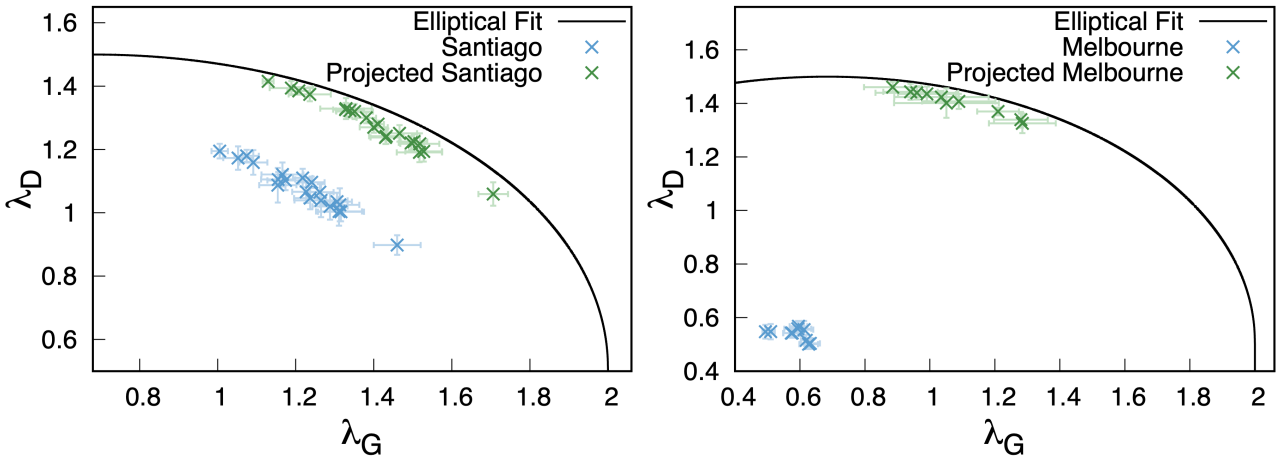

(a) Santiago (b) Melbourne

Figure 12.3: The eigenvalues of the ${}^2D$ and ${}^2\tilde{G}$ matrices (λ_D and λ_G, respectively) for various states prepared on IBM Quantum's (a) Santiago [7] and (b) Melbourne [8] quantum computers before and after error mitigation via projection are plotted against the elliptical fit [4] obtained from the unconstrained scan of λ_D versus λ_G. Note that the average value and standard deviation of ten trials per state preparation are shown.

12.5 Conclusions

In this paper, we prepare a fermion-exciton condensate—a single quantum state demonstrating both superconductivity and exciton condensation—on a quantum device. This both realizes a highly-correlated state of matter on a noisy intermediate-scale quantum device and verifies the theoretical hypothesis from Ref. [4] that such a state can be generated by entangling wave functions that separately exhibit particle-particle and exciton condensation. Further, the error mitigation technique introduced leads to signatures of fermion-pair (λ_D) and exciton condensation (λ_G) approaching the ideal dual existence of excitonic and fermionic behavior along the elliptical fit on NISQ devices, allowing for better-modelling of these highly-correlated dual condensate phases on even extremely-noisy devices.

An experimental system that may result in such an entanglement may be a bilayer system—as bilayers are often known to exhibit exciton condensation—in which the geometric orientation of the layers such as the twist angles are optimized to generate competition

Computer	**Quantum Volume**	**Full**		**Projected**	
		$\lambda_{\mathbf{G}}$	$\lambda_{\mathbf{D}}$	$\lambda_{\mathbf{G}}$	$\lambda_{\mathbf{D}}$
Fermionic	**Preparation**				
Melbourne	8	0.804	0.994	1.191	1.352
		0.921	0.597	1.387	1.303
		0.934	0.581	1.440	1.271
		0.910	0.567	1.461	1.261
Montreal	128	0.918	1.134	1.169	1.329
		1.193	0.868	1.472	1.255
		1.241	0.849	1.527	1.215
		1.267	0.824	1.580	1.176
Mumbai	128	0.866	1.051	1.217	1.334
		0.928	0.697	1.360	1.319
		0.925	0.636	1.435	1.278
		1.113	0.721	1.537	1.212
Bosonized	**Preparation**				
Melbourne	8	0.875	1.256	1.130	1.377
		1.013	0.919	1.328	1.334
		1.077	0.906	1.409	1.289
		1.094	0.914	1.422	1.281
Montreal	128	1.126	1.281	1.244	1.310
		1.306	1.107	1.454	1.265
		1.400	1.066	1.547	1.205
		1.406	1.041	1.567	1.188
Mumbai	128	0.934	1.295	1.138	1.364
		1.160	1.022	1.408	1.293
		1.080	0.965	1.376	1.311
		1.233	0.990	1.497	1.238
Santiago	32	1.169	1.278	1.264	1.304
		1.344	1.130	1.465	1.260
		1.390	1.100	1.517	1.225
		1.460	1.060	1.589	1.174

Table 12.1: Table of eigenvalues for the ${}^2\tilde{G}$ (λ_G) and ${}^2D$ (λ_D) matrices obtained from noise model simulating errors from real-world quantum computers both before (full) and after (projected) error mitigation via projection of appropriate components to zero.

between forces favoring an exciton condensate and a superconductor. It may also be possible to consider bilayers in which each layer is composed of a traditional superconductor, which can demonstrate particle-particle condensation. These systems should be studied both

computationally and experimentally as there are many open questions regarding the formation, properties, application, and stability of fermion-exciton condensates. The possibility of a hybridization of the properties of superconductors with those of an exciton condensate definitely motivate further examination of this new state of matter.

12.6 Supplemental Information

12.6.1 Methods

We include details on the procedure used to prepare the qubit states presented in the article; the methodology for reconstructing the particle-particle and the modified particle-hole density matrices (and subsequent signatures of condensation) from data obtained from the experimental quantum devices employed; and provide relevant information regarding the quantum devices.

Methodology for State Preparation:

Bosonic Preparation: Our previous work [4] has demonstrated that coexistence of exciton and particle-particle condensation is viable in systems composed of as few as four electrons ($N = 4$) in eight orbitals ($r = 8$) and is theoretically attainable via entanglement of wave functions demonstrating maximal character of each. Interpreting each qubit as a two-fermion geminal (as in Ref. [421]) which can either be occupied by a Cooper pair-like boson (represented as $|1\rangle$) or unoccupied (represented as $|0\rangle$), we have additionally shown that maximal exciton condensation in a four-electron, eight-orbital system is observed in qubit states described by the following wave function [5]

$$|\Psi_G\rangle = \frac{1}{\sqrt{2}}\left(|1100\rangle + |0011\rangle\right) \tag{12.4}$$

and that maximal character of superconductivity is observed in a qubit state described by [6]

$$|\Psi_D\rangle = \frac{1}{\sqrt{6}}(|1100\rangle + |1010\rangle + |1001\rangle + |0110\rangle + |0101\rangle + |0011\rangle). \tag{12.5}$$

Thus, an entanglement of these two wave functions should involve only six non-zero elements of the wave function and should contain only real contributions. A general quantum state preparation that satisfies these constraints and additionally demonstrates particle-hole symmetry is shown in Fig 10.2b.

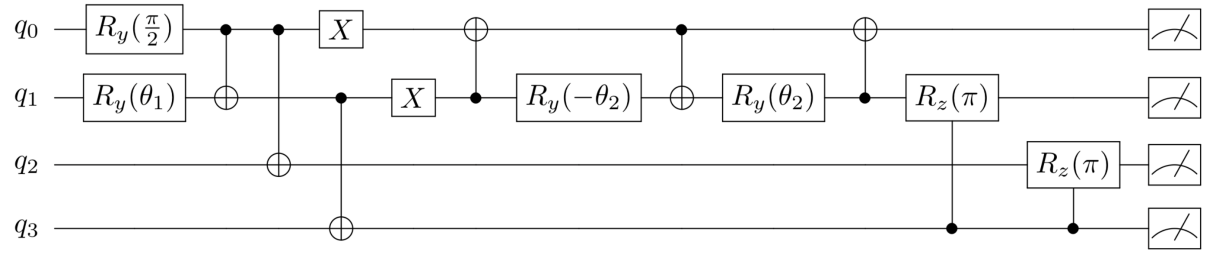

Figure 12.4: A schematic demonstrating the bosonic quantum state preparation that yields Eq. (12.6) where α, β, and γ depend on the angles of rotation (θ_1 and θ_2), where R_y and R_z represent rotations about the y and z axes of the Bloch sphere, and where two-qubit gates are represented such that the control qubit is specified by a dot connected to the target qubit, which is specified by the appropriate gate.

This state preparation yields

$$|\Psi\rangle = \alpha|1100\rangle - \beta|1010\rangle - \gamma|1001\rangle - \gamma|0110\rangle - \beta|0101\rangle + \alpha|0011\rangle \tag{12.6}$$

where α, β, and γ are positive (i.e., the phases of the components that correspond to α are 0, and the phases of the components that correspond to β and γ are π) with magnitudes depending on the angles of rotation (θ_1 and θ_2).

In order to determine the angles that correspond to quantum states demonstrating maximal dual condensate behavior (i.e., the fermion-exciton condensate), we construct the four-fermion wave function ($N = 4, r = 8$) in terms of the angles of rotation (θ_1 and θ_2) that correspond to the state preparation in Fig. 10.2b by converting the gates applied to their ma-

trix representation and by translating the geminal representation into the equivalent orbital form. The angles are then determined via multiobjective optimization–utilizing a sequential quadratic programming algorithm [377, 378] with gradients computed via second-order centered finite differences [379]–with respect to λ_{DG}, which is given by [4]

$$\lambda_{DG} = w_G \left(\lambda_G - \lambda_G^o\right) - (1 - w_G)\, \lambda_D \tag{12.7}$$

where w_G is the weight given to optimizing the largest eigenvalue of the modified particle-hole reduced density matrix (λ_G) to the value specified by λ_G^o and where the eigenvalue of the particle-particle reduced density matrix (λ_D) is unconstrained.

As λ_{DG} depends on both the signature of exciton condensation (λ_G) and that of superconducting states (λ_D), probing variable specified values should yield input angles that maximize the signature of particle-particle condensation (λ_D) for a specified signature of exciton condensation (λ_G^o). The result of this scan is shown in Fig. 12.7, and the optimized angles demonstrating maximal fermion-exciton condensate character—i.e., having λ_G/λ_D values that lie along the elliptical fit [4]—were utilized throughout this paper to prepare the quantum states on the experimental quantum devices, although—in a few instances—tweaks to the input parameters were made on the actual devices in an attempt to counteract device-specific preparation errors.

Fermionic Preparation: To directly represent each qubit as a single-fermionic orbital—which can either be occupied ($|1\rangle$) or unoccupied ($|0\rangle$)—the bosonic preparation, with the appropriate angles of rotation as determined from the multiobjective optimization, is directly translated to a fermionic preparation. This is accomplished as is shown in the qubit diagram in the main text and yields the following eight-qubit wave function:

$$|\Psi\rangle = \alpha|11110000\rangle - \beta|11001100\rangle - \gamma|11000011\rangle - \gamma|00111100\rangle - \beta|00110011\rangle + \alpha|00001111\rangle \tag{12.8}$$

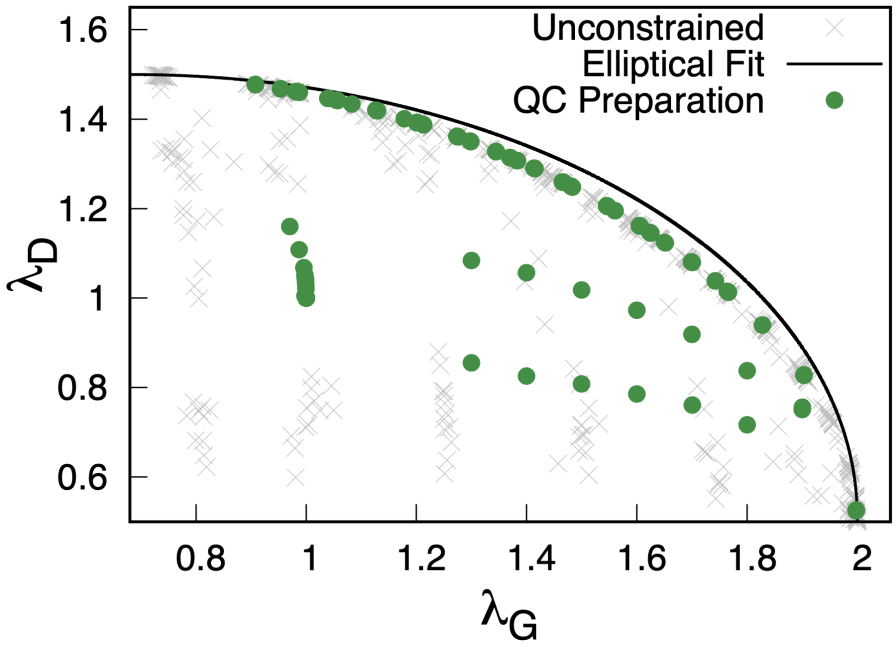

Figure 12.5: A scan of λ_D versus λ_G where the rotation angles in Fig. 10.2b are obtained via multiobjective optimization of λ_{DG} (see Eq. (12.7)) is plotted against the unconstrained scan of and the corresponding elliptical fit from Ref. [4]. These optimized angles are used to specify state preparations on the experimental quantum computers employed.

where α, β, and γ are identical to those in Eq. (12.6) for a given set of input angles (θ_1, θ_2). This translation is achieved by entangling pairs of adjacent qubits, which—as is shown in Ref. [6]—directly allows us to represent the electron pairs on a quantum computer as the usual difference between fermion and qubit statistics vanishes due to the pairing of adjacent qubits/orbitals that generates an extreme geminal.

Reconstruction of Density Matrices:

The portions of the reduced density matrices required to compute the signatures of superconductivity and exciton condensation are obtained by directly computing the expectation value for each element of the vector form of the wave function constructed from the "counts" data—accounting for the appropriate phases of each according to those expected from the state preparation—for the overall operator constructed from the tensor product of the appro-

priate creation and annihilation operators. Thus, in order to consider only fermionic—and not bosonic—creation and annihilation operators, the results for each of the bosonic preparations are classically converted during post-measurement analysis to be consistent with results obtained from fermionic preparations.

The subblock of the particle-particle reduced density matrix (^2D) associated with its largest eigenvalue [66, 364, 365] is given by

	$\hat{a}_1\hat{a}_0$	$\hat{a}_3\hat{a}_2$	$\cdots$	$\hat{a}_{r-1}\hat{a}_{r-2}$
$\hat{a}_0^\dagger\hat{a}_1^\dagger$	$\hat{a}_0^\dagger\hat{a}_1^\dagger\hat{a}_1\hat{a}_0$	$\hat{a}_0^\dagger\hat{a}_1^\dagger\hat{a}_3\hat{a}_2$	$\cdots$	$\hat{a}_0^\dagger\hat{a}_1^\dagger\hat{a}_{r-1}\hat{a}_{r-2}$
$\hat{a}_2^\dagger\hat{a}_3^\dagger$	$\hat{a}_2^\dagger\hat{a}_3^\dagger\hat{a}_1\hat{a}_0$	$\hat{a}_2^\dagger\hat{a}_3^\dagger\hat{a}_3\hat{a}_2$	$\cdots$	$\hat{a}_2^\dagger\hat{a}_3^\dagger\hat{a}_{r-1}\hat{a}_{r-2}$
$\vdots$	$\vdots$	$\vdots$	$\ddots$	$\vdots$
$\hat{a}_{r-2}^\dagger\hat{a}_{r-1}^\dagger$	$\hat{a}_{r-2}^\dagger\hat{a}_{r-1}^\dagger\hat{a}_1\hat{a}_0$	$\hat{a}_{r-2}^\dagger\hat{a}_{r-1}^\dagger\hat{a}_3\hat{a}_2$	$\cdots$	$\hat{a}_{r-2}^\dagger\hat{a}_{r-1}^\dagger\hat{a}_{r-1}\hat{a}_{r-2}$

where $\hat{a}_i^\dagger$ and $\hat{a}_i$ are fermionic creation and annihilation operators, respectively, for orbital (and hence qubit) i, which are given by

$$\hat{a}_i^\dagger = \begin{pmatrix} 0 & 0 \\ 1 & 0 \end{pmatrix}_i \tag{12.9}$$

and

$$\hat{a}_i = \begin{pmatrix} 0 & 1 \\ 0 & 0 \end{pmatrix}_i \tag{12.10}$$

in matrix form. The signature of superconductivity (λ_D) can then be computed from the subblock of the ^2D according to the eigenvalue equation

$$^2D v_D^i = \epsilon_D^i v_D^i \tag{12.11}$$

with the signature corresponding the largest eigenvalue (the maximum ϵ_D^i).

Similarly, only a portion of the particle-hole RDM (^2G) is associated with its large eigenvalues. This sub-matrix is composed of segments defined by p and q values according to

	$\hat{a}_q^\dagger \hat{a}_q$	$\hat{a}_{q+4}^\dagger \hat{a}_q$	$\hat{a}_q^\dagger \hat{a}_{q+4}$	$\hat{a}_{q+4}^\dagger \hat{a}_{q+4}$
$\hat{a}_p^\dagger \hat{a}_p$	$\hat{a}_p^\dagger \hat{a}_p \hat{a}_q^\dagger \hat{a}_q$	$\hat{a}_p^\dagger \hat{a}_p \hat{a}_{q+4}^\dagger \hat{a}_q$	$\hat{a}_p^\dagger \hat{a}_p \hat{a}_q^\dagger \hat{a}_{q+4}$	$\hat{a}_p^\dagger \hat{a}_p \hat{a}_{q+4}^\dagger \hat{a}_{q+4}$
$\hat{a}_p^\dagger \hat{a}_{p+4}$	$\hat{a}_p^\dagger \hat{a}_{p+4} \hat{a}_q^\dagger \hat{a}_q$	$\hat{a}_p^\dagger \hat{a}_{p+4} \hat{a}_{q+4}^\dagger \hat{a}_q$	$\hat{a}_p^\dagger \hat{a}_{p+4} \hat{a}_q^\dagger \hat{a}_{q+4}$	$\hat{a}_p^\dagger \hat{a}_{p+4} \hat{a}_{q+4}^\dagger \hat{a}_{q+4}$
$\hat{a}_{p+4}^\dagger \hat{a}_p$	$\hat{a}_{p+4}^\dagger \hat{a}_p \hat{a}_q^\dagger \hat{a}_q$	$\hat{a}_{p+4}^\dagger \hat{a}_p \hat{a}_{q+4}^\dagger \hat{a}_q$	$\hat{a}_{p+4}^\dagger \hat{a}_p \hat{a}_q^\dagger \hat{a}_{q+4}$	$\hat{a}_{p+4}^\dagger \hat{a}_p \hat{a}_{q+4}^\dagger \hat{a}_{q+4}$
$\hat{a}_{p+4}^\dagger \hat{a}_{p+4}$	$\hat{a}_{p+4}^\dagger \hat{a}_{p+4} \hat{a}_q^\dagger \hat{a}_q$	$\hat{a}_{p+4}^\dagger \hat{a}_{p+4} \hat{a}_{q+4}^\dagger \hat{a}_q$	$\hat{a}_{p+4}^\dagger \hat{a}_{p+4} \hat{a}_q^\dagger \hat{a}_{q+4}$	$\hat{a}_{p+4}^\dagger \hat{a}_{p+4} \hat{a}_{q+4}^\dagger \hat{a}_{q+4}$.

where the overall matrix is obtained by tiling these individual segments with an overall form given below.

p=0,q=0	p=0,q=1	$\cdots$	p=0,q=$\frac{N}{2}$−1
p=1,q=0	p=1,q=1	$\cdots$	p=1,q=$\frac{N}{2}$−1
$\vdots$	$\vdots$	$\ddots$	$\vdots$
p=$\frac{N}{2}$−1,q=0	p=$\frac{N}{2}$−1,q=1	$\cdots$	p=$\frac{N}{2}$−1,q=$\frac{N}{2}$−1

As the particle-hole RDM has a large eigenvalue caused by a ground-state-to-ground-state transition and not exciton condensation, it must be modified (to form the modified particle-hole RDM, $^2\tilde{G}$) to remove the extraneous large eigenvalue. This modification is accomplished by subtracting off

	$\hat{a}_q^\dagger \hat{a}_q$	$\hat{a}_{q+4}^\dagger \hat{a}_q$	$\hat{a}_q^\dagger \hat{a}_{q+4}$	$\hat{a}_{p+4}^\dagger \hat{a}_{p+4}$
$\hat{a}_p^\dagger \hat{a}_p$	${}^1D_p[0,0]{}^1D_q[0,0]$	${}^1D_p[0,0]{}^1D_q[0,1]$	${}^1D_p[0,0]{}^1D_q[1,0]$	${}^1D_p[0,0]{}^1D_q[1,1]$
$\hat{a}_p^\dagger \hat{a}_{p+4}$	${}^1D_p[0,1]{}^1D_q[0,0]$	${}^1D_p[0,1]{}^1D_q[0,1]$	${}^1D_p[0,1]{}^1D_q[1,0]$	${}^1D_p[0,1]{}^1D_q[1,1]$
$\hat{a}_{p+4}^\dagger \hat{a}_p$	${}^1D_p[1,0]{}^1D_q[0,0]$	${}^1D_p[1,0]{}^1D_q[0,1]$	${}^1D_p[1,0]{}^1D_q[1,0]$	${}^1D_p[1,0]{}^1D_q[1,1]$
$\hat{a}_{p+4}^\dagger \hat{a}_{p+4}$	${}^1D_p[1,1]{}^1D_q[0,0]$	${}^1D_p[1,1]{}^1D_q[0,1]$	${}^1D_p[1,1]{}^1D_q[1,0]$	${}^1D_p[1,1]{}^1D_q[1,1]$

from each segment defined by p and q where each one-particle density matrix is given by

$$\begin{array}{c|cc} & \hat{a}_p & \hat{a}_{p+4} \\ \hline \hat{a}_p^\dagger & \hat{a}_p^\dagger \hat{a}_p & \hat{a}_p^\dagger \hat{a}_{p+4} \\ \hat{a}_{p+4}^\dagger & \hat{a}_{p+4}^\dagger \hat{a}_p & \hat{a}_{p+4}^\dagger \hat{a}_{p+4} \end{array} \tag{12.12}$$

The signature of exciton condensation (λ_G) can then be computed from ${}^2\tilde{G}$ according to the eigenvalue equation

$${}^2\tilde{G} v_G^i = \epsilon_G^i v_G^i \tag{12.13}$$

with the signature corresponding the largest eigenvalue (the maximum ϵ_G^i).

Experimental Quantum Device Specifications:

Throughout this work, we have employed the ibmq_santiago [7] and ibmq_16_melbourne [8] IBM Quantum Experience devices, which are available online. Note that the bosonic state preparation was utilized for all Santiago results, and—unless otherwise stated—the fermionic state preparation was utilized for all Melbourne results. Both quantum devices are composed of fixed-frequency transmon qubits with co-planer waveguide resonators [272, 274]. Experimental calibration data and connectivity for these devices are included in the following sections of the Supplemental.

12.6.2 Calibration Data for IBM Quantum Devices Employed

Table 12.2: Calibration data for “Santiago”

Device:	ibmq_santiago (“Santiago”)					
Calibration Date:	06/11/21					
Version:	1.3.22					
Gate time (max, ns):	561.8					
Qubit:		0	1	2	3	4
	T2 (μs)	207.8	91.7	69.8	95.1	59.0
	f (GHz)	4.83	4.62	4.82	4.74	4.82
	T1 (μs)	125.8	156.0	116.8	157.0	78.7
	Gate Error (10^{-3})	0.26	0.20	0.18	0.16	0.48
	Readout Error (10^{-3})	24.1	15.0	9.7	7.3	30.7
Multi-Qubit:		0,1	1,2	2,3	3,4	
	Error (10^{-3})	8.3	6.1	4.8	6.1	

Table 12.3: Calibration data for “Melbourne”

Device:	ibmq_16_melbourne (“Melbourne”)																				
Calibration Date:	06/11/21																				
Version:	2.3.24																				
Gate time (max, ns):	1642.7																				
Qubit:		0	1	2	3	4	5	6	7	8	9	10	11	12	13	14					
	T2 (μs)	78.2	57.8	73.5	21.9	78.0	36.8	94.8	25.3	84.5	62.5	51.8	41.3	82.5	26.7	57.6					
	f (GHz)	5.12	5.24	5.04	4.89	5.02	5.07	4.93	4.98	4.75	4.97	4.95	5.00	4.76	4.97	5.01					
	T1 (μs)	69.5	58.0	61.4	69.7	69.9	21.5	78.5	32.3	109.5	43.3	47.3	49.7	71.7	28.7	43.8					
	Gate Error (10^{-3})	0.65	1.10	0.75	0.40	0.58	3.60	0.89	2.48	0.70	1.60	1.30	0.66	0.92	2.55	0.74					
	Readout Error (10^{-3})	24.8	46.8	39.8	75.1	38.8	55.6	27.5	64.2	38.7	41.5	42.6	42.0	30.8	71.8	45.5					
Multi-Qubit:		0,1	0,14	1,2	1,13	2,3	2,12	3,4	3,11	4,5	4,10	5,6	5,9	6,8	7,8	8,9	9,10	10,11	11,12	12,13	13,14
	Error (10^{-3})	23.1	23.4	15.2	45.2	24.4	55.1	14.7	35.3	34.0	28.9	109.1	32.0	40.9	37.8	32.4	30.4	34.1	37.1	37.4	49.0

12.6.3 Extended Results

Simulated Results

Computer	**QV**	**Full** λ_G	**Full** λ_D	**Proj.** λ_G	**Proj.** λ_D	**Tar.** λ_G	**Tar.** λ_D
Fermionic	**Preparation**						
Melbourne	8	0.804	0.994	1.191	1.352	1.286	1.286
		0.921	0.597	1.387	1.303	1.483	1.248
		0.934	0.581	1.440	1.271	1.546	1.205
		0.910	0.567	1.461	1.261	1.605	1.162
Montreal	128	0.918	1.134	1.169	1.329	1.286	1.286
		1.193	0.868	1.472	1.255	1.483	1.248
		1.241	0.849	1.527	1.215	1.546	1.205
		1.267	0.824	1.580	1.176	1.605	1.162
Mumbai	128	0.866	1.051	1.217	1.334	1.286	1.286
		0.928	0.697	1.360	1.319	1.483	1.248
		0.925	0.636	1.435	1.278	1.546	1.205
		1.113	0.721	1.537	1.212	1.605	1.162
Bosonized	**Preparation**						
Melbourne	8	0.875	1.256	1.130	1.377	1.286	1.286
		1.013	0.919	1.328	1.334	1.483	1.248
		1.077	0.906	1.409	1.289	1.546	1.205
		1.094	0.914	1.422	1.281	1.605	1.162
Montreal	128	1.126	1.281	1.244	1.310	1.286	1.286
		1.306	1.107	1.454	1.265	1.483	1.248
		1.400	1.066	1.547	1.205	1.546	1.205

		1.406	1.041	1.567	1.188	1.605	1.162
Mumbai	128	0.934	1.295	1.138	1.364	1.286	1.286
		1.160	1.022	1.408	1.293	1.483	1.248
		1.080	0.965	1.376	1.311	1.546	1.205
		1.233	0.990	1.497	1.238	1.605	1.162
Yorktown	8	0.908	1.240	1.174	1.352	1.286	1.286
		0.939	0.773	1.266	1.333	1.483	1.248
		0.929	0.760	1.259	1.304	1.546	1.205
		1.186	0.924	1.489	1.240	1.605	1.162
Rome	32	1.050	1.278	1.217	1.332	1.286	1.286
		1.163	1.048	1.378	1.307	1.483	1.248
		1.215	1.015	1.449	1.266	1.546	1.205
		1.276	1.003	1.506	1.229	1.605	1.162
Casablanca	32	0.921	1.291	1.138	1.370	1.286	1.286
		1.253	1.077	1.437	1.276	1.483	1.248
		1.285	1.054	1.481	1.248	1.546	1.205
		1.269	1.004	1.511	1.230	1.605	1.162
Bogota	32	0.845	1.278	1.095	1.394	1.286	1.286
		0.911	0.948	1.184	1.393	1.483	1.248
		0.939	0.934	1.232	1.375	1.546	1.205
		0.958	0.920	1.266	1.359	1.605	1.162
Santiago	32	1.169	1.278	1.264	1.304	1.286	1.286
		1.344	1.130	1.465	1.260	1.483	1.248
		1.390	1.100	1.517	1.225	1.546	1.205
		1.460	1.060	1.589	1.174	1.605	1.162
Athens	32	1.040	1.272	1.207	1.333	1.286	1.286

	1.177	1.045	1.394	1.301	1.483	1.248
	1.231	1.034	1.446	1.270	1.546	1.205
	1.300	0.997	1.537	1.211	1.605	1.162

Table 12.5: "Santiago" Device One Standard Deviation Ranges

UnMitigated			
$\lambda_G - stdev$	$\lambda_G + stdev$	$\lambda_D - stdev$	$\lambda_D + stdev$
1.106119524	1.202608949	1.032634603	1.142275989
1.197360473	1.333415971	0.985738175	1.092102568
1.208814761	1.274048835	1.077329851	1.114251012
1.195673444	1.277748932	1.010681147	1.081449226
1.399699456	1.520420531	0.867354256	0.929065155
1.257050206	1.375244907	0.973760795	1.033050067
1.24271821	1.332549323	0.978472889	1.061525591
1.227012131	1.296454483	1.040064675	1.089424906
1.112427103	1.219874228	1.083839569	1.159044964
1.251692038	1.369541989	0.958850919	1.048151358
0.98407235	1.025905282	1.172314364	1.21770465
1.043115579	1.105780529	1.160535078	1.198880205
1.014364063	1.089776566	1.136076222	1.209590419
1.055437463	1.127450622	1.119848501	1.19811167
1.111209536	1.199727224	1.080573093	1.12930971
1.127167038	1.221799983	1.070723529	1.133559956
1.193432848	1.243182206	1.081614364	1.138640211
1.190590353	1.262725915	1.031377654	1.101114269
1.267123458	1.344054637	1.00702801	1.063809474
1.262945248	1.36359222	0.973425029	1.077480496
Mitigated			
$\lambda_G - stdev$	$\lambda_G + stdev$	$\lambda_D - stdev$	$\lambda_D + stdev$
1.303049853	1.375532105	1.300438391	1.345237749
1.421051555	1.510959865	1.224190912	1.276879013
1.363983613	1.435099306	1.252706537	1.286649579
1.388445078	1.475983661	1.217921037	1.266478513
1.667942363	1.744565403	1.02216262	1.096441105
1.480203018	1.57500567	1.162103908	1.225370245
1.463897937	1.528738392	1.200178637	1.241857981
1.392579674	1.467892511	1.216507346	1.259321356
1.262841102	1.3942225	1.296548347	1.362088079
1.45886276	1.57518571	1.159283269	1.222251226
1.114645084	1.14351376	1.409501607	1.421429223
1.178807953	1.236264922	1.373563066	1.397399557
1.132798723	1.24490299	1.372379599	1.415538707
1.181658433	1.289446324	1.351957952	1.396565431
1.295858686	1.360645518	1.30514971	1.347629237
1.304227692	1.397840282	1.2963547	1.344148657
1.356516196	1.406435956	1.283049885	1.316173909
1.396331373	1.426624073	1.268962722	1.291246836
1.468936681	1.536472867	1.20174535	1.247617409
1.468310755	1.56749088	1.185573897	1.251042844

Table 12.6: "Santiago" Device Two Standard Deviation Ranges

UnMitigated			
$\lambda_G - 2 \times stdev$	$\lambda_G + 2 \times stdev$	$\lambda_D - 2 \times stdev$	$\lambda_D + 2 \times stdev$
1.057874811	1.250853662	0.977813911	1.197096682
1.129332725	1.40144372	0.932555978	1.145284765
1.176197725	1.306665872	1.058869271	1.132711593
1.1546357	1.318786675	0.975297107	1.116833266
1.339338919	1.580781068	0.836498806	0.959920605
1.197952855	1.434342257	0.944116158	1.062694704
1.197802653	1.37746488	0.936946537	1.103051942
1.192290956	1.331175658	1.015384559	1.114105022
1.05870354	1.273597791	1.046236872	1.196647661
1.192767063	1.428466965	0.914200699	1.092801578
0.963155884	1.046821748	1.149619222	1.240399792
1.011783104	1.137113004	1.141362515	1.218052769
0.976657812	1.127482818	1.099319123	1.246347517
1.019430884	1.163457202	1.080716917	1.237243255
1.066950692	1.243986068	1.056204785	1.153678018
1.079850565	1.269116455	1.039305315	1.164978169
1.168558169	1.268056885	1.053101441	1.167153134
1.154522572	1.298793696	0.996509347	1.135982576
1.228657868	1.382520227	0.978637279	1.092200206
1.212621762	1.413915706	0.921397295	1.12950823
Mitigated			
$\lambda_G - 2 \times stdev$	$\lambda_G + 2 \times stdev$	$\lambda_D - 2 \times stdev$	$\lambda_D + 2 \times stdev$
1.266808728	1.411773231	1.278038712	1.367637428
1.3760974	1.55591402	1.197846861	1.303223064
1.328425766	1.470657152	1.235735016	1.303621101
1.344675786	1.519752952	1.193642299	1.290757251
1.629630844	1.782876922	0.985023378	1.133580347
1.432801691	1.622406997	1.13047074	1.257003413
1.43147771	1.56115862	1.179338964	1.262697653
1.354923255	1.50554893	1.195100341	1.280728361
1.197150404	1.459913199	1.263778481	1.394857945
1.400701285	1.633347185	1.127799291	1.253735204
1.100210746	1.157948098	1.403537799	1.427393031
1.150079469	1.264993407	1.36164482	1.409317803
1.076746589	1.300955124	1.350800045	1.437118261
1.127764487	1.34334027	1.329654213	1.41886917
1.263465271	1.393038934	1.283909946	1.368869
1.257421397	1.444646577	1.272457721	1.368045636
1.331556316	1.431395836	1.266487873	1.332735922
1.381185023	1.441770423	1.257820666	1.302388893
1.435168587	1.57024096	1.178809321	1.270553438
1.418720693	1.617080943	1.152839423	1.283777318

Table 12.7: "Melbourne" Device One Standard Deviation Ranges

UnMitigated			
$\lambda_G - stdev$	$\lambda_G + stdev$	$\lambda_D - stdev$	$\lambda_D + stdev$
0.484424231	0.502670099	0.521404922	0.572931144
0.496754809	0.522657534	0.518757244	0.576071922
0.54852715	0.598121888	0.52608456	0.55799322
0.5483473	0.60383283	0.524651162	0.560084582
0.568122091	0.622323705	0.54754399	0.587416726
0.5840537	0.64092403	0.522147956	0.587372261
0.602642632	0.636068389	0.494554495	0.535562948
0.602477296	0.661408201	0.483707413	0.523261008
0.598038483	0.655219527	0.482523077	0.519166171
0.551875343	0.634652626	0.530766843	0.585759762
Mitigated			
$\lambda_G - stdev$	$\lambda_G + stdev$	$\lambda_D - stdev$	$\lambda_D + stdev$
0.796973483	0.973656014	1.440152461	1.480915671
0.832283511	1.087341283	1.414527297	1.464190898
0.856276249	1.024338638	1.413383725	1.47302444
0.90152728	1.08014262	1.407869113	1.462743687
0.890038893	1.180739107	1.400863102	1.445961684
0.976065936	1.201789035	1.379319615	1.435543214
1.145646901	1.273814438	1.355232865	1.384126915
1.197191138	1.362662227	1.309698505	1.368296281
1.181705714	1.387300512	1.289018076	1.361993975
0.889527864	1.212255564	1.346224683	1.455888612

Table 12.8: "Melbourne" Device Two Standard Deviation Ranges

UnMitigated			
$\lambda_G - 2 \times stdev$	$\lambda_G + 2 \times stdev$	$\lambda_D - 2 \times stdev$	$\lambda_D + 2 \times stdev$
0.475301297	0.511793034	0.495641812	0.598694254
0.483803447	0.535608896	0.490099905	0.604729261
0.523729781	0.622919257	0.51013023	0.573947549
0.520604535	0.631575594	0.506934452	0.577801292
0.541021285	0.649424511	0.527607622	0.607353095
0.555618535	0.669359195	0.489535803	0.619984413
0.585929753	0.652781267	0.474050268	0.556067175
0.573011843	0.690873654	0.463930615	0.543037805
0.56944796	0.683810049	0.464201531	0.537487718
0.510486701	0.676041268	0.503270384	0.613256221
Mitigated			
$\lambda_G - 2 \times stdev$	$\lambda_G + 2 \times stdev$	$\lambda_D - 2 \times stdev$	$\lambda_D + 2 \times stdev$
0.708632218	1.061997279	1.419770856	1.501297275
0.704754626	1.214870169	1.389695497	1.489022698
0.772245055	1.108369832	1.383563368	1.502844798
0.812219609	1.16945029	1.380431826	1.490180974
0.744688786	1.326089215	1.378313812	1.468510974
0.863204387	1.314650584	1.351207816	1.463655014
1.081563133	1.337898206	1.34078584	1.39857394
1.114455594	1.445397771	1.280399616	1.39759517
1.078908316	1.49009791	1.252530126	1.398481925
0.728164014	1.373619414	1.291392718	1.510720577

Part V

Machine Learning in Quantum Chemistry

CHAPTER 13

INTRODUCTION TO MACHINE LEARNING

Generally, machine learning algorithms estimate functional relationships without explicit instructions on how to analyze the dataset in order to develop a mapping between a set of inputs and a corresponding set of outputs. As chemical problems inherently demonstrate patterns—from molecular geometries to crystal structures to periodic trends such as electron affinity—, the application of artificial intelligence approaches that are capable of ascertaining and connecting such patterns seems well-suited for quantum chemical applications. Additionally, as scaling with increasing system sizes is a major problem in current computational techniques (see Sec. 1.3.6), the possibility of using machine learning to "learn" patterns in smaller molecular systems in order to predict energies and properties of larger molecular systems is enticing to computational chemists. These considerations have lead to a modern boon in the literature on machine learning techniques to treat quantum chemical problems.

In the following sections, a brief introduction to the terminology and techniques of machine learning will be given along with a discussion of the advantages and disadvantages of machine learning approaches and a survey of current applications of machine learning to quantum chemistry. For a more in-depth introduction to machine learning, see the texts given in Refs. [422–424], and for an additional discussion of machine learning in quantum chemistry, see the reviews presented in Refs. [425–428].

13.1 The Basics

13.1.1 Artificial Intelligence, Machine Learning, and Deep Learning

The terms artificial intelligence, machine learning, and deep learning are broad but interconnected terms that nonetheless have distinct applications. Artificial intelligence (AI) generally refers to techniques that enable computers to imitate human-like or super-human-like

intelligence. Such intelligence can be explicitly coded—such as early chess machines—or be "learned" without explicitly being programmed, i.e., machine learning. Machine learning (ML), which is the most common and rapidly-developing subfield of artificial intelligence, refers to a class of methods that enable a machine to perform intelligent tasks for which it hasn't been purposefully coded through building a statistical model based on some dataset. Machine learning approaches use such statistical techniques to extract hidden, complex patterns that are then represented as mathematical objects and can be applied to new data related to but outside of the original dataset. In recent years, such ML algorithms have been applied to problems including computer vision, speech-to-text, and recommendation systems. Deep learning (DL) algorithms are a subset of machine learning algorithms that specifically utilize multi-layered neural networks. In deep learning, function specification—the determination of what to learn from a given dataset—as well as data optimization are accomplished by the algorithm, unlike other types of machine learning where identifying features of interest by hand is required. Note that the neural networks that are utilized in DL approaches are comprised of layers of nodes where each node (or artificial neuron) is connected to other nodes within the layer and has an associated weight—which describes the importance of any given variable—and threshold value—which is a bias that indicates whether or not data is sent along to the next layer of nodes in the network. Deep learning approaches are popular in fields including speech recognition, economics, and, importantly, quantum chemistry. Convolutional neural networks (CNNs) are a further subset of deep learning algorithms that apply a convolution—a mathematical operation that describes the amount of overlap of one function as it is shifted over another [429]—in the place of matrix multiplication in at least one neural layer of the algorithm.

13.1.2 Types of Learning

Machine learning can be classified into the following categories: supervised, semi-supervised, and unsupervised.

Supervised Learning

In supervised learning, the training set (or dataset) is the set of N feature vectors $\mathbf{x}_i$ and their corresponding label y_i. As an example, if you would like to train a machine learning algorithm to be able to differentiate pictures of cats and dogs, the feature vector may correspond to the intensity of the pixels comprising a given image and the corresponding label would be either "cat" or "dog" depending on whether the image was of a cat or of a dog. In general, labels can either belong to a finite set of classes (such as "cat" or "dog") or be a real number/vector/matrix/etc. In a supervised learning algorithm, the training set is then used to construct a model such that when an input vector $\mathbf{x}$ is passed through the model, a prediction for the label y is output. Going back to the example, the model would be trained to recognize the patterns that make an image belong to the category "dog" or to the category "cat" from the dataset, and then the feature vector for an image that wasn't in the dataset would be characterized by the model to either be of a cat or of a dog.

Unsupervised Learning

In unsupervised learning, the training set is the set of N feature vectors $\mathbf{x}_i$ that have no corresponding label. The goal of unsupervised learning is to produce a model that takes a feature vector and transforms it into a number or vector useful for the solution of some practical problem. Unsupervised learning is often useful for grouping data into distinct clusters (referred to as clustering) without knowledge of what the clusters should be. For example, if you provide a training set of the feature vectors comprised of pixel intensities for your images of cats and dogs, a cluster unsupervised learning algorithm may separate

the images of cats from the images of dogs from the features alone without the labels being supplied. Unsupervised machine learning is also useful for visualization tasks, dimensionality reduction, and outlier detection.

Semi-Supervised Learning

In semi-supervised learning, a training set includes both labeled feature vectors and unlabelled feature vectors, usually with significantly more unlabelled than labelled features. Semi-supervised learning, like supervised learning, has the goal of creating a model that can convert a feature vector into a predicted label. The unlabelled feature vectors are included in the dataset to help the algorithm produce a better model than may be capable from a smaller training set with just labelled feature vectors.

13.1.3 Outline of Supervised Machine Learning Algorithm

As supervised learning is the most-common classification of machine learning as well as the type of learning conducted in this thesis, an outline of the process of supervised learning is provided. The first step of any ML approach is to construct a dataset composed of feature vectors and their corresponding labels, which need to be in machine-readable form ($\{\mathbf{x}_i, y_i\}$). In the above example of classifying pictures of dogs and cats, the input data—the pictures of the dogs—first needed to be converted into a vector of pixel intensities (a vector of numbers) in order to be "understood" by the machine. The output data—the labels of "cat" or "dog"—should also, in practice, be converted to a numerical value such as converting "cat" to -1 and "dog" to $+1$. Then, the learning algorithm needs to be chosen and/or constructed. For our example, a support vector machine (SVM) may be a suitable choice; this algorithm puts all feature vectors into a m-dimensional plot (where m is the dimension of your feature vector) and draws a hyperplane—called a decision boundary—that separates the features with positive labels (i.e., dogs) from those with negative labels (i.e., cats). This hyperplane

is defined by

$$\mathbf{wx} - b = 0 = (w^{(1)}x^{(1)} + w^{(2)}x^{(2)} + \cdots w^{(m)}x^{(m)}) - b \tag{13.1}$$

where $\mathbf{w}$ is a vector of weights and $\mathbf{x}$ is a generic feature vector. For such a feature vector, the predicted label corresponds to

$$y = sign(\mathbf{wx} - b) \in \{-1, +1\}. \tag{13.2}$$

The SVM algorithm then utilizes the training set to find the optimal values for $\mathbf{w}$ and b in order to yield a model that most-accurately matches its predictions for a feature vector in the training set to its corresponding label. This is done by solving the optimization problem [423]:

$$Minimize\ ||\mathbf{w}|| = \sqrt{\sum_{j=1}^{D} (w^{(j)})^2} \text{ subject to } y_i(\mathbf{wx}_i - b) \geq 1 \text{ for } i = 1, 2, \ldots, m.$$

The solution to this problem is called the model, and the process of building the model is referred to as training the model or simply training. As an aside on terminology, note that some machine learning algorithms are trained iteratively, i.e. the minimization is accomplished in an iterative manner. If this is the case, then the number of iterations—the number of times the entire training set is passed through the algorithm—is called an epoch, and sometimes many epochs are necessary.

Generally, then, the created model is tested by running the feature vectors of a different dataset called the testing set through the model to determine the accuracy with which the model predicts the labels of the testing set. In our example, this would equate to taking pictures of cats and dogs that hadn't been used in training the model and seeing whether the predicted label "cat" or "dog" matches the expected label.

13.2 Summary of Current Applications in Quantum Chemistry

The application of machine learning to chemical problems has intensified over the last several years, corresponding to a general boom in artificial intelligence techniques likely sparked by the recent, widespread availability of large datasets, advanced algorithms, and computational hardware capable of supporting previously prohibitively-expensive AI tasks. This is evinced by the fact that until approximately 2010 only a few hundred studies on machine learning in quantum chemistry had been conducted; however, for the year 2022 alone, 3654 articles in the Web of Science database have keywords that include "artificial intelligence", "machine learning", and/or "deep learning".

During this age of artificial intelligence for quantum chemistry, machine learning approaches have been utilized to predict molecular energies [430–433], potential energy surfaces [434–439], molecular forces [440, 441], density functionals [442–444], electron densities and molecular polarizabilities [445, 446], and molecular spectra [447]. Further machine learning approaches have been implemented for the development of novel and sustainable catalysts [448] and the design of new synthetic pathways [449]. Finally, machine learning electronic structure theory has allowed for the development of approximate quantum mechanical methods, the prediction of MP2 and coupled cluster energies from feature vectors composed of Hartree Fock orbitals, and direct prediction of many-electron wave functions [450–456]. However, these areas are in their early stages and have yet to demonstrate definite success in decreasing the degree of scaling with system size.

13.3 Pros and Cons of Machine Learning in Quantum Chemistry

Besides the aforementioned possible benefit of being able to train machine learning algorithms of "known" data from small-molecule systems in order to predict the properties and energies of larger molecules and hence circumvent scaling constraints of current quantum chemical

methodologies, machine learning approaches also provide the possibility for insights that may transform the field. By critically analyzing the structures and weights of successful machine learning algorithms, scientists may discover inherent patterns behind scientific principles, reaction pathways, chemical properties, etc. After all, the statistical approach of machine learning captures implicit information of the system that may not be obvious or may be impossible to recognize with traditional approaches alone.

However, machine learning does have practical drawbacks. For one, machine learning algorithms rely upon having a large set of highly-accurate training data. Having too few molecular systems in a training set will likely prevent accuracy in the machine learning algorithm. Further, if the training data is skewed or flawed in some manner, the model will possess the same flaw—or as it is generally stated: "Garbage in. Garbage out." Thus, an algorithm trained on molecular data derived from Hartree Fock won't be capable of predicting properties that depend upon correlation. Further, ML algorithms tend to lack generality. An algorithm trained only on hydrocarbons would likely be incapable of providing information regarding transition metal complexes. This is related to but distinct from the problem of overfitting where the model is too-specific to the training set and is incapable of generalizing to other feature vector inputs. Moreover, ML techniques are often not well-understood by the quantum chemistry community [425] with chemists often treating machine learning algorithms as black boxes. This can lead to inadequate technical expertise for the practitioners of such ML methodologies which can result in flawed training sets, overfitting, etc. Finally, translation of molecular properties and structures to a feature vector is a difficult task with no clear-cut answer.

CHAPTER 14

REDUCING THE QUANTUM MANY-ELECTRON PROBLEM TO TWO ELECTRONS WITH MACHINE LEARNING

Material from: Sager-Smith, L. M. & Mazziotti, D. A., Reducing the quantum many-electron problem to two electrons with machine learning. Journal of the American Chemical Society, published 2022, 144, 18959.

14.1 Chapter Synopsis

An outstanding challenge in chemical computation is the many-electron problem where computational methodologies scale prohibitively with system size. The energy of any molecule can be expressed as a weighted sum of the energies of two-electron wave functions that are computable from only a two-electron calculation. Despite the physical elegance of this extended "aufbau" principle, the determination of the distribution of weights—geminal occupations—for general molecular systems has remained elusive. Here we introduce a new paradigm for electronic structure where approximate geminal-occupation distributions are "learned" via a convolutional neural network. We show that the neural network learns the N-representability conditions, constraints on the distribution for it to represent an N-electron system. By training on hydrocarbon isomers with only 2-7 carbon atoms, we are able to predict the energies for isomers of octane as well as hydrocarbons with 8-15 carbons. The present work demonstrates that machine learning can be used to reduce the many-electron problem to an effective two-electron problem, opening new opportunities for accurately predicting electronic structure.

14.2 Introduction

For any molecular system, the Schrödinger equation can, *in theory*, be solved exactly using a full configuration interaction (FCI) calculation [457–459] with a complete basis set; however, *in practice*, the computational complexity of such an exact approach grows factorially with system size [459], making molecular systems with more than a few dozen electrons intractable. Over time, many approximate methodologies have been introduced in an attempt to obtain "good enough" solutions to the electronic Schrödinger equation that predict energies within chemical accuracy ($\sim$1 kcal/mol).

Hartree Fock theory—a mean-field approach—yields reasonable results for a wide array of molecular systems containing up to a few hundred atoms [458]; however, it fails in molecules in which the motions of electrons are significantly correlated. Techniques which more-accurately capture correlation energy such as many-body perturbation theory, coupled cluster theory, complete active-space self-consistent field theory, and others remain computationally expensive for large system sizes [458, 460]. The so-called many-electron problem—whereby the cost of highly-accurate *ab initio* computational methodologies scales in a prohibitive manner with system size—is hence an outstanding challenge in chemical computations.

Machine learning may enable us to circumvent this problem by allowing us to use information about smaller molecules to treat correlation in larger systems at a reduced cost [461]. It has been used to learn the energies of various molecular structures [430–433], new functionals for density functional theory (DFT) [442–444], inverse problems in electronic structure theory [462, 463], and even the many-body wave function of one-dimensional spin systems [455]. However, these areas are in their early stages and have yet to demonstrate definite success in decreasing the degree of scaling with system size.

In this *Article* we introduce a new paradigm for utilizing machine learning in quantum chemistry in which we reduce the quantum many-electron problem to a more tractable, bet-

ter scaling two-electron problem. As originally proposed by Bopp [464, 465], the energy of a molecule of arbitrary size can be expressed without approximation as a weighted sum of the energies of two-electron wave functions, known as geminals. However, despite its physical significance as an extension of the "aufbau" principle, the distribution of weights—geminal occupations—has remained elusive. Here, we show that the geminal-occupation distribution can be learned with machine learning. We use a convolutional neural network (CNN) to learn an effective temperature in a Boltzmann-like distribution for the geminal occupations. The effective temperature—or correlation temperature—is inversely related to the electron correlation. The neural network, we demonstrate, learns the N-representability of the distribution—the representability of the distribution by an N-electron system [50, 62, 66, 466], which appears as a nonzero temperature. The scheme can be viewed as a two-electron reduced density matrix (2-RDM) theory as the geminal occupations are an integral part of the 2-RDM. A schematic of the machine learning algorithm for predicting molecular energies is shown in Fig. 14.1.

We apply the machine learning algorithm to hydrocarbon systems. Specifically, by training a convolutional neural network on all isomers of ethane through heptane, we predict the correlation temperatures—and hence molecular energies—of all of the isomers of octane as well as all straight-chained hydrocarbons from octane through pentadecane. We find that this RDM-based machine learning method accurately recovers the correlation energy for larger hydrocarbon systems, with the N-representability conditions being learned by the CNN framework. Our approach—which scales as $O[n^6]$—improves upon the exponential scaling of traditional configuration-interaction calculations, foreshadowing the potential utility of this machine-learning reduced density matrix approach to the determination of accurate molecular energies. While polynomial-scaling levels of theory such as Coupled Cluster with Single and Double Excitations (CCSD) can be used to treat weakly-correlated systems such as the hydrocarbons presented in this manuscript, if trained on appropriate molecular data,

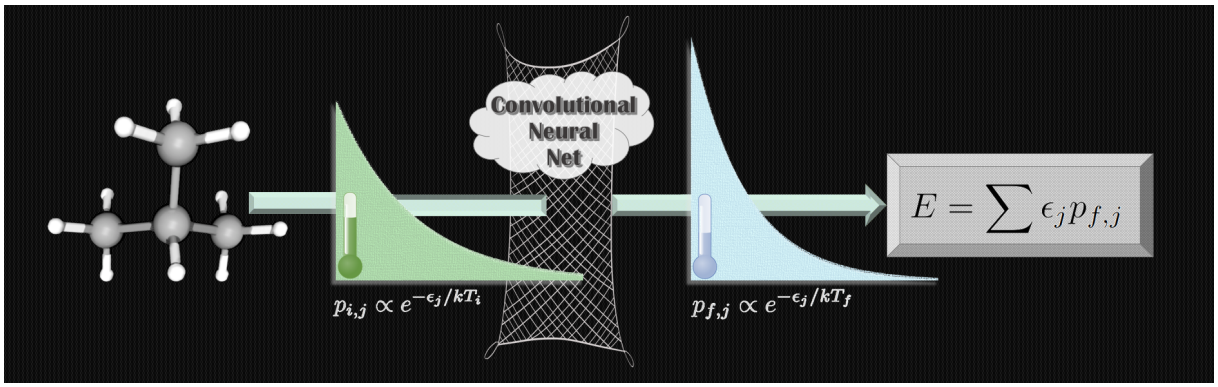

Figure 14.1: Graphic demonstrating algorithm flow. For a given molecule, a trained convolutional neural network is used to predict the Boltzmann-like correlation temperature (T_f) with the eigenfunctions of the reduced Hamiltonian (ϵ_j) and the Hartree Fock correlation temperature (T_i) as inputs. The correlation temperature (T_f) allows for the approximation of the geminal populations ($p_{f,j}$) by Eq. (14.4), which is sufficient for the prediction of the energy by Eq. (14.3).

our convolutional network approach may be capable of accurately recovering correlation energy for more highly-correlated systems.

14.3 Results and Discussion

Theory. Central to our modern understanding of chemistry is the concept of the molecular orbital. Any molecule's electronic structure can be readily understood in terms of its molecular orbitals which are filled from lowest-in-energy to highest-in-energy by the Pauli exclusion principle. When electrons of a molecule become strongly correlated, however, the orbital picture with unit filling of the lowest orbitals breaks down. Because electronic interactions are at most pairwise, the orbital picture can in principle be replaced by an exact two-electron (geminal) picture, which is derivable from 2-RDM theory.

The ground- or excited-state energy of any atom or molecule is expressible as an exact functional of the 2-RDM (^2D) [48, 50, 54, 66, 71, 80, 216, 330, 331, 338, 464, 466–495]

$$E = \int {}^2\hat{K}\, {}^2D(\bar{1}\bar{2}; 12) d1 d2 \tag{14.1}$$

where ${}^2\hat{K}$ is the reduced Hamiltonian operator

$$ {}^2\hat{K} = -\frac{N}{2}\left(\frac{\hat{p}_1^2}{2m} + \frac{\hat{p}_2^2}{2m} + \sum_k \frac{Z_k}{r_{1k}} + \sum_k \frac{Z_k}{r_{2k}}\right) + \frac{N(N-1)}{2}\frac{1}{r_{12}}. \tag{14.2} $$

In a finite orbital basis set, the operators are expressible as a reduced Hamiltonian matrix. Diagonalization of this reduced Hamiltonian matrix yields a set of eigenvalues and eigenvectors (or geminals). In the basis set of geminals, the Hamiltonian is a diagonal matrix consisting of its eigenvalues, the 2-RDM has a non-negative diagonal elements which we denote by p_i, and energy is the sum over the geminal eigenvalues of the Hamiltonian matrix ϵ_i weighted by the non-negative geminal occupations p_i:

$$ E = \sum_i p_i \epsilon_i. \tag{14.3} $$

By this transformation we express the energy as a functional of the eigenvalues of the reduced Hamiltonian ϵ_i, which are readily computed at the cost of the two-electron calculation, and the unknown geminal occupations p_i (see Fig. 14.2).

The German chemist Bopp originally proposed approximating the geminal occupation numbers by a Pauli-like filling scheme [464, 465]. He suggested choosing the lowest $N(N-1)/2$ to be equal to one. This approach, while analogous to the filling of orbitals in molecular-orbital theory, generates accurate energies for four-electron atoms and ions but energies for larger molecular systems that are too low. Coleman suggested that the filling of the geminal by two electrons—or the pseudo-particle called a pairon—should follow a fundamental probability distribution as in statistical mechanics [464]. He proposed a Boltzmann distribution for the geminal occupations based on the geminal energies. While such a distribution is not exact because the pairon pseudo-particles obey neither the Fermi-Dirac or Bose-Einstein

particle statistics, there exists a Boltzmann-like distribution given by

$$p_i = \frac{N(N-1)}{Z} e^{-\epsilon_i / kT^*} \tag{14.4}$$

and parameterized by a specific correlation temperature (T^*) such that the resultant approximate geminal probability distribution allows for the accurate computation of a molecule's energy according to Eq. (14.3). However, the ability to determine such a correlation temperature is currently only possible if the geminal energies (ϵ_i) and geminal populations (p_i) are both known.

Here, we train a convolutional neural network (CNN) to predict the correlation temperature for a given molecular system consistent with its ground-state energy. The convolutional neural network is trained on inputs corresponding to both geminal energies—expressed as partition functions given by

$$Z = \sum_i e^{-\epsilon_i / kT} \tag{14.5}$$

for a variety of temperatures—as well as the computed Hartree Fock correlation temperature (T^*_{HF}) and with training outputs corresponding to a Δ value representing the difference between the exact (i.e. configuration interaction) correlation temperature and the HF correlation temperature, i.e., $\Delta = T^*_{EXACT} - T^*_{HF}$. For larger molecular systems, we then predict the Δ values by reading in the geminal energies and Hartree Fock correlation temperatures for those molecules into the trained neural network. These Δ values are then added to the T^*_{HF}s in order to yield the exact correlation temperatures, which allows for the approximation of the geminal probability distributions and hence the molecular energies via Eq. (14.3).

In general, for two-electron reduced density matrix methodologies, the 2-RDM must be constrained to represent the N-electron wave function through application of N-representability constraints [50, 62, 66, 466]. Here, if N-representability conditions are not accounted for in

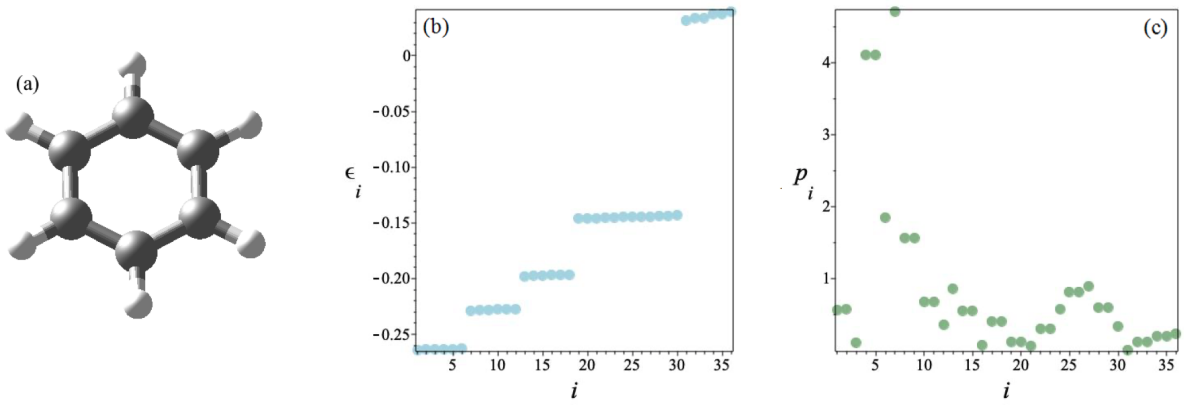

Figure 14.2: Example of geminal energies and probabilities. For (a) benzene, we can use the (b) geminal energies ϵ_i to learn the (c) geminal probabilities p_i—both of which are computed here from a $[N_e = 6,\ N_o = 6]$ complete active-space self-consistent-field (CASSCF) using the minimal Slater-type orbital basis set with six Gaussian primitive functions representing each Slater-type orbital (STO-6G). Knowing both geminal energies and geminal populations is sufficient to determine molecular energies via Eq. (14.3).

our Boltzmann-like machine learning approach, the correlation temperature would be zero, which corresponds to the lowest-energy geminal being fully occupied by all electron pairs. This electronic structure machine learning approach, however, maintains N-representability by learning correlation temperatures from N-representable training data and applying this inherent "learned" N-representability to the testing data.

See the Experimental section at the end of this document for additional details.

Energetic Predictions for Isomers of Octane. For the eighteen isomers of octane—with molecular geometries obtained from the PubChem database [496]—, the Hartree Fock and CASSCF energies are computed using Dunning's double-zeta (cc-pVDZ) basis set with complete active-space self-consistent-field (CASSCF) calculations employing a $[N_e = 8,\ N_o = 8]$ active space. Utilizing a convolutional neural network trained on hydrocarbons ranging from two to seven carbon atoms, the correlation temperature corresponding to the CASSCF energy is predicted for each of the octane isomers and used to compute the predicted CASSCF energies shown in Fig. 14.3(a). As can be seen from this figure, which shows energy versus isomer identifier, the predicted CASSCF energies (green circles) show

good agreement with the actual CASSCF energies (black boxes), vastly improving upon the Hartree Fock energies (blue diamonds), and hence our predictions capture the correlation energy in a fairly accurate manner.

Additionally, in order to demonstrate the generality of our reduced density matrix approach for "learning" molecular energies, Coupled Cluster Single Double (CCSD) energies are computed for the cc-pVDZ basis for hydrocarbons ranging from two to seven carbon atoms. The corresponding CCSD correlation temperatures are then used to train a convolutional neural net, and the correlation temperature corresponding to the CCSD energy is then predicted for each isomer of octane, with the resultant predicted CCSD energies shown in Fig. 14.3(b). Similar to the CASSCF energies from Fig. 14.3(a), the CCSD predicted energies (green circles) demonstrate good agreement with the actual CCSD energies (black boxes) when compared to the Hartree Fock energies (blue diamonds). Hence, for this second level of theory, our predictions capture correlation energies in a fairly accurate manner. Additional predictions corresponding to CCSD calculations utilizing the STO-6G basis set can be seen in the Supporting Information.

We next explore systems composed of larger hydrocarbons to determine whether such good agreement remains consistent as system size is increased while the training data remains the same.

Energetic Predictions for Large Hydrocarbon. For the eight straight-chained hydrocarbons ranging from octane to pentadecane—with molecular geometries obtained from the PubChem database [496]—, the Hartree Fock and CASSCF energies are computed using Dunning's double-zeta (cc-pVDZ) basis set with the CASSCF calculations employing a $[N_e = 8,\ N_o = 8]$ active space. Utilizing a convolutional neural network trained on hydrocarbons ranging from two to seven carbon atoms, the correlation temperature corresponding to the CASSCF energy is predicted for each of the octane to pentadecane hydrocarbon isomers and used to compute the predicted CASSCF energies shown in Fig. 14.4. As can be seen

from this figure, which shows energy per carbon versus number of carbons, the predicted CASSCF energies (green circles) show good agreement with the actual CASSCF energies (black boxes), vastly improving upon the Hartree Fock energies (blue diamonds), and hence our predictions capture the correlation energy in a fairly accurate manner. Although there is a slight increase in the error as system size is increased, it appears to be small enough that the energies of even larger hydrocarbon isomers may be able to be predicted in an accurate manner through use of our convolutional neural network trained on only hydrocarbons with seven or fewer carbon atoms. Similar promising results are obtained for predicting CASSCF energies for octane, nonane, decane, and undecane via a convolutional neural network trained on CASSCF calculations for hydrocarbons with two to seven carbons that utilize a [10,10] active space and the cc-pVTZ basis set as can be seen in the Supporting Information.

14.4 Conclusion

In this *Article*, we introduce a new paradigm based on a two-electron, reduced density matrix approach for the utilization of machine learning architecture in the prediction of accurate correlation energies for molecular systems at reduced computational expense. By employing a Boltzmann-like distribution for two-electron geminal populations parameterized by a correlation temperature, we train a convolutional neural network on correlation temperatures corresponding to CASSCF and CCSD calculations for smaller molecular systems in order to predict CASSCF and CCSD correlation temperatures for larger, more computationally-expensive molecular systems and hence obtain predicted CASSCF/CCSD energies. Moreover, the N-representability conditions are inherently maintained by our CNN framework—as evinced by nonzero correlation temperatures. This methodology for the prediction of CASSCF energies scales as $O[n^6]$ with the number of orbitals due to the diagonalization of the reduced Hamiltonian, which is an improvement over the exponential scaling of a traditional CASSCF calculation. See the Experimental section for additional comments

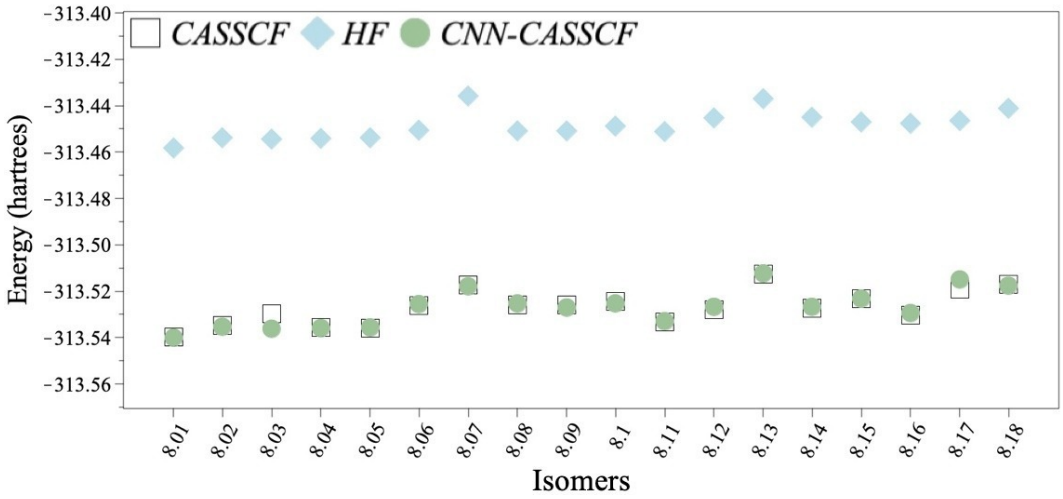

(a) CASSCF, cc-pVDZ, $[N_e = 8,\ N_o = 8]$

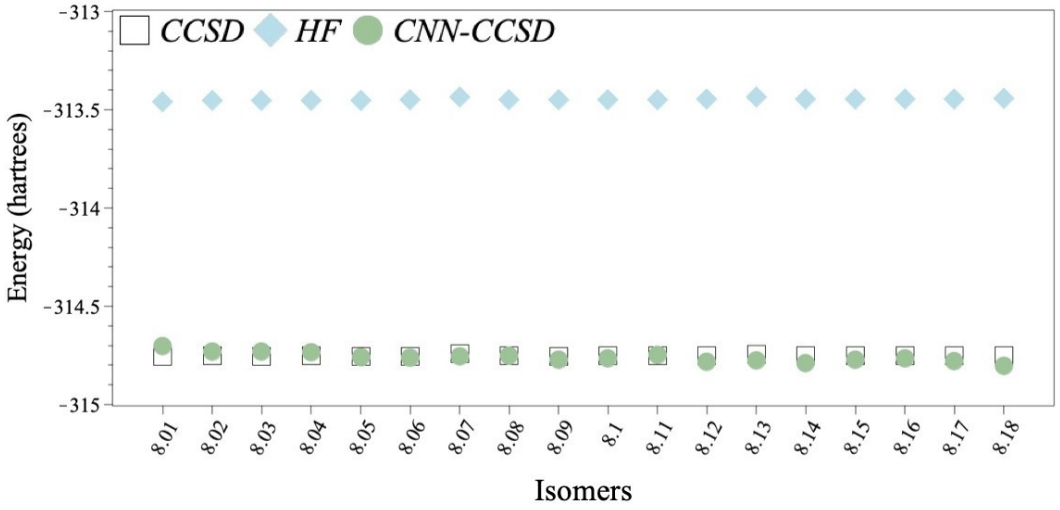

(b) CCSD, cc-pvDZ

Figure 14.3: Octane data. Hartree Fock energies (HF, blue diamonds), (a) Complete Active Space Self-Consistent Field/(b) Coupled Cluster Single Double (CASSCF/CCSD, black boxes) energies, and energy values predicted via utilization of Convolutional Neural Networks (CNN, green circles) are shown for the series of octane isomers. As can be seen, the CNN methodology trained on smaller hydrocarbon data fairly accurately recovers the correlation energy. Isomer labels are given by [8.01: 'Octane', 8.02: '2-Methylheptane', 8.03: '3-Methylheptane', 8.04: '4-Methylheptane', 8.05: '2,2-Dimethylhexane', 8.06: '2,3-Dimethylhexane', 8.07: '2,4-Dimethylhexane', 8.08: '2,5-Dimethylhexane', 8.09: '3,3-Dimethylhexane', 8.10: '3,4-Dimethylhexane', 8.11: '3-Ethylhexane', 8.12: '2,2,3-Trimethylpentane', 8.13: '2,2,4-Trimethylpentane', 8.14: '2,3,3-Trimethylpentane', 8.15: '2,3,4-Trimethylpentane', 8.16: '3-Ethyl-2-Methylpentane', 8.17: '3-Ethyl-3-Methylpentane', 8.18: '2,2,4,4-Tetramethylbutane']. Hartree Fock, CASSCF, and CCSD calculations are all computed here using Dunning's double-zeta (cc-pVDZ) basis set with the CASSCF calculations employing a $[N_e = 8,\ N_o = 8]$ active space.

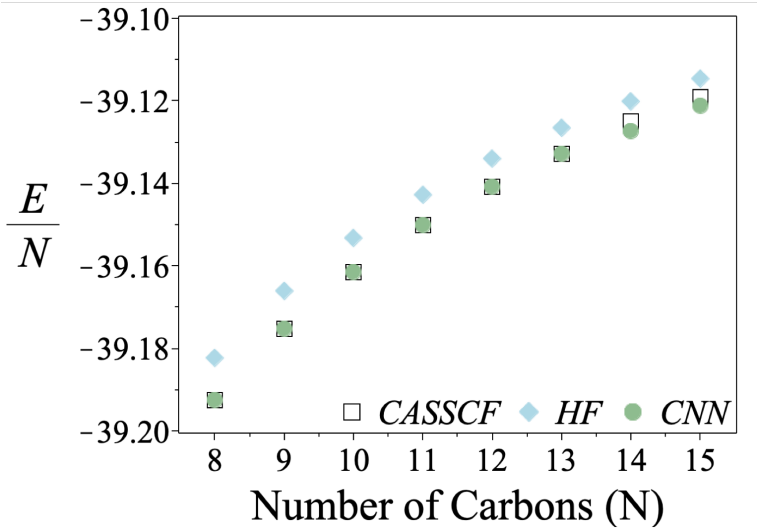

Figure 14.4: Large hydrocarbon data. Hartree Fock energies (HF, blue diamonds), Complete Active Space Self-Consistent Field energies (CASSCF, black boxes), and energy values predicted via utilization of Convolutional Neural Networks (CNN, green circles) per number of carbons are shown for the series of straight-chained hydrocarbons from octane through pentadecane. As can be seen, the CNN methodology trained on smaller hydrocarbon data fairly accurately recovers the correlation energy. Isomer labels are given by [8: 'Octane', 9: 'Nonane', 10: 'Decane', 11: 'Undecane', 12: 'Dodecane', 13: 'Tridecane', 14: 'Tetradecane', 15: 'Pentadecane']. Both Hartree Fock and CASSCF calculations are computed here using Dunning's double-zeta (cc-pVDZ) basis set with the CASSCF calculations employing a $[N_e = 8,\ N_o = 8]$ active space.

on computational scaling.

Demonstrating the power of this technique, we train a convolutional neural network on small hydrocarbon systems—with the number of carbon atoms ranging from two to seven—in order to predict CASSCF energies for larger hydrocarbon systems—with the number of carbons ranging from eight to fifteen. We find that our RDM-based machine learning approach accurately recovers the correlation energy for the larger hydrocarbon systems. Thus, our trained convolutional neural network allows us to predict CASSCF-like results at significantly lower computational expense.

While the hydrocarbons involved in training and testing this implementation of our machine-learning reduced density matrix approach do not demonstrate large degrees of correlation, the prediction of accurate correlation energies for larger molecular systems of the type included in the training set likely indicates that as long as the convolutional neural network is trained on appropriate small molecules, the energies of highly-correlated, larger molecules should be able to be obtained via our methodology. Specifically, if one wishes to predict the energy of a molecule which demonstrates a fairly-large degree of correlation, smaller correlated systems would likely be necessary to train the neural network. Application of our machine-learning reduced density matrix approach to highly-correlated systems is a future direction of this research.

This work foreshadows the promise of machine learning in molecular electronic structure calculations, demonstrating that "learning" information about less-expensive, smaller molecular systems can be directly applied to larger typically more-expensive molecules. Future electronic structure methodologies may even include pre-trained convolutional neural networks—possibly varying with the types of atoms, basis set, active space, functional groups, and/or degree of bond saturation inherent to the molecular system of interest—trained on FCI (or similarly expensive) correlation temperatures. This work serves as an initial step in the realization of a combined reduced-density-matrix and machine-learning approach that

may provide a real advance in decreasing computational expense for large, highly-correlated electronic structure calculations.

14.5 Experimental

Computational Methods. The molecular geometries for all hydrocarbon isomers are obtained from the PubChem database [496]. Molecular energies are then computed for Hartree Fock, Complete Active Space Self-Consistent Field (CASSCF), and Coupled Cluster Single Double (CCSD) levels of theory through use of a Dunning's double-zeta (cc-pVDZ) basis set, with the CASSCF calculations employing a $[N_e = 8,\ N_o = 8]$ active space. These calculations are accomplished via the Quantum Chemistry Toolbox [497] in the Maple computing environment [498]. Note that while—throughout this text—the size of the active space for the training and testing molecules is made identically $[N_e = 8,\ N_o = 8]$ for all CASSCF calculations, changing active space sizes with the number of carbons yielded similar results to those we present here. (See the Supporting Information for additional details.)

Computation of Geminal Energies and Populations. The reduced Hamiltonian (${}^2K$) shown in Eq. (14.2) is obtained by directly computing the one electron integrals and the electron repulsion integrals via the MOIntegrals function of the Quantum Chemistry Toolbox [497] in the Maple computing environment [498] and then applying the appropriate conversions to put it into the same orbital basis as the 2-RDM. The geminal energies (ϵ_i) then correspond to the eigenvalues of the ${}^2K$ matrix. The populations (p_i) of the geminals are then obtained via the following

$$p_i = \langle v_i|^2 D|v_i\rangle \tag{14.6}$$

where v_i is the eigenvector of the reduced Hamiltonian corresponding to the the geminal energy ϵ_i and where ${}^2D$ is the particle-particle reduced density matrix (2-RDM).

Convolutional Neural Network. *Model Inputs.* For a given molecular system, both the geminal energies (ϵ_i) and the Hartree Fock correlation temperature (T^*_{HF}) are input into the convolutional neural network. Specifically, the geminal energies are encoded as partition functions (Z)—computed according to Eq. (14.5)—for β values ranging from 0 to 20 by 0.4 where

$$\beta = \frac{1}{kT} \tag{14.7}$$

and where k is the Boltzmann constant. The Hartree Fock correlation temperature is obtained by inserting Eq. (14.5) into Eq. (14.4) which is inserted into Eq. (14.3) to obtain

$$E(T) = \frac{N(N-1)}{\sum_i e^{i\epsilon_i/kT}} \sum_j \epsilon_j e^{-\epsilon_j/kT} \tag{14.8}$$

and then temperature is optimized via scipy.optimize.minimize such that $|E_{HF} - E(T)|$ is minimized.

Model Outputs. For a given molecular system, the output of the convolutional neural net is a Δ value representing the difference between the Hartree Fock correlation temperature and the predicted CASSCF correlation temperature, i.e., $\Delta = T^*_{CAS} - T^*_{HF}$. From this output, the predicted correlation temperature corresponding to the CASSCF calculation can be computed by adding the output (Δ) to the Hartree Fock correlation temperature (T^*_{HF}), which can be used—along with the known geminal energies (ϵ_i)—to calculate the predicted CASSCF energy according to Eq. (14.8).

Training Data. All hydrocarbons isomers ranging from two to seven carbon atoms are used to train the convolutional neural net. Specifically, the training set—composed of twenty-one hydrocarbon molecules—follows: 2.01: 'Ethane', 3.01: 'Propane', 4.01: 'Butane', 4.02: '2-Methylpropane', 5.01: 'Pentane', 5.02: '2-Methylbutane', 5.03: '2,2-Dimethylpropane', 6.01: 'Hexane', 6.02: '2-Methylpentane', 6.03: '3-Methylpentane', 6.04: '2,2-Dimethylbutane', 6.05: '2,3-Dimethylbutane', 7.01: 'Heptane', 7.02: '3-Methylhexane', 7.03: '2-Methylhexane',

7.04: '2,2-Dimethylpentane', 7.05: '2,3-Dimethylpentane', 7.06: '2,4-Dimethylpentane', 7.07: '3,3-Dimethylpentane', 7.08: '3-Ethylpentane', 7.09: '2,2,3-Trimethylbutane'.

Testing Data. All isomers of octane as well as nonane, decane, undecane, dodecane, tridecane, tetradecane, and pentadecane are used to test the trained neural net. Specifically, the testing set follows: 8.01: 'Octane', 8.02: '2-Methylheptane', 8.03: '3-Methylheptane', 8.04: '4-Methylheptane', 8.05: '2,2-Dimethylhexane', 8.06: '2,3-Dimethylhexane', 8.07: '2,4-Dimethylhexane', 8.08: '2,5-Dimethylhexane', 8.09: '3,3-Dimethylhexane', 8.1: '3,4-Dimethyl hexane', 8.11: '3-Ethylhexane', 8.12: '2,2,3-Trimethylpentane', 8.13: '2,2,4-Trimethylpentane', 8.14: '2,3,3-Trimethylpentane', 8.15: '2,3,4-Trimethylpentane', 8.16: '3-Ethyl-2-Methyl pentane', 8.17: '3-Ethyl-3-Methylpentane', 8.18: '2,2,4,4-Tetramethylbutane', 9.01: 'Nonane', 10.01: 'Decane', 11.01: 'Undecane', 12.01: 'Dodecane', 13.01: 'Tridecane', 14.01: 'Tetradecane', 15.01: 'Pentadecane'.

CNN Specifics. The convolutional neural network is composed of an input layer, five additional dense layers, and an output layer. The input layer consists of partition functions and the Hartree Fock correlation temperature as specified in the *Model Inputs* section, and the output layer is a dense layer consisting of the Δ value described in the *Model Outputs* section. The additional dense layers have 503, 240, 100, 50, and 20 nodes, respectively. All dense nodes are initialized via the $he\_uniform$ kernel initializer with a $relu$ activation function. For the training of the convolutional net, loss is measured via mean absolute error, and the *adam* optimizer is implemented for $30,000$ epochs. This convolutional neural network is implemented using Keras—Python's deep learning API [499].

Computational Scaling For the testing set, scaling is dominated by the determination of the geminal energies, which are obtained via the diagonalization of the two-electron reduced Hamiltonian, a computation that scales as $O[r^6]$ where r is the number of orbitals in the active space. Thus, for a given molecule in the testing set, computational expense for prediction of molecular energies scales as $O[r^6]$. The computational expense of the training

set is dominated by the determination of the reference CASSCF or CCSD energies necessary to obtain the reference correlation temperature—which are known to scale approximately as $O[N!]$ and $O[N^6]$, respectively, for a given molecule where N for CASSCF is the number of active electrons and N for CCSD is the number of total electrons.

14.6 Supplemental Information

14.6.1 Prediction of CASSCF Energies with a Variable Active Space Size and the STO-6G Basis

In the main article to which this supplemental corresponds, the active space size for all complete active-space self-consistent field calculations is fixed to $[N_e = 8,\ N_o = 8]$ for all hydrocarbons used in both the training and testing sets. To test the necessity of this assumption, we additionally train a convolutional neural network on hydrocarbon data with variable active space sizes. Specifically, the following active spaces are used for the CASSCF hydrocarbon calculations: $[N_e = 2,\ N_o = 2]$ for isomers of ethane; $[N_e = 4,\ N_o = 4]$ for isomers of propane and butane; $[N_e = 6,\ N_o = 6]$ for isomers of pentane and hexane; and $[N_e = 8,\ N_o = 8]$ for isomers of heptane and octane. Note that the STO-6G basis is utilized for both Hartree Fock and CASSCF calculations and that an identical convolutional neural network to that described in the main text is implemented. As can be seen in Fig. 14.5—where hydrocarbons with two to seven carbon atoms were used to train the neural network that was tested on isomers of octane—the energies predicted from our CNN approach (green circles) still seem to capture the correlation energy accurately for the vast majority of octane isomers as it more-closely matches the CASSCF (black boxes) than the Hartree Fock (blue diamonds) calculations. However, from comparison of these results to those shown in the main text, it is apparent that restricting the training data to have the same active space as the testing data does produce some benefit, as the predicted energies in which active space

size is maintained for all hydrocarbons more-closely matches CASSCF energies.

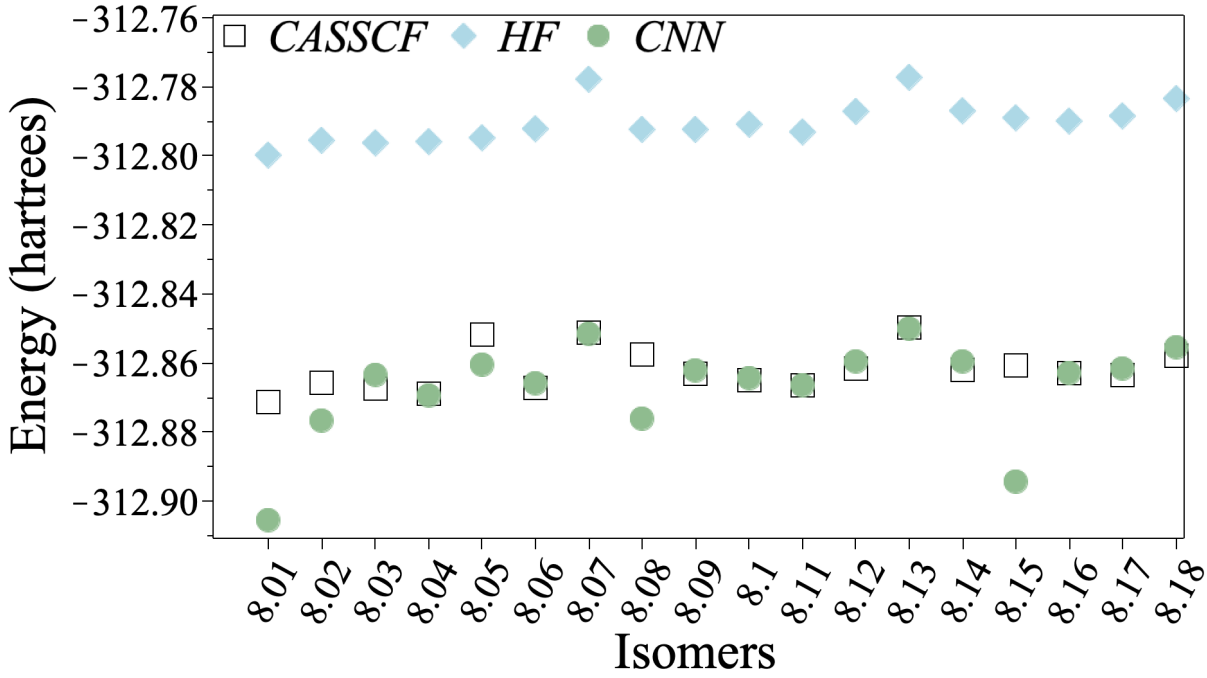

Figure 14.5: Hartree Fock energies (HF, blue diamonds), Complete Active Space Self-Consistent Field energies (CASSCF, black boxes), and energy values predicted via utilization of Convolutional Neural Networks (CNN, green circles) are shown for the series of octane isomers. As can be seen, the CNN methodology trained on smaller hydrocarbon data fairly accurately recovers the correlation energy. Isomer labels are given by [8.01: 'Octane', 8.02: '2-Methylheptane', 8.03: '3-Methylheptane', 8.04: '4-Methylheptane', 8.05: '2,2-Dimethylhexane', 8.06: '2,3-Dimethylhexane', 8.07: '2,4-Dimethylhexane', 8.08: '2,5-Dimethylhexane', 8.09: '3,3-Dimethylhexane', 8.10: '3,4-Dimethylhexane', 8.11: '3-Ethylhexane', 8.12: '2,2,3-Trimethylpentane', 8.13: '2,2,4-Trimethylpentane', 8.14: '2,3,3-Trimethylpentane', 8.15: '2,3,4-Trimethylpentane', 8.16: '3-Ethyl-2-Methylpentane', 8.17: '3-Ethyl-3-Methylpentane', 8.18: '2,2,4,4-Tetramethylbutane']. Both Hartree Fock and CASSCF calculations are computed here using the STO-6G basis set with the CASSCF calculations employing the following active spaces: $[N_e = 2,\ N_o = 2]$ for isomers of ethane; $[N_e = 4,\ N_o = 4]$ for isomers of propane and butane; $[N_e = 6,\ N_o = 6]$ for isomers of pentane and hexane; and $[N_e = 8,\ N_o = 8]$ for isomers of heptane and octane.

14.6.2 Prediction of CASSCF Energies with an [10,10] Active Space and cc-pVTZ Basis Set

The manuscript presents our machine learning approach for prediction of CASSCF energies utilizing a convolutional neural network trained on CASSCF energies computed using a $[N_e = 8,\ N_o = 8]$ active space and the cc-pVDZ basis set. Here, we additionally include the prediction of a selection of CASSCF energies utilizing a convolutional neural network trained on CASSCF energies computed using a $[N_e = 10,\ N_o = 10]$ active space and the cc-pVTZ basis set using an identical convolutional neural network to that described in the main text. As can be seen from Fig. 14.6—where hydrocarbons with two to seven carbon atoms were used to train the neural network that was tested on larger hydrocarbons—, the convolutional neural network methodology (CNN, green circles) trained on smaller hydrocarbon data fairly accurately recovers the correlation energy for all eighteen isomers of the straight-chain isomers of hydrocarbons with 8-11 carbon atoms. This is evinced by the degree to which the CNN results match CASSCF energies (CASSCF, black boxes) when compared to the Hartree Fock energies (HF, blue diamonds). This agreement of our machine learning approach with the CASSCF energies for $[N_e = 10,\ N_o = 10]$ active space calculations utilizing cc-PVTZ emphasizes that the results obtained in the main manuscript are neither reliant on active space nor basis set. Further, this is a demonstration that our reduced density matrix machine learning approach is capable of predicting the higher degree of correlation inherent to using both a larger basis set and active space.

14.6.3 Prediction of CCSD Energies with a STO-6G Basis Set

The manuscript presents our machine learning approach for prediction of CCSD energies utilizing a convolutional neural network trained on CCSD energies computed using the cc-pVDZ basis set. Here, we additionally include the prediction of CCSD energies utilizing a convolutional neural network trained on CCSD energies computed using the STO-6G basis

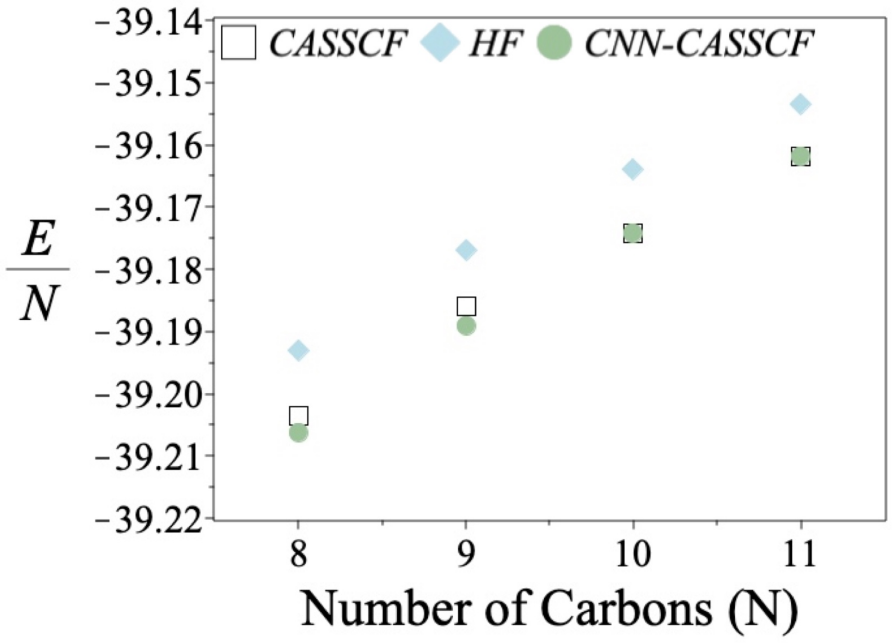

Figure 14.6: Hartree Fock energies (HF, blue diamonds), Complete Active Space Self-Consistent Field energies (CASSCF, black boxes), and energy values predicted via utilization of Convolutional Neural Networks (CNN, green circles) are shown for the series of octane isomers. As can be seen, the CNN methodology trained on smaller hydrocarbon data fairly accurately recovers the correlation energy. Isomer labels are given by [8: 'Octane', 9: 'Nonane', 10: 'Decane', 11: 'Undecane']. Both Hartree Fock and CASSCF calculations are computed here using the cc-pVTZ basis set with the CASSCF calculations employing the $[N_e = 10,\ N_o = 10]$ active space.

set utilizing an identical convolutional neural network to that described in the main text. As can be seen from Figs. 14.7 and 14.8—where hydrocarbons with two to seven carbon atoms were used to train the neural network that was tested on larger hydrocarbons—, the convolutional neural network methodology (CNN, green circles) trained on smaller hydrocarbon data fairly accurately recovers the correlation energy for all eighteen isomers of octane as well as the straight-chain isomers of hydrocarbons with 8-15 carbon atoms. This is evinced by the degree to which the CNN results match CCSD energies (CCSD, black boxes) when compared to the Hartree Fock energies (HF, blue diamonds). This agreement of our machine learning approach with the CCSD energies for calculations utilizing the STO-6G basis emphasizes that the results obtained in the main manuscript are not reliant on basis

set. Further, the large hydrocarbon data obtained for these CCSD calculations—able to be compared to exact CCSD results due to the small STO-6G basis set—additionally confirm that obtaining fairly-accurate correlation energies for these larger hydrocarbons is not reliant on utilization of the CASSCF level of theory but rather can be obtained for the CCSD level of theory.

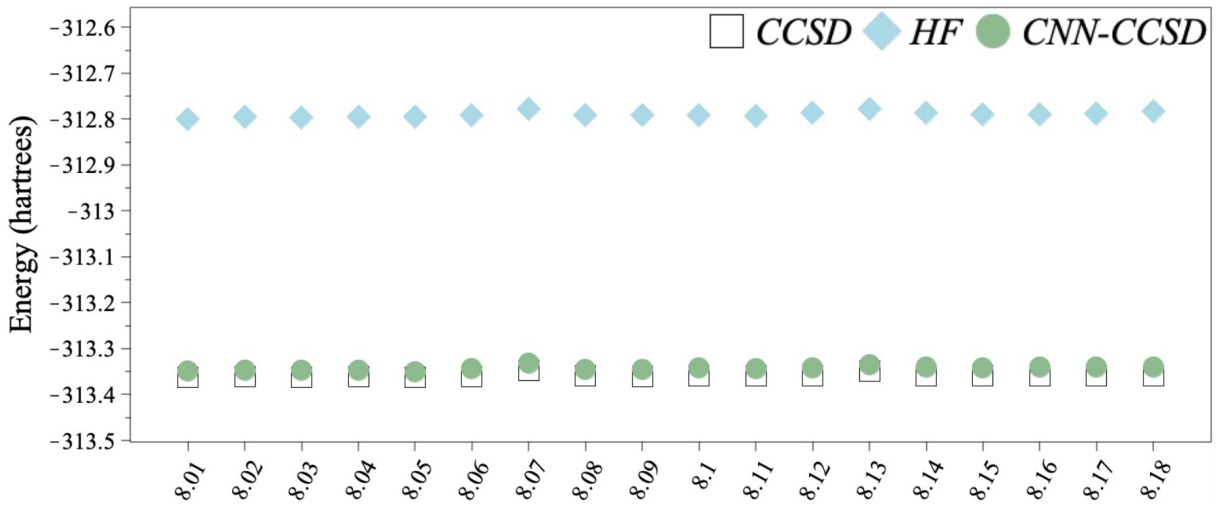

Figure 14.7: Hartree Fock energies (HF, blue diamonds), Coupled Cluster Single Double energies (CCSD, black boxes), and energy values predicted via utilization of Convolutional Neural Networks (CNN, green circles) are shown for the series of octane isomers. As can be seen, the CNN methodology trained on smaller hydrocarbon data fairly accurately recovers the correlation energy. Isomer labels are given by [8.01: 'Octane', 8.02: '2-Methylheptane', 8.03: '3-Methylheptane', 8.04: '4-Methylheptane', 8.05: '2,2-Dimethylhexane', 8.06: '2,3-Dimethylhexane', 8.07: '2,4-Dimethylhexane', 8.08: '2,5-Dimethylhexane', 8.09: '3,3-Dimethylhexane', 8.10: '3,4-Dimethylhexane', 8.11: '3-Ethylhexane', 8.12: '2,2,3-Trimethylpentane', 8.13: '2,2,4-Trimethylpentane', 8.14: '2,3,3-Trimethylpentane', 8.15: '2,3,4-Trimethylpentane', 8.16: '3-Ethyl-2-Methylpentane', 8.17: '3-Ethyl-3-Methylpentane', 8.18: '2,2,4,4-Tetramethylbutane']. Both Hartree Fock and CCSD calculations are computed here using the cc-pVDZ basis set.

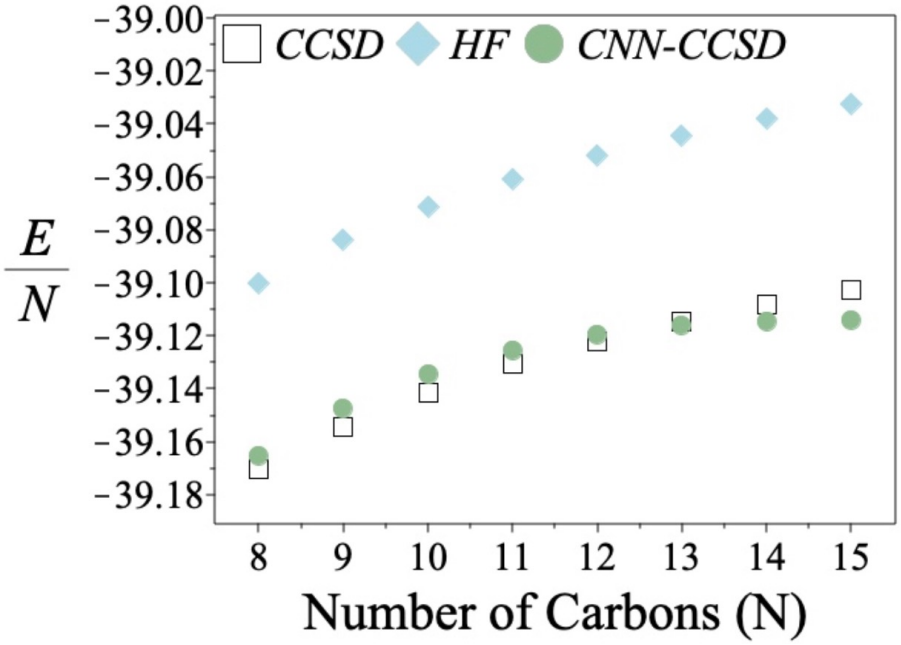

Figure 14.8: Large hydrocarbon data. Hartree Fock energies (HF, blue diamonds), Coupled Cluster Single Double energies (CCSD, black boxes), and energy values predicted via utilization of Convolutional Neural Networks (CNN, green circles) per number of carbons are shown for the series of straight-chained hydrocarbons from octane through pentadecane. As can be seen, the CNN methodology trained on smaller hydrocarbon data fairly accurately recovers the correlation energy. Isomer labels are given by [8: 'Octane', 9: 'Nonane', 10: 'Decane', 11: 'Undecane', 12: 'Dodecane', 13: 'Tridecane', 14: 'Tetradecane', 15: 'Pentadecane']. Both Hartree Fock and CCSD calculations are computed here using the STO-6G basis set.

REFERENCES

[1] C. Comte and P. Nozières. Exciton bose condensation : the ground state of an electron-hole gas - i. mean field description of a simplified model. *Journal de Physique*, 43(7): 1069–1081, 1982. doi:10.1051/jphys:019820043070106900.

[2] P. Nozières and C. Comte. Exciton bose condensation : the ground state of an electron-hole gas - II. spin states, screening and band structure effects. *Journal de Physique*, 43(7):1083–1098, 1982. doi:10.1051/jphys:019820043070108300.

[3] S.E. Brown. Organic superconductors: The bechgaard salts and relatives. *Physica C: Supercond.*, 514:279–289, 2015. ISSN 0921-4534. doi:https://doi.org/10.1016/j.physc.2015.02.030. Superconducting Materials: Conventional, Unconventional and Undetermined.

[4] L. M. Sager, S. Safaei, and D. A. Mazziotti. Potential coexistence of exciton and fermion-pair condensations. *Phys. Rev. B*, 101(8):081107, 2020. doi:10.1103/PhysRevB.101.081107.

[5] L. M. Sager, S. E. Smart, and D. A. Mazziotti. Preparation of an exciton condensate of photons on a 53-qubit quantum computer. *Phys. Rev. Res.*, 2(4), Nov 2020. ISSN 2643-1564. doi:10.1103/physrevresearch.2.043205.

[6] L. M. Sager and D. A. Mazziotti. Preparation of strongly correlated superconducting states on a quantum computer with hints of quantum advantage. *arXiv*, 2021.

[7] IBM-Q-Team. IBM-Q-5 Santiago backend specification v1.3.22, 2021.

[8] I. B. M. Q-Team. IBM-Q-15 Melbourne backend specification v2.0.0, 2019.

[9] F. Jensen. *Introduction to Computational Chemistry*. John Wiley and Sons, Inc., Hoboken, NJ, USA, 2006. ISBN 0470011874.

[10] S. E. Smart. *Reduced Density Matrix Approaches for Many-Body Simulations on Near-Term Quantum Computers*. PhD thesis, The University of Chicago, 2022.

[11] L. M. Sager and S. S. Iyengar. Proton relays in anomalous carbocations dictate spectroscopy, stability, and mechanisms: case studies on $C_2H_5^+$ and $C_3H_3^+$. *Phys. Chem. Chem. Phys.*, 19(40):27801–27816, 2017. doi:10.1039/c7cp05577c.

[12] A. O. Schouten, L. M. Sager, and D. A. Mazziotti. Exciton condensation in molecular-scale van der waals stacks. *J. Phys. Chem. Lett.*, 12(40):9906–9911, October 2021. doi:10.1021/acs.jpclett.1c02368.

[13] A. W. Schlimgen, K. Head-Marsden, L. M. Sager, P. Narang, and D. A. Mazziotti. Quantum simulation of open quantum systems using a unitary decomposition of operators. *Phys. Rev. Lett.*, 127:270503, Dec 2021. doi:10.1103/PhysRevLett.127.270503.

[14] L. M. Sager and D. A. Mazziotti. Cooper-pair condensates with nonclassical long-range order on quantum devices. *Phys. Rev. Res.*, 4(1), January 2022. doi:10.1103/physrevresearch.4.013003.

[15] L. M. Sager and D. A. Mazziotti. Simultaneous fermion and exciton condensations from a model hamiltonian. *Phys. Rev. B*, 105:035143, Jan 2022. doi:10.1103/PhysRevB.105.035143.

[16] L. M. Sager and D. A. Mazziotti. Entangled phase of simultaneous fermion and exciton condensations realized. *Phys. Rev. B*, 105:L121105, Mar 2022. doi:10.1103/PhysRevB.105.L121105.

[17] L. M. Sager, A. O. Schouten, and D. A. Mazziotti. Beginnings of exciton condensation in coronene analog of graphene double layer. *J. Chem. Phys.*, 156(15):154702, 2022. doi:10.1063/5.0084564.

[18] A. W. Schlimgen, K. Head-Marsden, L. M. Sager, P. Narang, and D. A. Mazziotti. Quantum simulation of the Lindblad equation using a unitary decomposition of operators. *Phys. Rev. Res.*, 4(2), June 2022. doi:10.1103/physrevresearch.4.023216.

[19] A. O. Schouten, L. M. Sager-Smith, and David A. Mazziotti. Large cumulant eigenvalue as a signature of exciton condensation. *Phys. Rev. B*, 105(24), June 2022. doi:10.1103/physrevb.105.245151.

[20] S. Warren, L. M. Sager-Smith, and D. A. Mazziotti. Quantum simulation of quantum phase transitions using the convex geometry of reduced density matrices. *Phys. Rev. A*, 106(1), July 2022. doi:10.1103/physreva.106.012434.

[21] A. W. Schlimgen, K. Head-Marsden, L. M. Sager-Smith, P. Narang, and David A. Mazziotti. Quantum state preparation and nonunitary evolution with diagonal operators. *Phys. Rev. A*, 106(2), August 2022. doi:10.1103/physreva.106.022414.

[22] S. Warren, L. M. Sager-Smith, and D. A. Mazziotti. Quantum phase transitions in a model hamiltonian exhibiting entangled simultaneous fermion-pair and exciton condensations. *Phys. Rev. B*, 106(16), October 2022. doi:10.1103/physrevb.106.165107.

[23] L. M. Sager-Smith and D. A. Mazziotti. Reducing the quantum many-electron problem to two electrons with machine learning. *JACS*, 144(41):18959–18966, October 2022. doi:10.1021/jacs.2c07112.

[24] A. O. Schouten, J. E. Klevens, L. M. Sager-Smith, J. Xie, J. S. Anderson, and D. A. Mazziotti. Potential for exciton condensation in a highly conductive amorphous polymer. *Phys. Rev. Mater.*, 7:045001, Apr 2023. doi:10.1103/PhysRevMaterials.7.045001.

[25] A. O. Schouten, L. M. Sager-Smith, and D. A. Mazziotti. Exciton-condensate-like amplification of energy transport in light harvesting. *PRX Energy*, 2:023002, Apr 2023. doi:10.1103/PRXEnergy.2.023002.

[26] E. Schrödinger. An undulatory theory of the mechanics of atoms and molecules. *Phys. Rev.*, 28:1049–1070, Dec 1926. doi:10.1103/PhysRev.28.1049.

[27] T. Engel and W. Hehre. *Quantum Chemistry & Spectroscopy*. Pearson, 3rd ed. edition, 2013.

[28] D. A. McQuarrie. *Quantum chemistry*. University Science Books, Sausalito, CA, 2nd ed. edition, 2008. ISBN 9781891389504.

[29] J. J. Sakurai and J. Napolitano. *Modern quantum mechanics*. Addison-Wesley, San Francisco, CA, 2nd ed. edition, 2011.

[30] A. Szabo and N. S. Ostlund. *Modern Quantum Chemistry: Introduction to Advanced Electronic Structure Theory*. Dover Publications, Inc., Mineola, 1st ed. edition, 1996.

[31] J. S. Townsend. *A modern approach to quantum mechanics*. University Science Books, Sausalito, CA, 2nd ed. edition, 2000.

[32] M. Born and R. Oppenheimer. Zur quantentheorie der molekeln. *Annalen der Physik*, 389(20):457–484, 1927. doi:https://doi.org/10.1002/andp.19273892002.

[33] J. C. Slater. A simplification of the Hartree-Fock method. *Phys. Rev.*, 81:385–390, Feb 1951. doi:10.1103/PhysRev.81.385.

[34] D. R. Hartree. The wave mechanics of an atom with a non-coulomb central field. Part II. Some results and discussion. *Math. Proc. Camb. Philos. Soc.*, 24(1):111–132, 1928. doi:10.1017/S0305004100011920.

[35] V. Fock. Näherungsmethode zur lösung des quantenmechanischen mehrkörperproblems. *Zeitschrift für Physik*, 61:126–148, 1930.

[36] G. Schubring. Hermann grassmann. extension theory. translated by, lloyd c. kannenberg. *Isis*, 94(2):386–387, 2003. doi:10.1086/379450.

[37] T. Yokonuma. *Tensor spaces and exterior algebra*. Translations of mathematical monographs, v. 108. American Mathematical Society, Providence, R.I, 1992. ISBN 0821845640.

[38] P. A. M. Dirac and N. H. D. Bohr. The quantum theory of the emission and absorption of radiation. *Proc. Roy. Soc. London*, 114(767):243–265, 1927. doi:10.1098/rspa.1927.0039.

[39] P. Jordan and E. Wigner. über das paulische äquivalenzverbot. *Zeitschrift für Physik*, 47(9-10):631–651, September 1928. doi:10.1007/bf01331938.

[40] V. Fock. Konfigurationsraum und zweite quantelung. *Zeitschrift für Physik*, 75(9-10): 622–647, September 1932. doi:10.1007/bf01344458.

[41] David A. Mazziotti. Lecture notes in advanced quantum chemistry, CHEM-362, 2019.

[42] I. Shavitt. The history and evolution of configuration interaction. *Mol. Phys.*, 94(1): 3–17, 1998. doi:10.1080/002689798168303.

[43] C. Møller and M. S. Plesset. Note on an approximation treatment for many-electron systems. *Phys. Rev.*, 46:618–622, Oct 1934. doi:10.1103/PhysRev.46.618.

[44] H. G. KÜMMEL. A biography of the coupled cluster method. In *Recent Progress in Many-Body Theories*. World Scientific, December 2002. doi:10.1142/9789812777843_0040.

[45] I. Shavitt and R. J. Bartlett. *Many-Body Methods in Chemistry and Physics*. Cambridge University Press, August 2009. doi:10.1017/cbo9780511596834.

[46] K. P. Lawley, editor. *Advances in Chemical Physics*. John Wiley & Sons, Inc., January 1987. doi:10.1002/9780470142943.

[47] B. O. Roos. *The Complete Active Space Self-Consistent Field Method and its Applications in Electronic Structure Calculations*, chapter 7, pages 399–445. John Wiley and Sons, Ltd, 1987. ISBN 9780470142943. doi:https://doi.org/10.1002/9780470142943.ch7.

[48] D. A. Mazziotti. *Reduced-Density-Matrix Mechanics: With Application to Many-electron Atoms and Molecule*, volume 134. Adv. Chem. Phys., Wiley, New York, 2007. ISBN 978-0-471-79056-3.

[49] D. A. Mazziotti. Two-electron reduced density matrix as the basic variable in many-electron quantum chemistry and physics. *Chem. Rev.*, 112(1):244–262, 2012. doi:10.1021/cr2000493.

[50] D. A. Mazziotti. Pure-N-representability conditions of two-fermion reduced density matrices. *Phys. Rev. A*, 94(3), 2016. doi:10.1103/PhysRevA.94.032516.

[51] D. A. Mazziotti. Large-scale semidefinite programming for many-electron quantum mechanics. *Phys. Rev. Lett.*, 106(8):083001, February 2011. doi:10.1103/PhysRevLett.106.083001.

[52] J. Cioslowski, editor. *Many-electron Densities and Reduced Density Matrices*. Springer Science & Business Media, 2013.

[53] M. Nakata, H. Nakatsuji, M. Ehara, M. Fukuda, K. Nakata, and K. Fujisawa. Variational calculations of fermion second-order reduced density matrices by semidefinite programming algorithm. *J. Chem. Phys.*, 114(19):8282–8292, 2001. doi:10.1063/1.1360199.

[54] D. A. Mazziotti. Realization of quantum chemistry without wave functions through first-order semidefinite programming. *Phys. Rev. Lett.*, 93:213001, November 2004. doi:10.1103/PhysRevLett.93.213001.

[55] Zhengji Zhao, Bastiaan J. Braams, Mituhiro Fukuda, Michael L. Overton, and Jerome K. Percus. The reduced density matrix method for electronic structure calculations and the role of three-index representability conditions. *J. Chem. Phys.*, 120(5): 2095–2104, 2004. doi:10.1063/1.1636721.

[56] Eric Cances, Gabriel Stoltz, and Mathieu Lewin. The electronic ground-state energy problem: A new reduced density matrix approach. *J. Chem. Phys.*, 125(6):064101, 2006. doi:10.1063/1.2222358.

[57] G. Gidofalvi and D. A. Mazziotti. Active-space two-electron reduced-density-matrix method: Complete active-space calculations without diagonalization of the n-electron Hamiltonian. *J. Chem. Phys.*, 129(13):134108, 2008. doi:10.1063/1.2983652.

[58] Neil Shenvi and Artur F. Izmaylov. Active-space n-representability constraints for variational two-particle reduced density matrix calculations. *Phys. Rev. Lett.*, 105(21), 2010. doi:10.1103/physrevlett.105.213003.

[59] D. A. Mazziotti. Structure of fermionic density matrices: Complete N-representability conditions. *Phys. Rev. Lett.*, 108(26):263002, June 2012. doi:10.1103/PhysRevLett.108.263002.

[60] Brecht Verstichel, Helen Van Aggelen, Ward Poelmans, and Dimitri Van Neck. Variational two-particle density matrix calculation for the hubbard model below half filling using spin-adapted lifting conditions. *Phys. Rev. Lett.*, 108(21), 2012. doi:10.1103/physrevlett.108.213001.

[61] Anthony W. Schlimgen, Charles W. Heaps, and David A. Mazziotti. Entangled electrons foil synthesis of elusive low-valent vanadium oxo complex. *J. Phys. Chem. Lett.*, 7(4):627–631, 2016. doi:10.1021/acs.jpclett.5b02547.

[62] Mario Piris. Global method for electron correlation. *Phys. Rev. Lett.*, 119(6), November 2017. doi:10.1103/physrevlett.119.063002.

[63] L. D. Landau. The damping problem in wave mechanics. In D. Ter Haar, editor, *Collected Papers of L.D. Landau*, pages 8–18. Pergamon, 1965. ISBN 978-0-08-010586-4. doi:https://doi.org/10.1016/B978-0-08-010586-4.50007-9.

[64] J. von Neumann. Wahrscheinlichkeitstheoretischer aufbau der quantenmechanik. *Nachrichten von der Gesellschaft der Wissenschaften zu Göttingen, Mathematisch-Physikalische Klasse*, 1927:245–272, 1927.

[65] R. H. Tredgold. Density matrix and the many-body problem. *Phys. Rev.*, 105:1421–1423, Mar 1957. doi:10.1103/PhysRev.105.1421.

[66] A. J. Coleman. Structure of fermion density matrices. *Rev. Mod. Phys.*, 35:668–686, July 1963. doi:10.1103/RevModPhys.35.668.

[67] A J Coleman and V I Yukalov. *Reduced Density Matrices*. Lecture Notes in Chemistry. Springer, Berlin, Germany, 2000 edition, April 2000.

[68] M. Altunbulak. *The Pauli Principle, Representation Theory, and Geometry of Flag Varieties*. PhD thesis, Bilkent University, 2008.

[69] A. A. Klyachko. The pauli exclusion principle and beyond, 2009.

[70] D. A. Mazziotti. First-order semidefinite programming for the two-electron treatment of many-electron atoms and molecules. *ESAIM Math. Model. Numer. Anal.*, 41(2): 249–259, 2007. doi:10.1051/m2an:2007021.

[71] D. A. Mazziotti. Large-scale semidefinite programming for many-electron quantum mechanics. *Phys. Rev. Lett.*, 106:083001, Feb 2011. doi:10.1103/PhysRevLett.106.083001.

[72] J. M. Montgomery, E. Alexander, and D. A. Mazziotti. Prediction of the existence of lich: A carbene-like organometallic molecule. *J. Phys. Chem. A*, 124(46):9562–9566, 2020. doi:10.1021/acs.jpca.0c07134.

[73] S. E. Smart, P. G. Scrape, L. J. Butler, and D. A. Mazziotti. Using reduced density matrix techniques to capture static and dynamic correlation in the energy landscape for the decomposition of the ch2ch2ono radical and support a non-irc pathway. *J. Chem. Phys.*, 149(2):024302, 2018. doi:10.1063/1.5024512.

[74] A. W. Schlimgen and D. A. Mazziotti. Analytical gradients of variational reduced-density-matrix and wavefunction-based methods from an overlap-reweighted semidefinite program. *J. Chem. Phys.*, 149(16):164111, 2018. doi:10.1063/1.5043104.

[75] F. Colmenero and C. Valdemoro. Approximating q-order reduced density matrices in terms of the lower-order ones. ii. applications. *Phys. Rev. A*, 47:979–985, Feb 1993. doi:10.1103/PhysRevA.47.979.

[76] F. Colmenero and C. Valdemoro. Self-consistent approximate solution of the second-order contracted schröudinger equation. *Int. J. Quantum Chem.*, 51:369–388, 1994.

[77] C. Valdemoro, L.M. Tel, and E. Pérez-Romero. The contracted schrödinger equation: Some results. In P.-O. Löwdin, J. R. Sabin, M. C. Zerner, J. Karwowski, and M. Karelson, editors, *Advances in Quantum Chemistry*, volume 28, pages 33–46. Academic Press, 1997. doi:https://doi.org/10.1016/S0065-3276(08)60205-1.

[78] H. Nakatsuji and K. Yasuda. Direct determination of the quantum-mechanical density matrix using the density equation. *Phys. Rev. Lett.*, 76:1039–1042, Feb 1996. doi:10.1103/PhysRevLett.76.1039.

[79] K. Yasuda and H. Nakatsuji. Direct determination of the quantum-mechanical density matrix using the density equation. ii. *Phys. Rev. A*, 56:2648–2657, Oct 1997. doi:10.1103/PhysRevA.56.2648.

[80] D. A. Mazziotti. Contracted schrödinger equation: Determining quantum energies and two-particle density matrices without wave functions. *Phys. Rev. A*, 57:4219–4234, Jun 1998. doi:10.1103/PhysRevA.57.4219.

[81] D. A. Mazziotti. 3,5-contracted schrödinger equation: Determining quantum energies and reduced density matrices without wave functions. *Int. J. Quantum Chem.*, 70(4-5): 557–570, 1998. doi:https://doi.org/10.1002/(SICI)1097-461X(1998)70:4/5<557::AID-QUA2>3.0.CO;2-U.

[82] K. Yasuda. Direct determination of the quantum-mechanical density matrix: Parquet theory. *Phys. Rev. A*, 59:4133–4149, Jun 1999. doi:10.1103/PhysRevA.59.4133.

[83] D. A. Mazziotti. Pursuit of n-representability for the contracted schrödinger equation through density-matrix reconstruction. *Phys. Rev. A*, 60:3618–3626, Nov 1999. doi:10.1103/PhysRevA.60.3618.

[84] D. A. Mazziotti. Comparison of contracted Schrödinger and coupled-cluster theories. *Phys. Rev. A*, 60:4396–4408, Dec 1999. doi:10.1103/PhysRevA.60.4396.

[85] D. A. Mazziotti. Complete reconstruction of reduced density matrices. *Chem. Phys. Lett.*, 326(3):212–218, 2000. ISSN 0009-2614. doi:https://doi.org/10.1016/S0009-2614(00)00773-9.

[86] D. A. Mazziotti. Purification of correlated reduced density matrices. *Phys. Rev. E*, 65: 026704, Jan 2002. doi:10.1103/PhysRevE.65.026704.

[87] D. A. Mazziotti. Variational method for solving the contracted schrödinger equation through a projection of the n-particle power method onto the two-particle space. *J. Chem. Phys.*, 116(4):1239–1249, 2002. doi:10.1063/1.1430257.

[88] D. A. Mazziotti. Approximate solution for electron correlation through the use of schwinger probes. *Chem. Phys. Lett.*, 289(5):419–427, 1998. ISSN 0009-2614. doi:https://doi.org/10.1016/S0009-2614(98)00470-9.

[89] D. A. Mazziotti. Anti-Hermitian contracted Schrödinger equation: Direct determination of the two-electron reduced density matrices of many-electron molecules. *Phys. Rev. Lett.*, 97:143002, Oct 2006. doi:10.1103/PhysRevLett.97.143002.

[90] D. A. Mazziotti. Two-electron reduced density matrices from the anti-Hermitian contracted Schrödinger equation: Enhanced energies and properties with larger basis sets. *J. Chem. Phys.*, 126(18):184101, 2007. doi:10.1063/1.2723115.

[91] H. Kamerlingh Onnes. Further experiments with liquid helium. c. on the change of electric resistance of pure metals at very low temperatures etc. IV. the resistance of pure mercury at helium temperatures. In *Through Measurement to Knowledge*, pages 261–263. Springer Netherlands, 1991. doi:10.1007/978-94-009-2079-8_15.

[92] P. Kapitza. Viscosity of liquid helium below the λ-point. *Nature*, 141(3558):74–74, January 1938. doi:10.1038/141074a0.

[93] J. F. ALLEN and A. D. MISENER. Flow of liquid helium II. *Nature*, 141(3558):75–75, January 1938. doi:10.1038/141075a0.

[94] F. LONDON. The λ-phenomenon of liquid helium and the bose-einstein degeneracy. *Nature*, 141(3571):643–644, April 1938. doi:10.1038/141643a0.

[95] L. TISZA. Transport phenomena in helium II. *Nature*, 141(3577):913–913, May 1938. doi:10.1038/141913a0.

[96] F. London. *Superfluids: Macroscopic theory of superconductivity*. Structure of Matter Series. Wiley, 1950.

[97] L. Tisza. The theory of liquid helium. *Phys. Rev.*, 72(9):838–854, November 1947.

[98] T. Matsubara and J. M. Blatt. Bose einstein condensation of correlated pairs. *Prog. Theor. Phys.*, 23(3):451–474, March 1960. doi:10.1143/ptp.23.451.

[99] L. Onsager. Magnetic flux through a superconducting ring. *Phys. Rev. Lett.*, 7:50–50, Jul 1961. doi:10.1103/PhysRevLett.7.50.

[100] J. M. Blatt, K. W. Böer, and W. Brandt. Bose-einstein condensation of excitons. *Phys. Rev.*, 126:1691–1692, Jun 1962. doi:10.1103/PhysRev.126.1691.

[101] M. H. Anderson, J. R. Ensher, M. R. Matthews, C. E. Wieman, and E. A. Cornell. Observation of bose-einstein condensation in a dilute atomic vapor. *Science*, 269(5221): 198–201, 1995. ISSN 0036-8075. doi:10.1126/science.269.5221.198.

[102] C. C. Bradley, C. A. Sackett, J. J. Tollett, and R. G. Hulet. Evidence of bose-einstein condensation in an atomic gas with attractive interactions. *Phys. Rev. Lett.*, 75:1687–1690, August 1995. doi:10.1103/PhysRevLett.75.1687.

[103] I. Georgescu. 25 years of BEC. *Nature Rev. Phys.*, 2(8):396–396, July 2020. doi:10.1038/s42254-020-0211-7.

[104] Y.-H. Zhou, D. Park, and Y. Iwasa. Review on progresses and challenges of key mechanical issues in high-field superconducting magnets. *Nat. Sci. Rev.*, January 2023. doi:10.1093/nsr/nwad001.

[105] S. Bravyi, O. Dial, J. M. Gambetta, D. Gil, and Z. Nazario. The future of quantum computing with superconducting qubits. *J. App. Phys.*, 132(16):160902, October 2022. doi:10.1063/5.0082975.

[106] L. V. Keldysh. Coherent states of excitons. *Phys.-Uspekhi*, 60(11):1180–1186, 2017. ISSN 1468-4780. doi:10.3367/ufne.2017.10.038227.

[107] D. V. Fil and S. I. Shevchenko. Electron-hole superconductivity (review). *Low Temp. Phys.*, 44(9):867–909, 2018. ISSN 1063-777X. doi:10.1063/1.5052674.

[108] J. P. Eisenstein and A. H. MacDonald. Bose-einstein condensation of excitons in bilayer electron systems. *Nature*, 432(7018):691–694, December 2004. ISSN 1476-4687. doi:10.1038/nature03081.

[109] R. Balili, V. Hartwell, D. Snoke, L. Pfeiffer, and K. West. Bose-Einstein condensation of microcavity polaritons in a trap. *Science*, 316(5827):1007–1010, 2007. ISSN 0036-8075. doi:10.1126/science.1140990.

[110] J. Kasprzak, M. Richard, S. Kundermann, A. Baas, P. Jeambrun, J. M. J. Keeling, F. M. Marchetti, M. H. Szymanska, R. André, J. L. Staehli, V. Savona, P. B. Littlewood, B. Deveaud, and Le Si Dang. Bose-Einstein condensation of exciton polaritons. *Nature*, 443:409, September 2006. doi:10.1038/nature05131.

[111] H. Deng, H. Haug, and Y. Yamamoto. Exciton-polariton bose-einstein condensation. *Rev. Mod. Phys.*, 82(2):1489–1537, May 2010. doi:10.1103/revmodphys.82.1489.

[112] M. S. Fuhrer and A. R. Hamilton. Chasing the exciton condensate. *Physics*, 9:80, 2016. doi:10.1103/Physics.9.80.

[113] A. Einstein. Quantentheorie des einatomigen idealen gases. *K.P.A.W.*, pages 261–267, 1924. doi:10.1002/3527608958.ch27.

[114] S. N. Bose and A. Einstein. Planck's law and light quantum hypothesis. *Zeitscrift für Physik*, 26:178, 1924.

[115] F. London. On Bose-Einstein condensation. *Phys. Rev.*, 54:947–954, December 1938. doi:10.1036/1097-8542.757474.

[116] N. N. Bogolyubov. A contribution to the theory of super-fluidity. *Bull. Acad. Sci. URSS. Sér. Phys. [Izvestia Akad. Nauk SSSR]*, 11:77–90, 1947.

[117] L.D. Landau and E.M. Lifshitz. *Statistical Physics*. Elsevier, 1980. doi:10.1016/c2009-0-24487-4.

[118] L. Pitaevskii and S. Stringari. *Bose-Einstein Condensation and Superfluidity*. Number Vol. 164 in International Series of Monographs on Physics. OUP Oxford, 1st ed. edition, 2016. ISBN 9780198758884.

[119] O. Penrose and L. Onsager. Bose-einstein condensation and liquid helium. *Phys. Rev.*, 104:576–584, November 1956. doi:10.1103/PhysRev.104.576.

[120] M. Schwartz. Bose-Einstein condensation, Statistical Mechanics Lecture 12, *Harvard*, 2019.

[121] M. Combescot, R. Combescot, and F. Dubin. Bose–Einstein condensation and indirect excitons: a review. *Rep. Prog. Phys.*, 80(6):066501, March 2017. doi:10.1088/1361-6633/aa50e3.

[122] A. Griffin, D. Snoke, and S. Stringari, editors. *Bose-Einstein Condensation*. Cambridge University Press, Cambridge, England, July 1996.

[123] L. Landau. Theory of the superfluidity of helium II. *Phys. Rev.*, 60(4):356–358, August 1941. doi:10.1103/physrev.60.356.

[124] A Griffin, D W Snoke, and S Stringari, editors. *Bose-Einstein Condensation*. Cambridge University Press, Cambridge, England, April 1995.

[125] G. Baym, J.-P. Blaizot, M. Holzmann, F. Laloë, and D. Vautherin. The transition temperature of the dilute interacting bose gas. *Phys. Rev. Lett.*, 83(9):1703–1706, August 1999. doi:10.1103/physrevlett.83.1703.

[126] M. Holzmann and W. Krauth. Transition temperature of the homogeneous, weakly interacting bose gas. *Phys. Rev. Lett.*, 83(14):2687–2690, October 1999. doi:10.1103/physrevlett.83.2687.

[127] K. B. Davis, M. -O. Mewes, M. R. Andrews, N. J. van Druten, D. S. Durfee, D. M. Kurn, and W. Ketterle. Bose-einstein condensation in a gas of sodium atoms. *Phys. Rev. Lett.*, 75:3969–3973, November 1995. doi:10.1103/PhysRevLett.75.3969.

[128] J. Bardeen, L. N. Cooper, and J. R. Schrieffer. Theory of superconductivity. *Phys. Rev.*, 108:1175–1204, December 1957. doi:10.1103/PhysRev.108.1175.

[129] W. Pauli. The connection between spin and statistics. *Phys. Rev.*, 58(8):716–722, 1940. doi:10.1103/physrev.58.716.

[130] C. Regal. *Experimental realization of BCS-BEC crossover physics with a Fermi gas of atoms*. PhD thesis, University of Colorado, Boulder, 2006.

[131] L. N. Cooper. Bound electron pairs in a degenerate Fermi gas. *Phys. Rev.*, 104(4): 1189–1190, November 1956. doi:10.1103/physrev.104.1189.

[132] R. M. Fernandes. BCS theory of superconductivity. In *Lecture Notes*, 2015.

[133] M. Tinkham. *Introduction to Superconductivity: v. 1*. Dover Books on Physics. Dover Publications, Mineola, NY, 2 edition, June 2004.

[134] N. N. Bogoliubov. On a new method in the theory of superconductivity. *Il Nuovo Cimento*, 7(6):794–805, March 1958. doi:10.1007/bf02745585.

[135] C. N. Yang. Concept of off-diagonal long-range order and the quantum phases of liquid He and of superconductors. *Rev. Mod. Phys.*, 34:694–704, October 1962. doi:10.1103/RevModPhys.34.694.

[136] F. Sasaki. Eigenvalues of fermion density matrices. *Phys. Rev.*, 138:B1338–B1342, June 1965. doi:10.1103/PhysRev.138.B1338.

[137] J. M. Blatt. Electron pairs in the theory of superconductivity. *Prog. Theor. Phys.*, 23 (3):447–450, 1960.

[138] A. J. Coleman. Structure of fermion density matrices. ii. antisymmetrized geminal powers. *J. Math. Phys.*, 6:1425–31, July 1963. doi:10.1063/1.1704794.

[139] C. Tresca, G. Profeta, G. Marini, G. B. Bachelet, A. Sanna, M. Calandra, and L. Boeri. Why mercury is a superconductor. *Phys. Rev. B*, 106:L180501, Nov 2022. doi:10.1103/PhysRevB.106.L180501.

[140] J.E. Hirsch, M.B. Maple, and F. Marsiglio. Superconducting materials classes: Introduction and overview. *Phys. C: Supercond. Appl.*, 514:1–8, July 2015. doi:10.1016/j.physc.2015.03.002.

[141] N. Dasenbrock-Gammon, E. Snider, R. McBride, H. Pasan, D. Durkee, N. Khalvashi-Sutter, S. Munasinghe, S. E. Dissanayake, K. V. Lawler, A. Salamat, and R. P. Dias. Evidence of near-ambient superconductivity in a n-doped lutetium hydride. *Nature*, 615(7951):244–250, March 2023. doi:10.1038/s41586-023-05742-0.

[142] S A Moskalenko and D W Snoke. *Bose-Einstein Condensation of Excitons and Biexcitons*. Cambridge University Press, Cambridge, MA, February 2000.

[143] J. Frenkel. On the transformation of light into heat in solids. I. *Phys. Rev.*, 37:17–44, Jan 1931. doi:10.1103/PhysRev.37.17.

[144] J. Frenkel. On the transformation of light into heat in solids. II. *Phys. Rev.*, 37: 1276–1294, May 1931. doi:10.1103/PhysRev.37.1276.

[145] G. H. Wannier. The structure of electronic excitation levels in insulating crystals. *Phys. Rev.*, 52:191–197, Aug 1937. doi:10.1103/PhysRev.52.191.

[146] N. F. Mott and M. J. Littleton. Conduction in polar crystals. i. electrolytic conduction in solid salts. *J. Chem. Soc., Faraday Trans.*, 34:485, 1938. doi:10.1039/tf9383400485.

[147] X.-Y. Zhu, Q. Yang, and M. Muntwiler. Charge-transfer excitons at organic semiconductor surfaces and interfaces. *Acc. Chem. Res.*, 42(11):1779–1787, April 2009. doi:10.1021/ar800269u.

[148] W. Kohn and D. Sherrington. Two kinds of bosons and bose condensates. *Rev. Mod. Phys.*, 42:1–11, January 1970. doi:10.1103/RevModPhys.42.1.

[149] Y. E. Lozovik and V. I. Yudson. A new mechanism for superconductivity: Pairing between spatially separated electrons and holes. *Sov. Phys. JETP*, 44(2):389–397, 1976.

[150] X. Liu, J. I. A. Li, K. Watanabe, T. Taniguchi, J. Hone, B. I. Halperin, P. Kim, and C. R. Dean. Crossover between strongly coupled and weakly coupled exciton superfluids. *Science*, 375(6577):205–209, January 2022. doi:10.1126/science.abg1110.

[151] Y. F. Lu, H. Kono, T. I. Larkin, A. W. Rost, T. Takayama, A. V. Boris, B. Keimer, and H. Takagi. Zero-gap semiconductor to excitonic insulator transition in ta2nise5. *Nat. Commun.*, 8(1), February 2017. doi:10.1038/ncomms14408.

[152] L. V. Keldysh and Y. V. Kopaev. Possible instability of the semimetallic state toward coulomb interaction. *Sov. Phys. Solid State*, 6:2219, 1965.

[153] L. V. Keldysh and A. Kozlov. Collective properties of excitons in semiconductors. *J. Exp. Theor. Phys.*, 1968.

[154] Yu. E. Lozovik and V. I. Yudson. Superconductivity at dielectric pairing of spatially separated quasiparticles. *Solid State Commun.*, 19(4):391–393, 1976. ISSN 0038-1098. doi:10.1016/0038-1098(76)91360-0.

[155] C. Garrod and M. Rosina. Particle-hole matrix: Its connection with the symmetries and collective features of the ground state. *J. Math. Phys.*, 10(10):1855–1861, 1969. ISSN 0022-2488. doi:10.1063/1.1664770.

[156] S. Safaei and D. A. Mazziotti. Quantum signature of exciton condensation. *Phys. Rev. B*, 98:045122, 2018. doi:10.1103/PhysRevB.98.045122/Users/lmsager/Downloads/IOPEXPORT_BIB.bib.

[157] J. P. Eisenstein. Exciton condensation in bilayer quantum hall systems. *Annu. Rev. Condens. Matter Phys.*, 5(1):159–181, 2014. ISSN 1947-5454. doi:10.1146/annurev-conmatphys-031113-133832.

[158] Tim Byrnes, Na Young Kim, and Yoshihisa Yamamoto. Exciton-polariton condensates. *Nat. Phys.*, 10(11):803–813, October 2014. ISSN 1745-2481. doi:10.1038/nphys3143.

[159] J. Keeling and S. Kéna-Cohen. Bose–einstein condensation of exciton-polaritons in organic microcavities. *Annu. Rev. Phys. Chem.*, 71(1):435–459, 2020. doi:10.1146/annurev-physchem-010920-102509. PMID: 32126177.

[160] S. Pannir-Sivajothi, J. A. Campos-Gonzalez-Angulo, L. A. Martínez-Martínez, S. Sinha, and J. Yuen-Zhou. Driving chemical reactions with polariton condensates. *Nat. Commun.*, 13(1), March 2022. doi:10.1038/s41467-022-29290-9.

[161] H. Min, R. Bistritzer, J.-J. Su, and A. H. MacDonald. Room-temperature superfluidity in graphene bilayers. *Phys. Rev. B*, 78(12):121401, 2008. doi:10.1103/PhysRevB.78.121401.

[162] A. Perali, D. Neilson, and A. R. Hamilton. High-temperature superfluidity in double-bilayer graphene. *Phys. Rev. Lett.*, 110:146803, 2013. doi:10.1103/PhysRevLett.110.146803.

[163] M. M. Fogler, L. V. Butov, and K. S. Novoselov. High-temperature superfluidity with indirect excitons in van der waals heterostructures. *Nat Commun*, 5(1):4555, 2014. ISSN 2041-1723. doi:10.1038/ncomms5555.

[164] J. I. A. Li, T. Taniguchi, K. Watanabe, J. Hone, A. Levchenko, and C. R. Dean. Negative Coulomb drag in double bilayer graphene. *Phys. Rev. Lett.*, 117:046802, July 2016. doi:10.1103/PhysRevLett.117.046802.

[165] J. I. A. Li, T. Taniguchi, K. Watanabe, J. Hone, and C. R. Dean. Excitonic superfluid phase in double bilayer graphene. *Nat. Phys.*, 13(8):751–755, Aug 2017. ISSN 1745-2481. doi:10.1038/nphys4140.

[166] L. Ma, P. X. Nguyen, Z. Wang, Y. Zeng, K. Watanabe, T. Taniguchi, A. H. MacDonald, K. F. Mak, and J. Shan. Strongly correlated excitonic insulator in atomic double layers. *Nature*, 598(7882):585–589, 2021. ISSN 1476-4687. doi:10.1038/s41586-021-03947-9.

[167] X. Hu, T. Hyart, D. I. P., and E. Rossi. Quantum-metric-enabled exciton condensate in double twisted bilayer graphene. *arXiv*, 2020.

[168] D.I. Pikulin and T. Hyart. Interplay of exciton condensation and the quantum spin hall effect ininas/gasbbilayers. *Phys. Rev. Lett.*, 112(17), Apr 2014. ISSN 1079-7114. doi:10.1103/physrevlett.112.176403.

[169] B. Debnath, Y. Barlas, D. Wickramaratne, M. R. Neupane, and R. K. Lake. Exciton condensate in bilayer transition metal dichalcogenides: Strong coupling regime. *Phys. Rev. B*, 96(17), Nov 2017. ISSN 2469-9969. doi:10.1103/physrevb.96.174504.

[170] G. W. Burg, N. Prasad, K. Kim, T. Taniguchi, K. Watanabe, A. H. MacDonald, L. F. Register, and E. Tutuc. Strongly enhanced tunneling at total charge neutrality in double-bilayer graphene-wse2 heterostructures. *Phys. Rev. Lett.*, 120(17), Apr 2018. ISSN 1079-7114. doi:10.1103/physrevlett.120.177702.

[171] Z. Wang, D. A. Rhodes, K. Watanabe, T. Taniguchi, J. C. Hone, J. Shan, and K. F. Mak. Evidence of high-temperature exciton condensation in two-dimensional atomic double layers. *Nature*, 574(7776):76–80, 2019. ISSN 1476-4687. doi:10.1038/s41586-019-1591-7.

[172] Y. Shimazaki, I. Schwartz, K. Watanabe, T. Taniguchi, M Kroner, and A. Imamoğlu. Strongly correlated electrons and hybrid excitons in a moiré heterostructure. *Nature*, 580(7804):472–477, Apr 2020. ISSN 1476-4687. doi:10.1038/s41586-020-2191-2.

[173] P. Rickhaus, F. K. de Vries, J. Zhu, E. Portoles, G. Zheng, M. Masseroni, A. Kurzmann, T. Taniguchi, K. Watanabe, A. H. MacDonald, and et al. Correlated electron-hole state

in twisted double-bilayer graphene. *Science*, 373(6560):1257–1260, Sep 2021. ISSN 1095-9203. doi:10.1126/science.abc3534.

[174] S. S. Ataei, D. Varsano, E. Molinari, and M. Rontani. Evidence of ideal excitonic insulator in bulk MoS_2 under pressure. *Proc. Nat. Acad. Sci.*, 118(13), March 2021. doi:10.1073/pnas.2010110118.

[175] Q. Gao, Y.-H. Chan, Y. Wang, H. Zhang, P. Jinxu, S. Cui, Y. Yang, Z. Liu, D. Shen, Z. Sun, J. Jiang, T. C. Chiang, and P. Chen. Evidence of high-temperature exciton condensation in a two-dimensional semimetal. *Nat. Commun.*, 14(1), February 2023. doi:10.1038/s41467-023-36667-x.

[176] L. V. Butov, A. Zrenner, G. Abstreiter, G. Böhm, and G. Weimann. Condensation of indirect excitons in coupled alas/gaas quantum wells. *Phys. Rev. Lett.*, 73:304–307, July 1994. doi:10.1103/PhysRevLett.73.304.

[177] L. Sigl, F. Sigger, F. Kronowetter, J. Kiemle, J. Klein, K. Watanabe, T. Taniguchi, J. J. Finley, U. Wurstbauer, and A. W. Holleitner. Signatures of a degenerate many-body state of interlayer excitons in a van der waals heterostack. *Phys. Rev. Res.*, 2(4): 042044, 2020. doi:10.1103/PhysRevResearch.2.042044.

[178] A. Kogar, M. S. Rak, S. Vig, A. A. Husain, F. Flicker, Y. I. Joe, L. Venema, G. J. MacDougall, T. C. Chiang, E. Fradkin, J. van Wezel, and P. Abbamonte. Signatures of exciton condensation in a transition metal dichalcogenide. *Science*, 358(6368):1314–1317, 2017. ISSN 0036-8075. doi:10.1126/science.aam6432.

[179] X. Liu, K. Watanabe, T. Taniguchi, B. I. Halperin, and P. Kim. Quantum Hall drag of exciton condensate in graphene. *Nat. Phys.*, 13(8):746–750, August 2017. ISSN 1745-2481. doi:10.1038/nphys4116.

[180] D. Nandi, A. D. K. Finck, J. P. Eisenstein, L. N. Pfeiffer, and K. W. West. Exciton condensation and perfect Coulomb drag. *Nature*, 488:481–484, 2012. doi:10.1038/nature11302.

[181] P. Shekhar, M. Malac, V. Gaind, N. Dalili, A. Meldrum, and Z. Jacob. Momentum-resolved electron energy loss spectroscopy for mapping the photonic density of states. *ACS Photonics*, 4(4):1009–1014, April 2017. doi:10.1021/acsphotonics.7b00103.

[182] Z. Li, M. Nadeem, Z. Yue, D. Cortie, M. Fuhrer, and X. Wang. Possible excitonic insulating phase in quantum-confined sb nanoflakes. *Nano Lett.*, 19(8):4960–4964, July 2019. doi:10.1021/acs.nanolett.9b01123.

[183] I. V. Blinov and A. H. MacDonald. Interlayer coherence in superconductor bilayers. *Phys. Rev. B*, 106:224504, Dec 2022. doi:10.1103/PhysRevB.106.224504.

[184] P. W. Anderson. Twenty-five years of high-temperature superconductivity – a personal review. *J. Phys.: Conf. Ser.*, 449:012001, July 2013. doi:10.1088/1742-6596/449/1/012001.

[185] A. P. Drozdov, P. P. Kong, V. S. Minkov, S. P. Besedin, M. A. Kuzovnikov, S. Mozaffari, L. Balicas, F. F. Balakirev, D. E. Graf, V. B. Prakapenka, E. Greenberg, D. A. Knyazev, M. Tkacz, and M. I. Eremets. Superconductivity at 250 K in lanthanum hydride under high pressures. *Nature*, 569(7757):528–31, 2019.

[186] M. Kellogg, J. P. Eisenstein, L. N. Pfeiffer, and K. W. West. Vanishing Hall resistance at high magnetic field in a double-layer two-dimensional electron system. *Phys. Rev. Lett.*, 93:036801, 2004. doi:10.1103/PhysRevLett.93.036801.

[187] E. Tutuc, M. Shayegan, and D. A. Huse. Counterflow measurements in strongly correlated GaAs hole bilayers: Evidence for electron-hole pairing. *Phys. Rev. Lett.*, 93: 36802, 2004. doi:10.1103/PhysRevLett.93.036802.

[188] D. Varsano, S. Sorella, D. Sangalli, M. Barborini, S. Corni, E. Molinari, and M. Rontani. Carbon nanotubes as excitonic insulators. *Nat Commun*, 8(1), 2017.

[189] H. Deng, G. Weihs, C. Santori, J. Bloch, and Y. Yamamoto. Condensation of semiconductor microcavity exciton polaritons. *Science*, 298(5591):199–202, 2002. ISSN 0036-8075. doi:10.1126/science.1074464.

[190] I. B. Spielman, J. P. Eisenstein, L. N. Pfeiffer, and K. W. West. Resonantly enhanced tunneling in a double layer quantum Hall ferromagnet. *Phys. Rev. Lett.*, 84:5808–5811, 2000. doi:10.1103/PhysRevLett.84.5808.

[191] M. Kellogg, I. B. Spielman, J. P. Eisenstein, L. N. Pfeiffer, and K. W. West. Observation of quantized Hall drag in a strongly correlated bilayer electron system. *Phys. Rev. Lett.*, 88:126804, 2002. doi:10.1103/PhysRevLett.88.126804.

[192] K. Lee, J. Xue, D. C. Dillen, K. Watanabe, T. Taniguchi, and E. Tutuc. Giant frictional drag in double bilayer graphene heterostructures. *Phys. Rev. Lett.*, 117:046803, July 2016. doi:10.1103/PhysRevLett.117.046803.

[193] A. Tartakovskii. Excitons in 2d heterostructures. *Nature Reviews Physics*, 2(1):8–9, 2019. doi:10.1038/s42254-019-0136-1.

[194] Sunny Gupta, Alex Kutana, and Boris I. Yakobson. Heterobilayers of 2d materials as a platform for excitonic superfluidity. *Nat Commun*, 11(1):2989, 2020. ISSN 2041-1723. doi:10.1038/s41467-020-16737-0.

[195] M. Lang and J. Müller. Organic superconductors. *The Physics of Superconductors*, pages 453–554, 2004. doi:10.1007/978-3-642-18914-2_7.

[196] D. Jèrome. Organic conductors: From charge density wave TTF-TCNQ to superconducting $(TMTSF)_2PF_6$. *Chem. Inform.*, 36(7), 2005. doi:10.1002/chin.200507281.

[197] A. Kobayashi, E. Fujiwara, and H. Kobayashi. Single-component molecular metals with extended-TTF dithiolate ligands. *ChemInform*, 36(7), 2005. doi:10.1002/chin.200507262.

[198] A. G. Lebed. *The Physics of Organic Superconductors and Conductors*. Springer, 2008.

[199] D. Jérome, A. Mazaud, M. Ribault, and K. Bechgaard. Superconductivity in a synthetic organic conductor $(tmtsf)_2pf_6$. *Journal de Physique Lettres*, 41(4):95–98, 1980. doi:10.1051/jphyslet:0198000410409500.

[200] Y. Okano, B. Zhou, H. Tanaka, T. Adachi, Y. Ohishi, M. Takata, S. Aoyagi, E. Nishibori, M. Sakata, A. Kobayashi, and H. Kobayashi. High-pressure (up to 10.7 GPa) crystal structure of single-component molecular metal $[Au(tmdt)_2]$. *J. Am. Chem. Soc.*, 131(20):7169–7174, 2009. doi:10.1021/ja9010018. PMID: 19405466.

[201] M. R. Bryce. Recent progress on conducting organic charge-transfer salts. *Chem. Soc. Rev.*, 20:355–390, 1991. doi:10.1039/CS9912000355.

[202] H. Cui, H. Kobayashi, S. Ishibashi, M. Sasa, F. Iwase, R. Kato, and A. Kobayashi. A single-component molecular superconductor. *J. Am. Chem. Soc.*, 136(21):7619–7622, 2014. doi:10.1021/ja503690m. PMID: 24816031.

[203] L. Valade, D. de Caro, C. Faulmann, and K. Jacob. $TTF[Ni(dmit)_2]_2$: From single-crystals to thin layers, nanowires, and nanoparticles. *Coord. Chem. Rev.*, 308:433–444, 2016. ISSN 0010-8545. doi:https://doi.org/10.1016/j.ccr.2015.05.014. Perspectives in Coordination Chemistry on the Occasion of the 40th anniversary of the LCC-CNRS, Toulouse, France.

[204] B. Zhou, S. Ishibashi, T. Ishii, T. Sekine, R. Takehara, K. Miyagawa, K. Kanoda, E. Nishibori, and A. Kobayashi. Single-component molecular conductor $[Pt(dmdt)_2]$—a three-dimensional ambient-pressure molecular Dirac electron system. *Chem. Commun.*, 55:3327–3330, 2019. doi:10.1039/C9CC00218A.

[205] L. Brossard, M. Ribault, L. Valade, and P. Cassoux. The first 3D molecular superconductor under pressure? : $TTF[Ni(dmit)_2]_2$. *Physica B+C*, 143(1-3):378–380, 1986. doi:10.1016/0378-4363(86)90145-2.

[206] P. Foury-Leylekian, S. Petit, I. Mirebeau, André G., M. de Souza, M. Lang, E. Ressouche, A. Moradpour, and J.-P. Pouget. Low-temperature structural effects in the $(TMTSF)_2PF_6$ and AsF_6 bechgaard salts. *Phys. Rev. B*, 88(2):024105, 2013. doi:10.1103/PhysRevB.88.024105.

[207] Suchithra Ashoka Sahadevan, Alexandre Abhervé, Noemi Monni, Pascale Auban-Senzier, Hengbo Cui, Reizo Kato, Maria Laura Mercuri, and Narcis Avarvari. Radical cation salts of tetramethyltetrathiafulvalene (tm-ttf) and tetramethyltetraselenafulvalene (tm-tsf) with chlorocyananilate-based anions. *Crystal Growth & Design*, 20(10): 6777–6786, 2020. doi:10.1021/acs.cgd.0c00873.

[208] Xiang Li, Yu-Han Liu, Guang-Zhou Zhu, and Feng Gao. Stabilization and isolation of radical cation and dication salts of a tetrathiafulvalene derivative functionalized with amino groups. *New J. Chem.*, 44:16959–16964, 2020. doi:10.1039/D0NJ04033A.

[209] Jun-ichi Yamada and Toyonari Sugimoto. *TTF Chemistry: Fundamentals and Applications of Tetrathiafulvalene*. Springer, 2004.

[210] H. Kobayashi, A. Kobayashi, Y. Sasaki, G. Saito, and H. Inokuchi. The crystal structure of $(TMTTF)_2ReO_4$. *Bull. Chem. Soc. Jpn.*, 57(7):2025–2026, 1984. doi:10.1246/bcsj.57.2025.

[211] H. Kobayashi, M. Takahashi, R. Kato, A. Kobayashi, and Y. Sasaki. The crystal structure and electrical resistivity of $(BPDT-TTF)_2I_3$. *Chem. Lett.*, 13(8):1331–1334, 1984. doi:10.1246/cl.1984.1331.

[212] Pubchem Tetrathiafulvalene. Pubchem compound summary for cid 99451, tetrathiafulvalene, 2022.

[213] S. Safaei and D. A. Mazziotti. Quantum signature of exciton condensation. *Phys. Rev. B*, 98(4):045122, 2018. doi:10.1103/PhysRevB.98.045122.

[214] J. C. Sancho-García and A. J. Pérez-Jiménez. Theoretical study of stability and charge-transport properties of coronene molecule and some of its halogenated derivatives: A path to ambipolar organic-based materials? *J. Chem. Phys.*, 141(13):134708, 2014. doi:10.1063/1.4897205.

[215] K. Uehara, H. Kano, K. Matsuo, H. Hayashi, M. Fujiki, H. Yamada, and N. Aratani. Mirror-image cofacial coronene dimers characterized by cd and cpl spectroscopy: A twisted bilayer nanographene. *Chem. Photo. Chem.*, 5(11):974–978, 2021. doi:https://doi.org/10.1002/cptc.202100166.

[216] D. A. Mazziotti. Enhanced constraints for accurate lower bounds on many-electron quantum energies from variational two-electron reduced density matrix theory. *Phys. Rev. Lett.*, 117(15):153001, October 2016. doi:10.1103/PhysRevLett.117.153001.

[217] D. A. Mazziotti. Dual-cone variational calculation of the two-electron reduced density matrix. *Phys. Rev. A*, 102:052819, Nov 2020. doi:10.1103/PhysRevA.102.052819.

[218] D. A. Mazziotti. Variational minimization of atomic and molecular ground-state energies via the two-particle reduced density matrix. *Phys. Rev. A*, 65:062511, Jun 2002. doi:10.1103/PhysRevA.65.062511.

[219] J.-N. Boyn, J. Xie, J. S. Anderson, and D. A. Mazziotti. Entangled electrons drive a non-superexchange mechanism in a cobalt quinoid dimer complex. *J. Phys. Chem. Lett.*, 11(12):4584–4590, 2020. doi:10.1021/acs.jpclett.0c01248.

[220] A. Kawamura, J. Xie, J.-N. Boyn, K. A. Jesse, A. J. McNeece, E. A. Hill, K. A. Collins, J. A. Valdez-Moreira, A. S. Filatov, J. W. Kurutz, D. A. Mazziotti, and J S. Anderson. Reversible switching of organic diradical character via iron-based spin-crossover. *J. Am. Chem. Soc.*, 142(41):17670–17680, 2020. doi:10.1021/jacs.0c08307.

[221] A. Raeber and D. A. Mazziotti. Large eigenvalue of the cumulant part of the two-electron reduced density matrix as a measure of off-diagonal long-range order. *Phys. Rev. A*, 92:052502, November 2015. doi:10.1103/PhysRevA.92.052502.

[222] Péter R. Surján. An introduction to the theory of geminals. *Topics in Current Chemistry Correlation and Localization*, pages 63–88, 1999. doi:10.1007/3-540-48972-x_4.

[223] Harrison Shull. Natural spin orbital analysis of hydrogen molecule wave functions. *J. Chem. Phys.*, 30(6):1405–1413, 1959. doi:10.1063/1.1730212.

[224] Y. Cao, V. Fatemi, S. Fang, K. Watanabe, T. Taniguchi, E. Kaxiras, and P. Jarillo-Herrero. Unconventional superconductivity in magic-angle graphene superlattices. *Nature*, 556(7699):43—50, Mar 2018. ISSN 1476-4687. doi:10.1038/nature26160.

[225] D. A. Mazziotti. Contracted schrödinger equation: Determining quantum energies and two-particle density matrices without wave functions. *Phys. Rev. A*, 57:4219–4234, June 1998. doi:10.1103/PhysRevA.57.4219.

[226] R. P. Feynman. Simulating physics with computers. *Int. J. Theor. Phys.*, 21:467–488, 1982. doi:https://doi.org/10.1007/BF02650179.

[227] P. Kaye, R. Laflamme, and M. Mosca. *An Introduction to Quantum Computing*. Oxford University Press, London, England, November 2006.

[228] pyQuil. Introduction to quantum computing¶, 2022.

[229] R. LaPierre. *Introduction to quantum computing*. Springer Nature, Cham, Switzerland, September 2021.

[230] D. McMahon. *Quantum Computing Explained*. Wiley - IEEE. Wiley-Blackwell, Hoboken, NJ, November 2007.

[231] J. D. Hidary. *Quantum computing: An applied approach*. Springer Nature, Cham, Switzerland, 1 edition, September 2019.

[232] E. G. Rieffel and W. H. Polak. *Quantum Computing*. Scientific and Engineering Computation. MIT Press, London, England, April 2011.

[233] A. E. Hassanien, M. Elhoseny, and J. Kacprzyk, editors. *Quantum computing: An environment for intelligent large scale real application*. Studies in Big Data. Springer International Publishing, Basel, Switzerland, 1 edition, October 2017.

[234] L Accardi, M Ohya, and N Watanabe. *Quantum Information and Computing*. World Scientific Publishing, Singapore, Singapore, December 2006.

[235] W. Scherer. *Mathematics of quantum computing*. Springer International Publishing, Basel, Switzerland, 1 edition, June 2019.

[236] K. L. Sharkey, A. Chance, and A. Khan. *Quantum chemistry and computing for the curious*. Packt Publishing, Birmingham, England, May 2022.

[237] H. P. Paudel, M. Syamlal, S. E. Crawford, Y.-L. Lee, R. A. Shugayev, P. Lu, P. R. Ohodnicki, D. Mollot, and Y. Duan. Quantum computing and simulations for energy applications: Review and perspective. *ACS Engineering Au*, 2(3):151–196, January 2022. doi:10.1021/acsengineeringau.1c00033.

[238] P. J. Ollitrault, A. Miessen, and I. Tavernelli. Molecular quantum dynamics: A quantum computing perspective. *Acc. Chem. Res.*, 54(23):4229–4238, November 2021. doi:10.1021/acs.accounts.1c00514.

[239] H. Liu, G. H. Low, D. S. Steiger, T. Häner, M. Reiher, and M. Troyer. Prospects of quantum computing for molecular sciences. *Mat. Theor.*, 6(1), March 2022. doi:10.1186/s41313-021-00039-z.

[240] M. Motta and J. E. Rice. Emerging quantum computing algorithms for quantum chemistry. *WIREs Comp. Mol. Sci.*, 12(3), December 2021. doi:10.1002/wcms.1580.

[241] P. Benioff. The computer as a physical system: A microscopic quantum mechanical Hamiltonian model of computers as represented by Turing machines. *J. Stat. Phys.*, 22(5):563–591, May 1980. doi:10.1007/bf01011339.

[242] J. Preskill. Quantum computing 40 years later, 2021.

[243] P.W. Shor. Algorithms for quantum computation: discrete logarithms and factoring. In *Proceedings 35th Annual Symposium on Foundations of Computer Science*. IEEE Comput. Soc. Press, 1994. doi:10.1109/sfcs.1994.365700.

[244] D. Deutsch. Quantum theory, the Church–Turing principle and the universal quantum computer. *Proc. Roy. Soc. Lon. A*, 400(1818):97–117, July 1985. doi:10.1098/rspa.1985.0070.

[245] D. Deutsch and R. Jozsa. Rapid solution of problems by quantum computation. *Proc. Roy. Soc. Lon. A*, 439(1907):553–558, December 1992. doi:10.1098/rspa.1992.0167.

[246] E. Knill. Conventions for quantum pseudocode. Technical report, OSTI, June 1996.

[247] D. G. Cory, A. F. Fahmy, and T. F. Havel. Ensemble quantum computing by NMR spectroscopy. *Proc. Nat. Acad. Sci.*, 94(5):1634–1639, March 1997. doi:10.1073/pnas.94.5.1634.

[248] L. M. K. Vandersypen, M. Steffen, G. Breyta, C. S. Yannoni, M. H. Sherwood, and I. L. Chuang. Experimental realization of shor's quantum factoring algorithm using nuclear magnetic resonance. *Nature*, 414(6866):883–887, December 2001. doi:10.1038/414883a.

[249] A. Peruzzo, J. McClean, P. Shadbolt, M.-H. Yung, X.-Q. Zhou, P. J. Love, A. Aspuru-Guzik, and J. L. O'Brien. A variational eigenvalue solver on a photonic quantum processor. *Nat. Commun.*, 5(1), July 2014. doi:10.1038/ncomms5213.

[250] A. Kandala, A. Mezzacapo, K. Temme, M. Takita, M. Brink, J. M. Chow, and J. M. Gambetta. Hardware-efficient variational quantum eigensolver for small molecules and quantum magnets. *Nature*, 549(7671):242–246, September 2017. doi:10.1038/nature23879.

[251] M. S. Anis, H. Abraham, A. Offei, R. Agarwal, G. Agliardi, M. Aharoni, I. Y. Akhalwaya, G. Aleksandrowicz, T. Alexander, and M. Amy et al. Qiskit: An open-source framework for quantum computing, 2021.

[252] S. Pakin and P. Coles. The problem with quantum computers. *Sci. Am.*, June 2019.

[253] Qiskit Team. Investigating quantum hardware using quantum circuits, 2020.

[254] J. Preskill. Quantum computing in the NISQ era and beyond. *Quantum*, 2:79, June 2018. doi:10.22331/q-2018-08-06-79.

[255] B. Nachman, M. Urbanek, W. A. de Jong, and C. W. Bauer. Unfolding quantum computer readout noise. *arXiv*, October 2019.

[256] Y. Zhang, H. Deng, Q. Li, H. Song, and L. Nie. Optimizing quantum programs against decoherence: Delaying qubits into quantum superposition. *2019 International Symposium on Theoretical Aspects of Software Engineering (TASE)*, 2019. doi:10.1109/tase.2019.000-2.

[257] D. McClure. What does the error rate on the ibmq website mean, December 2019.

[258] E. Magesan, J. M. Gambetta, and J. Emerson. Characterizing quantum gates via randomized benchmarking. *Phys. Rev. A*, 85(4), November 2012. doi:10.1103/physreva.85.042311.

[259] A. Asfaw, T. Alexander, P. Nation, and J. Gambetta. Get to the heart of real quantum hardware, February 2020.

[260] J. Gambetta and S. Sheldon. Cramming more power into a quantum device, March 2019.

[261] A. W. Cross, L. S. Bishop, S. Sheldon, P. D. Nation, and J. M. Gambetta. Validating quantum computers using randomized model circuits. *Phys. Rev. A*, 100(3), 2019. doi:10.1103/physreva.100.032328.

[262] D. Gottesman. An introduction to quantum error correction and fault-tolerant quantum computation. *Proceedings of Symposia in Applied Mathematics Quantum Information Science and Its Contributions to Mathematics*, pages 13–58, 2010. doi:10.1090/psapm/068/2762145.

[263] P. Jordan and E. Wigner. Über das paulische Äquivalenzverbot. *Eur. Phys. J. A*, 47 (9-10):631–651, 1928. doi:10.1007/bf01331938.

[264] J. T. Seeley, M. J. Richard, and P. J. Love. The Bravyi-Kitaev transformation for quantum computation of electronic structure. *J. Chem. Phys.*, 137(22):224109, December 2012. doi:10.1063/1.4768229.

[265] S. B. Bravyi and A. Y. Kitaev. Fermionic quantum computation. *Annals of Physics*, 298(1):210–226, May 2002. doi:10.1006/aphy.2002.6254.

[266] S. Mcardle, S. Endo, A. Aspuru-Guzik, S. C. Benjamin, and X. Yuan. Quantum computational chemistry. *Reviews of Modern Physics*, 92(1), 2020.

[267] S. E. Smart and D. A. Mazziotti. Quantum solver of contracted eigenvalue equations for scalable molecular simulations on quantum computing devices. *Phys. Rev. Lett.*, 126(7):070504, February 2021.

[268] J. Tilly, H. Chen, S. Cao, D. Picozzi, K. Setia, Y. Li, E. Grant, L. Wossnig, I. Rungger, G. H. Booth, and J. Tennyson. The variational quantum eigensolver: A review of methods and best practices. *Phys. Rep.*, 986:1–128, November 2022. doi:10.1016/j.physrep.2022.08.003.

[269] S. E. Smart, J.-N. Boyn, and D. A. Mazziotti. Resolving correlated states of benzyne with an error-mitigated contracted quantum eigensolver. *Phys. Rev. A*, 105(2), February 2022.

[270] R. Ma, B. Saxberg, C. Owens, N. Leung, Y. Lu, J. Simon, and D. I. Schuster. A dissipatively stabilized Mott insulator of photons. *Nature*, 566(7742):51–57, 2019. doi:10.1038/s41586-019-0897-9.

[271] A. Wallraff, D. I. Schuster, A. Blais, L. Frunzio, R.-S. Huang, J. Majer, S. Kumar, S. M. Girvin, and R. J. Schoelkopf. Strong coupling of a single photon to a superconducting qubit using circuit quantum electrodynamics. *Nature*, 431(7005):162–167, 2004. doi:10.1038/nature02851.

[272] J. Koch, T. M. Yu, J. Gambetta, A. A. Houck, D. I. Schuster, J. Majer, A. Blais, M. H. Devoret, S. M. Girvin, R. J. Schoelkopf, and et. al. Charge-insensitive qubit design derived from the cooper pair box. *Phys. Rev. A*, 76(4), December 2007. doi:10.1103/PhysRevA.76.042319.

[273] M. Göppl, A. Fragner, M. Baur, R. Bianchetti, S. Filipp, J. M. Fink, P. J. Leek, G. Puebla, L. Steffen, A. Wallraff, and et al. Coplanar waveguide resonators for circuit quantum electrodynamics. *J. Appl. Phys.*, 104(11):113904, 2008. doi:10.1063/1.3010859.

[274] J. M. Chow, A. D. Córcoles, J. M. Gambetta, C. Rigetti, B. R. Johnson, J. A. Smolin, J. R. Rozen, G. A. Keefe, M. B. Rothwell, M. B. Ketchen, and et al. Simple all-microwave entangling gate for fixed-frequency superconducting qubits. *Phys. Rev. Lett.*, 107(8), 2011. doi:10.1103/PhysRevLett.107.080502.

[275] G. Andersson. *Circuit Quantum Electrodynamics with a Transmon Qubit in a 3d Cavity*. Master's Thesis. Walther Meißner Institut, 2015.

[276] H. J. Lipkin, N. Meshkov, and A. J. Glick. Validity of many-body approximation methods for a solvable model: (i.) exact solutions and perturbation theory. *Nucl. Phys. A*, 62:188–198, February 1965. doi:10.1016/0029-5582(65)90862-X.

[277] R. Pérez, M. C. Cambiaggio, and J. P. Vary. T expansion and the Lipkin model. *Phys. Rev. C*, 37:2194–2198, May 1988. doi:10.1103/PhysRevC.37.2194.

[278] J. Stein. Unitary flow of the bosonized large-N Lipkin model. *J. Phys. G Nucl. Part. Phys.*, 26(4):377–385, March 2000. doi:10.1088/0954-3899/26/4/304.

[279] D. A. Mazziotti. Exactness of wave functions from two-body exponential transformations in many-body quantum theory. *Phys. Rev. A*, 69:012507, January 2004. doi:10.1103/PhysRevA.69.012507.

[280] S. E. Smart, D. I. Schuster, and D. A. Mazziotti. Experimental data from a quantum computer verifies the generalized Pauli exclusion principle. *Communications Physics*, 2(1), 2019.

[281] W. Heisenberg. Mehrkörperproblem und resonanz in der quantenmechanik. *Z. Phys.*, 38(6-7):411–426, 1926. doi:10.1007/bf01397160.

[282] P. A. M. Dirac. The physical interpretation of quantum mechanics. *Proc. Roy. Soc. Lond.*, 112:621, 1926.

[283] R. E. Borland and K. Dennis. The conditions on the one-matrix for three-body fermion wavefunctions with one-rank equal to six. *J. Phys. B: At. Mol. Opt. Phys.*, 5(1):7–15, 1972. doi:10.1088/0022-3700/5/1/009.

[284] C. Schilling, D. Gross, and M. Christandl. Pinning of fermionic occupation numbers. *Phys. Rev. Lett.*, 110(4), 2013.

[285] C. L. Benavides-Riveros, J. M. Gracia-Bondía, and M. Springborg. Quasipinning and entanglement in the lithium isoelectronic series. *Phys. Rev. A*, 88(2), 2013. doi:10.1103/PhysRevA.88.022508.

[286] R. Chakraborty and D. A. Mazziotti. Generalized pauli conditions on the spectra of one-electron reduced density matrices of atoms and molecules. *Phys. Rev. A*, 89(4), 2014. doi:10.1103/PhysRevA.89.042505.

[287] M. Walter, D. Gross, and J. Eisert. Multipartite entanglement. *Springer Tr Mod Phys*, pages 293–330, 2016. doi:10.1002/9783527805785.ch14.

[288] D. Bouwmeester, J.-W. Pan, M. Daniell, H. Weinfurter, and A. Zeilinger. Observation of three-photon Greenberger-Horne-Zeilinger entanglement. *Phys. Rev. Lett.*, 82(7): 1345–1349, 1999. doi:10.1103/physrevlett.82.1345.

[289] C. Zhang, Y.-F. Huang, Z. Wang, B.-H. Liu, C.-F. Li, and G.-C. Guo. Experimental Greenberger-Horne-Zeilinger-type six-photon quantum nonlocality. *Phys. Rev. Lett.*, 115(26):260402, 2015. doi:10.1103/PhysRevLett.115.260402.

[290] X.-L. Wang, L.-K. Chen, W. Li, H.-L. Huang, C. Liu, C. Chen, Y.-H. Luo, Z.-E. Su, D. Wu, Z.-D. Li, and et al. Experimental ten-photon entanglement. *Phys. Rev. Lett.*, 117(21):210502, 2016. doi:10.1103/PhysRevLett.117.210502.

[291] C. F. Roos, M. Riebe, H. Häffner, W. Hänsel, J. Benhelm, G. P. T. Lancaster, C. Becher, F. Schmidt-Kaler, and R. Blatt. Control and measurement of three-qubit entangled states. *Science*, 304(5676):1478–1480, 2004. doi:10.1126/science.1097522.

[292] Y. Ji, J. Bian, X. Chen, J. Li, X. Nie, H. Zhou, and X. Peng. Experimental preparation of Greenberger-Horne-Zeilinger states in an Ising spin model by partially suppressing the nonadiabatic transitions. *Phys. Rev. A*, 99(3), 2019. doi:10.1103/physreva.99.032323.

[293] M. Neeley, R. C. Bialczak, M. Lenander, E. Lucero, M. Mariantoni, A. D. O'Connell, D. Sank, H. Wang, M. Weides, J. Wenner, and et al. Generation of three-qubit entangled states using superconducting phase qubits. *Nature*, 467(7315):570–573, 2010. doi:10.1038/nature09418.

[294] L. Dicarlo, M. D. Reed, L. Sun, B. R. Johnson, J. M. Chow, J. M. Gambetta, L. Frunzio, S. M. Girvin, M. H. Devoret, R. J. Schoelkopf, and et al. Preparation and measurement of three-qubit entanglement in a superconducting circuit. *Nature*, 467(7315): 574–578, 2010. doi:10.1038/nature09416.

[295] R. Barends, J. Kelly, A. Megrant, A. Veitia, D. Sank, E. Jeffrey, T. C. White, J. Mutus, A. G. Fowler, B. Campbell, and et al. Superconducting quantum circuits at the surface code threshold for fault tolerance. *Nature*, 508(7497):500–503, 2014. doi:10.1038/nature13171.

[296] D. Cruz, R. Fournier, F. Gremion, A. Jeannerot, K. Komagata, T. Tosic, J. Thiesbrummel, C. L. Chan, N. Macris, M.-A. Dupertuis, and C. Javerzac-Galy. Efficient quantum algorithms for ghz and w states, and implementation on the ibm quantum computer. *Adv. Quantum Technol.*, 2(5-6):1900015, 2019. doi:10.1002/qute.201900015.

[297] M. Treinish and D. M. Rodríguez. GHZ state example. *GitHub*, 2022.

[298] Qiskit. Measurement error mitigation. *Qiskit 0.19.6 Documentation*, June 2020.

[299] Qiskit. Tensored measurement calibration. *Qiskit 0.19.6 Documentation*, June 2020.

[300] I. B. M. Q-Team. IBM-Q-5 Yorktown backend specification v2.0.0, 2019.

[301] I. B. M. Q-Team. IBM-Q-53 Rochester backend specification v1.2.0, 2020.

[302] J. Devore. *Chapter 7: Statistical Intervals Based on a Single Sample*, pages 267–299. Cengage Learning, 8 edition, 2012.

[303] F. Verstraete, J. I. Cirac, and J. I. Latorre. Quantum circuits for strongly correlated quantum systems. *Physical Review A*, 79(3), 2009.

[304] P. Smith-Goodson. Quantum volume: A yardstick to measure the performance of ..., November 2019.

[305] G. J. Mooney, C. D. Hill, and L. C. L. Hollenberg. Entanglement in a 20-qubit superconducting quantum computer. *Scientific Reports*, 9(1), 2019.

[306] H.-L. Huang, D. Wu, D. Fan, and X. Zhu. Superconducting quantum computing: a review. *Science China Information Sciences*, 63(8), 2020.

[307] K. Head-Marsden, J. Flick, C. J. Ciccarino, and P. Narang. Quantum information and algorithms for correlated quantum matter. *Chem. Rev.*, 121(5):3061–3120, March 2021.

[308] S. E. Smart and D. A. Mazziotti. Quantum-classical hybrid algorithm using an error-mitigating N-representability condition to compute the mott metal-insulator transition. *Phys. Rev. A (Coll. Park.)*, 100(2), August 2019.

[309] L. M. Sager and D. A. Mazziotti. Emergent phase of simultaneous fermion and exciton condensations realized. *arXiv*, 2021.

[310] T. Helgaker, P. Jorgensen, and J. Olsen. *Molecular electronic-structure theory*. John Wiley & Sons, Nashville, TN, February 2013.

[311] H. Lischka, D. Nachtigallová, A. J. A. Aquino, P. G. Szalay, F. Plasser, F. B. C. Machado, and M. Barbatti. Multireference approaches for excited states of molecules. *Chem. Rev.*, 118(15):7293–7361, August 2018.

[312] F. A. Evangelista. Perspective: Multireference coupled cluster theories of dynamical electron correlation. *J. Chem. Phys.*, 149(3):030901, 2018. doi:10.1063/1.5039496.

[313] A. Aspuru-Guzik, A. D. Dutoi, P. J. Love, and M. Head-Gordon. Simulated quantum computation of molecular energies. *Science*, 309(5741):1704–1707, September 2005.

[314] S. Lloyd. Universal quantum simulators. *Science*, 273(5278):1073–1078, August 1996.

[315] D. Lu, B. Xu, N. Xu, Z. Li, H. Chen, X. Peng, R. Xu, and J. Du. Quantum chemistry simulation on quantum computers: theories and experiments. *Phys. Chem. Chem. Phys.*, 14:9411–9420, 2012. doi:10.1039/C2CP23700H.

[316] V. E. Elfving, B. W. Broer, M. Webber, J. Gavartin, M. D. Halls, K. P. Lorton, and A. D. Bochevarov. How will quantum computers provide an industrially relevant computational advantage in quantum chemistry? *arXiv*, page 1–20, Sep 2020.

[317] I. L. Chuang and M. A. Nielsen. Prescription for experimental determination of the dynamics of a quantum black box. *J. Mod. Opt.*, 44(11-12):2455–2467, 1997. doi:10.1080/09500349708231894.

[318] E. Knill, D. Leibfried, R. Reichle, J. Britton, R. B. Blakestad, J. D. Jost, C. Langer, R. Ozeri, S. Seidelin, and D. J. Wineland. Randomized benchmarking of quantum gates. *Phys. Rev. A*, 77:012307, Jan 2008. doi:10.1103/PhysRevA.77.012307.

[319] C. H. Baldwin, K. Mayer, N. C. Brown, C. Ryan-Anderson, and D. Hayes. Re-examining the quantum volume test: Ideal distributions, compiler optimizations, confidence intervals, and scalable resource estimations. *Quantum*, 6(707):707, May 2022.

[320] A. W. Cross, L. S. Bishop, S. Sheldon, P. D. Nation, and J. M. Gambetta. Validating quantum computers using randomized model circuits. *Phys. Rev. A*, 100(3), September 2019.

[321] T. Lubinski, S. Johri, P. Varosy, J. Coleman, L. Zhao, J. Necaise, C. H. Baldwin, K. Mayer, and T. Proctor. Application-oriented performance benchmarks for quantum computing, 2021.

[322] T. Proctor, K. Rudinger, K. Young, E. Nielsen, and R. Blume-Kohout. Measuring the capabilities of quantum computers. *Nat. Phys.*, 18(1):75–79, January 2022.

[323] M. Sarovar, T. Proctor, K. Rudinger, K. Young, E. Nielsen, and R. Blume-Kohout. Detecting crosstalk errors in quantum information processors. *Quantum*, 4(321):321, September 2020.

[324] D. A. Mazziotti. Contracted Schrödinger equation: determining quantum energies and two-particle density matrices without wave functions. *Phys. Rev. A*, 57:4219–4234, June 1998. doi:10.1103/PhysRevA.69.012507.

[325] C. Valdemoro, L. M. Tel, E. Pérez-Romero, and D. R. Alcoba. Four new forms of the contracted Schrödinger equation and their connection with the second-order hypervirial condition. *Int. J. Quantum Chem.*, 108(6):1090–1096, 2008. doi:https://doi.org/10.1002/qua.21576.

[326] D. A. Mazziotti. Variational method for solving the contracted Schrödinger equation through a projection of the N-particle power method onto the two-particle space. *J. Chem. Phys.*, 116(4):1239–1249, 2002. doi:10.1063/1.1430257.

[327] D. A. Mazziotti. Multireference many-electron correlation energies from two-electron reduced density matrices computed by solving the anti-Hermitian contracted Schrödinger equation. *Phys. Rev. A*, 76:052502, Nov 2007. doi:10.1103/PhysRevA.76.052502.

[328] D. A. Mazziotti. Anti-Hermitian part of the contracted Schrödinger equation for the direct calculation of two-electron reduced density matrices. *Phys. Rev. A*, 75:022505, Feb 2007. doi:10.1103/PhysRevA.75.022505.

[329] A. E. Rothman, J. J. Foley, and D. A. Mazziotti. Open-shell energies and two-electron reduced density matrices from the anti-Hermitian contracted Schrödinger equation: A spin-coupled approach. *Phys. Rev. A*, 80:052508, Nov 2009. doi:10.1103/PhysRevA.80.052508.

[330] G. Gidofalvi and D. A. Mazziotti. Direct calculation of excited-state electronic energies and two-electron reduced density matrices from the anti-hermitian contracted schrödinger equation. *Phys. Rev. A*, 80:022507, Aug 2009. doi:10.1103/PhysRevA.80.022507.

[331] A M Sand and D A Mazziotti. Enhanced computational efficiency in the direct determination of the two-electron reduced density matrix from the anti-hermitian contracted schrödinger equation with application to ground and excited states of conjugated π-systems. *J. Chem. Phys.*, 143(13):134110, October 2015.

[332] S. E. Smart, P. G. Scrape, L. J. Butler, and D. A. Mazziotti. Using reduced density matrix techniques to capture static and dynamic correlation in the energy landscape for the decomposition of the CH_2CH_2ONO radical and support a non-IRC pathway. *J. Chem. Phys.*, 149(2):024302, 2018. doi:10.1063/1.5024512.

[333] A. W. Schlimgen and D. A. Mazziotti. Static and dynamic electron correlation in the ligand noninnocent oxidation of nickel dithiolates. *J. Phys. Chem. A*, 121(48): 9377–9384, December 2017.

[334] E. J. Sturm and D. A. Mazziotti. Highly accurate excited-state energies from direct computation of the 2-electron reduced density matrix by the anti-Hermitian contracted Schrödinger equation. *Mol. Phys.*, pages 1–9, September 2015.

[335] J. W. Snyder Jr. and D. A. Mazziotti. Photoexcited tautomerization of vinyl alcohol to acetylaldehydevia a conical intersection from contracted Schrödinger theory. *Phys. Chem. Chem. Phys.*, 14:1660–1667, 2012. doi:10.1039/C2CP23065H.

[336] J. W. Snyder and D. A. Mazziotti. Photoexcited conversion of gauche-1,3-butadiene to bicyclobutane via a conical intersection: Energies and reduced density matrices from the anti-Hermitian contracted Schrödinger equation. *J. Chem. Phys.*, 135(2):024107, 2011. doi:10.1063/1.3606466.

[337] L. Greenman and D. A. Mazziotti. Balancing single- and multi-reference correlation in the chemiluminescent reaction of dioxetanone using the anti-Hermitian contracted Schrödinger equation. *J. Chem. Phys.*, 134(17):174110, 2011. doi:10.1063/1.3585691.

[338] J W Snyder, Jr, A E Rothman, J J Foley, 4th, and D A Mazziotti. Conical intersections in triplet excited states of methylene from the anti-hermitian contracted schrödinger equation. *J. Chem. Phys.*, 132(15):154109, April 2010.

[339] N. D. Jansen, M. Loucks, S. Gilbert, C. Fleming-Dittenber, J. Egbert, and K. L. C. Hunt. Shannon and von neumann entropies of multi-qubit schrödinger's cat states. *Phys. Chem. Chem. Phys.*, 24(13):7666–7681, March 2022.

[340] IBM. IBM Quantum Experience, 2022.

[341] V. L. Ginzburg. High-temperature superconductivity (history and general review). *Sov. Phys. Usp.*, 34(4):283–288, apr 1991. doi:10.1070/pu1991v034n04abeh002361.

[342] A. Glatz, I. A. Sadovskyy, U. Welp, W.-K. Kwok, and G. W. Crabtree. The quest for high critical current in applied high-temperature superconductors. *J. Supercond. Nov. Magn.*, 33:127–141, 2020.

[343] Y. Cao, V. Fatemi, S. Fang, K. Watanabe, T. Taniguchi, E. Kaxiras, and P. Jarillo-Herrero. Unconventional superconductivity in magic-angle graphene superlattices. *Nature*, 556(7699):43–50, 2018. doi:10.1038/nature26160.

[344] Y. Cao, D. Rodan-Legrain, O. Rubies-Bigorda, J. Min Park, K. Watanabe, T. Taniguchi, and P. Jarillo-Herrero. Tunable correlated states and spin-polarized phases in twisted bilayer–bilayer graphene. *Nature*, 583(7815):215–220, 2020. doi:10.1038/s41586-020-2260-6.

[345] A. Uri, S. Grover, Y. Cao, J. Crosse, K. Bagani, D. Rodan-Legrain, Y. Myasoedov, K. Watanabe, T. Taniguchi, P. Moon, and et al. Mapping the twist-angle disorder and Landau levels in magic-angle graphene. *Nature*, 581(7806):47–52, 2020. doi:10.1038/s41586-020-2255-3.

[346] R. P. Feynman. *Chapter II Application of Quantum Mechanics to Liquid Helium*, volume 1 of *Progress in Low Temperature Physics*. Elsevier, 1955.

[347] A. J. Leggett. Superfluidity. *Rev. Mod. Phys.*, 71:S318–S323, Mar 1999. doi:10.1103/RevModPhys.71.S318.

[348] C.J. Gorter. *Progress in Low Temperature Physics*. Elsevier Science, 2011. ISBN 9780080872988.

[349] Y. Guo, R. Dubessy, M. de Herve, A. Kumar, T. Badr, A. Perrin, L. Longchambon, and H. Perrin. Supersonic rotation of a superfluid: A long-lived dynamical ring. *Phys. Rev. Lett.*, 124:025301, Jan 2020. doi:10.1103/PhysRevLett.124.025301.

[350] Y. Hao, S. Pang, X. Zhang, and L. Jiang. Quantum-confined superfluid reactions. *Chem. Sci.*, 11:10035–10046, 2020. doi:10.1039/D0SC03574B.

[351] G. Del Pace, W. J. Kwon, M. Zaccanti, G. Roati, and F. Scazza. Tunneling transport of unitary fermions across the superfluid transition. *Phys. Rev. Lett.*, 126:055301, Feb 2021. doi:10.1103/PhysRevLett.126.055301.

[352] P. Roushan, C. Neill, J. Tangpanitanon, V. M. Bastidas, A. Megrant, R. Barends, Y. Chen, Z. Chen, B. Chiaro, A. Dunsworth, A. Fowler, B. Foxen, M. Giustina, E. Jeffrey, J. Kelly, E. Lucero, J. Mutus, M. Neeley, C. Quintana, D. Sank, A. Vainsencher, J. Wenner, T. White, H. Neven, D. G. Angelakis, and J. Martinis. Spectroscopic signatures of localization with interacting photons in superconducting qubits. *Science*, 358(6367):1175–1179, 2017. ISSN 0036-8075. doi:10.1126/science.aao1401.

[353] K. Head-Marsden, J. Flick, C. J. Ciccarino, and P. Narang. Quantum information and algorithms for correlated quantum matter. *Chem. Rev.*, 2021. doi:10.1021/acs.chemrev.0c00620.

[354] S. E. Smart and D. A. Mazziotti. Quantum-classical hybrid algorithm using an error-mitigating N-representability condition to compute the Mott metal-insulator transition. *Phys. Rev. A*, 100(2), aug 2019. doi:10.1103/physreva.100.022517.

[355] K. Bharti, A. Cervera-Lierta, T. H. Kyaw, T. Haug, S. Alperin-Lea, A. Anand, M. Degroote, H. Heimonen, J. S. Kottmann, T. Menke, W.-K. Mok, S. Sim, L.-C. Kwek, and A. Aspuru-Guzik. Noisy intermediate-scale quantum (NISQ) algorithms. *arXiv*, Jan 2021.

[356] F. Arute, K. Arya, R. Babbush, D. Bacon, J. C. Bardin, R. Barends, R. Biswas, S. Boixo, F. G. S. L. Brandao, D. A. Buell, and et al. Quantum supremacy using a programmable superconducting processor. *Nature*, 574(7779):505–510, 2019.

[357] Y. Wu, W.-S. Bao, S. Cao, F. Chen, M.-C. Chen, X. Chen, T.-H. Chung, H. Deng, Y. Du, D. Fan, M. Gong, C. Guo, C. Guo, S. Guo, L. Han, L. Hong, H.-L. Huang, Y.-H. Huo, L. Li, N. Li, S. Li, Y. Li, F. Liang, C. Lin, J. Lin, H. Qian, D. Qiao, H. Rong, H. Su, L. Sun, L. Wang, S. Wang, D. Wu, Y. Xu, K. Yan, W. Yang, Y. Yang, Y. Ye, J. Yin, C. Ying, J. Yu, C. Zha, C. Zhang, H. Zhang, K. Zhang, Y. Zhang, H. Zhao, Y. Zhao, L. Zhou, Q. Zhu, C.-Y. Lu, C.-Z. Peng, X. Zhu, and J.-W. Pan. Strong quantum computational advantage using a superconducting quantum processor. *arXiv*, Jun 2021.

[358] A. J. Coleman. Electron pairs in the quasichemical-equilibrium and Bardeen-Cooper-Schrieffer theories. *Phys. Rev. Lett.*, 13:406–407, Sep 1964. doi:10.1103/PhysRevLett.13.406.

[359] A. Raeber and D. A. Mazziotti. Large eigenvalue of the cumulant part of the two-electron reduced density matrix as a measure of off-diagonal long-range order. *Phys. Rev. A*, 92(5):052502, 2015. doi:10.1103/physreva.92.052502.

[360] J. M. Blatt. *Theory of superconductivity*. Academic Press Inc., 1964.

[361] F. Bloch. Off-diagonal long-range order and persistent currents in a hollow cylinder. *Phys. Rev.*, 137(3A), 1965.

[362] A. Khamoshi, F. A. Evangelista, and G. E. Scuseria. Correlating AGP on a quantum computer. *Quantum Sci. Technol.*, 6(1):014004, 2021.

[363] A. J. Coleman. The structure of fermion density matrices. III. Long-range order. *J. Low. Temp. Phys.*, 74(1-2):1–17, 1989. doi:10.1007/bf00681750.

[364] K. Head-Marsden and D. A. Mazziotti. Pair 2-electron reduced density matrix theory using localized orbitals. *J. Chem. Phys.*, 147(8):084101, 2017.

[365] W. Poelmans, M. Van Raemdonck, B. Verstichel, S. De Baerdemacker, A. Torre, L. Lain, G. E. Massaccesi, D. R. Alcoba, P. Bultinck, and D. Van Neck. Variational optimization of the second-order density matrix corresponding to a seniority-zero configuration interaction wave function. *J. Chem. Theory Comput.*, 11(9):4064–4076, 2015.

[366] O. Klein. Quelques remarques sur le traitement approximatif du problème des électrons dans un réseau cristallin par la mecanique quantique. *J. Phys. Radium*, 9(1):1–12, 1938.

[367] T. Keilmann and J. J. García-Ripoll. Dynamical creation of bosonic Cooper-like pairs. *Phys. Rev. Lett.*, 100:110406, Mar 2008.

[368] L.-A. Wu and D. A. Lidar. Qubits as parafermions. *J. Math. Phys.*, 43(9):4506–4525, 2002.

[369] D. A. Mazziotti and A. R. Mazziotti. Quantum simulation of molecules without fermionic encoding of the wave function. *arXiv*, Jan 2021.

[370] K. Naftchi-Ardebili, N. W. Hau, and D. A. Mazziotti. Rank restriction for the variational calculation of two-electron reduced density matrices of many-electron atoms and molecules. *Phys. Rev. A*, 84:052506, Nov 2011. doi:10.1103/PhysRevA.84.052506.

[371] M.A. Nielsen and I.L. Chuang. *Quantum Computation and Quantum Information*. Cambridge University Press, 2010. ISBN 9781139495486.

[372] A. Asfaw, A. Corcoles, L. Bello, Y. Ben-Haim, M. Bozzo-Rey, S. Bravyi, N. Bronn, L. Capelluto, A. Carrera Vazquez, J. Ceroni, R. Chen, A. Frisch, J. Gambetta, S. Garion, L. Gil, S. De La Puente Gonzalez, F. Harkins, T. Imamichi, H. Kang, A. H. Karamlou, R. Loredo, D. McKay, A. Mezzacapo, Z. Minev, R. Movassagh, G. Nannicini, P. Nation, A. Phan, M. Pistoia, A. Rattew, J. Schaefer, J. Shabani, J. Smolin, J. Stenger, K. Temme, M. Tod, S. Wood, and J. Wootton. Multiple qubits and entangled states. In *Learn Quantum Computation Using Qiskit*, chapter 2.2. Qiskit, 2020.

[373] IBM-Q-Team. Ibm quantum simulators, 2023.

[374] Isaac L. Chuang. *Distance measures for quantum information*, page 399–424. Cambridge University Press, 2010.

[375] F. P. Laussy, T. Taylor, I. A. Shelykh, and A. V. Kavokin. Superconductivity with excitons and polaritons: Review and extension. *J. Nanophotonics*, 6(1):1–22, 2012. doi:10.1117/1.JNP.6.064502.full.

[376] P. Skopelitis, E. D. Cherotchenko, A. V. Kavokin, and A. Posazhennikova. Interplay of phonon and exciton-mediated superconductivity in hybrid semiconductor-superconductor structures. *Phys. Rev. Lett.*, 120:107001, March 2018. doi:10.1103/PhysRevLett.120.107001.

[377] maple. Maple, 2019.

[378] P. E. Gill, W. Murray, and M. A. Saunders. SNOPT: An SQP algorithm for large-scale constrained optimization. *SIAM Rev.*, 47(1):99–131, 2005. doi:10.1137/S0036144504446096.

[379] B. Fornberg. Calculation of weights in finite difference formulas. *SIAM Rev.*, 40(3): 685–691, 1998.

[380] Christine A. Schwerdtfeger and David A. Mazziotti. Convex-set description of quantum phase transitions in the transverse ising model using reduced-density-matrix theory. *J. Chem. Phys.*, 130(22):224102, 2009. doi:10.1063/1.3143403.

[381] Gergely Gidofalvi and David A. Mazziotti. Computation of quantum phase transitions by reduced-density-matrix mechanics. *Phys. Rev. A*, 74(1), May 2006. doi:10.1103/physreva.74.012501.

[382] V. Zauner, D. Draxler, L. Vanderstraeten, J. Haegeman, and F. Verstraete. Symmetry breaking and the geometry of reduced density matrices. *New J. Phys.*, 18(11):113033, 2016. doi:10.1088/1367-2630/18/11/113033.

[383] R. W. Richardson. Exact eigenstates of the pairing-force Hamiltonian. ii. *J. Math. Phys.*, 6:1034–1051, July 1965. doi:10.1063/1.1704367.

[384] K.M. Rabe and U.V. Waghmare. First-principles model hamiltonians for ferroelectric phase transitions. *Ferroelectrics*, 151(1):59–68, 1994. doi:10.1080/00150199408244723.

[385] M. Ostilli and C. Presilla. The exact ground state for a class of matrix hamiltonian models: Quantum phase transition and universality in the thermodynamic limit. *J. Stat. Mech. Theory Exp.*, 11, 2006. doi:10.1088/1742-5468/2006/11/P11012. cited By 5.

[386] D. Debnath, M.Z. Malik, and A. Chatterjee. A semi exact solution for a metallic phase in a holstein-hubbard chain at half filling with gaussian anharmonic phonons. *Sci. Rep.*, 11(1), 2021. doi:10.1038/s41598-021-91604-6. cited By 0.

[387] M.-L. Cai, Z.-D. Liu, W.-D. Zhao, Y.-K. Wu, Q.-X. Mei, Y. Jiang, L. He, X. Zhang, Z.-C. Zhou, and L.-M. Duan. Observation of a quantum phase transition in the quantum rabi model with a single trapped ion. *Nat. Commun.*, 12(1), 2021. doi:10.1038/s41467-021-21425-8. cited By 1.

[388] C. Farías and S. Davis. Multiple metastable states in an off-lattice potts model. *Physica A*, 581, 2021. doi:10.1016/j.physa.2021.126215. cited By 0.

[389] R.W. Richardson. A restricted class of exact eigenstates of the pairing-force Hamiltonian. *Phys. Lett.*, 3(6):277–279, 1963. ISSN 0031-9163. doi:https://doi.org/10.1016/0031-9163(63)90259-2.

[390] R.W. Richardson. Application to the exact theory of the pairing model to some even isotopes of lead. *Phys. Lett. A*, 5(1):82–84, 1963. doi:10.1016/s0375-9601(63)80039-0. cited By 80.

[391] R.W. Richardson and N. Sherman. Exact eigenstates of the pairing-force Hamiltonian. *Nucl. Phys.*, 52(C):221–238, 1964. doi:10.1016/0029-5582(64)90687-X. cited By 366.

[392] S. Korenblit, D. Kafri, W.C. Campbell, R. Islam, E.E. Edwards, Z.-X. Gong, G.-D. Lin, L.-M. Duan, J. Kim, K. Kim, and C. Monroe. Quantum simulation of spin models on an arbitrary lattice with trapped ions. *New J. Phys.*, 14, 2012. doi:10.1088/1367-2630/14/9/095024. cited By 77.

[393] J J Hernández-Sarria, A Argüelles, and K Rodríguez. Quantum magnetism in spin-3/2 chains. *J. Phys.: Conf. Ser.*, 614:012005, jul 2015. doi:10.1088/1742-6596/614/1/012005.

[394] D.J.J. Farnell, R.F. Bishop, and J. Richter. Non-coplanar model states in quantum magnetism applications of the high-order coupled cluster method. *J. Stat. Phys.*, 176 (1):180–213, 2019. doi:10.1007/s10955-019-02297-1. cited By 0.

[395] M. Środa, E. Dagotto, and J. Herbrych. Quantum magnetism of iron-based ladders: Blocks, spirals, and spin flux. *Phys. Rev. B*, 104(4), 2021. doi:10.1103/PhysRevB.104.045128. cited By 0.

[396] N. Debergh and F. L. Stancu. On the exact solutions of the lipkin-meshkov-glick model. *Journal of Physics A: Mathematical and General*, 34(15):3265–3276, apr 2001. doi:10.1088/0305-4470/34/15/305.

[397] W. D. Heiss. On the thermodynamic limit of the lipkin model. *Journal of Physics A: Mathematical and General*, 39(32):10081–10086, jul 2006. doi:10.1088/0305-4470/39/32/s10.

[398] O. Castaños, R. López-Peña, J. G. Hirsch, and E. López-Moreno. Classical and quantum phase transitions in the Lipkin-Meshkov-Glick model. *Phys. Rev. B*, 74:104118, September 2006. doi:10.1103/PhysRevB.74.104118.

[399] G. Co' and S. De Leo. Analytical and numerical analysis of the complete Lipkin–Meshkov–Glick Hamiltonian. *Int. J. Mod. Phys. E*, 27(05):1850039, 2018. doi:10.1142/S0218301318500398.

[400] J. Cioslowski, R. Erdahl, and B. Jin. *On Calculating Approximate and Exact Density Matrices*. Kluwer Academic/Plenum Publishers, 2000.

[401] R. Xia, T. Bian, and S. Kais. Electronic structure calculations and the Ising Hamiltonian. *J. Phys. Chem. B*, 122(13):3384–3395, 2018. doi:10.1021/acs.jpcb.7b10371. PMID: 29099600.

[402] A. Chu, J. Will, J. Arlt, C. Klempt, and A.M. Rey. Simulation of xxz spin models using sideband transitions in trapped bosonic gases. *Phys. Rev. Lett.*, 125(24), 2020. doi:10.1103/PhysRevLett.125.240504. cited By 2.

[403] A. Khamoshi, F.A. Evangelista, and G.E. Scuseria. Correlating AGP on a quantum computer. *Quantum Sci. Technol.*, 6(1), 2021. doi:10.1088/2058-9565/abc1bb. cited By 5.

[404] Z.-X. Hu, Z. Papić, S. Johri, R.N. Bhatt, and P. Schmitteckert. Comparison of the density-matrix renormalization group method applied to fractional quantum hall systems in different geometries. *Phys. Lett., Sec. A*, 376(30-31):2157–2161, 2012. doi:10.1016/j.physleta.2012.05.031. cited By 19.

[405] H. Zheng, H. J. Changlani, K. T. Williams, B. Busemeyer, and L. K. Wagner. From real materials to model hamiltonians with density matrix downfolding. *Front. Phys.*, 6:43, 2018. ISSN 2296-424X. doi:10.3389/fphy.2018.00043.

[406] M.K. Al-Sugheir, M.A. Awawdeh, H.B. Ghassib, and E. Alhami. Bose-einstein condensation in one-dimensional optical lattices: Bogoliubov's approximation and beyond. *Can. J. Phys.*, 94(7):697–703, 2016. doi:10.1139/cjp-2016-0019. cited By 0.

[407] J. von Delft, A. D. Zaikin, D. S. Golubev, and W. Tichy. Parity-affected superconductivity in ultrasmall metallic grains. *Phys. Rev. Lett.*, 77:3189–3192, Oct 1996. doi:10.1103/PhysRevLett.77.3189.

[408] M. Degroote, T. M. Henderson, J. Zhao, J. Dukelsky, and G. E. Scuseria. Polynomial similarity transformation theory: A smooth interpolation between coupled cluster doubles and projected BCS applied to the reduced BCS Hamiltonian. *Phys. Rev. B*, 93: 125124, Mar 2016. doi:10.1103/PhysRevB.93.125124.

[409] S. Pannir-Sivajothi, J. Campos-Gonzalez-Angulo, L. Martínez-Martínez, S. Sinha, and J. Yuen-Zhou. Driving chemical reactions with polariton condensates. *arXiv*, 2021. doi:10.21203/rs.3.rs-653808/v1.

[410] A. O. Schouten, L. M. Sager, and D. A. Mazziotti. Exciton condensation in molecular-scale van der Waals stacks. *J. Phys. Chem. Lett.*, 12(40):9906–9911, 2021. doi:10.1021/acs.jpclett.1c02368. PMID: 34612652.

[411] M.C. Cambiaggio and A. Plastino. Quasi spin pairing and the structure of the lipkin model. *Z. Phys., A At. nucl.*, 288(2):153–159, 1978. doi:10.1007/BF01408644. cited By 21.

[412] F. Pennini and A. Plastino. Complexity and disequilibrium as telltales of superconductivity. *Physica A*, 506:828–834, 2018. doi:10.1016/j.physa.2018.05.003. cited By 4.

[413] A. R. Plastino, G. L. Ferri, and A. Plastino. Interaction between different kinds of quantum phase transitions. *Quantum Rep.*, 3(2):253–261, 2021. ISSN 2624-960X. doi:10.3390/quantum3020015.

[414] P. Ring and P. Schuck. *The nuclear many-body problem*. Springer, 2004.

[415] M.C. Cambiaggio, A.M.F. Rivas, and M. Saraceno. Integrability of the pairing Hamiltonian. *Nucl. Phys. A*, 624(2):157–167, 1997. doi:10.1016/s0375-9474(97)00418-1.

[416] P. Van Isacker and K. Heyde. Exactly solvable models of nuclei. *Scholarpedia*, 9(2): 31279, 2014. doi:10.4249/scholarpedia.31279. revision #143319.

[417] M. Buzzi, D. Nicoletti, M. Fechner, N. Tancogne-Dejean, M. A. Sentef, A. Georges, T. Biesner, E. Uykur, M. Dressel, A. Henderson, T. Siegrist, J. A. Schlueter, K. Miyagawa, K. Kanoda, M.-S. Nam, A. Ardavan, J. Coulthard, J. Tindall, F. Schlawin, D. Jaksch, and A. Cavalleri. Photomolecular high-temperature superconductivity. *Phys. Rev. X*, 10:031028, Aug 2020. doi:10.1103/PhysRevX.10.031028.

[418] H. Liu, Y. Zong, P. Wang, H. Wen, H. Wu, J. Xia, and Z. Wei. Excitons in two-dimensional van der waals heterostructures. *J. Phys. D Appl. Phys.*, 54(5):053001, nov 2020. doi:10.1088/1361-6463/abbf75.

[419] H. M. Bretscher, P. Andrich, Y. Murakami, D. Golež, B. Remez, P. Telang, A. Singh, L. Harnagea, N. R. Cooper, A. J. Millis, P. Werner, A. K. Sood, and A. Rao. Imaging the coherent propagation of collective modes in the excitonic insulator Ta_2NiSe_5 at room temperature. *Sci. Adv.*, 7(28), 2021. doi:10.1126/sciadv.abd6147.

[420] Y. Jiang, S. Chen, W. Zheng, B. Zheng, and A. Pan. Interlayer exciton formation, relaxation, and transport in tmd van der waals heterostructures. *Light Sci. Appl.*, 10 (1), 2021. doi:10.1038/s41377-021-00500-1.

[421] A. Khamoshi, F. A. Evangelista, and G. E. Scuseria. Correlating AGP on a quantum computer. *Quantum Sci. Technol*, 6(1):014004, nov 2020. doi:10.1088/2058-9565/abc1bb.

[422] E. Alpaydin. *Introduction to Machine Learning*. Adaptive Computation and Machine Learning. MIT Press, Cambridge, MA, 3 edition, 2014. ISBN 978-0-262-02818-9.

[423] A. Burkov. *The hundred-page machine learning book*. A. Burkov, January 2019.

[424] Aurelien Geron. *Hands-on machine learning with scikit-learn, keras, and TensorFlow*. O'Reilly Media, Sebastopol, CA, 2 edition, October 2019.

[425] J. A. Keith, V. Vassilev-Galindo, B. Cheng, S. Chmiela, M. Gastegger, K.-R. Müller, and A. Tkatchenko. Combining machine learning and computational chemistry for predictive insights into chemical systems. *Chem. Rev.*, 121(16):9816–9872, July 2021. doi:10.1021/acs.chemrev.1c00107.

[426] M. Meuwly. Machine learning for chemical reactions. *Chem. Rev.*, 121(16):10218–10239, June 2021. doi:10.1021/acs.chemrev.1c00033.

[427] T. F. G. G. Cova and A. A. C. C. Pais. Deep learning for deep chemistry: Optimizing the prediction of chemical patterns. *Front. Chem.*, 7, November 2019. doi:10.3389/fchem.2019.00809.

[428] A. Karthikeyan and U. D. Priyakumar. Artificial intelligence: machine learning for chemical sciences. *J. Chem. Sci.*, 134(1), December 2021. doi:10.1007/s12039-021-01995-2.

[429] Wolfram. Convolution, 2023.

[430] S H Sureshbabu, M Sajjan, S Oh, and S Kais. Implementation of quantum machine learning for electronic structure calculations of periodic systems on quantum computing devices. *J. Chem. Inf. Model.*, 61(6):2667–2674, June 2021.

[431] Artem Borin and Dmitry A. Abanin. Approximating power of machine-learning ansatz for quantum many-body states. *Phys. Rev. B*, 101:195141, May 2020. doi:10.1103/PhysRevB.101.195141.

[432] Torlai, G. *Augmenting Quantum Mechanics with Artificial Intelligence*. PhD thesis, University of Waterloo, 2018.

[433] K Ch'ng, J Carrasquilla, R G Melko, and E Khatami. Machine learning phases of strongly correlated fermions. *Phys. Rev. X*, 7:031038, Aug 2017. doi:10.1103/PhysRevX.7.031038.

[434] J. Behler and M. Parrinello. Generalized neural-network representation of high-dimensional potential-energy surfaces. *Phys. Rev. Lett.*, 98:146401, Apr 2007. doi:10.1103/PhysRevLett.98.146401.

[435] B. J. Braams and J. M. Bowman. Permutationally invariant potential energy surfaces in high dimensionality. *Int. Rev. Phys. Chem.*, 28(4):577–606, October 2009. doi:10.1080/01442350903234923.

[436] A. P. Bartók, M. C. Payne, R. Kondor, and G. Csányi. Gaussian approximation potentials: The accuracy of quantum mechanics, without the electrons. *Phys. Rev. Lett.*, 104:136403, Apr 2010. doi:10.1103/PhysRevLett.104.136403.

[437] J. S. Smith, O. Isayev, and A. E. Roitberg. ANI-1: an extensible neural network potential with DFT accuracy at force field computational cost. *Chem. Sci.*, 8(4): 3192–3203, 2017. doi:10.1039/c6sc05720a.

[438] E. V. Podryabinkin and A. V. Shapeev. Active learning of linearly parametrized interatomic potentials. *Comp. Mat. Sci.*, 140:171–180, December 2017. doi:10.1016/j.commatsci.2017.08.031.

[439] E. V. Podryabinkin, E. V. Tikhonov, A. V. Shapeev, and A. R. Oganov. Accelerating crystal structure prediction by machine-learning interatomic potentials with active learning. *Phys. Rev. B*, 99:064114, Feb 2019. doi:10.1103/PhysRevB.99.064114.

[440] S. Chmiela, A. Tkatchenko, H. E. Sauceda, I. Poltavsky, K. T. Schütt, and K.-R. Müller. Machine learning of accurate energy-conserving molecular force fields. *Sci. Adv.*, 3(5), May 2017. doi:10.1126/sciadv.1603015.

[441] S. Chmiela, H. E. Sauceda, K.-R. Müller, and A. Tkatchenko. Towards exact molecular dynamics simulations with machine-learned force fields. *Nat. Commun.*, 9(1), September 2018. doi:10.1038/s41467-018-06169-2.

[442] F Brockherde, L Vogt, L Li, M E Tuckerman, K Burke, and K-R Müller. Bypassing the Kohn-Sham equations with machine learning. *Nat. Commun.*, 8(1):872, October 2017.

[443] J. C. Snyder, M. Rupp, K. Hansen, K.-R. Müller, and K. Burke. Finding density functionals with machine learning. *Phys. Rev. Lett.*, 108:253002, Jun 2012. doi:10.1103/PhysRevLett.108.253002.

[444] J Gedeon, J Schmidt, M J P Hodgson, J Wetherell, C L Benavides-Riveros, and M A L Marques. Machine learning the derivative discontinuity of density-functional theory. *Mach. Learn.: Sci. Technol.*, 3(1):015011, March 2022.

[445] K. Ryczko, D. A. Strubbe, and I. Tamblyn. Deep learning and density-functional theory. *Phys. Rev. A*, 100(2), aug 2019. doi:10.1103/physreva.100.022512.

[446] D. M. Wilkins, A. Grisafi, Y. Yang, K. U. Lao, R. A. DiStasio, and M. Ceriotti. Accurate molecular polarizabilities with coupled cluster theory and machine learning. *PNAS*, 116(9):3401–3406, February 2019. doi:10.1073/pnas.1816132116.

[447] M. Gastegger, J. Behler, and P. Marquetand. Machine learning molecular dynamics for the simulation of infrared spectra. *Chem. Sci.*, 8(10):6924–6935, 2017. doi:10.1039/c7sc02267k.

[448] J. R. Kitchin. Machine learning in catalysis. *Nat. Cat.*, 1(4):230–232, April 2018. doi:10.1038/s41929-018-0056-y.

[449] B. Maryasin, P. Marquetand, and N. Maulide. Machine learning for organic synthesis: Are robots replacing chemists? *Angew. Chem. Int. Ed.*, 57(24):6978–6980, April 2018. doi:10.1002/anie.201803562.

[450] H. Li, C. Collins, M. Tanha, G. J. Gordon, and D. J. Yaron. A density functional tight binding layer for deep learning of chemical hamiltonians. *J. Chem. Theor. Comp.*, 14 (11):5764–5776, October 2018. doi:10.1021/acs.jctc.8b00873.

[451] M. Welborn, L. Cheng, and T. F. Miller. Transferability in machine learning for electronic structure via the molecular orbital basis. *J. Chem. Theor. Comp.*, 14(9): 4772–4779, July 2018. doi:10.1021/acs.jctc.8b00636.

[452] L. Cheng, M. Welborn, A. S. Christensen, and T. F. Miller. A universal density matrix functional from molecular orbital-based machine learning: Transferability across organic molecules. *J. Chem. Phys.*, 150(13):131103, April 2019. doi:10.1063/1.5088393.

[453] M. Sugawara. Numerical solution of the Schrödinger equation by neural network and genetic algorithm. *Comp. Phys. Commun.*, 140(3):366–380, November 2001. doi:10.1016/s0010-4655(01)00286-7.

[454] S. Manzhos and T. Carrington. An improved neural network method for solving the schrödinger equation. *Can. J. Chem.*, 87(7):864–871, July 2009. doi:10.1139/v09-025.

[455] G Carleo and M Troyer. Solving the quantum many-body problem with artificial neural networks. *Science*, 355(6325):602–606, February 2017.

[456] K. T. Schütt, M. Gastegger, A. Tkatchenko, K.-R. Müller, and R. J. Maurer. Unifying machine learning and quantum chemistry with a deep neural network for molecular wavefunctions. *Nat. Commun.*, 10(1), November 2019. doi:10.1038/s41467-019-12875-2.

[457] P J Knowles and N C Handy. Unlimited full configuration interaction calculations. *J. Chem. Phys.*, 91(4):2396–2398, August 1989.

[458] F Jensen. *Introduction to computational chemistry*. John Wiley & Sons, Nashville, TN, 3 edition, February 2017.

[459] C W Bauschlicher, Jr, S R Langhoff, and P R Taylor. Accurate quantum chemical calculations. In *Advances in Chemical Physics*, Advances in chemical physics, pages 103–161. John Wiley & Sons, Inc., Hoboken, NJ, USA, March 2007.

[460] P G Mezey, M G Papadopoulos, R Zalesny, and J Leszczynski, editors. *Linear-scaling techniques in computational chemistry and physics*. Challenges and Advances in Computational Chemistry and Physics. Springer, Dordrecht, Netherlands, 2011 edition, March 2011.

[461] M. Sajjan, J. Li, R. Selvarajan, S. H. Sureshbabu, S. S. Kale, R. Gupta, V. Singh, and S. Kais. Quantum machine learning for chemistry and physics. *Chem. Soc. Rev.*, page Online, 2022. doi:10.1039/D2CS00203E.

[462] K. Mills, M. Spanner, and I. Tamblyn. Deep learning and the Schrödinger equation. *Phys. Rev. A*, 96:042113, Oct 2017. doi:10.1103/PhysRevA.96.042113.

[463] X Wang, A. Kumar, C. R. Shelton, and B. M. Wong. Harnessing deep neural networks to solve inverse problems in quantum dynamics: machine-learned predictions of time-dependent optimal control fields. *Phys. Chem. Chem. Phys.*, 22:22889, 2020. doi:10.1039/D0CP03694C.

[464] A J Coleman and V I Yukalov. *Reduced Density Matrices*. Lecture Notes in Chemistry. Springer, Berlin, Germany, 2000 edition, April 2000.

[465] D Ter Haar. Theory and applications of the density matrix. *Rep. Prog. Phys.*, 24(1): 304–362, January 1961.

[466] N. Shenvi and A. F. Izmaylov. Active-space N-representability constraints for variational two-particle reduced density matrix calculations. *Phys. Rev. Lett.*, 105:213003, Nov 2010. doi:10.1103/PhysRevLett.105.213003.

[467] C Garrod and J K Percus. Reduction of the N-particle variational problem. *J. Math. Phys.*, 5(12):1756–1776, December 1964.

[468] R M Erdahl. Representability. *Int. J. Quantum Chem.*, 13(6):697–718, June 1978.

[469] R M Erdahl. Two algorithms for the lower bound method of reduced density matrix theory. *Rep. math. phys.*, 15(2):147–162, April 1979.

[470] R Erdahl and V H Smith, editors. *Density matrices and density functionals*. Springer, Dordrecht, Netherlands, September 2011.

[471] D. A. Mazziotti. Comparison of contracted schrödinger and coupled-cluster theories. *Phys. Rev. A*, 60:4396–4408, Dec 1999. doi:10.1103/PhysRevA.60.4396.

[472] R M Erdahl and B Jin. The lower bound method for reduced density matrices. *Theochem*, 527(1-3):207–220, August 2000.

[473] M Nakata, H Nakatsuji, M Ehara, M Fukuda, K Nakata, and K Fujisawa. Variational calculations of fermion second-order reduced density matrices by semidefinite programming algorithm. *J. Chem. Phys.*, 114(19):8282–8292, May 2001.

[474] D. A. Mazziotti. Variational minimization of atomic and molecular ground-state energies via the two-particle reduced density matrix. *Phys. Rev. A*, 65:062511, Jun 2002. doi:10.1103/PhysRevA.65.062511.

[475] Z Zhao, B J Braams, M Fukuda, M L Overton, and J K Percus. The reduced density matrix method for electronic structure calculations and the role of three-index representability conditions. *J. Chem. Phys.*, 120(5):2095–2104, February 2004.

[476] G. Gidofalvi and D. A. Mazziotti. Spin and symmetry adaptation of the variational two-electron reduced-density-matrix method. *Phys. Rev. A*, 72:052505, Nov 2005. doi:10.1103/PhysRevA.72.052505.

[477] D A Mazziotti. Quantum chemistry without wave functions: two-electron reduced density matrices. *Acc. Chem. Res.*, 39(3):207–215, March 2006.

[478] D. A. Mazziotti. Anti-hermitian part of the contracted schrödinger equation for the direct calculation of two-electron reduced density matrices. *Phys. Rev. A*, 75:022505, Feb 2007. doi:10.1103/PhysRevA.75.022505.

[479] E Cancès, G Stoltz, and M Lewin. The electronic ground-state energy problem: a new reduced density matrix approach. *J. Chem. Phys.*, 125(6):64101, August 2006.

[480] D. A. Mazziotti. Anti-hermitian part of the contracted schrödinger equation for the direct calculation of two-electron reduced density matrices. *Phys. Rev. A*, 75:022505, Feb 2007. doi:10.1103/PhysRevA.75.022505.

[481] R M Erdahl. The lower bound method for density matrices and semidefinite programming. In *Reduced-Density-Matrix Mechanics: With Application to Many-Electron Atoms and Molecules*, Advances in chemical physics, pages 61–91. John Wiley & Sons, Inc., Hoboken, NJ, USA, March 2007.

[482] S Kais. Entanglement, electron correlation, and density matrices. In *Reduced-Density-Matrix Mechanics: With Application to Many-Electron Atoms and Molecules*, Advances in Chemical Physics, pages 493–535. John Wiley & Sons, Inc., Hoboken, NJ, USA, March 2007.

[483] G Gidofalvi and D A Mazziotti. Active-space two-electron reduced-density-matrix method: complete active-space calculations without diagonalization of the N-electron hamiltonian. *J. Chem. Phys.*, 129(13):134108, October 2008.

[484] D. A. Mazziotti. Parametrization of the two-electron reduced density matrix for its direct calculation without the many-electron wave function. *Phys. Rev. Lett.*, 101: 253002, Dec 2008. doi:10.1103/PhysRevLett.101.253002.

[485] David A Mazziotti. Two-electron reduced density matrix as the basic variable in many-electron quantum chemistry and physics. *Chem. Rev.*, 112(1):244–262, January 2012.

[486] D. A. Mazziotti. Structure of fermionic density matrices: Complete n-representability conditions. *Phys. Rev. Lett.*, 108:263002, Jun 2012. doi:10.1103/PhysRevLett.108.263002.

[487] B Verstichel, H van Aggelen, W Poelmans, and D Van Neck. Variational two-particle density matrix calculation for the hubbard model below half filling using spin-adapted lifting conditions. *Phys. Rev. Lett.*, 108:213001, May 2012. doi:10.1103/PhysRevLett.108.213001.

[488] W Poelmans, M Van Raemdonck, B Verstichel, S De Baerdemacker, A Torre, L Lain, G E Massaccesi, D R Alcoba, P Bultinck, and D Van Neck. Variational optimization of the second-order density matrix corresponding to a seniority-zero configuration interaction wave function. *J. Chem. Theory Comput.*, 11(9):4064–4076, September 2015. doi:10.1021/acs.jctc.5b00378.

[489] A W Schlimgen, C W Heaps, and D A Mazziotti. Entangled electrons foil synthesis of elusive low-valent vanadium oxo complex. *J. Phys. Chem. Lett.*, 7(4):627–631, February 2016.

[490] S Hemmatiyan, M Sajjan, A W Schlimgen, and D A Mazziotti. Excited-state spectra of strongly correlated molecules from a reduced-density-matrix approach. *J. Phys. Chem. Lett.*, 9(18):5373–5378, September 2018.

[491] D R Alcoba, A Torre, L Lain, G E Massaccesi, O B Oña, E M Honoré, W Poelmans, D Van Neck, P Bultinck, and S De Baerdemacker. Direct variational determination of the two-electron reduced density matrix for doubly occupied-configuration-interaction wave functions: The influence of three-index N-representability conditions. *J. Chem. Phys.*, 148(2):024105, January 2018.

[492] J-N Boyn, J Xie, J S Anderson, and D A Mazziotti. Entangled electrons drive a non-superexchange mechanism in a cobalt quinoid dimer complex. *J. Phys. Chem. Lett.*, 11(12):4584–4590, June 2020.

[493] J Xie, J-N Boyn, A S Filatov, A J McNeece, D A Mazziotti, and J S Anderson. Redox, transmetalation, and stacking properties of tetrathiafulvalene-2,3,6,7-tetrathiolate bridged tin, nickel, and palladium compounds. *Chem. Sci.*, 11(4):1066–1078, December 2019.

[494] J-N Boyn and D A Mazziotti. Accurate singlet-triplet gaps in biradicals via the spin averaged anti-hermitian contracted schrödinger equation. *J. Chem. Phys.*, 154(13): 134103, April 2021.

[495] S Ewing and D A Mazziotti. Correlation-driven phenomena in periodic molecular systems from variational two-electron reduced density matrix theory. *J. Chem. Phys.*, 154(21):214106, June 2021.

[496] S Kim, J Chen, T Cheng, A Gindulyte, J He, S He, Q Li, B A Shoemaker, P A Thiessen, B Yu, L Zaslavsky, J Zhang, and E E Bolton. PubChem in 2021: new data content and improved web interfaces. *Nucleic Acids Research*, 49(D1):D1388–D1395, 11 2020. ISSN 0305-1048. doi:10.1093/nar/gkaa971.

[497] J M Montgomery and D A Mazziotti. Maple's quantum chemistry package in the chemistry classroom. *J. Chem. Educ.*, 97(10):3658–3666, October 2020.

[498] Maplesoft. *Maple*. Maplesoft, a division of Waterloo Maple Inc., 2022.

[499] F Chollet. Keras, 2015.

[500] Claude E. Shannon. A mathematical theory of communication. *The Bell System Technical Journal*, 27(3):379–423, 1948. doi:10.1002/j.1538-7305.1948.tb01338.x.

[501] L. V. Butov. Exciton condensation in coupled quantum wells. *Solid State Commun.*, 127(2):89–98, 2003. ISSN 0038-1098. doi:10.1016/S0038-1098(03)00312-0.

[502] Jung-Jung Su and Allan H. MacDonald. Spatially indirect exciton condensate phases in double bilayer graphene. *Phys. Rev. B*, 95(4):045416, January 2017. doi:10.1103/PhysRevB.95.045416.

[503] M. Zarenia, A. Perali, D. Neilson, and F. M. Peeters. Enhancement of electron-hole superfluidity in double few-layer graphene. *Sci. Rep.*, 4(1):7319, 2014. ISSN 2045-2322. doi:10.1038/srep07319.

[504] P. H. Handel and C. Kittel. Van der waals interactions and exciton condensation. *Proc. Natl. Acad. Sci.*, 68(12):3120–3121, 1971. ISSN 0027-8424. doi:10.1073/pnas.68.12.3120.

[505] M. Kellogg, J. P. Eisenstein, L. N. Pfeiffer, and K. W. West. Vanishing hall resistance at high magnetic field in a double-layer two-dimensional electron system. *Phys. Rev. Lett.*, 93:036801, July 2004. doi:10.1103/PhysRevLett.93.036801.

[506] Daniel Garisto. A brief etymology of particle physics, May 2017.

[507] Qiskit. Source code for qiskit.ignis.mitigation.measurement.fitters, November 2019.

[508] Ariadna J. Torres-Arenas, Qian Dong, Guo-Hua Sun, Wen-Chao Qiang, and Shi-Hai Dong. Entanglement measures of w-state in noninertial frames. *Phys. Lett. B*, 789: 93–105, 2019. doi:10.1016/j.physletb.2018.12.010.

[509] A. P. Drozdov, M. I. Eremets, I. A. Troyan, V. Ksenofontov, and S. I. Shylin. Conventional superconductivity at 203 kelvin at high pressures in the sulfur hydride system. *Nature*, 525(7567):73–76, 2015. doi:10.1038/nature14964.

[510] N. Meshkov, A. J. Glick, and H. J. Lipkin. Validity of many-body approximation methods for a solvable model: (ii). linearization procedures. *Nucl. Phys.*, 62(2):199–210, 1965. ISSN 0029-5582. doi:10.1016/0029-5582(65)90863-1.

[511] A. J. Glick, H. J. Lipkin, and N. Meshkov. Validity of many-body approximation methods for a solvable model: (iii). diagram summations. *Nucl. Phys.*, 62(2):211–224, 1965. ISSN 0029-5582. doi:10.1016/0029-5582(65)90864-3.

[512] E. Hanamura and H. Haug. Condensation effects of excitons. *Phys. Rep.*, 33(4):209–284, 1977. ISSN 0370-1573. doi:10.1016/0370-1573(77)90012-6.

[513] M. Yu. Kharitonov and K. B. Efetov. Electron screening and excitonic condensation in double-layer graphene systems. *Phys. Rev. B*, 78:241401, December 2008. doi:10.1103/PhysRevB.78.241401.

[514] qiskit 2021. Qiskit 0.28.0 documentation, June 2021.

[515] N. C. Rubin and D. A. Mazziotti. Strong electron correlation in materials from pair-interacting model Hamiltonians. *J. Phys. Chem. C*, 119(26):14706–14713, 2015. doi:10.1021/jp5130266.

[516] F. Bloch. Off-diagonal long-range order and persistent currents in a hollow cylinder. *Phys. Rev.*, 137:A787–A795, February 1965. doi:10.1103/PhysRev.137.A787.

[517] Lawrence J. Dunne. High-temperature superconductivity and long-range order in strongly correlated electronic systems. *Int. J. Quantum Chem.*, 115(20):1443–1458, 2015. ISSN 1097-461X. doi:10.1002/qua.24959.

[518] K. Pelzer, L. Greenman, G. Gidofalvi, and D. A. Mazziotti. Strong correlation in acene sheets from the active-space variational two-electron reduced density matrix method: Effects of symmetry and size. *J. Phys. Chem. A*, 115(22):5632–5640, 2011. doi:10.1021/jp2017192.

[519] P. B. Littlewood. Models of coherent exciton condensation. *J. Phys. Condens. Matter*, 16:S3597–S3620, 2004. doi:10.1088/0953-8984/16/35/003.

[520] D. Snoke. Spontaneous bose coherence of excitons and polaritons. *Science*, 298:1368–1372, 2002. doi:10.1126/science.1078082.

[521] A. A. High. Spontaneous coherence in a cold exciton gas. *Nature*, 483:584–588, 2012.

[522] J. A. Seamons, C. P. Morath, J. L. Reno, and M. P. Lilly. Coulomb drag in the exciton regime in electron-hole bilayers. *Phys. Rev. Lett.*, 102:26804, 2009.

[523] K. Yang. Quantum ferromagnetism and phase transitions in double-layer quantum Hall systems. *Phys. Rev. Lett.*, 72:732–735, 1994.

[524] K. Moon. Spontaneous interlayer coherence in double-layer quantum Hall systems: Charged vortices and Kosterlitz-Thouless phase transitions. *Phys. Rev. B*, 51:5138–5170, 1995.

[525] R. V. Gorbachev, A. K. Geim, M. I. Katsnelson, K. S. Novoselov, T. Tudorovskiy, I. V. Grigorieva, A. H. MacDonald, S. V. Morozov, K. Watanabe, T. Taniguchi, and L. A. Ponomarenko. Strong Coulomb drag and broken symmetry in double-layer graphene. *Nat. Phys.*, 8:896, October 2012. doi:10.1038/nphys2441.

[526] Brian Skinner. Interlayer excitons with tunable dispersion relation. *Phys. Rev. B*, 93: 235110, June 2016. doi:10.1103/PhysRevB.93.235110.

[527] G. H. Lee. Electron tunneling through atomically flat and ultrathin hexagonal boron nitride. *Appl. Phys. Lett.*, 99:243114, 2011.

[528] B. N. Narozhny and A. Levchenko. Coulomb drag. *Rev. Mod. Phys.*, 88:25003, 2016. doi:10.1103/RevModPhys.88.025003.

[529] X.-G. Wen and A. Zee. Neutral superfluid modes and 'magnetic' monopoles in multilayered quantum Hall systems. *Phys. Rev. Lett.*, 69:1811–1814, 1992.

[530] A. R. Champagne, A. D. K. Finck, J. P. Eisenstein, L. N. Pfeiffer, and K. W. West. Charge imbalance and bilayer two-dimensional electron systems at nt = 1. *Phys. Rev. B*, 78:205310, 2008.

[531] A. Kou, B. E. Feldman, A. J. Levin, B. I. Halperin, K. Watanabe, T. Taniguchi, and A. Yacoby. Electron-hole asymmetric integer and fractional quantum Hall effect in bilayer graphene. *Science*, 345(6192):55–57, 2014. ISSN 0036-8075. doi:10.1126/science.1250270.

[532] J. Lambert and R. Côté. Quantum Hall ferromagnetic phases in the landau level n = 0 of a graphene bilayer. *Phys. Rev. B*, 87:115415, 2013. doi:10.1103/PhysRevB.87.115415.

[533] P. Maher, L. Wang, Y. Gao, C. Forsythe, T. Taniguchi, K. Watanabe, D. Abanin, Z. Papić, P. Cadden-Zimansky, J. Hone, P. Kim, and C. R. Dean. Tunable fractional quantum Hall phases in bilayer graphene. *Science*, 345(6192):61–64, 2014. ISSN 0036-8075. doi:10.1126/science.1252875.

[534] K. Lee, B. Fallahazad, J. Xue, D. C. Dillen, K. Kim, T. Taniguchi, K. Watanabe, and E. Tutuc. Chemical potential and quantum Hall ferromagnetism in bilayer graphene. *Science*, 345(6192):58–61, 2014. ISSN 0036-8075. doi:10.1126/science.1251003.

[535] L. Wang. One-dimensional electrical contact to a two-dimensional material. *Science*, 342:614–617, 2013.

[536] N. P. R. Hill. Frictional drag between parallel two-dimensional electron gases in a perpendicular magnetic field. *J. Phys. Condens. Matter*, 8:L557–L562, 1996.

[537] L. Vandenberghe and S. Boyd. Semidefinite programming. *SIAM Rev.*, 38(1):49–95, 1996. doi:10.1137/1038003.

[538] C. Song, K. Xu, W. Liu, C.-P. Yang, S.-B. Zheng, H. Deng, Q. Xie, K. Huang, Q. Guo, L. Zhang, and et al. 10-qubit entanglement and parallel logic operations with a superconducting circuit. *Phys. Rev. Lett.*, 119(18), 2017. doi:10.1103/physrevlett.119.180511.

[539] A. Schilling, M. Cantoni, J. D. Guo, and H. R. Ott. Superconductivity above 130 K in the Hg–Ba–Ca–Cu–O system. *Nature*, 363(6424):56–58, 1993. doi:10.1038/363056a0.

[540] J. A. Flores-Livas, L. Boeri, A. Sanna, G. Profeta, R. Arita, and G. Eremets. A perspective on conventional high-temperature superconductors at high pressure: Methods and materials. *Phys. Rep.*, 856:1–78, 2020. doi:10.1016/j.physrep.2020.02.003.

[541] M. Somayazulu, M. Ahart, A. K. Mishra, Z. M. Geballe, M. Baldini, Y. Meng, V. V. Struzhkin, and R. J. Hemley. Evidence for superconductivity above 260 K in lanthanum superhydride at megabar pressures. *Phys. Rev. Lett.*, 122(2), 2019. doi:10.1103/physrevlett.122.027001.

[542] J. G. Bednorz and K. A. Müller. Possible high T_c superconductivity in the Ba–La–Cu–O system. *Z. Phys. B. - Condensed Matter*, 64:189–193, 1986. doi:10.1007/BF01303701.

[543] Isabel C. Santos, Vasco Gama, Sandra Rabaça, Luís F. Veiros, Fernando Nogueira, José A. Paixão, and Manuel Almeida. Structural diversity in conducting bilayer salts (cnb-edt-ttf)4a. *CrystEngComm*, 22:8313–8321, 2020. doi:10.1039/D0CE01433H.

[544] Pubchem Benzene. Pubchem compound summary for cid 241, benzene, 2022.

[545] Pubchem Aniline. Pubchem compound summary for cid 6115, aniline, 2022.

[546] Pubchem Fluorobenzene. Pubchem compound summary for cid 10008, fluorobenzene, 2022.

[547] L. Cincio, Y. Subaşı, A. T. Sornborger, and P. J. Coles. Learning the quantum algorithm for state overlap. *New J. Phys.*, 20(11):113022, 2018. doi:10.1088/1367-2630/aae94a.

[548] P. Murali, J. M. Baker, A. Javadi-Abhari, F. T. Chong, and M. Martonosi. Noise-adaptive compiler mappings for noisy intermediate-scale quantum computers. *Proceedings of the Twenty-Fourth International Conference on Architectural Support for Programming Languages and Operating Systems*, April 2019. doi:10.1145/3297858.3304075.

[549] N. M. Linke, S. Johri, C. Figgatt, K. A. Landsman, A. Y. Matsuura, and C. Monroe. Measuring the rényi entropy of a two-site fermi-hubbard model on a trapped ion quantum computer. *Phys. Rev. A*, 98(5), 2018. doi:10.1103/physreva.98.052334.

[550] K. Temme, S. Bravyi, and J. M. Gambetta. Error mitigation for short-depth quantum circuits. *Phys. Rev. Lett.*, 119(18), March 2017. doi:10.1103/physrevlett.119.180509.

[551] I. B. M. Q-Team. IBM-Q-5 Rome backend specification v1.0.0, 2020.

[552] Y. Subaşı, L. Cincio, and P. J. Coles. Entanglement spectroscopy with a depth-two quantum circuit. *J. Phys. A: Math. Theor.*, 52(4):044001, July 2019. doi:10.1088/1751-8121/aaf54d.

[553] M. R. Perelshtein, A. I. Pakhomchik, A. A. Melnikov, A. A. Novikov, A. Glatz, G. S. Paraoanu, V. M. Vinokur, and G. B. Lesovik. Advanced quantum supremacy using a hybrid algorithm for linear systems of equations. *arXiv*, April 2020. doi:https://arxiv.org/pdf/2003.12770.pdf.

[554] M. Bianucci and M. Bologna. About the foundation of the kubo generalized cumulants theory: A revisited and corrected approach. *J. Stat. Mech. Theory Exp.*, 2020(4): 043405, April 2020. doi:10.1088/1742-5468/ab7755.

[555] T. Juhász and D. A. Mazziotti. The cumulant two-particle reduced density matrix as a measure of electron correlation and entanglement. *J. Chem. Phys.*, 125(17):174105, 2006. doi:10.1063/1.2378768.

[556] D. R. Alcoba, R. C. Bochicchio, L. Lain, and A. Torre. On the measure of electron correlation and entanglement in quantum chemistry based on the cumulant of the second-order reduced density matrix. *J. Chem. Phys.*, 133(14):144104, 2010. doi:10.1063/1.3503766.

[557] Y. Pavlyukh and J. Berakdar. Accessing electronic correlations by half-cycle pulses and time-resolved spectroscopy. *Phys. Rev. A*, 90:053417, November 2014. doi:10.1103/PhysRevA.90.053417.

[558] E. Ramos-Cordoba, P. Salvador, and E. Matito. Separation of dynamic and nondynamic correlation. *Phys. Chem. Chem. Phys.*, 18:24015–24023, 2016. doi:10.1039/C6CP03072F.

[559] O. Werba, A. Raeber, K. Head-Marsden, and D. A. Mazziotti. Signature of van der waals interactions in the cumulant density matrix. *Phys. Chem. Chem. Phys.*, 21: 23900–23905, 2019. doi:10.1039/C9CP03361K.

[560] J. E. Harriman. Reduced-density-matrix cumulants and correlation. *Phys. Rev. A*, 75: 032513, March 2007. doi:10.1103/PhysRevA.75.032513.

[561] J. T. Skolnik and D. A. Mazziotti. Cumulant reduced density matrices as measures of statistical dependence and entanglement between electronic quantum domains with application to photosynthetic light harvesting. *Phys. Rev. A*, 88:032517, September 2013. doi:10.1103/PhysRevA.88.032517.

[562] T. H. Dunning. Gaussian basis sets for use in correlated molecular calculations. i. the atoms boron through neon and hydrogen. *J. Chem. Phys.*, 90(2):1007–1023, 1989. doi:10.1063/1.456153.

[563] W. J. Hehre, R. F. Stewart, and J. A. Pople. Self-consistent molecular-orbital methods. i. use of gaussian expansions of slater-type atomic orbitals. *J. Chem. Phys.*, 51(6): 2657–2664, 1969. doi:10.1063/1.1672392.

[564] D. A. Mazziotti. Approximate solution for electron correlation through the use of schwinger probes. *Chemical Physics Letters*, pages 419–427, 1998.

[565] S. Pannir-Sivajothi, J. A. Campos-Gonzalez-Angulo, L. A. Martínez-Martínez, S. Sinha, and J. Yuen-Zhou. Driving chemical reactions with polariton condensates. *arXiv*, June 2021.

[566] Jonathan Schmidt, Carlos L. Benavides-Riveros, and Miguel A. L. Marques. Reduced density matrix functional theory for superconductors. *Phys. Rev. B*, 99(22):224502, jun 2019. doi:10.1103/physrevb.99.224502.

[567] S. Boixo, S. V. Isakov, V. N. Smelyanskiy, R. Babbush, N. Ding, Z. Jiang, M. J. Bremner, J. M. Martinis, and H. Neven. Characterizing quantum supremacy in near-term devices. *Nat. Phys.*, 14(6):595–600, June 2018.

[568] A. Erhard, J. J. Wallman, L. Postler, M. Meth, R. Stricker, E. A. Martinez, P. Schindler, T. Monz, J. Emerson, and R. Blatt. Characterizing large-scale quantum computers via cycle benchmarking. *Nat. Commun.*, 10(1):5347, November 2019.

[569] T. J. Proctor, A. Carignan-Dugas, K. Rudinger, E. Nielsen, R. Blume-Kohout, and K. Young. Direct randomized benchmarking for multiqubit devices. *Phys. Rev. Lett.*, 123:030503, Jul 2019. doi:10.1103/PhysRevLett.123.030503.

[570] R. Harper, S. T. Flammia, and J. J. Wallman. Efficient learning of quantum noise. *Nat. Phys.*, 16(12):1184–1188, December 2020.

[571] K. Wright, K. M. Beck, S. Debnath, J. M. Amini, Y. Nam, N. Grzesiak, J.-S. Chen, N. C. Pisenti, M. Chmielewski, C. Collins, K. M. Hudek, J. Mizrahi, J. D. Wong-Campos, S. Allen, J. Apisdorf, P. Solomon, M. Williams, A. M. Ducore, A. Blinov, S. M. Kreikemeier, V. Chaplin, M. Keesan, C. Monroe, and J. Kim. Benchmarking an 11-qubit quantum computer. *Nat. Commun.*, 10(1):5464, November 2019.

[572] A. Cornelissen, J. Bausch, and A. Gilyén. Scalable benchmarks for gate-based quantum computers, 2021.

[573] I. G. Ross. Calculations of the energy levels of acetylene by the method of antisymmetric molecular orbitals, including $\sigma - \pi$ interaction. *Transactions of the Faraday Society*, 48:973, 1952. doi:10.1039/tf9524800973.

[574] M. R. Schafroth. Theory of superconductivity. *Phys. Rev.*, 96:1442–1442, Dec 1954. doi:10.1103/PhysRev.96.1442.